UNIVERSITY OF OKLAHOMA
GRADUATE COLLEGE

QUANTITATIVE PRECIPITATION ESTIMATION WITH PHASED ARRAY RADARS

A DISSERTATION
SUBMITTED TO THE GRADUATE FACULTY
in partial fulfillment of the requirements for the
Degree of
DOCTOR OF PHILOSOPHY

by AIMEE MICHELLE MATLAND
Norman, Oklahoma
2026

Downloaded from SHAREOK. Persistent Handle URL: https://hdl.handle.net/11244/342399

QUANTITATIVE PRECIPITATION ESTIMATION WITH PHASED ARRAY RADARS

A DISSERTATION APPROVED FOR THE
SCHOOL OF METEOROLOGY

BY THE COMMITTEE CONSISTING OF

Dr. Pierre Kirstetter (Chair)

Dr. Robert Palmer

Dr. Alexander Ryzhkov

Dr. Greg McFarquhar

Dr. Jessica Ruyle

©Copyright by AIMEE MICHELLE MATLAND 2026

All Rights Reserved.

Acknowledgments

I sincerely thank my academic advisors, Dr. Pierre Kirstetter and Dr. Robert Palmer, for engaging in spirited and sometimes argumentative dialogue that has challenged me and helped me become a more robust researcher. I thank my committee members, Dr. Greg McFarquhar, Dr. Alexander Ryzhkov, and Dr. Jessica Ruyle, for their guidance and feedback. I am grateful to my colleagues at NOAA/NSSL, Jacob Carlin and Petar Bukovcic, for their collaboration and guidance on useful tools that enhanced the quality of this research. I thank NASA and the science collaborators on the FINESST Grant for their inputs and participation. For the PROWEX campaign, I would like to thank the Horus team engineers and Jonah Pehl, who performed data processing, for their dedication and team-driven results. Beyond this, I would like to thank Dr. Robert Palmer for advocating my involvement in the ARRC Strategic Planning Process, to the students involved in the ARRC Student Affairs Committee for their inspiration and ideas for the future. I thank Yagmur Derin for helping me exercise and demonstrate true teamwork as a part of the IPC14 planning process and both her and Noah Brauer for being excellent collaborators on projects external to this dissertation that enhanced my broader understanding of the field of precipitation science. I would also like to thank Dr. Kirstetter and Dr. Watters for involving me in the planning for the Baseline Precipitation Network (BSPN) project. I also acknowledge NOAA and NASA for providing access to critical datasets integral to this work. Finally, I thank my family for their encouragement throughout this journey.

Table of Contents

Acknowledgments iv

List of Tables viii

List of Figures ix

Abstract xxii

1 Introduction 1
1.1 Motivation 1
1.1.1 Current Operational Radar Gaps for QPE 3
1.1.2 Emerging Opportunities with Phased Array Radar 5
1.2 Shared Insights for QPE Innovation 7
1.2.1 Community and Stakeholder Insights 9
1.3 Science Questions and Objectives 28
1.3.1 Structure of the Dissertation 32

2 Background 34
Background 39
2.0.1 Precipitation Types 39
2.0.2 The Particle Size Distribution 43
2.1 Quantitative Precipitation Estimation 46
2.2 Polarimetric Radar 46
2.2.1 Hardware: Dish versus Phased Array 49
2.2.2 Sampling of the Atmosphere in Time and Space 52
2.3 Field Campaigns with Polarimetric Radar 53
2.3.1 The Horus Phased Array Radar and Science Testing Alongside Radar System Integration 54
2.4 Polarimetric Radar Variables 66
2.4.1 Equivalent Reflectivity Factor (Z) 67
2.4.2 Differential Reflectivity (Z_{dr}) 69
2.4.3 Correlation Coefficient (ρ_{hv}) 70
2.4.4 Backscatter Differential Phase (ϕ_{dp}) and Specific Differential Phase (K_{dp}) 70

2.4.5 Specific Attenuation (A) and Differential Specific Attenuation (A_{dp}) . . . 71
2.4.6 Non-polarimetric Variables: Radial Velocity (v_r) and Spectrum Width (σ_v) . . . 72
2.5 Spectral Bin Microphysics Model . . . 72
2.6 Microphysical Retrievals from Radar Data . . . 78
2.6.1 Traditional Approaches and Metrics . . . 78
2.6.2 Polarimetric Approaches . . . 82
2.6.3 Detecting Processes in the Atmosphere . . . 83
2.7 Spaceborne Radar QPE and Convective Fluxes . . . 86
2.7.1 Bridging Satellite Spatial Limitations . . . 86
2.7.2 Bridging Satellite Temporal Limitations with Ground-Based Radar 87

3 Time Continuity: QPE and Radar Variable Improvements . . . 90
3.1 Impact of Enhanced Temporal Sampling on Z . . . 94
3.1.1 Data . . . 94
3.1.2 Methods . . . 97
3.2 Integrating Temporal Resolution Requirements . . . 105
3.2.1 Variogram Analysis . . . 105
3.2.2 Uncertainty of Radar Reflectivity . . . 107
3.2.3 Uncertainty for Quantitative Precipitation Estimation . . . 112
3.2.4 Micro-Rain Radar Validation Study . . . 119
3.3 Balancing Data Quality and Revisit Time . . . 123

4 Space Continuity: QPE Improvements . . . 126
4.1 Continuity Equation for Radar-Estimated Mass . . . 126
4.2 Evaluating Continuity-Based Observables for QPE . . . 129
4.3 Association of Rain Rate with PAR Polarimetric Radar Variables and Derivatives . . . 155
4.4 Rank Correlation and Feature Selection for PAR Predictors of Rain Rate 159
4.5 Probabilistic Rain Rate Estimates at Fine Scales and Comparative Estimator Analysis . . . 161
4.6 Application of the Continuity Equation in Convection . . . 171

5 Satellite Opportunities: Enhancing the Continuity Framework . . . 186
5.1 Temporal Bridging of Sat Gaps with PAR . . . 186
5.1.1 Convective Weather Demonstration . . . 189
5.1.2 Analysis . . . 194
5.1.3 Conclusions . . . 198

5.2 NASA FINESST Proposal: Combining Radar Observations from Ground and Space . . . 199
5.2.1 Objectives . . . 205
5.2.2 Potential Sources of Uncertainty . . . 208
5.2.3 Future Applications . . . 210

6 Conclusions and Future Work . . . 211

7 Appendix A: Derivation of Reflectivity . . . 215

8 Appendix B: Derivation of Continuity Equation . . . 218
8.1 Radar Sensitivity to Hydrometeor Size . . . 218

9 Appendix C: Analysis of GPM Algorithm . . . 222
9.1 Introduction . . . 222
9.2 Methodology . . . 226
9.2.1 Dataset . . . 226
9.2.2 K-means Clustering . . . 231
9.3 Results . . . 233
9.3.1 Dataset Observations . . . 233
9.3.2 Convective K-means Clustering Results . . . 236
9.3.3 Factors Contributing to Bias . . . 239
9.3.4 Supervised Learning R-D_m Algorithm Improvements . . . 243
9.4 Summary and Considerations for Future Work . . . 245

10Appendix D: Blueprint for Future Field Campaigns: Shared Leadership and Inclusive Decision-Making . . . 256

Reference List . . . 264

List of Tables

2.1 Proposed instruments for the PROWEX campaign 61

3.1 Horus PAR settings and observed event information. Horus is located at 35.18 Latitude ,-97.45 Longitude operating in an RHI mode. (Palmer et al. (2023b) and `https://arrc.ou.edu/radar_horus.html`) 95

3.2 MRR Settings and event information for the considered MRR data located at 34.98 Latitude, -97.53 Longitude 97

4.1 Performance of MRR R estimators using different combinations of Z the temporal and vertical derivatives of Z. 136

4.2 Performance metrics (correlation and bias) for rain rate estimators using different linear combinations of predictors for the mean (μ) and standard deviation (σ) components of the GAMLSS model. 171

5.1 Radar Specifications for the considered data (NASA (2023a), Palmer et al. (2023b), Masaki et al. (2020), and `https://arrc.ou.edu/radar_horus.html`) 190

9.1 MRMS Variables derived from a horizontal 1 km x 1 km grid matched to each 5 km diameter GPM-DPR beam surface footprint provided alongside DPR variables listed in Table 9.2 for the 2-year dataset covered in this study 227

9.2 DPR Level-2 products were included for each footprint provided alongside their associated footprint-centered latitude and longitude for the 2-year dataset covered in this study. Variables are analogous to those discussed in Iguchi et al. (2010) and the DPR L2/3 Product Format Documentation Version 5.3 229

List of Figures

1.1 IPC-14 Student and Early Career Workshop focus areas were identified with the use of a pre-conference survey distributed to the community through advertisements to working groups and universities in the area of precipitation science. 11

1.2 Inspired by the work of Moncrieff (2010), this figure shows the interconnected Earth-system components that collectively influence atmospheric processes. While past work has improved understanding of the ocean, land, cryosphere, atmospheric chemistry, and biogeochemistry, a critical unresolved element is convective organization, whose feedbacks extend throughout the full range of atmospheric scales. 13

1.3 In-conference poll illustrating the primary end-use applications reported by student and early-career workshop participants. 14

1.4 Summary of participant-indicated spatial and temporal scales, showing preferred resolutions from 100 m to 1 km and timescales from 1 min to 1 hr 15

1.5 Rain-rate error versus sampling interval. Faster PAR sampling reduces error from about 0.3 to 0.15 when the true rain rate is 1 in/hr. 31

2.1 Precipitation is understood by developed theories that cover different scales of motion. The planetary (or large) scale of motion, the synoptic scale (approximately up to the length across the contiguous United States and lasting 1 day to 1 week), the mesoscale (approximately the length of the state of Oklahoma and lasting 1 hr to 1 day), and the microscale. 35

2.2 Stratiform precipitation tends to be characterized by low rain rates, less than about 10 mm/hr, and weak vertical air motion, less than about 2 m/s. Convective precipitation is characterized by higher rain rates and stronger vertical air motion (Houze Jr (1997a)). 40

2.3 Within an observed volume of space (e.g., radars illuminate volumes of space), particles come in many shapes and sizes (e.g., with different equivalent diameters, D). The PSD represents the number of drops of each diameter. In microphysics models, this can be represented either as discrete diameter bins or as a continuous distribution (e.g., a gamma or exponential distribution). 44

2.4 Both PAR and dish-style radars (center) are capable of focusing transmitted and received energy to achieve narrow beamwidths, can be designed as dual-polarimetric systems, and often include a radome. Traditional dish-style radars (left) feature a single transmit and receive beam that, due to mechanical steering, can take 5-6 min to complete a VCP (e.g., NEXRAD), which inherently features gaps in vertical coverage. PAR (right) can simultaneously receive any number of programmed beams to help close gaps in vertical coverage. (Dish radar image from NOAA National Severe Storms Laboratory (2025b)) 51

2.5 Radar reflectivity (dBZ) versus slant-range (km) to 10 km for an observation of a convective precipitating system observed on July 3, 2025. This figure shows the radar blind range with the use of PPC+ to be at an estimated 691 m from the antenna, which is a great improvement over the 4.8 km blind range observed without the use of PPC. 56

2.6 Proposed operating scenarios for the PROWEX campaign are shown including (a) a crossed scan with Horus operating with an S-band RHI crossed with RaXPol operating orthogonally with an RHI, (b) RaXPol crossing paths in an RHI with both Horus and PX-1000, and (c) Horus RHIs crossed with a vertically pointing RaXPol at the location of the reference precipitation observation at KAEFS. 62

2.7 The radar variables of Z, ϕ_{dp}, A, Z_{dr}, K_{dp}, and ρ_{hv} are conceptually summarized. Z is sensitive to the size of the drops, as this impacts the magnitude of the power scattered to the radar. ϕ_{dp} is impacted by the cumulative size and concentration through the whole path of travel of the radar wave. A practically provides the attenuation of the radar signal by each radar bin. Z_{dr} is impacted by the size and shape of hydrometeors, as these variables depend on power reflected back for two antenna polarizations. K_{dp} is the range derivative of ϕ_{dp} showing how ϕ_{dp} changes for each radar bin. ρ_{hv} is close to a value of 1 for volumes with particle homogeneity in returns for both polarizations. (Content from this figure has been adapted from material in Basara (2022)) . . . 68

2.8 Microphysical processes evolve as a function of time and height. For the 1D SBM model, a distribution of hydrometeors is set at some altitude in an initial thermodynamic environment defined by temperature (T), pressure (P), and relative humidity (RH). Then the model steps forward in time and progresses downwards in altitude as the particles fall. At each altitude and time step the distribution and thermodynamic environment are updated as the particles undergo processes like evaporation, sublimation, melting, shedding, and drop breakup. These processes evolve as a function of time and height. Symbol Key: Axial Ratio (AR), Particle Temperature (T_p), Mass of ice (mi), Mass of water inside the particle (mwi), Mass of water on the outside of the particle (mwo), density of moist air (ra), heat (h), saturation vapor pressure (es), mixing ratio (q), Reynolds number (R), Kinematic viscosity of air (nu), Particle terminal velocity (V_t) 75

2.9 The 1D SBM model generates microphysics particle properties like particle aspect ratio, orientation, density, liquid water content, and ice water content. These, as well as radar-influencing variables like temperature and radar wavelength, are fed into the radar operator, which performs T-matrix calculations to produce simulated polarimetric radar variables. 76

3.1 RHI observation depiction showing five minutes of radar reflectivity data collected every 0.76 s by the Horus phased array radar on July 7, 2024. Applications like QPE or validation with in-situ instruments require averaging the true underlying continuous signal over an application time domain, depicted by a box surrounding 30 s of data. Within this application interval, a representative value is shown with a red dashed line along with an uncertainty range delineated with dashed green lines. Any instantaneous observation taken to represent the interval may lack representativeness due to the underlying signal's range of variation within this time domain. 91

3.2 (a) Event 1 on July 7, 2024 at 23:20 UTC (b) Event 2 on May 12, 2023 at 1:38 UTC 96

3.3 An example of a gaussian variogram model fit (bold line) to an emperical variogram compiled from a single radar range gate from MRR observations separated by interdistances from 60 s to 2000 s. The variogram metrics discussed in this chapter are marked: sill, range, and nugget. . 101

3.4 July 7, 2024 (a) temporal range (decorrelation time), (b) sill, and (c) percent nugget and the May 12, 2023 (d) temporal range, (e) sill, and (f) percent nugget. 108

3.5 Histograms depicting the distribution of variogram parameters are shown for July 7, 2024 (a)temporal range (decorrelation time), (b) sill, and (c) percent nugget and the May 12, 2023 (d) temporal range, (e) sill, and (f) percent nugget. The temporal lag of 30 s, 2 min and 5 min are highlighted with the temporal range histograms (a, d) 109

3.6 Estimates of Z uncertainty, or expected temporal observation error $E_{o,t}$, are shown for July 7$^{\text{th}}$ over various temporal domains, T = (a) 5 min, (b) 2 min, and (c) 30 s. Estimates of Z are shown for May 12$^{\text{th}}$ for T = (d) 5 min, (e) 2 min, and (f) 30 s. Shaded areas represent the 25/75th percentiles and 10/90th percentiles of the uncertainty values for all the blocks in the considered dataset. 111

3.7 90th percentile of the population of additive rain rate error $|R_{ref} - R|$ with contours indicating the percent error $\frac{|R_{ref}-R|}{R_{ref}}$ plotted verses R_{ref} (y-axis) and sampling interval Δt (x-axis). 115

3.8 50th percentile of the population of additive rain rate error $|R_{reftrue} - R|$ with contours indicating the percent error $\frac{|R_{ref}-R|}{R_{ref}}$ plotted verses R_{ref} (y-axis) and sampling interval Δt (x-axis). 116

3.9 50th percentile of rain rate magnitude error (mm/hr, y-axis) versus resolution volume ($m^3 * 10^7$, x-axis in log-scale). July 7^{th} with T = (a) 5 min, (b) 2 min, and (c) 30 s. The rain rate error for the observed event on May 12^{th} is also shown for T = (d) 5 min, (e) 2 min, and (f) 30 s. 117

3.10 Correlation between the reference rain rate sampled at the minimum sampling interval (e.g. 0.76 s or 2 s) over $T = 30$ s (blue), 2 min (green), and 5 min (red) for (a) the July 7, 2024 case with a minimum sampling interval of 0.76 s and (b) the May 12, 2023 case with a minimum sampling interval of 2 s 119

3.11 MRR key variogram metrics for all four events in table 3.2 taken at the KAEFS observation site are combined into histograms showing the number of observation points for values of (a) range (minutes), (b) sill (dBZ^2), and (c) nugget (percent of sill). These metric values are shown versus altitude for each individual observation case for (d) range, (e) sill, and (f) nugget where the blue curves are variogram metrics estimated on September 30, 2021, the red curves on October 4, 2023, the yellow curves on April 13, 2019, and the purple curves on October 25, 2019. . 120

3.12 MRR estimates of r^2, square of the pearson correlation, between kriging estimated rain rates and in-situ 2DVD distrometer rain rates over various block sizes. Densely sampled kriging blocks (sampling every one minute) are indicated by blue markers and sparsely sampled blocks (sampling over one minute per block) indicated by red markers. This result is shown for 24-hour MRR observations over the days of October 4, 2023 (first plot), September 30, 2021 (second plot), April 13, 2019 (third plot), and October 25, 2019 (fourth plot). 122

4.1 A pseudo-PAR case study conducted on October 25, 2019, using a 24 GHz FMCW Micro Rain Radar co-located with a 2DVD disdrometer and two Parsivel2 disdrometers at KAEFS. The time-resolution of both measurements was 1-minute. (a) Photograph of the measurement site, (b) KAEFS location (farm icon) on WSR-88D composite reflectivity plot with radar site shown by a radar icon, and (c) 24-hour MRR attenuated reflectivity time–height plot. 131

4.2 (a) The 600 m altitude at which MRR reflectivity values are extracted. (b) Overlay of MRR reflectivity and disdrometer-observed R over 24 hours. (c) CFAD showing mean, 25th, and 75th percentiles of reflectivity for the day, illustrating precipitation behavior in the time and altitude derivatives of Z. (d) Horizontally incident T-matrix–derived Z outputs at S-band from the 1D SBM for hail melting in a downdraft from 4 km to the surface over 700 s. (e) Comparison of Z extracted at 600 m with ideal surface rain rate values, and CFAD of simulated Z over 700 s. . . 134

4.3 Comparison of the relationship between reflectivity height derivatives and R for observed (blue) and simulated (red) datasets. Both exhibit a power-law dependence, illustrating the consistent physical relationship between reflectivity gradients and rainfall intensity across distinct regimes. The observed curve corresponds to the warm-rain event at KAEFS, while the simulated curve corresponds to the hail-melting downdraft case from the SBM model. 137

4.4 Table listing the PAR variables referenced in this section and their notations 138

4.5 Radar variables (a) Z, (d) Z_{DR}, and (g) K_{DP} (left column) as well as their altitude derivatives (center column; (b) dZ/dh, (e) dZ_{DR}/dh, and (h) dK_{DP}/dh) and their time derivatives (right column; (c) dZ/dt, (f), and (i) dK_{DP}/dt) from time 10:19:61 UTC on August 8, 2023 near Norman, Oklahoma. The 0° C isotherm is marked by a horizontal black line at 4.5 km in altitude. An angled dashed black line marks a zone of near-surface beam blockage in sub-figures a and b. All variables are considered to be quasi-continuous in space and time; each RHI scan is completed within 16 s. 143

4.6 MRMS surface precipitation rate collocated with the radar variables and their derivatives is shown in Figure 4.5 at 10:18 UTC. 144

4.7 R can be derived at every range bin from PAR returns using an algorithm of choice. This work considers a probabilistic R estimate using an additive regression model to predict R from unique polarimetric PAR variables. 151

4.8 A composite Z extracted from the MRMS operational product viewer shows the spatial coverage of the frontal system near Norman, Oklahoma (USA), on August 8, 2023, that contained localized hail at (a) the measurement start time of 10:16 UTC, (b) the measurement end time of 10:34 UTC (National Severe Storms Laboratory, NOAA (2024)), and (c) a sounding taken at 12 UTC in Norman revealing a freezing level near 4.5 km (University of Wyoming Department of Atmospheric Science (2023)). 153

4.9 Target PAR horizontal latitude/longitude samples relative to MRMS latitude/longitude locations. 154

4.10 Logic flow diagram for training and estimating the predictand (R) given an input set of PAR variable predictors (PAR variables). The predictors are first quality controlled to remove extreme outliers and redundant variables or variables with negligible correlation to the predictand by referencing a rank correlation matrix. A GAMLSS feature selection is performed to down-select important variables for predicting R. The selected variables for the mean and the standard deviation σ, are trained to fit the predictand as a summation of penalized splines. The resulting predictand represents both the expected value and the variability of the R. 155

4.11 Conditional distributions of MRMS R values in the y-axis relative to the radar variables in the x-axis (first column), the time derivative of radar variables in the x-axis (second column), and the altitude derivative of the radar variables in the x-axis (third column). In each panel, the thick black line represents the median (50th percentile), the dark gray-shaded region represents the area between the 25th and 75th percentiles, and the light gray-shaded region represents the area between the 10th and 90th percentiles. 156

4.12 Considered and selected predictors for the estimation of mean R resulting in a trained probabilistic estimator with terms $\mu(dZ/dt,\ Z_{\mathrm{DR}},\ dZ_{\mathrm{DR}}/dt,\ K_{\mathrm{DP}},\ dK_{\mathrm{DP}}/dh)$. (a) GAMLSS is used to select these predictors and (b) generate continuous probabilistic R estimates every 16 s. (c) A predictor sensitivity analysis shows the highest correlation to be with the inclusion of all selected PAR variables. It is compared to correlations and bias metrics for estimators using predictors of Z only polarimetric variables, and derivatives only from the set of considered predictors. . . 160

4.13 Time series of Horus estimated probabilistic QPE at various distances from the radar, including the estimated median (center black curve), 25th and 75th percentiles (inner curves), and 90th and 10th percentiles (outer curves). The included training data (MRMS gauge corrected Rs) at each distance from the radar is marked in red and constitutes 14 percent of the total continuous MRMS data set. Error bars are overlaid on the MRMS Rs to indicate the potential for time errors by the MRMS data capture. 162

4.14 Scatter plot of MRMS R vs. estimated R for various GAMLSS-based estimators. 163

4.15 Linear correlation, explained variance, and bias table for various GAMLSS-based estimators relative to R 164

4.16 Density plot of uncertainty values for various GAMLSS-based estimators: (red) an estimator including all chosen PAR variables as listed in Figure 4.12, (green) an estimator only including Z as a predictor, (orange) an estimator only considering the standard radar variables from 4.12, and (purple) an estimator only considering the altitude and time derivative predictors from 4.12 165

4.17 The PX-1000 X-band polarimetric radar system is used for high-resolution precipitation observations. 167

4.18 Observed precipitation structure and intensity during the study period, as measured by the PX-1000 radar. 168

4.19 Reflectivity (Z), the time derivative of reflectivity (dZ/dt), and the height derivative of reflectivity (dZ/dh) are derived from PX-1000 radar profiles. 169

4.20 Example of the GAMLSS (Generalized Additive Model for Location, Scale, and Shape) regression fit used to estimate rain rate from derivative-based predictors. 169

4.21 Time series of rain rate estimation results showing observed and modeled values over the study period. 170

4.22 Photographs of the EF1 tornado observed near Norman, Oklahoma, on June 3, 2025. Panels (a) and (b) show two views of the same tornado as it moved east toward the Canadian River. (Media (2025),Compilations (2025)). 172

4.23 (a) Approximate path of the June 3, 2025, Norman, OK, tornado relative to the Horus radar and NSSL's TOTAL trailer at the Lloyd Noble Center. (b) Zoomed view of the instrument deployment showing the locations of Horus and the TOTAL disdrometer. (Compilations (2025)). 173

4.24 (a) Photograph of the Horus mobile radar taken prior to the June 3, 2025 convective event. (b) Disdrometer-derived rain rates during the event, which reached values up to 150 mm/hr. 174

4.25 MRMS observations during the June 3, 2025 event. (a) Low-Level Rotation (LLR) exceeding 0.014 at 22:00 UTC near the tornado path. (b) Composite reflectivity at 22:26 UTC, showing maximum values up to 55 dBZ, indicative of heavy rainfall. 174

4.26 Radial Doppler velocity from Horus at 22:26 UTC, showing mainly westerly winds exceeding 20 m/s. 175

4.27 3D wind components measured at 22:26 UTC on June 3, 2025, with respect to the KTLX WSR-88D Radar using a multistatic retrieval technique. Panels show (a) U (east–west), (b) V (north–south), and (c) W (vertical) wind velocities. 176

4.28 Microphysical measurement estimates derived from Horus Z and Z_{dr} at 3.78° elevation on June 3, 2025. (a) PPI map of estimated liquid water content (LWC, g/m^3). (b) Histogram of drop diameters calculated using Equation (4.7). (c) Histogram of estimated drop terminal velocities from Equation (4.6). 178

4.29 (a) Sector of the Z field between 273.9° and 240.8° from north used for process rate analysis at 4.85° elevation. Beam-blocked regions were manually removed for each elevation. (b) Example at 2.69° showing two excluded sectors (red dashed outlines). 179

4.30 Distributions of the four flux terms used in the analysis. 180

4.31 Relationship between p and the divergence of the 3D wind field. Positive divergence generally corresponds to reductions in LWC (negative p), while negative divergence (convergence) is associated with LWC generation within the storm. 182

4.32 Dependence of the p–divergence relationship on liquid water content (LWC). Panels show the relationship for different LWC ranges (kg/m): (a) $0.1 \times 10^{-5} < \text{LWC} < 2 \times 10^{-5}$, (b) $2 \times 10^{-5} < \text{LWC} < 4 \times 10^{-5}$, (c) $4 \times 10^{-5} < \text{LWC} < 8 \times 10^{-5}$, and (d) $8 \times 10^{-5} < \text{LWC} < 20 \times 10^{-5}$. These subsets illustrate that the mass generation trend varies with LWC magnitude. 183

4.33 Dependence of p on wind magnitude. Strong positive horizontal winds combined with small or near-zero vertical winds are associated with large process rate magnitudes. This is consistent with the flux analysis in Figure 4.30a,b, which shows horizontal advection as the dominant contributor, while vertical motions (especially strong downdrafts) also influence the process rates, as seen in Figure 4.30c. 184

4.34 The relationship between surface rain rate R and the continuity-equation flux terms. R is estimated using the S-band R–Z relation $R(Z) = 1.94 \times 10^{-2} Z^{0.694}$ (Ryzhkov et al. (2022)). Panels (a–d) show R versus $flux_a$, $flux_b$, $flux_c$, and $flux_d$, with $flux_b$ exhibiting the strongest linear relationship. LWC remains most strongly correlated with R, reflecting their shared dependence on reflectivity. 185

5.1 DPR attenuation-corrected Ku-band estimated surface reflectivity at 23:38:18 UTC on July 7, 2024, over (a) the DPR swath and (b) zoomed in on the location of Horus (blue dot) along with the Horus RHI extent (blue dashed line); DPR cross sections of attenuation-corrected reflectivity along the black dotted line in (b) for (c) Ka-band and (d) Ku-band; Cross sections of DPR estimated hydrometeor distribution parameters: (e) the log of the normalized intercept parameter N_w and (f) the mass-weighted mean diameter; Collocated Horus RHI S-band reflectivity (g) at native resolution and (h) resampled to the resolution of the GPM-DPR; In panels (c) to (f), the horizontal dotted lines figure the isotherm 0° C altitude. 192

5.2 Horus snapshot of (a) Z, (b) Z_{DR}, and (c) K_{DP} as well as (d) dZ/dt, (e) dZ_{DR}/dt, and (f) dK_{DP}/dt at 23:38:18 UTC on July 7, 2024. The horizontal dotted line indicates the isotherm 0°C altitude. 194

5.3 Horus decorrelation time of (a) Z, (b) Z_{DR}, and (c) K_{DP} over a variogram fit in time from 23:19:21 UTC to 23:59:59 UTC 198

5.4 This work will develop retrievals predicting precipitation process-rates, fluxes, and vertical motion from simulated radar returns from individual and combined instruments that builds upon current work on PAR precipitation rate retrievals. (Note: Figure not to scale) 203

5.5 Process classification improves probabilistic precipitation rate estimation performance, allowing for continuous PAR estimates of precipitation in time and space (from Stephens et al. (2019).) 204

9.1 The dataset analyzed in this appendix is composed of variables calculated from an MRMS grid (about 1 km square) matched to the 5 km diameter DPR footprints (depends on local zenith angle) captured over CONUS from June 2014 to October 2016, as well as associated DPR Level-2 products. 225

9.2 Strip-plot analysis illustrating the separation of variables between Cluster 0 (blue) and Cluster 1 (orange) through K-means clustering utilizing the full dataset, including precipitation classified as convective, stratiform with no bright band, and stratiform with a bright band. Each strip-plot depicts the distribution of a specific variable within each cluster, highlighting distinctive patterns and cluster separations, including (a) stdpix, (b) elt, (c) rain rate bias defined to be the DPR rain rate minus the MRMS rain rate at the surface, (d) bbh, (e) bbw, (f) hst, (g) fip, (h) piams, and (i) flh. For visualization purposes the plot contains a random subset of the full data set of 255,586 data points for visualization. 234

9.3 Percentage of outlier DPR observations (with a rain rate bias $>$ 10 mm/hr) in Cluster 1 from the DPR two-year dataset associated with stdpix $>$ 2.2 dB, indicating high R_{MRMS} variability within the DPR footprint; piams $>$ 6.06 dB, indicating high matched scan path integrated attenuation; fip $>$ 4 indicating heavy ice; and elt $>$ 368 meters, indicating high elevation. Importantly, the portion of the data that is classified to be convective is shaded in yellow, motivating a further focus on convective-type precipitation in Section 3b. 235

9.4 The elbow method (Kumar et al. (2011)) was used to choose the number of clusters for the K-means clustering analysis in (a) section 3a utilizing the complete dataset and (b) section 3b, a subset of the full dataset classified as convective precipitation 237

9.5 Strip-plot analysis illustrating the separation of variables between Cluster 0 (red), 1 (blue), 2 (green), 3 (purple), 4 (orange), and 5 (yellow) through K-means clustering utilizing only datapoints from the full dataset classified as convective. Each strip-plot depicts the distribution of a specific variable within each cluster, highlighting distinctive patterns and cluster separations, including (a) stdpix, (b) elt, (c) hst, (d) piams, (e) rain rate bias defined to be the DPR rain rate minus the MRMS rain rate at the surface, and (f) fip. For visualization purposes the plot contains a random subset of the full data set of 61,302 convective data points for visualization. This visual analysis provides insights into the role of individual variables in defining cluster boundaries and identifying key features that distinguish clusters within the dataset. 248

9.6 Violin plots showing MRMS rain rate (mm/hr) associated with each convective cluster. 249

9.7 Spatial distribution of convective k-means clusters over CONUS. 250

9.8 Separation between Cluster 2 and Cluster 3 in (a) D_m and (b) N_w . . . 251

9.9 Violin plots showing MRMS standard deviation (mm/hr) associated with each convective cluster from Section 3b. 251

9.10 (a) Rain rate bias plots of Cluster 2 (green) and Cluster 3 (purple) and (b) after NUBF correction was applied allowing Cluster 2 to take the value of each individial data points lower 75th confidence bound for rain rate and allowing Cluster 2 to take the upper bound of each points confidence interval. A reduced RR bias due to NUBF correction motivates the conclusion that these clusters have biases driven by NUBF. 252

9.11 Depiction of multiple-scattering correction: red points indicate a subset of Cluster 1 from the convective dataset with a heavy ice flag greater than 20 and a difference between the DPR normal-scan reflectivity and the DPR matched-scan reflectivity greater than 6 dB. The blue points in indicate the same subset of points transformed using the Ku-band TRMM Rain Relationship as in Iguchi et al. (2000). A reduced RR bias due to multiple scattering correction motivates the conclusion that these clusters have a population of datapoints with biases driven by multiple scattering. 253

9.12 Violin plot of the difference in reflectivity between the matched scan (dependent on the dual-frequency algorithm) and the normal scan (Ku-only) reflectivities for each convective cluster. 254

9.13 Convective cluster rain rate correlation and bias for a random test set containing 30% of the convective observations in the matched MRMS/DPR dataset (top row) and rain rate correlation and bias for the same 30% test set of data points passed through GAMLSS optimized R-D_m relationships trained on 70% of the dataset for each cluster . . . 255

Abstract

While substantial progress has been made in ground-based quantitative precipitation estimation (QPE) over the past two decades with the introduction of dual-polarized scanning radars, some key questions remain unresolved: (1) how can we accurately capture the rapid temporal and spatial variability of precipitation, especially in convective storms? and (2) how can radar systems better resolve microphysical and dynamical processes that directly influence rainfall estimation accuracy? Addressing these questions to make QPE estimates more reliable has implications for applications including weather and flood forecasting and water-resource management. To this end, the 2017 decadal survey identified key priorities that include quantifying global precipitation rates and phase (rain and snow/ice) at convective and orographic scales sufficient to capture flash flooding and larger-scale impacts, as well as characterizing hydrometeor microphysical processes through measurements of hydrometeor distributions and precipitation rates with an accuracy of approximately 5%. Research using conventional mechanically scanning dish radars with dual polarization has shaped our current approaches for hydrometeor classification, particle size distribution estimation, precipitation typology, and rainfall estimation. However, important gaps remain for capturing rapidly evolving precipitation features, storm structure, and microphysical processes with sufficient spatiotemporal resolution.

Since 2022, the Advanced Radar Research Center (ARRC) at the University of Oklahoma (OU) has deployed a prototype all-digital phased array radar (PAR) as part of an effort supported by the National Oceanic and Atmospheric Administration's (NOAA) National Severe Storm Lab (NSSL) to demonstrate the benefits and practical use of PAR technology for future weather observations. The goal of this work is to

examine PAR QPE and to enhance our understanding of the benefits of PAR's spatiotemporal information content to QPE and the estimation of precipitation process rates. In support of the decadal survey goals, this work presents a supervised learning framework using PAR's denser sampling of the atmosphere that enhances precipitation quantification at convective scales relevant to flash flooding, demonstrates the improvement of radar variable estimation across multiple meteorological timescales, introduces a method for retrieving microphysical process rates, and provides an approach for quantifying uncertainty in both radar variable and rainfall rate estimates. In the pursuit of PAR benefits for global precipitation observation coverage, PAR's ability to bridge satellite observation gaps and target novel insights with spaceborne and ground-based approaches is explored within convection.

Multiple radar types and scanning strategies have been used to obtain data with high temporal and/or spatial representativeness in incremental steps throughout this work from 2021 to 2025 to validate the benefits of PAR relevant to QPE. Prior to 2022, micro-rain radar (MRR) observations enabled vertically pointed radar reflectivity retrievals at 24 GHz. Beginning in 2023, Horus began taking Range Height Indicator (RHI) observations of storms, which provided high temporal resolution observations at a single azimuth, yielding RHIs with revisit times of 2 seconds to sample convective precipitation events. A new QPE retrieval framework using supervised learning was developed to integrate proposed altitude and time derivatives of radar variables (referred to hereafter as PAR variables) with information content from the vertical profiles of radar variables afforded by these measurements. These RHI observations, as well as RHI observations taken in 2024 wherein the temporal revisit time was reduced to 0.76 seconds, allowed for the characterization of decorrelation times and temporal sampling errors for two convective events, leading to recommendations for the required sampling timesteps for weather radar QPE. The dense spatiotemporal PAR sampling

is explored through the continuity equation applied to condensed water content as a rigorous theoretical framework for the interpretation of precipitation process rates. Observations taken in 2024 further allowed for the exploration of three-dimensional flux terms to create estimates of sources and sink rates (process rates) for liquid water content observed by the radar through rotated imaging scans capable of completing full radar-volume coverage in 24 seconds.

The data analysis in this work focuses on exercising PAR variables for the improvement of QPE, characterizing temporal sampling errors afforded by faster temporal updates, and demonstrating the estimation of atmospheric process rates by using three-dimensional radar variables available due to PAR's high spatial sampling. Overall, this work demonstrates the need for fast sampling from PAR to meet radar quality requirements given temporal scales of applications and weather variability. Novel quantification of precipitation process rates has been explored in convective storms, opening a door for interfacing radar and numerical weather modeling. These steps lay the groundwork for key Radar NEXT system specifications and for creating a roadmap for operational QPE that takes into account horizontal and vertical atmospheric fluxes.

Chapter 1

Introduction

1.1 Motivation

Weather forecasters, hydrologists, and climatologists need quantitative precipitation estimates (QPE) to predict flash floods, monitor droughts, guide farm management and irrigation decisions, and assess long-term water resource availability. QPE is a subdiscipline within atmospheric science that seeks to improve the accuracy and availability of precipitation rate estimated quantities such as rain rate (R) and snow rate (S) which typically have units of mm/hr. Herein, we will note the precipitation rate of all precipitation phases as R. A major motivation for the existence of this subdiscipline is the significance of water storage and exchanges between the atmosphere and the (sub)surface for science and applications that impact the environment and society. Errors in QPE can propagate through various atmospheric and hydrologic models when R is used as an input to the models, which ultimately influences decision support systems and public safety outcomes across spatial and temporal scales. These errors can impact the accuracy of estimated precipitation rates and add discontinuities to long-term climatological studies. Long-standing single point measurement techniques from in-situ instruments at the surface have been supplemented with the advent of ground weather radar networks to provide increased spatiotemporal continuity to precipitation observation and estimation across land. However, these networks have still

presented spatial gaps and temporal resolution issues for QPE. One example of efforts to mitigate gaps and fine-tune QPE algorithms is the Multi-Radar Multi-Sensor (MRMS) system used for severe weather forecasting in the United States (U.S.), that results from a collaboration between the NOAA National Severe Storms Laboratory (NSSL) and the Cooperative Institute for Severe and High-Impact Weather Research and Operations (CIWRO) (formerly CIMMS) at the University of Oklahoma, with the system made operational by the National Weather Service (NWS) in 2014. MRMS delivers precipitation rate R at two-minute temporal resolution and every 0.01° over the contiguous United States (CONUS), which has been critical for improving flash flood forecasting (Gourley et al. (2017a)). MRMS combines information from the National Weather Surveillance Radar–1988 Doppler (WSR-88D) network covering the CONUS, also known as NEXt generation RADar (NEXRAD). MRMS R is carefully conditioned with a decision tree that chooses appropriate situational R performance.

Over time, QPE has been sourced from various sensing instruments, not just from weather radars. The success of MRMS sits on the shoulders of a progression of improvements from the earliest form of QPE measurement technologies, the rain gauge, which in its most basic form collects rainfall in a basin over a specified time interval, a standardized technology that dates back to the reign of King Sejong of Korea's Joseon Dynasty in 1441 (Cho (2015)), which is a practical evolution of the rudimentary human and animal need to anticipate storms that dates through our evolution (De Bruijn and Romero (2018), Azevedo et al. (2023), Cooper et al. (2023)). In modern times, improvements to QPE have included those to surface in situ measurements and the development and expansion of remote-sensing techniques in various forms until they spanned the globe. Each improvement has helped to enable the amount of available QPE information content and its accuracy. Disdrometers, for example, expanded the in situ information space from rain gauge technology that captures discretized rain rates to capture

particle size distributions (PSDs) and precipitation microphysics with higher temporal resolution and dimensionality. Weather radars are remote sensing instruments that have been in use since 1941, a technology that allowed for QPE estimates at far contiguous ranges from the physical location of the sensing instrument above land instead of single point locations, and with typically faster update times (Hitschfeld (1986)). In the US, a major advance occurred when the National Weather Service (NWS) began operational weather radar use, eventually establishing the NEXRAD radar network, which has helped to provide the critical weather intelligence used to protect US lives, infrastructure, and national security by enabling early warnings for extreme weather events and decision support for the future (NWS (2025)). Dual-polarization upgrades further enhanced scientists' ability to infer hydrometeor size, shape, and concentration, leading to measurable improvements in forecasting skill, hydrologic prediction, and climate-scale precipitation analyses (Zhang et al. (2019)). Despite these advances, the pursuit for further improved QPE continues as gaps still remain in the representation of rapidly evolving precipitation processes.

1.1.1 Current Operational Radar Gaps for QPE

Conventional dish-based weather radars like the WSR-88Ds scan the atmosphere according to pre-planned and predictable volume coverage plans (VCPs), which most commonly involve a set of 360° pedestal rotations at various elevation angles. For example, VCP 12 and 212 are the typical VCPs selected for the WSR-88Ds in the advent of precipitation which covers azimuthal rotations for 14 elevation angles from 0.5° to 19.5° in about 5 min (National Weather Service (2015)). Because there are only 14 elevation angles in the VCP and because the WSR-88D has a radar beam with a 1° beamwidth that is mechanically rotated over 5 min, there are necessarily spatiotemporal gaps in the VCP that introduce representativeness errors in radar variables and

retrieval algorithms over the considered 5-minute temporal block. Other classic error sources come from instrument calibration, radar signal attenuation, nonuniform beam-filling (NUBF), beam blockage by buildings or terrain, a physical separation between the radar beam and the desired earth surface that is exacerbated by the earth's curvature, the vertical variations of precipitation, and the natural error arising because of the indirect and volume-integrated nature of a radar measurement relative to the true underlying hydrometeor properties. These concerns have been widely documented by weather radar scientists (e.g., Delrieu et al. (2009)). Within these concerns, temporal sampling errors within QPE-application temporal resolutions specifically remain understudied, even though they are increasingly important and can result in propagated errors for applications that use QPE.

Attempts have been made by the National Weather Service to help mitigate this deficiency by increasing temporal sampling density for applications through efforts like MRMS, which aims to aggregate out-of-phase radar observations with near 5 min VCPs to create about 2 min QPE updates on a 1 km square grid (Zhang et al. (2016a)). The WSR-88D Supplemental Adaptive Intra-Volume Low-Level Scan (SAILS) is another attempt that impacts QPE by reducing low-level scan times from 5 min to 2.5 min via an added return to the lowest elevation angle in the middle of the VCP cycle. Other VCP adaptations exist that terminate the scan early if no precipitation is detected (Radar Operations Center, National Weather Service / NOAA (2011)) or create additional returns mid-cycle to mid-level elevation angles (Radar Operations Center, National Weather Service / NOAA (2016)). While these approaches partly address the course 5 min revisit times of VCP 12 and 212, the system has a mechanically imposed limitation for these improvements set by the pedestal's physical operating limits that are not compatible with precipitation variability. An ideal atmospheric sampling radar would sample quasi-continuously in time and space to understand and impactfully

reduce spatiotemporal sampling errors.

1.1.2 Emerging Opportunities with Phased Array Radar

Phased array radar (PAR) is a transformative technological advancement to the QPE discipline because it employs electronically steered radar beams that dramatically speed up VCP completion times. A PAR is shown as a part of this work to demonstrate the completion of a full volume scan in 24 s rather than 5 min. This demonstrated VCP performance comes from a PAR developed at the University of Oklahoma's (OU's) Advanced Radar Research Center (ARRC), funded by NOAA's NSSL, called Horus. Horus is a mobile, all-digital S-band PAR capable of sampling over 60 radar elevations within a single pulse repetition interval (e.g., 2 ms) using imaging techniques that allow for simultaneous beamforming on receive. Horus has also demonstrated fast Range–Height Indicator (RHI) scans (without the use of imaging) of 60 elevation angles in 16 s (Palmer et al. (2023b)). RHIs differ from VCPs in that they are collected at a single azimuth angle rather than covering full 360°rotations for various elevations. Similarly, NSSL's fixed-site Advanced Technology Demonstrator (ATD) has shown that 1 min volume scans are possible with PAR technology (Torres and Wasielewski (2022)). These VCP times contrast sharply with the 5 min WSR-88D VCP.

NOAA is supporting the demonstration of PAR technology through analyses involving two instruments: Horus and the ATD (Palmer et al. (2023b), Torres and Wasielewski (2022)). Both radars are S-band dual-polarization PARs with Horus being built and operated by the ARRC and the ATD acquired from the Massachusetts Institute of Technology's Lincoln Laboratory and operated by NSSL. Unlike the ATD, the all-digital Horus has independent transmit and receive channels at each antenna element, allowing for software-defined beamforming as well as rapid volumetric scanning. This accounts for the faster update times reported by Horus. The ATD is at a

fixed site, while Horus is a mobile PAR system.

Reports over the last two decades spanning 2005–2025 (National Severe Storms Laboratory (2025)) indicate that NSSL has continually invested in PAR development through a phased strategy, beginning with defining system requirements and evaluating the feasibility of agile-beam radar concepts, followed by laboratory and simulation studies addressing antenna design, signal processing, and polarimetric challenges. By the late 2010s, this work matured into prototype development and engineering validation for the ATD, and by 2020 the program had shifted toward system-level testing, calibration, and real-world data collection, along with delivering formal feasibility assessments to Congress. This forward-looking research has occurred alongside algorithm improvements from a switch from single-pol to dual-pol technology for the whole NEXRAD network which began in 2011 and was completed in 2013 (Senesac (2020)). Recent efforts have continued to refine calibration approaches, explore adaptive scanning strategies, and incorporate forecaster feedback through operational testing in NOAA's Hazardous Weather Testbed (Torres et al. (2016)). In 2025, these activities expanded to include focused field demonstrations of rapid-update, flexible scanning capabilities and early evaluations of beam-control techniques and forecaster usability. NSSL has also funded the ARRC to perform fundamental research showing the benefits of PAR for weather-applications like QPE, tornado detection, and hail studies, as well as research for PAR system operability and integration.

The Horus PAR effort funded through NSSL began its science investigations and weather demonstrations in 2021, including a QPE component aimed at determining how PAR can enhance surface precipitation estimation. This dissertation presents several examples using Horus to illustrate these concepts, though the methods extend broadly to PAR technology as a whole which includes the ATD.

Through fast sampling, the use of PAR is a step towards observing previously

unresolvable microphysical processes and precipitation fluxes. This is one major benefit of PAR, but it also enables the development of process-informed, PAR QPE techniques as an alternative to empirical relationships derived from sparsely sampled radar VCPs.

1.2 Shared Insights for QPE Innovation

The idea generation and the intentional development of PAR QPE comes to fruition through coordinated actions and a public commitment to invest in the future. Thus the rate and relevance of QPE advancements are heavily influenced by strategic decision-making frameworks, leadership models, and community coordination. Beyond this, PAR development and its impact on QPE intersect the fields of atmospheric physics, hydrology, engineering, data science, and policy, making it an inherently interdisciplinary focus area. This work looks at QPE advancements that take advantage of PAR sampling, but it is also developed considering international scientist inputs in the field of precipitation science and will be framed relative to the aspirations and ideas for PAR of science stakeholders within NOAA to motivate the broader perspectives described through this work. The science-advancement process relies on distributed leadership, which is reinforced through conference-based scientific exchange that enables broad information sharing, consensus building, and cross-group collaboration. Inclusive and shared science leadership drives advancement through the flow of communication across research institutions, agencies, early-career networks, and science stakeholders.

The QPE-advancement cycle with a prototype PAR like Horus is interdisciplinary because it relies on an understanding of how PAR works, the limitations of PAR system performance at various instrument development stages or with different design approaches, the makeup of hydrometeors in the atmosphere and how they interact with radar waves, and the physics of storm evolution at meso- and micro-scales. QPE

advancement can occur alongside PAR development, as is shown in this work, but just as system integration occurs in stages, so will new QPE discoveries then occur in stages.

This work began in 2021 when the Horus PAR began taking its first atmospheric observations. PAR development beyond this point focused on improving key technical features influencing QPE, such as beam geometry, signal processing, and calibration. These improvements led to high spatiotemporal sampling that enabled the system's fast-scanning capabilities that are exploited by this work to improve QPE, especially for capturing precipitation dynamics for extreme or rapidly evolving storm systems.

The integration of new QPE methods in parallel with Horus integration required frequent engagement and iterative feedback between the team responsible for implementing updates to align the technical development with the QPE scientific objectives while also taking into consideration the science objectives of other science stakeholders taking part in the "science integration" targeting different science questions. However, attempts to maintain this level of interaction were not always received constructively, which at times hindered communication and created tension within the team. These experiences highlight the importance of fostering inclusive and respectful collaboration, particularly when ensuring that stakeholders can contribute effectively to holistic system development.

This work targets key science questions posed by the 2017 decadal survey, a bottom-up survey effort for defining key science challenges called "Thriving on Our Changing Planet: A Decadal Strategy for Earth Observations from Space." Two priorities set by the decadal survey are to quantify rates of precipitation and its phase (rain and snow/ice) worldwide at convective and orographic scales suitable to capture flash floods and beyond and to characterize the microphysical processes and interactions of hydrometeors by measuring hydrometeor distribution and precipitation rate to within

5% (National Academies of Sciences, Engineering, and Medicine (2019). In addition to relying on published literature and the decadal survey, this work integrates global and local perspectives derived from in-person engagement activities from the field of precipitation science to create impact that aligns with community-identified priority areas, local operational perspectives provided through the lens of NSSL, and PAR system developers. This work also touches on instances where collaborative efforts were limited or disrupted by more centralized decision-making and inefficiencies that can arise when communication becomes siloed, but the main body of work targets new techniques and frameworks for the use of PAR data to improve QPE.

1.2.1 Community and Stakeholder Insights

To contextualize PAR-based QPE research with both community and broad science-stakeholder perspectives, the results of a workshop facilitated during the 14th International Precipitation Conference (IPC-14) and targeted interviews with QPE experts in NOAA and the OU/NOAA Cooperative Institute for Severe and High-Impact Weather Research and Operations (CIWRO) are highlighted. These activities provide complementary insights because international workshops capture broad community priorities and readiness, while interviews offer in-depth expert perspectives on operational and scientific considerations. Together, they help frame and inform the research questions targeted in this work by a broader context that helps to maximize the impact of the research direction for PAR-QPE and the recommendations for future work proposed in Chapter 6.

1.2.1.1 Community Insights

Workshops and conferences provided a platform for collaborative discussion on community priorities for next-generation radar systems. For instance, the IPC14 Student and

Early-Career Workshop facilitated by a two-person early-career/student team involved 132 participants from 16 countries in structured dialogues meant to extract community views on the major priority areas for precipitation science. Participants contributed through pre-workshop surveys and six two-person moderator-led breakout discussions whose takeaways were captured by rapporteurs. This virtual workshop was planned ahead of the IPC14 in-person conference on May 24, 2023 with the goal of facilitating an open, inclusive, and collaborative environment for discussion between students and young scientists in the field.

The overarching question posed to student and early-career scientists participating in the workshop was, "What should be highlighted more in precipitation science that is not happening currently?"

The conference featured six high-level lightning talks from students and early-career scientists working in focus areas selected through the use of a pre-conference survey wherein respondents were asked to confirm their status as student and/or early-career scientist working in precipitation science as well as their answer to the following question through a ranked-choice vote: "Outside of your primary research area, what emerging areas do you believe are the most important topic areas that will impact the future of precipitation research?" The results of the rankings are shown in Figure 1.1.

The ranked topics were narrowed down into six encompassing themes that cover key science questions in the field of precipitation science: climate change and extremes, regional precipitation patterns, precipitation modeling, solid precipitation, clouds and convection, and applications. For example, according to climate models, the 21st century stands to undergo increases in evaporation over most of the global ocean and decreases in soil moisture over most land area (Dai (2011)). Changes to teleconnections like the El Niño Southern Oscillation and a shifting ITCZ will cause further regional precipitation changes that will impact effects seen at higher resolution scales

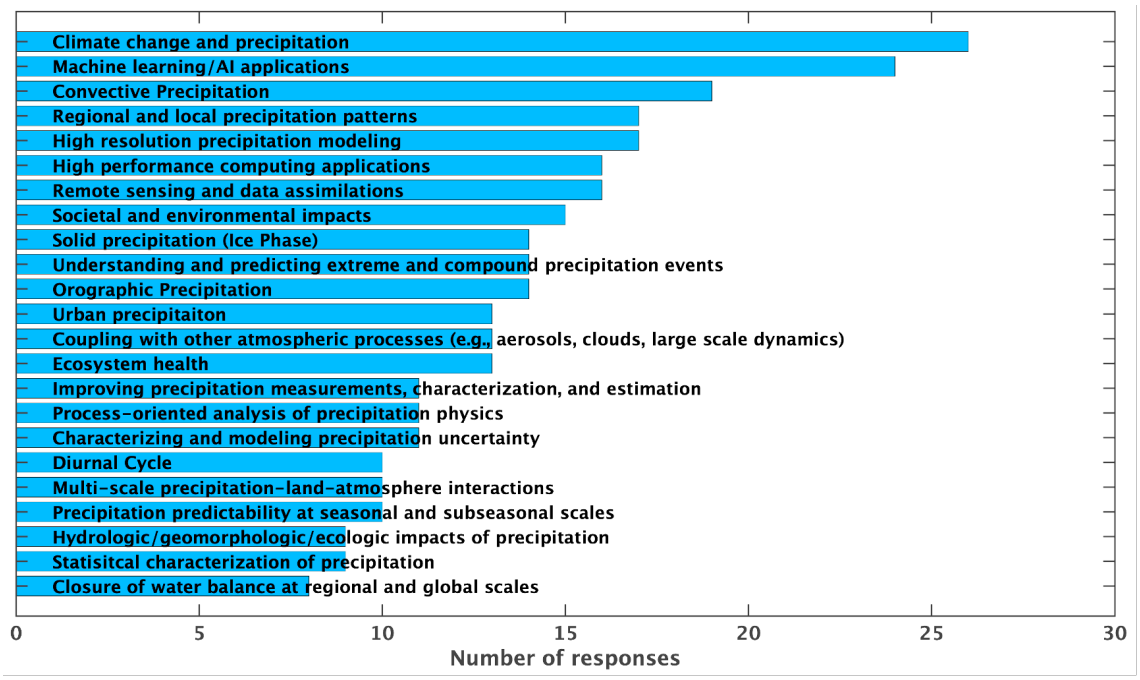


Figure 1.1: IPC-14 Student and Early Career Workshop focus areas were identified with the use of a pre-conference survey distributed to the community through advertisements to working groups and universities in the area of precipitation science.

like convective and orographic scales (Mamalakis et al. (2021)).

This is part of the reason that we want weather and climate models that include large-scale system coupling into the convection process and microphysics (Pendergrass (2020)), as is depicted as a connected system of feedbacks in Figure 1.2. Past research has largely focused on improving our scientific understanding of Earth-system components, such as the ocean, land, cryosphere, atmospheric chemistry, and biogeochemistry, that inform our knowledge of weather and climate. These components are tightly interlinked and together shape atmospheric process occurrences. However, a critical gap in our Earth-system understanding involves convective organization: how clouds move, evolve, aggregate, and interact across scales (Pendergrass (2020), Pendergrass et al. (2016)). For context, a cumulonimbus cloud spans 1–10 km and evolves over hours (Moncrieff (2010)). Improved modeling of convective organization is essen-

tial for advancing climate models toward accurately representing atmospheric water transport, with downstream benefits for energy-budget studies, high-resolution weather forecasting, and long-term climate prediction (Moncrieff (2010)). The continuum spanning microphysical to planetary scales is crucial for understanding both convective and stratiform precipitation. Stratiform precipitation often occurs alongside convection or as its remnant, linking mesoscale convective processes to broader studies of the hydrological cycle and radiative feedbacks. Changes in convective organization alter cloud cover, which in turn affects planetary albedo and the distribution of radiative energy, further emphasizes the importance of advancing our understanding and modeling of convection across scales.

This will aid our understanding of global energy and water balances, which will further help us understand how extreme weather and precipitation changes will occur. Along the lines of orography and everywhere within the cryosphere, we want to quantify rates of accumulation, snow melt, ice melt, and sublimation from snow and ice at scales driven by topographic variability (Mamalakis et al. (2021)). Furthermore, we need to better represent the organization of convection because convective clouds can form heavy rainfall and are associated with precipitation extremes (Pendergrass (2020)). We do all this to improve our quantification of global precipitation because it is a direct input to precipitation applications. Understanding precipitation improves our understanding of hydrological processes and aids decision support that helps to reduce disaster risk associated with impacts like floods and landslides (Mamalakis et al. (2021)).

Breakout sessions were held within the workshop under the pre-selected themes, led by groups of two to three moderators and one rapporteur, including students and early-career scientists from across agencies (e.g., the National Center for Atmospheric Research (NCAR), NOAA, the Cooperative Institute for Severe and High-Impact Weather

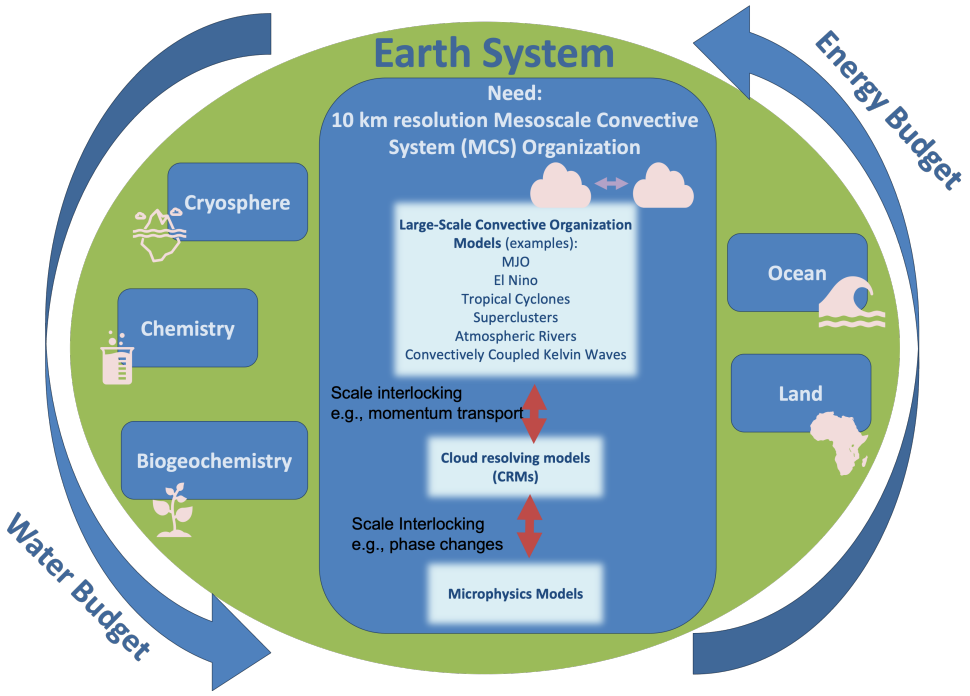


Figure 1.2: Inspired by the work of Moncrieff (2010), this figure shows the interconnected Earth-system components that collectively influence atmospheric processes. While past work has improved understanding of the ocean, land, cryosphere, atmospheric chemistry, and biogeochemistry, a critical unresolved element is convective organization, whose feedbacks extend throughout the full range of atmospheric scales.

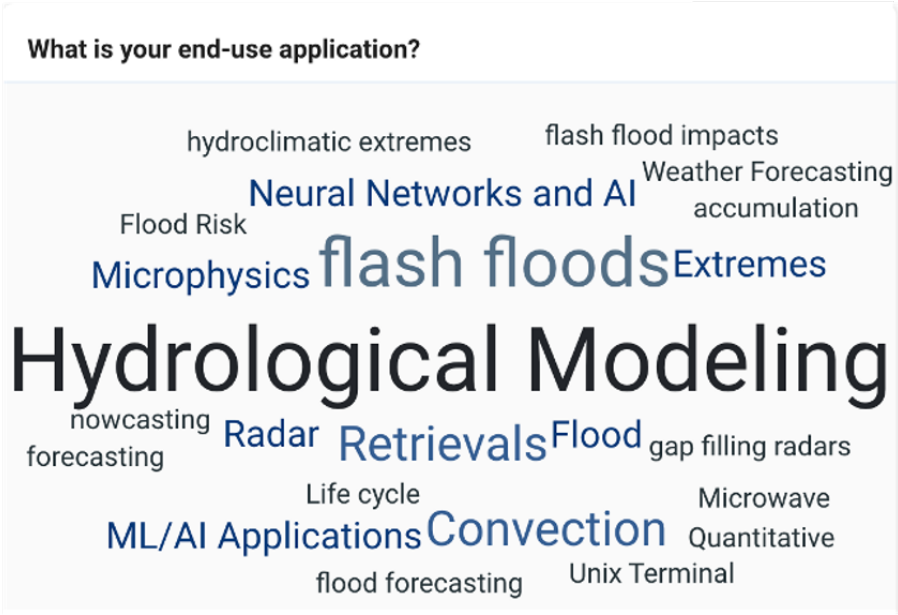


Figure 1.3: In-conference poll illustrating the primary end-use applications reported by student and early-career workshop participants.

Research and Operations (CIWRO), the Cooperative Institute for Climate and Satellites–Maryland (CICS-MD), and the Cooperative Institute for Research in Environmental Sciences (CIRES)) and universities (e.g., OU, University of Michigan (U-M), University of Wisconsin–Madison (UW-Madison), and the Indian Institute of Technology Hyderabad (IITH)). The workshop rapporteurs collected takeaways for all topic areas, but highlighted in this work will be the subset of these takeaways that are directly relevant to PAR QPE.

The end-use applications for QPE were highlighted via a live poll, with results shown in Figure 1.3 to be applications ranging from weather extremes, QPE, and nowcasting, with a high focus on hydrological modeling. Furthermore, the spatial and temporal scales of interest to the participants were recorded for resolutions from 100 m to 1 km and timescales from 1 min to 1 hr, as shown in Figure 1.4.

These workshop polls show how QPE applications drive the data needs within QPE, which call for high spatiotemporal observations of the atmosphere.

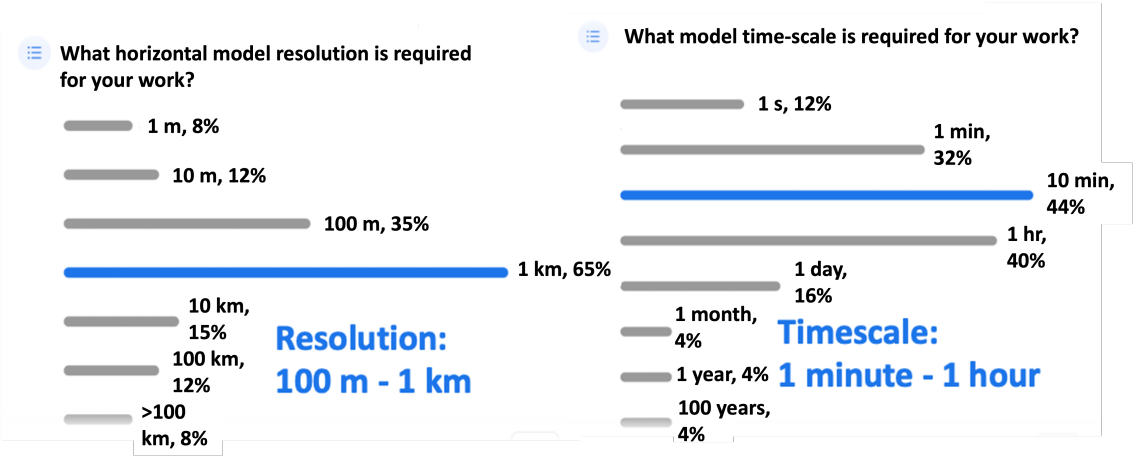


Figure 1.4: Summary of participant-indicated spatial and temporal scales, showing preferred resolutions from 100 m to 1 km and timescales from 1 min to 1 hr

Furthermore, breakout-session takeaways collected by the rapporteurs highlighted several priorities relevant to PAR QPE. Participants emphasized the need for higher-quality observations, along with greater spatial resolution and reduced latency (especially for satellite retrievals) to support diverse applications. They noted the importance of developing and providing probabilistic products, acknowledging that precipitation estimation is inherently uncertain and that this uncertainty must be effectively communicated to end users. The discussions also underscored the value of increasing data availability in regions with data inequity and improving observational continuity. Participants identified multi-sensor data assimilation as a crucial pathway for enhancing precipitation quantification, and they stressed the need for improved validation between models and observations. Both observation-based and process-based model validation approaches, such as leveraging multisource datasets or multi-model comparisons, respectively, were highlighted as key tools for advancing QPE in storm-resolving models.

1.2.1.2 Stakeholder Insights

In 2025, targeted interviews were conducted with less than twenty experts recognized for their knowledge of QPE working at NOAA and CIWRO to provide a broader organizational context to the priority areas for QPE as well as PAR efforts within these. These discussions focused on perceived challenges, opportunities, and strategic considerations for integrating PAR into operational environments. The questions posed to participants are listed below, followed by a synthesized summary of the responses. In this context, "synthesized" means that the data from the interviews were consolidated by examining overlapping ideas, highlighting shared themes, and organizing related observations into a unified narrative. The outcome is a thematic interpretation derived from collective input rather than an account of individual responses. All interviewees were invited to review the synthesized summary and were given the opportunity to provide feedback to ensure the summary accurately reflected their views.

- What have been some of the greatest improvements to QPE at NSSL and CIWRO that you have seen in your career?
- What do you see as the largest areas of improvement for QPE at NSSL and CIWRO, and in your view, how do we bridge this gap?
- Looking 5-10 years ahead, what role do you think the phased array technology focus area will play in shaping the future of NSSL and CIWRO within your department?
- What are some of the biggest uncertainties/risks for scaling that you see in the future development of phased array within other areas of NSSL, like MRMS and WoF? What level of effort is required to overcome these?

- What areas of interdisciplinary collaboration do you think are necessary for the future of phased array within NSSL and CIWRO?
- Are there any other improvements/technologies that you think could have an equal or greater impact on improving QPE at NSSL and CIWRO?

Synthesized Interviewee Responses:

> Over the past two decades in the United States, quantitative precipitation estimation (QPE) has advanced driven by innovations in radar technology, algorithm development, and network integration. The most transformative technological advance during this period has been the transition from single- to dual-polarization radar (dual-pol), which has expanded radar observations beyond reflectivity (Z) by introducing physically meaningful dimensionality through variables such as differential reflectivity (Z_{dr}), specific differential phase (K_{dp}), and specific attenuation (A). Co-polar correlation coefficient (ρ_{hv}) has not shown computational benefits for QPE but serves an important role for data quality control. These measurements enabled hydrometeor classification and more robust rainfall estimation. In practice, the operational impact of dual-polarization has been multiplied through network-scale mosaic products that integrate observations across the NEXRAD radar network. The network-scale integration of Level II radar data within the Multi-Radar, Multi-Sensor (MRMS) framework, combined with gauge calibration, has enabled coherent national-scale precipitation mosaics and greatly improved near-real-time precipitation estimation across the Continental United States (CONUS). These gains have been built with the means of sustained research and devel-

opment programs which have operated to translate scientific advances into operational capability.

This combination of technological innovation and institutional commitment has fundamentally improved the way forecasters diagnose precipitation processes. Dual-polarization observations now allow operational meteorologists to better characterize winter precipitation, distinguish mixed-phase environments, identify hydrometeor types, and improve estimation of liquid water equivalent in snowfall. Over time, dual-pol has been meaningfully integrated into operational software workflows and many of its products have been automated, reducing the burden on forecasters to manually interpret raw polarimetric variables. Dual-pol and radar networking represent a real success story of transitioning research to operations.

Snow estimation, an existing frontier in the field of QPE, has greatly improved with the use of dual-pol technology, with further improvements expected. Snow QPE poses particular challenges even with the use of dual-pol information content in part because traditional Z-S and Z_{DR}-S relationships are unreliable due to turbulence, particle orientation variability, and the low reflectivity of sparse snow concentrations. K_{dp} estimates also tend to be noisy in snow-dominated regions requiring significant averaging and K_{dp} tends to be very low in dry snow, often on the order of 0.3 deg/km. In stratiform precipitation regimes in particular, a flat phase response combined with low values of K_{dp} can make snow estimation difficult. Hail contamination also impacts K_{dp} estimation because it causes sharp

bumps in differential phase from which K_{dp} is estimated by a range derivative, so the choice of range scale for the derivative can have a major impact on K_{dp} accuracy in these situations. Despite the challenges associated with K_{dp}, it has a major advantage in that it is a lower moment of the particle size distribution than reflectivity, so it has a computational advantage being equally sensitivity to all hydrometeor sizes. The use of higher frequencies and oversampling to improve K_{dp}, alongside the consideration of new variables like linear depolarization ratio (LDR) to enhance information content where K_{dp} is low are some potential paths forward for this dual-pol approach.

A combined K_{dp} and Z algorithm shows promise for improving snow QPE but has not yet been operationally implemented. Similarly, the use of A has been an extremely meaningful advance for heavy rain, helping address a chronic underestimation problem in extreme events. But mixed rain and hail, more broadly mixed-phase precipitation, remain challenging.

QPE improvements using dual-polarized variables and merged radar techniques have slowed in recent years leaving remaining obstacles that dual-pol cannot address such as radar coverage. The existing radar network has fundamental geographic gaps, most pronounced in the western United States and Alaska due to the network architecture of NEXRAD. Expanded radar coverage through gap-filling and low-Earth orbit (LEO) satellite observations hold an opportunity for helping to bridge these gaps. However, the use of gap-filling radars, particularly non-federal or out-of-network radars, to help over-

come coverage concerns is a time-consuming integration challenge for MRMS. In addition, the small scale of the variable Z_{dr} and biases that can occur for it make network-wide Z_{dr} consistency a challenge. Vertical representativeness also limits QPE accuracy, as conventional radar beams often overshoot near-surface precipitation at long ranges or become blocked in complex terrain. Even when a vertical column of the atmosphere can be observed, the melting layer, most common in stratiform precipitation, is a complex feature to interpret for QPE because while dry snow and ice have a permittivity (real component) around 3 to 3.17, rain has a high permittivity of approximately 80 so that melting hydrometeors can have permittivities that span from 3 to 80 as they transition phases. More generally, complications for hydrometeor classification and precipitation estimation techniques dependent on classification arise due to the presence of mixed-phase hydrometers, or rain mixed with hail, anywhere within the observed radar field of view.

Efforts to mitigate these limitations include projecting radar returns taken aloft to the surface using microphysical models, microphysical regime characterization, and deploying gap-filling radars, and refining vertical profile of reflectivity (VPR) correction techniques. One example of microphysical regime characterization beyond melting layer identification is the identification of the dendritic growth layer (DGL) using dual-polarized variables, this microphysical region is typically near 4 km in altitude and is a region of active ice crystal production. Even with the use of all of these mitigation techniques,

advection further complicates the estimation of near surface QPE.

Extreme rainfall estimation shares these challenges, with quickly changing storm dynamics, and has been identified to require significant improvement due to its impact on people and property as well as its small-scale and dynamic behavior as an atmospheric modulator. Rain rates in intense convection are routinely underestimated, a small microphysical change can result in large changes to QPE. The additional lack of an adequate retrieval of convective environmental drivers like humidity and latent heat mean that convective extreme rainfall systems remain undetermined.

PAR represents a potential paradigm shift for QPE with its rapid volumetric scanning enabling high-temporal-resolution storm capture, with potential to improve microphysical depiction, statistical estimation, and nowcasting. For hydrology and flood forecasting however a question still exists as to whether the sub-kilometer rainfall variability with a high update rate that PAR can resolve is meaningful for hydrologic prediction. Some simulation studies in urban contexts examining sensitivity at fine scales have been done, but more joint precipitation and hydrologic modeling analysis is needed. The hydrologic response may not be sensitive to improved resolution due to spatiotemporal averaging involved in the estimation of watershed forcing via basin lag times. The honest assessment is that PAR may not have a transformative impact on hydrologic modeling and is not strictly necessary for flash flood forecasting. The real gains of PAR are likely to come from high-resolution modeling, weather forecasting,

and microphysical insights that improve the physical understanding underpinning QPE algorithms.

The integration of high-resolution radar observations with numerical weather prediction (NWP) models has lagged behind sensor innovation. Outdated microphysical parameterizations and assimilation schemes limit the full utility of advanced radar data in forecasting, for example the Warn-on-Forecast (WoF) system has not yet been updated to work with dual-polarization data. More study and effort is required to realize the impact of dual-pol and the potential impacts of PAR for NWP.

Realizing these benefits for PAR also involves technical and operational challenges. For example, calibration of polarimetric variables with PAR is a question in focus that needs to be solved because polarimetric accuracy impacts many operational retrievals, including for QPE. New problems will arise as the technology scales from demonstrators to an operational network. Rapid-update, high-volume data will require efficient processing systems and scalable algorithms. Integration with MRMS and WoF will necessitate algorithmic updates to maintain interoperability. Progress will depend on sustained collaboration among radar engineers, microphysical modelers, forecasters, hydrologists, social scientists, and infrastructure planners to ensure that observational advances translate into improved modeling and decision support. There is a strong case for establishing a culture of transparency and a public-facing collaborative channel that can bring together PAR stakeholders across the weather enterprise.

Other technologies are also poised to strengthen QPE capabilities by expanding the diversity, density, and perspective of precipitation observations. With an internet-of-things perspective on the current technology landscape, progress will increasingly come from combining multiple observing approaches rather than relying on any single all-encompassing technology. Satellite instruments and spaceborne radars provide large-scale and global context for precipitation systems, helping to constrain retrievals where surface observations are sparse. AI-based retrieval methods can fuse multiple data streams to improve surface precipitation estimation and extract information from sensors not originally designed for meteorology. For example, opportunistic sensing offers particularly large potential gains: microwave communication links from commercial cellular and point-to-point networks experience signal attenuation during precipitation, creating dense, already-deployed measurement paths that can be repurposed for QPE and gap filling. Airborne instruments enable targeted, high-resolution sampling of extreme events and can provide quality observations during field campaigns. As previously mentioned, supplemental gap-filling radars can address localized coverage deficiencies where they matter most for operations. Model and satellite-derived estimation of key environmental variables like relative humidity, temperature, and pressure can also improve precipitation estimation when integrated with radar data. Finally, advances in detecting non-meteorological targets, including space debris, may provide additional value streams that influence the design and long-term sustainability of future ob-

serving systems.

Expanding or replacing the radar network is deeply entangled with political, economic, and institutional realities. For example, incorporating permanent non-federal radars into MRMS may be constrained by institutional and regulatory barriers requiring political support, securing addresses, land access, and local buy-in. Gap-filling radars often operate on subscription-based data models, raising questions about long-term data access and government reliance on commercial providers. The federal government is currently engaged in data buys from commercial radar operators, a pragmatic solution that poses an alternative to an assumed national infrastructure responsibility. Under this model, the government must define performance standards while remaining open to diverse data providers and developing standards and pathways for data adoption. For example, opportunistic microwave link data which has shown promise for QPE, involves developing trusting relationships with private industry. Whether future observing systems continue down the path of a multi-platform solution or if PAR gains widespread adoption, future networking systems must be able to opportunistically ingest information from various available radar types, scanning modes, and data sources.

If the government invests in PAR as a widespread infrastructure, a clear cost-benefit analysis should be performed, including researching the cost-benefit of a wide array of PAR architectures (e.g., cylindrical PAR architecture studies were possibly abandoned prematurely, and simplifying architectures providing a cost benefit have not been heav-

ily considered). The benefit should be determined from an application and a social science perspective in addition to the current focus on PAR data quality.

Historically, radars have been sold on the tornado problem using a life-safety argument. For the dual-pol upgrade, the benefit drivers for dual-pol were microphysical identification first with QPE improvement coming later because it took longer to demonstrate convincingly. This lag was used as an argument against the cost of the upgrade at the time. QPE has historically been a key factor in the adoption of new weather sensing technologies, so demonstrating the benefit of PAR for QPE is essential, and framing QPE improvements in terms of societal benefits, such as reduced flood losses, greater infrastructure resilience, and improved disaster mitigation, will be critical for securing long-term investment in PAR and network expansion. Cost-benefit is a social science problem as much as a meteorological one.

At the same time, the scientific process itself remains iterative and exploratory: as one expert noted, "the theory guides, but the experiment decides." Outlier studies and exploratory science are therefore essential, since not every observation conforms to the expected framework, and those that do not are often the most scientifically informative. The PAR community should remain open to the possibility that the most valuable PAR benefits may not be the ones easiest to quantify upfront. Enabling the community with more advanced observing systems can lead to new discoveries. The usefulness of the added information content and large data volume from PAR may reveal itself

over time alongside the advancement of new analysis techniques such as with AI, for example.

An advantage of PAR is the increase in information content it can provide with additional network-scale benefits when many systems operate concurrently. The data volumes produced by PAR networks will be substantially larger than current systems. The community should approach this wealth of data with an open mind, as advances in computing, storage, and data pipelines have historically always risen to meet such challenges in the past, and there is no reason to believe this time will be different.

While PAR offers a potential paradigm shift of improvements, operational deployment is likely 10–15 years away. There are many PAR applications, including QPE, but PAR also opens the door to replacing conventional Doppler wind estimation with a full high-update-rate 3D wind field retrieval either by algorithmic means or using passive receivers in combination with PAR. This has clear implications for the characterization of storm dynamics. Another impact opportunity with PAR as mentioned, is the coupling of WoF with PAR data's fast volume updates. Strategically, experts emphasize coordinated development of observational systems and numerical models to ensure radar and algorithmic advances are matched by improvements in microphysics and data assimilation. Modular testbeds for sensor integration, expanded interdisciplinary collaboration, and robust verification frameworks are recommended to accelerate progress. Near-term gains are expected from continuing to enhance VPR cor-

rection, snow estimation, and radar-gauge fusion used in current systems, while long-term QPE innovation will be shaped by PAR and/or multi-radar solutions alongside AI-enabled data analysis with the expectation that these are guided by physical understanding and robust verification techniques.

In summary, dual-pol and merged multi-sensor data have fundamentally transformed QPE over the past two decades. QPE experts understand that filling gaps and solving challenges within the existing weather observation schema will require a logistical solution that involves cost-benefit, adaptability for the use of many sensing instruments, software infrastructure and algorithmic upgrades, data quality verification, and a careful transition plan to operations. PAR holds the potential to reshape precipitation science in important ways, but experts emphasize that its benefits are a piece of a larger networked weather-information system where the tradeoffs of many system permutations can be weighed. Importantly, many scientists stress that this progress must be pursued with humility: through sustained investment in core science, transparent cost–benefit analysis, genuine interdisciplinary collaboration, an openness to exploratory discovery, and a willingness to follow the evidence wherever it leads.

The priorities highlighted by the decadal survey, by the students participating in the IPC-14 student and early career workshop, and those identified by the NOAA and CIWRO QPE experts all focus on improved precipitation estimation accuracy. These groups serve as priority informants who have helped to shape the key science questions addressed in this work.

1.3 Science Questions and Objectives

The priority informants from the previous section all emphasize the need for accurate, reliable, well-validated, and high-resolution QPE as well as the need for precipitation phase and microphysics distinction. The decadal survey developed specific goals around quantifying rates of precipitation (rain and ice/snow) and drop size distributions to a specified level of accuracy and characterizing microphysical processes at convective, orographic, and flash-flood suitable scales (i.e., at higher spatiotemporal resolution). The questions posed to different informants varied, leading the IPC-14 workshop participants to focus more on community-driven priorities, admittedly with a US-centered focus since most were from US-based universities or agencies, probabilistic products, data equity, and validation, while the NOAA and CIWRO experts were led to discuss their specific opinions on technology advancements for the US. Thus, these opinions help to inform community-inspired science questions tempered by perspectives working within a space of operational realism.

Probabilistic QPE methods had been proposed before the time that the decadal survey was developed (Kirstetter et al. (2015a)), and can continue to be used with PAR data. The main advancement of PAR for the joint priorities set by the informants is higher spatiotemporal resolution, allowing it to target convective, orographic, and flash-flood-suitable scales. In addition to this, PAR will enable new methods for characterizing microphysical processes with information relevant for flux retrievals. This work expands to offering perspectives for PAR opportunities for the validation of satellite concepts targeting the same goals. These focus areas align with science questions targeted by the 2017 decadal survey.

The workshop informants helped to frame a user-oriented priority perspective that reaches beyond the science questions targeted by this work, including the need for low-

latency observations, improved data continuity and equity over the globe by patching under-observed regions, and more model validation through model-observation comparisons with various datasets and types of data.

The only priority NOAA and CIWRO QPE experts did not highlight was the need for more model validation, but it should be noted that no participant with specific QPE forecasting expertise was interviewed. It should then be noted that NSSL's Warn-on-Forecast System does have interest in this priority area. For example, Guerra et al. (2022) applied an object-based spatial tracking and verification approach to compare storm objects from WoFS with radar observations from MRMS. Because of the phrasing of the interview questions, the NOAA and CIWRO interviewees tended to describe the evolution of QPE during their careers as a series of advancements mirroring technology upgrades for weather radar that expanded the available spatiotemporal atmospheric observation space. In the end, their goal is to serve applications like flood forecasting, infrastructure resilience, and decision support. To address data continuity, they focus on the near-term opportunities that can be provided by gap-filling radars with some acknowledgment about the usefulness of satellites. The priority element that may influence the choice of gap-filling radar is the need for low-latency data collection. Thus ground-based radar may be preferred with an open need for faster gauge corrections applied to radar-based QPE products. Thus the NOAA and CIWRO QPE expert interviewees had perspectives that aligned with the priorities that were independently set by the IPC14 student and early career workshop, with one major exception. While the goal of the IPC14 workshop was to facilitate an open, inclusive, and collaborative environment for discussion between students and young scientists in the field, the interviews with experts from NOAA and CIWRO were individual interviews. The outlying emphasis called for by the interviewees was a need for more collaboration between groups since QPE is a multifaceted problem that would benefit from engineers,

forecasters, modelers, and hydrologists all working together to translate technological advances like PAR into operational gains.

This work aims to leverage the unique capabilities of PAR to address the science questions posed by the decadal survey and the priority informants discussed in the previous section. A central objective is to develop QPE algorithms optimized to utilize PAR sampling. PAR's ability to revisit the same volume of the atmosphere at sub-minute temporal resolution provides an unprecedented opportunity to reduce uncertainty in radar observables through faster sampling and to exploit space and time continuity in ways that are challenging or near-impossible with conventional mechanically scanned radars. Reduced uncertainty in radar reflectivity and precipitation rates using probabilistic QPE methods afforded by faster sampling with PAR will be demonstrated with two convective case studies, which directly support the decadal survey goal of achieving more accurate precipitation rates to a measurable level of uncertainty at spatial scales necessary for convective, orographic, and flash-flood environments. For example, for an application time resolution of 2 min used in flash flood forecasting from this work, Figure 1.5 shows how faster sampling reduces the R error from 0.3 in/hr at 2 min sampling to 0.15 in/hr for 30 s sampling for R =1 in/hr.

A major component of this work is the development of a continuity equation-based precipitation retrieval framework that uses PAR-enabled temporal and spatial sampling to better constrain fluxes as well as sources and sinks of condensed hydrometeor mass in the atmosphere, a critical contribution targeted by the decadal survey that calls for microphysical process interpretations at high spatiotemporal resolution. This framework relies on estimates of both 3D wind and derivatives of PAR-mass retrievals within the radar VCP grid. 3D derivatives from PAR variables alone, excluding wind, also provide useful information content for QPE through the inclusion of fingerprints of advection and vertical mass changes. To quantify the benefits of PAR sampling for

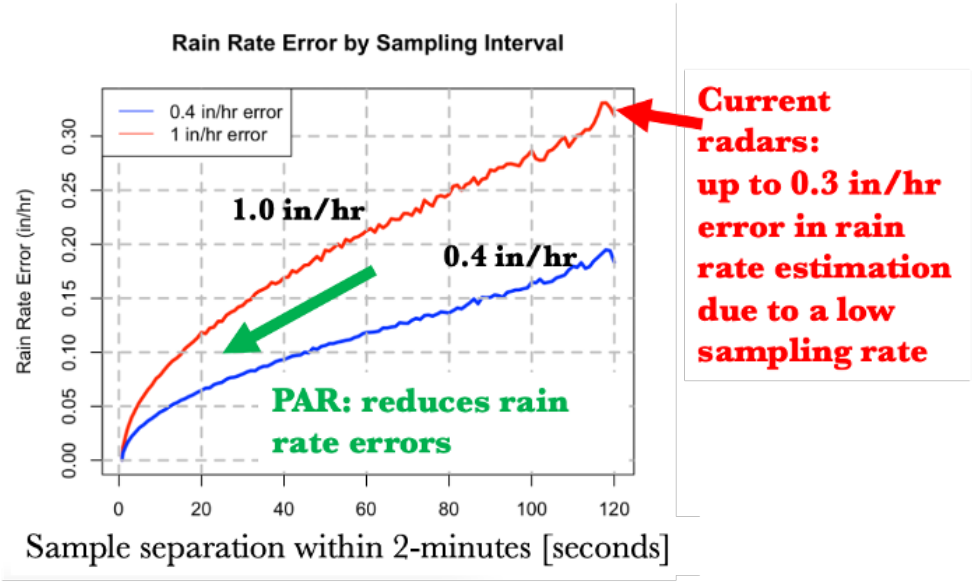


Figure 1.5: Rain-rate error versus sampling interval. Faster PAR sampling reduces error from about 0.3 to 0.15 when the true rain rate is 1 in/hr.

QPE, this research will evaluate QPE performance improvements through targeted simulations and field deployment case studies. This work will also demonstrate methods for the use of gradients to help with precipitation process classification, a further delineation that is shown to aid QPE through the assignment of unique process-conditioned estimators.

Because spaceborne observations are the only tools for global precipitation monitoring, a priority highlighted during the IPC14 student and early career workshop, this research will also explore synergies between PAR and satellite observations. For example, time-delayed satellite observations are proposed by the National Aeronautics and Space Administration's (NASA's) INvestigation of Convective Updrafts (INCUS) mission to study vertical mass flux trends globally (Van den Heever et al. (2022)). This work will consider how PAR can provide fast sampling of atmospheric profiles of radar variables to provide context for the intermittently sampled spaceborne radar observations and to assess through measurement whether the proposed INCUS sampling time

separations are sufficient for capturing convection.

Finally, the project will culminate in a set of recommendations for the future of QPE with PAR, informed by the technical analyses and case studies carried out throughout the research. These recommendations will outline opportunities for joining information content from space- and ground-based PAR measurements, sampling strategies, extensions of temporal analyses to the full suite of polarimetric variables, and opportunities for coupling PAR-based continuity retrievals with numerical weather prediction frameworks such as WRF to improve model performance. The results will contribute to the conceptual design of future field experiments and help guide the integration of PAR capabilities into next-generation operational weather radar networks.

1.3.1 Structure of the Dissertation

The approaches have been organized in this dissertation as follows: Chapter 2 provides the fundamental radar and precipitation science background necessary to understand the QPE approaches implemented in this work. The spatiotemporal benefits of PAR are addressed sequentially. Chapter 3 shows the studies performed, which highlight the temporal improvements afforded to QPE by faster sampling through two convective case studies. Chapter 4 follows this to consider the benefits of the spatial information content available through the use of PAR at fast updates by utilizing the continuity equation. The benefits are shown incrementally, mirroring the path of their discovery alongside Horus integration milestones that incrementally added further system capabilities. This chapter shows both how derivatives of polarimetric variables can be used as new PAR variables to improve QPE and how the use of derivatives in addition to 3D wind information can help to improve storm process assessments at high resolution. Chapter 5 opens the discussion of PAR for global coverage by discussing opportunities where PAR can help to validate and supplement observations from current and

planned satellite radars. Finally, Chapter 6 concludes the work with recommendations for PAR-QPE science and community prioritization.

Together these contributions help to provide a framework for the utilization of PAR's contribution to the field of QPE in the form of spatiotemporal resolution.

Chapter 2

Background

We have discussed the major science questions targeted in this work, which include whether and by how much QPE can be improved by the use of PAR technology. Knowing the errors associated with radar variables is useful for answering this question. As we will see, the errors vary depending on the time scales associated with the data's end-use application. The science questions also include a question about whether the more continuous spatial and temporal sampling offered by PAR technology can be used to estimate precipitation process rates which are used in precipitation modeling schemes, and whether an increase in spatial information content can help to improve QPE. This chapter provides the background context required to proceed to the topics of spatiotemporal advancements on QPE as well as opportunities for the use of PAR to bridge and validate certain satellite mission concepts, which follow.

Precipitation is governed by atmospheric processes across multiple scales, necessitating a diverse range of observations and modeling approaches. This work considers one specific modeling framework, the spectral bin microphysics model, and leverages controlled radar-observed case studies to examine various aspects of PAR capabilities relevant to the improvement of microscale QPE. Key concepts are outlined in this chapter, including the particle size distribution (PSD), which underpins all hydrometeor observations, the influence of atmospheric motion at different scales on precipitation dynamics, and advances in observational technology, such as polarimetric radar and spaceborne sensors, that enable improved QPE. These observational capabilities

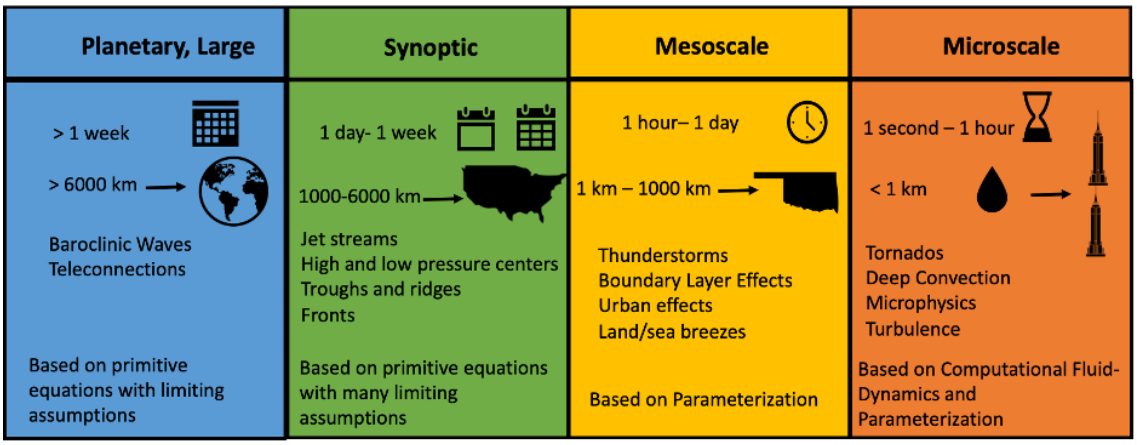


Figure 2.1: Precipitation is understood by developed theories that cover different scales of motion. The planetary (or large) scale of motion, the synoptic scale (approximately up to the length across the contiguous United States and lasting 1 day to 1 week), the mesoscale (approximately the length of the state of Oklahoma and lasting 1 hr to 1 day), and the microscale.

are essential not only for real-time monitoring but also for informing and validating atmospheric models.

There are four major scales of motion typically categorized for the atmosphere, depicted in Figure 2.1. Baroclinic waves and teleconnections are examples of some of the largest patterns theorized to perturb precipitation on the planetary scale with spatial scales greater than 6000 km and evolution time scales greater than one week (Cavallo (2021a)). The synoptic scale, which includes phenomena such as jet streams, high and low pressures in the atmosphere such as troughs and ridges, and frontal boundaries, operates on time scales from 1 day to 1 week and spatial scales from 1000 km to 6000 km (Cavallo (2021a)). Both the synoptic and planetary scales of atmospheric motion are most often modeled with idealized primitive equations (Navier-Stokes), that are constrained with limiting assumptions such as the atmosphere being in a state of hydrostatic balance, conforming to a shallow-atmosphere approximation, containing ideal gasses, or being in a state of geostrophic balance (Holton and Hakim (2013)). The mesoscale has a more local and immediate impact at a spatial scale of 1 km to

1000 km and occurs over a time scale of 1 hour to 1 day (Cavallo (2021a)). The mesoscale is the scale of motion that is used to study large thunderstorms, boundary layer effects, urban effects, and land/sea breeze effects on precipitation, which is most typically modeled with parameterization schemes (Cavallo (2021a)). The scale of most interest in this work is finer than all of the aforementioned scales: the microscale. The microscale can be observed by radar and can be modeled by spectral bin microphysics models via parameterization. The microscale can be thought of as precipitation processes that occur from 1 s to 1 hr within a spatial resolution smaller than 1 km (Cavallo (2021a)). Grounding the visualization of this scale by comparison to commonly known objects, as depicted by Figure 2.1, the size scale of the microscale extends from the size of a raindrop to the size of two stacked Empire State Buildings. Systems within the microscale include tornadoes, deep convective cells, turbulence, and microphysical processes (Cavallo (2021a)). Microphysical processes and convective systems at the microscale as observed by PAR and simulated by spectral bin microphysics models are the phenomena in focus in this work.

Microphysical models can be categorized into two major types: bulk schemes and spectral bin microphysics schemes. Both are parameterized to update the distributions of hydrometeor sizes (PSD) that undergo the influence of processes like evaporation, sublimation, collision-coalescence, melting, shedding, and drop breakup. While bulk models update parameters such as total mass and number concentrations associated with a statistical distribution (e.g., gamma distribution), spectral bin microphysics models update the number of hydrometeors within a series of particle size bins to provide a more detailed description of the evolution of PSDs. Alongside hydrometeor phase and composition information, the PSD defined in these models is the critical component that defines the mass in each model spatiotemporal grid. Processes that work to modify the PSD depend on the drop size and can thus alter the shape of the

PSD through their unique impact on each particle size. The integrated effective mass change over a model grid's PSD due to an imposed process is defined to be the process rate, p, in this work. As will be seen, this work will introduce how p can be extracted with the use of three-dimensional PAR observations via the mass continuity equation.

Radar observations indirectly inform geophysical variables such as the PSD and derived variables (moments) such as the precipitation rate, hydrometeor classes, and sizes. QPE retrievals from weather radar have been extensively advanced from initially proposed relationships between the radar equivalent reflectivity (Z) and the rain rate (R) proposed by Marshal and Palmer in 1948 (Marshall and Palmer (1948), Ryzhkov et al. (2022)). Thanks to their spatially and temporally more continuous observations, PAR has the potential to better capture the temporal and spatial variations of the PSD and its moments than dish-based radars. Process rates informed by these captured spatiotemporal variations quantify how quickly a specific microphysical process, such as evaporation or collision and coalescence, is happening in the atmosphere. These rates are crucial for modeling precipitation because they determine the evolution of hydrometeors in storms. In this work, a process rate is defined as the temporal rate sourcing or sinking of mass associated with the PSD in a hypothetical volume of atmosphere (e.g., a radar resolution volume) that results from the combined contribution of various microphysical processes. It is expressed in units of kilograms per second per cubic meter. Generally radar retrievals convert observations in the form of radar variables into an estimate of a geophysical parameter of interest, such as rain rate, using theoretical and empirical methods. Radar data streams from multiple radars can be integrated into a common framework to derive hydrometeorological products (e.g., Multi-Radar/Multi-Sensor System; MRMS; Zhang et al., 2016). Radar-based QPE is also often calibrated with precipitation estimates from in-situ instruments such as rain gauges (Habibi et al. (2021), Pradhan et al. (2022a)).

Progress in precipitation science and applications with weather radar is being spearheaded by new technology that targets faster sampling of storms, both on the ground and in space. While observations of storms with ground-based and spaceborne radars have been invaluable to improve the science and applications of satellite constellations and radar networks for over more than 20 years, they have been largely limited to more discrete storm snapshots. From space, weather radar observations miss the storm's temporal evolution, so fixed vertical profiles of equivalent radar reflectivity are interpreted in terms of columns of microphysics; however, without factoring in the storm's temporal evolution and the motions in the vertical columns that quickly alter their microphysical structure. While storm evolution can occur within a minute, ground-based dish radars do not sample the atmosphere at a fast enough rate to adequately capture storm evolution. For instance, the current WSR-88D radar sampling updates can take approximately 5 min. Temporal evolution is now a focus of both ground-based and spaceborne observations that drives the design of future sensors and technologies. In particular, the National Aeronautics and Space Administration (NASA) Investigation of Convective Updrafts (INCUS) mission Van den Heever et al. (2024) is designed to target moist convection that rapidly creates and alters the structure of clouds through time-separated radar observations. Rapid changes in clouds can be observed by a convoy of satellite radars at the fast time scales that govern the underlying moist convection processes in convective updrafts (e.g., 30 s). Because each satellite radar detects the distribution of condensed water (estimated condensed water) within its field of view, the convoy detects the change in this condensed water over the time separating the convoy members. Such satellite missions target vertical transport above the freezing level because they are planned to operate at Ka-band which attenuates quickly in rain (Van den Heever et al. (2022)). They will likely miss convective properties in regions of liquid phase with high water content in the convective cores. Recent ground-based

polarimetric PARs provide more frequent observations and thus more frequent estimates of microphysics parameter profiles, which means that ground-based PARs can capture their changes several times over the time separating satellite convoy members (Palmer et al. (2023b)). They capture the targeted changes in storms at less attenuated frequencies (e.g. S-band), especially resulting from moist convection, both below and above the freezing level, hence providing vertical continuity that is missing with space observations.

This chapter introduces foundational concepts for improved QPE with the use of PAR at the microscale, ranging from microphysical basics such as PSD, the formation of rainfall, and hydrometeor types to the function of weather radar, including PAR, which enables QPE through radar retrievals. In addition, the spectral bin microphysics model used throughout this work to analyze PAR concepts is described.

Background

2.0.1 Precipitation Types

Hydrometeor classes are foundational to the study of precipitation microphysics. Accumulated surface rainfall is produced by various types of cloud formations that arise due to varying planetary-, synoptic-, and meso-scale processes. Clouds exist within approximately the lowest 10 km of the atmosphere, in the troposphere, and are often capped by the tropopause, which is at different levels for different parts of the globe. Each cloud type is supported by a unique set of environmental factors that promote their generation. The microphysics of clouds and their produced precipitation is relatively well understood. Individually, the physical characteristics of hydrometeors and the mechanisms involved in their formation have been well-studied. However,

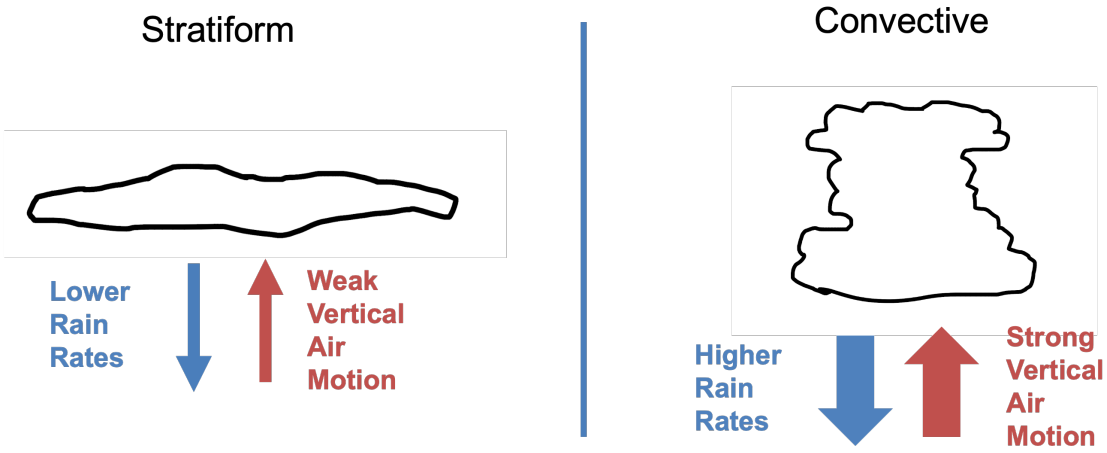


Figure 2.2: Stratiform precipitation tends to be characterized by low rain rates, less than about 10 mm/hr, and weak vertical air motion, less than about 2 m/s. Convective precipitation is characterized by higher rain rates and stronger vertical air motion (Houze Jr (1997a)).

distinguishing the physical characteristics of the precipitation produced by clouds is challenging due to the numerous interacting hydrometeors, the mutual influences of microphysics, and atmospheric movements on a larger scale. These interactions result in the existence of a diverse range of precipitation embodiments. Conventional weather radar's observation of precipitation is limited, as it does not provide access to crucial quantities such as vertical velocity or particle phase. Nevertheless, a radar performing a volumetric scan of the atmosphere enables differentiation between two types of situations. The intensity of vertical air movements and the efficiency of rain-generating processes leave a distinctive signature, allowing for distinction between "stratiform" and "convective" situations as shown in Figure 2.2. We are referring here to the work of Houze (1993), Steiner et al. (1995), and Rosenfeld and Ulbrich (2003).

For a stratiform situation

$$|V_{air}| \ll |V_{hydrometeor}|$$

and for convective situations

$$|V_{air}| \geq |V_{hydrometeor}|$$

Stratiform precipitation is typically produced by clouds whose altitude extends beyond the 0° C isotherm. These clouds exhibit a distinct structure, with the upper part in the ice phase and the lower part in the liquid phase. In the highest regions, solid-phase particles grow through various mechanisms, such as vapor deposition and aggregation. Their descent is facilitated by moderate but persistent vertical air movements, less than about 2 m/s. However, as the particles descend, they encounter the 0°C isotherm, causing them to melt. This melting process results in the formation of large drops that fall rapidly. The weakness of the vertical circulation leads to the stratification of particle size, with a well-defined intermediate zone known as the melting layer. This layer has an upper limit near the 0° C isotherm and a lower limit a few hundred meters below. During melting, ice crystals form a thin layer of liquid water, appearing as large drops of water. This phenomenon causes an increase in the equivalent radar reflectivity factor, commonly referred to as the "bright band," which significantly disturbs the estimation of precipitation intensity by weather radar. Above the melting layer, the reflectivity decreases with increasing altitude, while below it, its evolution becomes more regular. For further information on this topic, the interested reader is referred to Fabry (1996), Fabry and Szyrmer (1999), Tremblay (2005), and Franco et al. (2005). Stratiform precipitation systems have a limited vertical extent and a significant lifespan, lasting several hours. Stratiform precipitation is characterized by smaller mean drop sizes (mean diameter $D_m < 1.5$ mm) and smaller rain rates (< 10 mm.h^{-1}), with a distinct geographical extent (about 10–1000 km) and limited spatial variability. In the midlatitudes, stratiform rain is commonly observed in the

fronts of midlatitude cyclones, in large-scale warm advection in baroclinic cyclones, in orographic contexts, and in the rear of mesoscale convective systems (Houze Jr (1997a), Munchak et al. (2012), Thurai et al. (2021)).

Convective clouds have a greater vertical extent compared to stratiform clouds. In the process of convection, shown on the right in Figure 2.2, less dense air rises, cools, and condenses to form cumulus or cumulonimbus clouds. Water particles have time to grow by vapor diffusion or collision-coalescence to large sizes as they are pushed upwards by a strong updraft (Thomas et al. (2020), Chandrakar et al. (2024)). Particles fall as precipitation only when they are heavy enough to counteract the upward motion. This process is particularly common in the tropics. Convective precipitation is characterized by vertical air movements ranging from 2 to 10 m/s or more, which prolongs the residence time of hydrometeors within the system. This leads to the efficient development of precipitation. Precipitating particles grow in the liquid phase through coalescence or icing/riming at high altitudes. Most convection does not extend vertically throughout the entire cloud, and it only occurs in a portion. This vertical organization features an ice phase aloft, an intermediate mixing layer where convection occurs, and a liquid phase below. The convective mixing layer is typically thicker than its stratiform equivalent. Particles in both the liquid and solid phases likely coexist throughout the convection zone. The mixing layer is predominantly distributed on either side of the 0° C isotherm. In contrast to stratiform situations, convective systems exhibit a certain vertical homogeneity and a variable horizontal extent. Primarily driven by lifts that can carry large particles aloft, they are characterized by columns of high reflectivity as sensed by weather radars. Convective formations are more variable horizontally and have a shorter lifespan, typically lasting only a few hours. Convective precipitation is characterized by larger mean drop sizes ($D_m > 1.5$ mm) and heavier rain rates ($>$ 10 mm/hr). Convection is often associated with precipitation

extremes. Convective precipitation typically occurs in horizontally localized convective cells, which include most clouds in the tropics, and is associated with extreme events and frozen hydrometeors like hail and graupel (Houze Jr (1997a), Munchak et al. (2012), Thurai et al. (2021)).

It is useful to note some methods employed to distinguish between convective and stratiform precipitation that will be introduced in Section 2.6.3. These include analyses of the vertical profile of reflectivity and the echo top height, as observed by both satellite and ground-based radar systems. While differences between satellite and ground-based measurements arise from variations in viewing geometry and radar operating frequency, such radar-derived profiles are valuable not only for precipitation classification purposes but also for providing context on the microphysical processes that influence the particle size distribution.

2.0.2 The Particle Size Distribution

In hydrometeorology, many important quantities can be derived from the Particle Size Distribution (PSD). Noted $N(D)$, the PSD represents the number of hydrometeors N of size D $[mm]$ per unit volume (Figure 2.3). It is noted $N(D)$ and has units of particles per cubic meter per millimeter $[mm^{-1}.m^{-3}]$. Importantly, the PSD is an underlying physical quantity that many precipitation sensors seek to determine for the interpretation of remote sensing observations for QPE and for parameterizations in numerical models.

Derived PSD quantities that can describe a population of hydrometeors within a radar resolution volume include the particle number concentration (N_t $[m^{-3}]$), the mean particle diameter (D_m $[mm]$), the liquid water content (LWC $[g.m^{-3}]$), the precipitation rate (R $[mm.h^{-1}]$) and radar variables such as the radar reflectivity factor (Z $[mm^{-6}.m^{-3}]$). These quantities are derived from the PSD and often referred to in

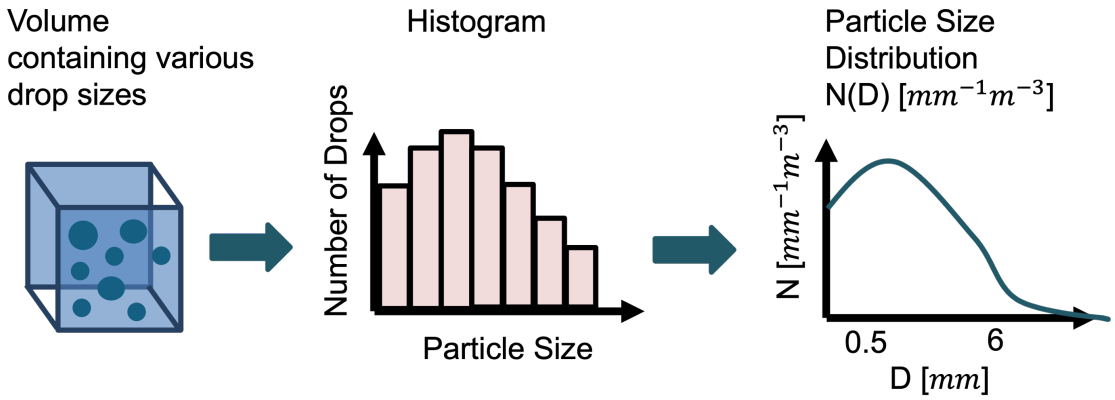


Figure 2.3: Within an observed volume of space (e.g., radars illuminate volumes of space), particles come in many shapes and sizes (e.g., with different equivalent diameters, D). The PSD represents the number of drops of each diameter. In microphysics models, this can be represented either as discrete diameter bins or as a continuous distribution (e.g., a gamma or exponential distribution).

hydrometeorology as moments of the PSD. For example, Z is derived in Equation (2.3) to be the integral over all drop sizes in a distribution of $D^6N(D)$. Because D is taken to the power of 6, assuming a spherical raindrop, it is referred to as the 6^{th} moment of the PSD.

Now we will consider other important moments of the PSD to hydrometeorology, which will be defined with reference to Kirstetter (2022). The 0^{th} moment of the PSD is N_t defined as

$$N_t = \int_0^\infty N(D)dD. \tag{2.1}$$

The characteristic hydrometeor size, D_m, can be provided with units of $[mm]$. It is the 1^{st} moment of the PSD defined as

$$D_m = \frac{1}{N_t}\int_0^\infty DN(D)dD. \tag{2.2}$$

$$Z = \int_0^\infty D^6 N(D) dD. \tag{2.3}$$

The LWC in units of gm^{-3} is used in radar hydrometeorology for short-term weather prediction and in satellite precipitation estimation. It is defined as the mass of water associated with the PSD, and it is computed as the integral of the density of liquid water (ρ_l) multiplied by the volume of each drop (all assumed here to be spheres), further multiplied by the PSD as:

$$LWC = \int_0^\infty \frac{\pi D^3}{6} N(D) dD. \tag{2.4}$$

Finally, if we estimate the vertical velocity of hydrometeors, $v(D)$, which is the drop terminal velocity when no vertical wind is present (e.g., Brandes et al. (2002) has estimations for liquid raindrops), then the rain rate (R) in units of $[mm.h^{-1}]$ is also a moment of the drop size distribution defined as:

$$R = \rho_l \int_0^\infty \frac{\pi D^3}{6} N(D) v(D) dD = \rho_l \int_0^\infty \frac{\pi D^3}{6} N(D) v(D) dD. \tag{2.5}$$

From rain rate, accumulated rainfall over any time period t can be determined as

$$R_{total} = Rt. \tag{2.6}$$

If R is expressed in $[mm\ h^{-1}]$ and time is expressed in hours, then R_{total} takes units of mm.

2.1 Quantitative Precipitation Estimation

The moments of the PSD cannot be directly observed in the atmosphere or, in the case of rain rate, at the surface of the Earth. Thus, they must be measured with in-situ instruments or estimated with remote sensing, typically by means of radar observations. At the time of the writing of this dissertation, most current ground-based radar systems probing the atmosphere in search of PSD moments for microscale analyses, which have feedbacks to atmospheric dynamics at all scales, are, and are expected to be in the future, polarimetric radar systems. These systems sense scattering of hydrometeors which provide information about the shape and size of particles and must always be validated by localized measurements in the form of in situ measurements.

2.2 Polarimetric Radar

Polarimetric radar will be introduced in its context relative to other existing remote sensing technologies, including microwave links and satellites used to provide observational coverage at various scales of motion, starting with the ground reference in situ instruments that facilitate calibrated performance for all remote sensing instruments targeting atmospheric hydrometeors.

Two of the most fundamental in-situ ground-based instruments often regarded as the "ground truth" for rainfall measurements are the rain gauge and the disdrometer. Rain gauges, such as the electric tipping-bucket type, measure accumulated rainfall at regular intervals, while disdrometers estimate PSDs using various techniques, including impact, optical sensing, or laser-beam measurements as hydrometeors fall through the device (Kathiravelu et al. (2016)). Many state and national agencies maintain extensive networks of gauges and disdrometers, providing observations that support

scientific analyses at synoptic, mesoscale, and microscales. These reference measurements are also widely used to calibrate and validate precipitation retrieval algorithms developed for other remote sensing platforms, including ground-based radar, satellite radar, geostationary satellite infrared sensors, and microwave links.

When environmental conditions such as temperature, pressure, and humidity are needed, measurements can be obtained directly via radiosondes or estimated from satellite observations and plotted on Skew-T diagrams. For example, the Time-Resolved Observations of Precipitation Structure and Storm Intensity with a Constellation of Smallsats (TROPICS) mission estimates environmental parameters using millimeter-wave sounder channels: oxygen absorption lines for temperature and water-vapor lines for humidity, without relying on ancillary in-situ data (Kidd et al. (2022)). Such environmental measurements are routinely available on land but are generally not collected within precipitation, making them particularly valuable for analyses at global-, synoptic-, and meso-scales.

Remotely sensed microwave links capture the along-path attenuation impacting communication signals when precipitation occurs within their line of sight (Eshel et al. (2021)). When this signal information is appropriately dense, these measurements can be corroborated to estimate precipitation rates on scales ranging from the microscale to the mesoscale.

Satellite measurements can be taken from two major types of platforms: geostationary and low-earth orbiting. Geostationary satellites using infrared provide data at resolutions comparable with weather radar products (e.g., about 2 km and 5 min for GOES-16) that can span up to a hemisphere of the globe, making this type of measurement useful over a large range of scales of atmospheric motion. Low Earth orbiting satellites typically house passive microwave instruments and radar. These are useful at the microscale because they provide a snapshot of dense information content at this

scale. Because they are onboard moving platforms, they can collect information with global representativeness over time.

A ground-based weather radar collects spatiotemporally dense samples of the atmosphere in the form of radar variables, available within a grid of resolution volumes whose size is defined by the radar beamwidth and pulse bandwidth (e.g., beamwidth of 3 °and range resolution of 20 m). Individual radars such as the Horus PAR or vertically pointing radars like MRRs are used to observe precipitation at the microscale. Networks of radars exist, like the NEXRAD network, making this useful at microscale and mesoscale over land. Information content from any set of remote sensing instruments can also be combined, as has been done for IMERG with spaceborne sensors and MRMS with ground-based sensors. As will be discussed in Chapter 5.1, the advent of ground-based PAR radar introduces the opportunity for unique spaceborne retrieval evaluations and enhancement by matching observations from both orbital and suborbital platforms, especially for upcoming satellite missions using time-separated observations that focus on convection, such as INCUS (Van den Heever et al. (2024)).

Traditional weather radar operates by transmitting single-polarization electromagnetic waves into the atmosphere and analyzing the energy that is scattered back to the receiver. Polarimetric radar, on the other hand, involves the reception of two orthogonal polarizations that are impacted by hydrometeors in the atmosphere in different ways. The NEXRAD (WSR-88D) system transmits a single, effectively randomized polarization, often approximated as a 45 °slant orientation, but receives simultaneously on orthogonal horizontal and vertical polarizations (Doviak et al. (2000)). Polarimetric radar has allowed scientists to imagine new possibilities for understanding the shape, size, orientation, and received signals after they interact with hydrometeors in the atmosphere, which has allowed for hydrometeor classification and data quality improvements in QPE. Polarimetric radars widely in use today use parabolic dish systems.

Newly emerging radars are PAR systems that provide new spatiotemporal capabilities for sampling the atmosphere.

2.2.1 Hardware: Dish versus Phased Array

Ground-based weather radars, whether dish-style or phased array, operate on the same fundamental principles. They transmit pulses of electromagnetic energy into the atmosphere using an antenna system, emitting both horizontally and vertically polarized signals. As this energy propagates through the atmosphere, it is focused in a specific direction, creating an antenna gain that determines how much power reaches a particular location in space. The beam is not infinitely narrow, and its beamwidth defines the radial resolution of the volume being sampled.

When this transmitted energy encounters hydrometeors (like raindrops or hail), a portion is scattered back toward the radar. The collective response from all particles within the radar's resolution volume contributes to the returned signal. Rayleigh scattering occurs when the radiated particles are small relative to the wavelength of the radar, inducing a dipole moment in the particles so they backscatter energy at the same frequency as the incident wave (Young (1982)). Assuming Rayleigh scattering, the reflected power is proportional to the sixth power of the drop diameter, D^6, allowing estimates of drop size distribution within that volume.

These operational characteristics apply to both traditional dish radars and more advanced phased array systems. However, all weather radars have inherent limitations that can impact QPE. These include calibration, terrain-induced beam blockage, attenuation by precipitation (both airborne and on the radome), the presence of a "cone of silence" where no measurements can be taken directly above the radar due to limited coverage aloft in elevation by design of the antenna and pedestal, atmospheric refraction, the inability to measure transverse winds (only radial velocity is available if the

system is a Doppler radar), resolution limits due to beamwidth and pulse duration, range aliasing from limited pulse repetition intervals, beam broadening with distance, vertical variations of precipitation, and gaps in both spatial and temporal coverage. Specific to PAR, Ho et al. (2024) also indicates that a challenge with planar phased arrays is a degradation in polarimetric variable fidelity when the beam steers far off broadside and in regions of low SNR.

The operational radars in use today are largely dish radar systems operated in networks such as the NEXt generation RADar (NEXRAD) network composed of 160 WSR-88D (Weather Surveillance Radar - 1988, Doppler) radars across the contiguous United States, the European Meteorological Network (EUMETNET) and the Operational Programme on the Exchange of Weather Radar Information (OPERA) in Europe (Huuskonen et al. (2014)), and the China New Generation Weather Radar (CINRAD) (Min et al. (2019)) for example. These radars provide periodic volume coverage, for example approximately every 5 min, by rotating in azimuth at a series of elevation angles. One notable drawback of conventional dish radars is their limited temporal and vertical spatial sampling. Because they mechanically scan through elevation angles, there is a tradeoff between coverage and update speed. PARs address this by electronically steering their beams, significantly reducing scan time and improving vertical coverage frequency.

Figure 2.4 shows a Venn diagram comparing the similarities and differences between PAR and dish-based radars. Phased array systems can be developed in two ways: using analog beamforming or digital beamforming. In analog beamforming, a common signal is distributed through phase shifters and attenuators to each antenna element, steering the beam in the desired direction. The received signal is then coherently combined and downconverted for digital processing. In contrast, digital beamforming digitizes signals directly at each antenna element. This allows for simultaneous processing of multiple

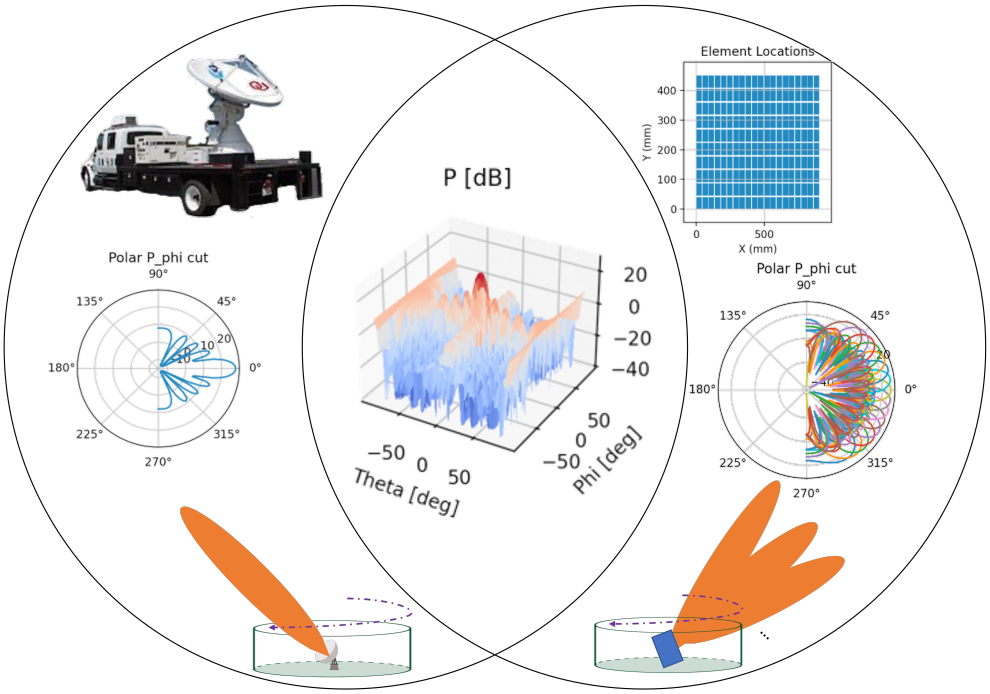


Figure 2.4: Both PAR and dish-style radars (center) are capable of focusing transmitted and received energy to achieve narrow beamwidths, can be designed as dual-polarimetric systems, and often include a radome. Traditional dish-style radars (left) feature a single transmit and receive beam that, due to mechanical steering, can take 5-6 min to complete a VCP (e.g., NEXRAD), which inherently features gaps in vertical coverage. PAR (right) can simultaneously receive any number of programmed beams to help close gaps in vertical coverage. (Dish radar image from NOAA National Severe Storms Laboratory (2025b))

receive beams in different directions, enabling rapid and flexible sampling of the atmosphere. All incoming energy is captured and later digitally steered and analyzed, offering significant advantages in speed and adaptability. The Horus PAR, which will be introduced in Section 2.3.1 is of the latter type, an all-digital PAR. Thus, as Horus is the PAR demonstrator used in this work, when we refer to PARs henceforth, we assume they use electronically steered transmit and receive beams to scan the atmosphere more quickly than dish radars are capable of and have additional beamforming capabilities due to their all-digital design. Horus has been demonstrated to be capable of, for example, completing a 360 ˚azimuth mechanical rotation while sampling the atmosphere with a imaged RHI (digitally beamformed RHI with simultaneous receive beams in elevation), completing a volume scan in 24 s. This work advocates for the use of continuous RHI sampling of the atmosphere to the benefit of QPE and quantification of process rates at the storm scale while maintaining a high temporal volume revisit time. This is because vertical continuity has been shown to be important for microphysical process studies that impact QPE (e.g., Ryzhkov et al. (2013a), Kirstetter et al. (2013)).

2.2.2 Sampling of the Atmosphere in Time and Space

The temporal volume revisit time, or resolution, of radar observations is a key limiting factor in the accuracy of QPE and microphysical retrievals. Dish radars are limited by the time it takes them to steer mechanically in order to complete a VCP. For example, in highly dynamic environments that characterize the limited lifetime of localized convective updrafts and downdrafts, the 5-minute time scale may miss key alterations in the storm dynamics. Moroda et al. (2021) found that convective cell restructuring within a larger system could happen in only a few minutes. Just as sampling at or above the Nyquist frequency for band-limited signals in radar signal processing pre-

serves the sample autocorrelation, sampling a non-strictly band-limited atmospheric phenomenon's evolution in temporal increments below the signal decorrelation time is important for preserving the time dependency of the signal's information content.

The spatial sparsity of radar observations within their VCPs is a key limiting factor in the accuracy of QPE and microphysical retrievals. Atmospheric phenomena are fundamentally governed by mass continuity. Current dish-based VCPs fail to provide the 3D spatial context required to close the mass-continuity equation. The advent of PAR in addition to 3D-wind retrieval and estimation techniques is a scientific leap forward with a major potential to improve modeling and forecasts. When used in combination, these technologies can enable simultaneous or near-simultaneous mass flux estimates in 3D. The estimated closure of the continuity equation applied to condensed hydrometeor mass observed by a radar can improve QPE and can allow for the quantification of hydrometeor process rates in the atmosphere.

2.3 Field Campaigns with Polarimetric Radar

To validate the closure of the continuity equation with PARs, a targeted field campaign titled Precipitation Process Wind Experiment (PROWEX) was designed and implemented with Horus as a part of this work. The eventual success of this radar-based field campaign hinged on careful coordination of sampling strategies between multiple instruments, prototype PAR capabilities and integration timelines, and on effectively navigating the organizational processes that shaped project implementation.

2.3.1 The Horus Phased Array Radar and Science Testing Alongside Radar System Integration

During the integration of new radar subsystems and signal processing features for the Horus prototype PAR from 2022 to 2025, several scientific experiments were conducted in parallel to assess radar performance and validate early capabilities. This system integration project phase represented a unique overlap between engineering development and scientific exploration, where each integration milestone was accompanied by data collections and test campaigns while the University of Oklahoma's (OU's) Advanced Radar Research Center (ARRC) engineering team intermittently evaluated calibration stability, data quality, and functional readiness.

Building beyond the advancements brought by dual-polarization technology to the weather radar community, the Horus PAR program is funded by NOAA/NSSL and has aimed to fund the continued development of dual-polarized weather radar technology through enhancements brought by a fully digital PAR. The goal of the project has been in part to demonstrate that PAR can be developed to maintain the polarimetric quality provided by current dish radars while also enhancing information content through faster spatiotemporal sampling of the atmosphere. It is a prototype instrument that has been serving as a testbed for the development of future PAR systems (Palmer et al. (2023b)).

Horus is a mobile S-band PAR developed at OU's ARRC. The full PAR design is composed of an array of dual-polarized antennas to create a grid of 40 by 40 elements (25 panels each with $8 \times 8 = 64$ dual-polarization elements), each with dual-polarized channels, with an aperture of 2.03 m $\times$ 2.03 m to achieve a 2.58°beamwidth at broadside (Palmer et al. (2023a)).

Horus has been under constant integration since its idea conception, which was contributed to by ARRC graduate students, staff, and faculty. A proof-of-concept array

was ready to begin demonstrative tests in the spring of 2022. Data collection began in December 2022 with a single panel of 8 x 40 active elements such that Horus could collect wide fan-beam atmospheric observations, aiding in the testing of a mutual coupling calibration approach that involves illuminating single transmit elements with a known signal and receiving from all neighboring elements iteratively until all transmit elements have been activated, then minimizing each element's amplitude and phase errors relative to ideal to arrive at a uniform array prior to applying any beamforming techniques (Herndon et al. (2024), Fulton (2022)). Other updates to functionality were implemented following this, including expanding to dual-pol calibration using holographic near-field back projection (Raghunathan and Gowri (2018)) and progressive pulse compression (PPC) (Aquino et al. (2021a)).

PPC allows for closer-in-range coverage by reducing the blind range while maintaining a high signal-to-noise ratio (SNR). It also preserves the sensitivity typically achieved by transmitting a long pulse and receiving with a matched filter that correlates the received signal with the transmitted waveform (Aquino et al. (2021a)). The SNR of a radar system is the ratio of the power energy transmitted in a pulse, defined to be the peak transmit power multiplied by the pulse duration, to the thermal system noise power $N = kTB$, where k is Boltzmann's constant, T is the temperature in Kelvin, and B is the noise bandwidth. Rather than transmitting a pulse of length, $\tau = 32$ microseconds, for example, which causes a blind range $R_b = c{*}\tau/2 = 4.8$ km but maintains a high $SNR = P_t * \tau/(kTB)$, PPC splits the pulse into segments, allowing for the reception of previously transmitted sections while continuing to progressively transmit remaining sections of the transmitted pulse in the sequence. This reduces the blind range to $R = c * (\tau/N_s)/2$ where N_s is the number of sections in question while maintaining nearly as high of an SNR as that of the PPC pulse's long-pulse counterpart (Aquino et al. (2021b)). An updated algorithm for PPC, called PPC+,

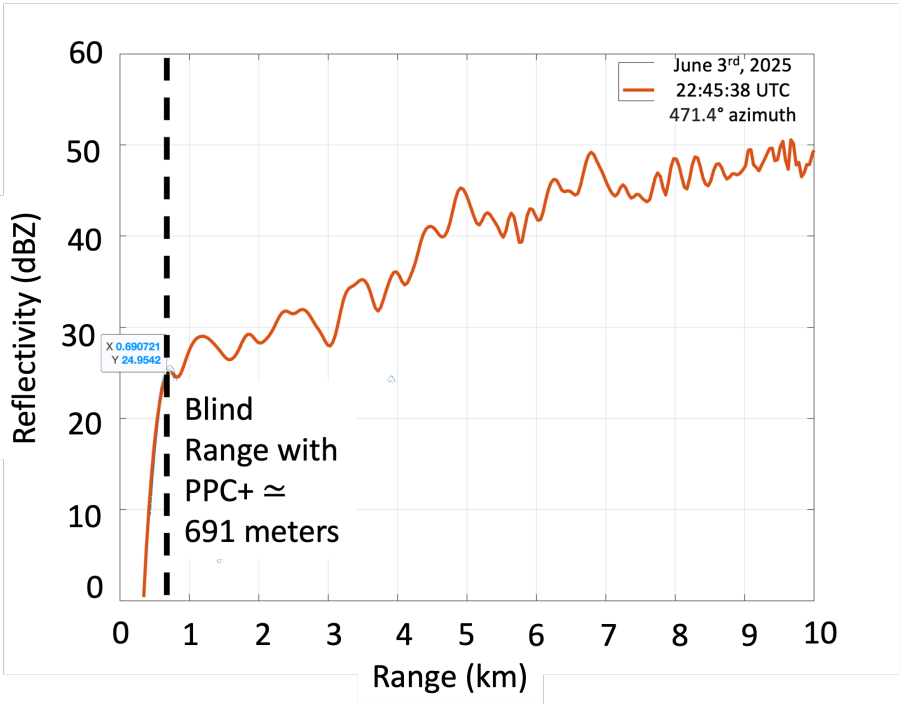


Figure 2.5: Radar reflectivity (dBZ) versus slant-range (km) to 10 km for an observation of a convective precipitating system observed on July 3, 2025. This figure shows the radar blind range with the use of PPC+ to be at an estimated 691 m from the antenna, which is a great improvement over the 4.8 km blind range observed without the use of PPC.

further reduces the blind range with an improvement on the matched filter used in receive mode(Salazar et al. (2024)). Figure 2.5 shows a single-ray observation from Horus taken during a convective precipitation event that clearly shows the blind range. Instead of a blind range of 4.8 km, a blind range of about 691 m is observed due to the application of PPC+, which has been a significant improvement for the purposes of our analysis in Chapter 4.

Polarimetric science analysis, such as is described in this work, must be able to assume that the radar system being used is well-calibrated. Near-field antenna measurement is a technique implemented to provide flexibility and rigor to the array calibration assessment by measuring an antenna pattern close to the array panel in its near-field

rather than in the far-field, providing flexibility for the assessment of various beamforming schemes. The far field is the focusing distance required for an antenna where the electric and magnetic fields converge to near-orthogonal in the far field region at a distance of $2D^2/\lambda$. Taking the maximum dimension of the array to be the diagonal along the 2.03 x 2.03 m array, the maximum dimension is $D = \sqrt{(2 * 2.03^2)} = 2.87\ m$ and the wavelength at 3 GHz is $\lambda = (3 * 10^8)/(3 * 10^9) = 0.10\ m$ where 3e8 m/s is the speed of light in a vacuum so that the far-field region begins at a distance of 164.74 m. The near-field measurements, taken near the antenna as indicated by their name, are distances close to the antenna below 164.74 m so long as the measurement is taken outside the reactive near-field region near the face of the antenna (Slater (1994)). When a near-field measurement is taken, a back projection to the panel of the array called a hologram can be calculated, which reconstructs the amplitude and phase present across the face of the array, or at each antenna element. By this method, the calibration of the array after mutual coupling calibration can be assessed explicitly, and the calibrated near-field measurement can be transformed to the far-field to assess total antenna gain, which allows for flexibility for testing various beamforming schemes.

In August of 2023, Horus was ready to be tested with more populated elements: 832 elements comprised of 13 panels. This allowed Horus to take pencil-beam, or fully focused, measurements with horizontal and vertical beamwidths of 2.6 °and minimum power sensitivities of about 4.3 dBZ at 50 km and the ability to perform digital beamforming techniques such as imaging with real-time I/Q recording in receive, which allows for creative post-processing techniques including imaging (Palmer et al. (2023b), Schvartzman et al. (2021), ARRC (2023)). This is because the received signal $s(t) = I(t) + jQ(t)$ contains amplitude and phase information of the returned signal, which can be manipulated in post-processing to produce directional estimates of v_r and polarimetric variables. Later the pulse compression was upgraded to PPC+ to further

reduce the blind range (Salazar et al. (2024)).

Hardware and software upgrades continually evolving from the first demonstrative tests in the spring of 2022 meant that Horus scheduling time from 2022 to 2025 for scientific study observations was limited, in addition to tests needing to adapt to evolving radar capabilities. Thus, to begin our study of processes in the atmosphere, we began by looking at 24 GHz frequency modulated continuous wave (FMCW) vertically pointing micro-rain radar (MRR) observations collocated with a distrometer on October 25th, 2019, to show that vertical profiles of radar variables can be processed to return height and time derivatives of radar variables, which can be used to improve QPE by analyzing height and time derivative trends relative to surface precipitation rates. This is detailed in Chapter 4. Following the processing of this MRR data, observations were taken on May 11, 2023, with a wide fan-beam measurement due to the availability of a partially populated phased array with 8x40 elements. The array was populated with 5 panels vertically and 1 panel horizontally, resulting in a vertical 3 dB beamwidth of 2.6 degrees and a horizontal 3 dB beamwidth of 6.7 degrees, as is discussed in Chapter 3.

Following the population of a 13-panel array of elements, RHI measurements were taken on August 8, 2023, with a calibrated 13-panel active antenna array, making a pencil beam with a 2.6° beamwidth in azimuth and elevation, which were matched to MRMS rain rates at the surface. The MRMS radar only QPE at a spatial resolution of 1 km and a temporal resolution of 2 min was used for this study. They were calibrated using hourly rain-gauge values. To refine the MRMS QPE estimates so that rain rates could be captured at the native beam-observation timing of the KTLX WSR-88D within the Horus coverage area, collaborative work was performed with the MRMS team to extract refined time estimates of QPE from their processing chain. A paper was drafted entitled “Quantitative Precipitation Estimation with Phased Array

Radars" based on this work but was not published due to the identification of sources of error that could impact the results: 1) the exclusion of advective derivatives from the QPE estimation and 2) an unknown offset error in the pointing direction of Horus. To identify the offset error, the Horus RHI measurements of reflectivity on August 8, 2023, were resampled to the WSR-88D grid and correlated to the WSR-88D reflectivity, sweeping over angles of +10°and -10° from the indicated pointing direction in the Horus metadata. While offset angles were found to minimize the correlation between KTLX and Horus, these offset angles were not consistent for other tested times within the Horus deployment window for each event. The comparison of Horus to MRMS QPE was abandoned in pursuit of more closely matched measurements. A request by our team was made in May 2025 to include a Global Navigation Satellite System (GNSS) compass to solve the 5 to 10 degree offset uncertainty in azimuth. To our knowledge the compass has not been installed yet, but an encoder was installed to track pointing accuracy of the pedestal motion during the course of a volume scan in February 2025. Tests of the encoder reveal up to a + or - 0.15 degree offset of the angles when the pedestal is rotating relative to a defined starting position. No solution is currently implemented to determine exact radar heading on Earth; however, this means that this heading must be estimated by hand for each Horus deployment, as is the case for all the considered observations in this dissertation.

As new Horus measurements continued to come online, an opportunity for another pseudo-phased array measurement came up wherein precipitation measurements were taken on March 9, 2024, at the Kessler Atmospheric and Ecological Field Station (KAEFS) in Oklahoma (34.98°N, -97.52°W) in combination with crossed rainbow RHI measurements from PX-1000 (ARRC (2025)) to capture orthogonal components of reflectivity variations and temporal reflectivity variations directly above the radar. This measurement allowed for the demonstration of PAR-based returns for improving

QPE in stratiform rainfall. It also offered the opportunity to match Horus observations with an overpass of the GPM spaceborne radar.

On September 27, 2023, a kickoff meeting was held to propose a targeted field campaign called the Precipitation Process Wind Experiment (PROWEX), including the other Horus science project stakeholders, including researchers leading the investigation of passive receivers to work with Horus measurements to capture high spatiotemporal measurements of 3D winds (Emmerson et al. (2025)), as well as collaborators from NOAA NSSL involved in the integration of a new mobile precipitation test bed called the TOTAL trailer housing a suite of precipitation measurement equipment, including a disdrometer and an MRR (Anthony et al. (2025)). The PROWEX plan was later discussed with collaborators on the NASA Investigation of Convective Updrafts (INCUS) science team to see if the science objectives could help to aid our joint mission targeting science priorities set in the 2017 Decadal Survey (National Academies of Sciences, Engineering, and Medicine (2019)): "Characterize the microphysical processes and interactions of hydrometeors by measuring the hydrometeor distribution and precipitation rate to within 5%." Our approach covers a part of this target since ground-based radar observations and spaceborne W-, Ka-, and Ku-band observations can be used approximately identify the temporal and spatial evolution of precipitation processes and drop size distribution characteristics through the life cycle of convection. Our additional use of probabilistic estimators isolates the uncertainty metric for estimated precipitation rates.

The PROWEX science objective targets fluxes and process rates in the atmosphere that are related to the convective mass flux targeted by INCUS. PROWEX aims at observing vertical velocities and derivatives of polarimetric variables. Given the available instruments listed in Figure 2.1, and the scanning limitation of Horus in September 2023 (no azimuthal rotation or scanning implemented), a few test scenarios were con-

Table 2.1: Proposed instruments for the PROWEX campaign

Instrument Type	Instrument	Use Case
Ground-based mobile PAR	OU Horus (S-band)	Derive mass-derivatives
Ground-based passive receivers	OU X- or S-band passive receivers	Estimate 3D winds
Space-based radar	NASA GPM DPR (Ku- and Ka-band)	Capture a collocated overpass
Ground-based mobile radar	OU RaXPol (X-band)	Derive dual-Doppler motions
Ground-based mobile radar	OU PX-1000 (X-band)	Derive dual-Doppler motions
Vertically Pointing Radar	Micro-Rain Radar MRR-Pro (24 GHz FMCW)	Measure vertical motions
2DVD Disdrometer	1-minute rain rate	Capture Surface PSD and Rain Rate
Parsivel Disdrometer	1-minute rain rate	Capture Surface PSD and Rain Rate
Temperature, humidity, wind, and pressure sensors	1-minute interval	Study relationships between environmental conditions, processes, and fluxes

sidered to achieve the science goals shown in Figure 2.6: 1) A crossed scan with Horus operating with an S-band RHI crossed with RaXPol (ARRC (2020)) operating orthogonally with an RHI, 2) RaXPol crossing paths in an RHI with both Horus and PX-1000, and 3) Horus RHIs crossed with a vertically pointing RaXPol.

Scenario 1 and 2 scans would allow for the calculation of vertical motion of hydrometeors via a dual-Doppler approach (Gao et al. (1999), Potvin et al. (2012), Ray et al. (1978)). A full derivation for the dual-Doppler method is given by Huddleston (2012). The advantage of the first two scenarios is that they would also provide horizontal u (x-directed) and v (y-directed) estimates of velocity through crossed Doppler radar measurements, with a disadvantage being that the vertical velocities derived would need to be estimated through a dual-Doppler technique, opening the risk for uncertainty in

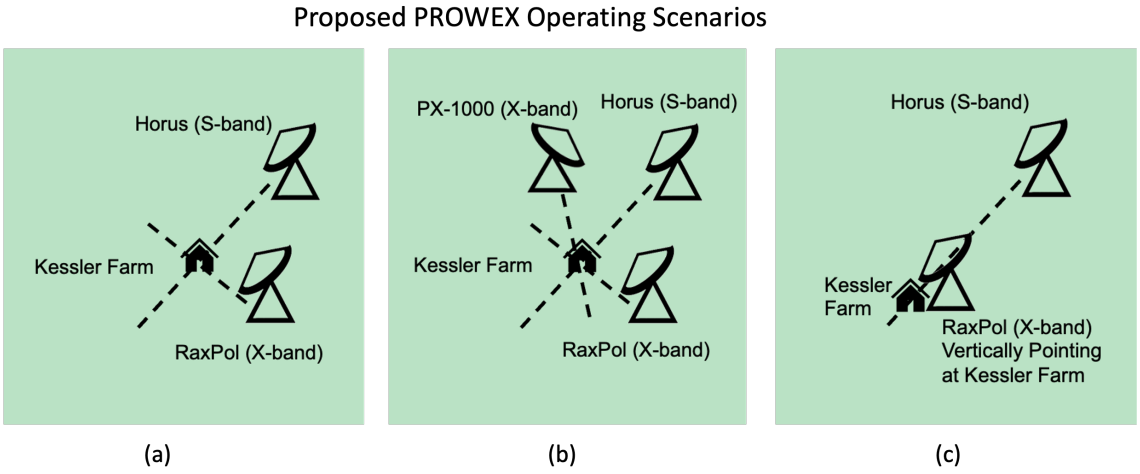


Figure 2.6: Proposed operating scenarios for the PROWEX campaign are shown including (a) a crossed scan with Horus operating with an S-band RHI crossed with RaXPol operating orthogonally with an RHI, (b) RaXPol crossing paths in an RHI with both Horus and PX-1000, and (c) Horus RHIs crossed with a vertically pointing RaXPol at the location of the reference precipitation observation at KAEFS.

computation. Additionally, in scenario 1, the difference in frequency would need to be accounted for via a frequency transform on the radar data, which would add some uncertainty. In scenario 2, the dual-Doppler calculation could be performed at X-band to estimate vertical velocities crossed with a Horus RHI. In scenario 3, dual-Doppler would not need to be used, as a vertically pointing Doppler radar is able to capture the velocity of falling hydrometeors directly. The deployment of a passive receiver would solve the problem for this scenario of collecting estimates of the u and v (horizontally directed), and w (vertically directed) hydrometeor motions. In the proposed scenario, with Kessler farm (KAEFS) approximately 23 km from the Horus deployment site, the vertical resolution of Horus would be 1.058 km.

Scenario 3 was chosen due to the direct estimation method for vertical velocity. The experiment was performed on July 7, 2024. To enhance the measurement further, rather than operating RaXPol vertically, it was operated in a crossed-rainbow RHI scheme so that it could capture orthogonal motions relative to itself and vertical mo-

tions at periodic time intervals when the antenna was pointing vertically. RaXPol was positioned approximately 300 m from a mesonet station located at the top of a hill and approximately 300 m from in situ measurements, including a vertically pointing MRR and disdrometer. A 3D passive receiver was deployed to operate with RaXPol, but the data collected was corrupted due to a hardware malfunction during deployment. Thus, a full continuity experiment could not be directly computed using data from this deployment.

Array calibration was performed for the 2024 Horus measurements, showing good performance, but later it was identified that there was a phase offset between the H and V polarizations of the array. On May 7, 2025, an announcement was sent to the Horus science stakeholders in a two-step process: first to the ARRC faculty members listed in the PAR proposal, who then had the responsibility of sending the information on to the graduate students performing the data processing and analysis using differential radar variables impacted by the calibration offset. The new calibration efforts were revealed to now show alignment between the H/V and Tx/Rx beams to within $\pm 0.1^{\circ}$, which would help to improve measurements taken later in 2025. The identified calibration offset raised some polarimetric variable quality concerns associated with data taken prior to May 7th, 2025 and became a major motivator in this work to restrict analyses to single-pol reflectivity.

Azimuthal rotation became available in June 2025, which allowed for volume scans of the atmosphere with mechanically rotated vertical imaging scans (Schvartzman et al. (2021)) which are designed to transmit on a spoiled beam of transmit energy in the vertical dimension and receive on multiple simultaneous beams to complete an RHI scan covering 13 elevation angles.

While calibration efforts and practical challenges gathering 3D wind retrievals for the July 7, 2024 PROWEX measurement did not promote the full analysis for the

PROWEX science priorities, this event happened to coincide with an overpass of the GPM Satellite radar (NASA Global Precipitation Measurement Mission (2020)), which helped to demonstrate the benefits of temporal bridging for space-based analyses with fast PAR temporal sampling within a convective event. A paper titled "Temporal Bridging of Satellite Gaps with Phased Array Radar: A Convective Weather Demonstration" was drafted and submitted to the Bulletin of the American Meteorological Society as discussed in Chapter 3.

Our team continued to pursue PROWEX objectives at all stages of new Horus integrative updates. On June 3, 2025, in pursuit of PROWEX science objectives, Horus measurements with newly enabled 3D volume scans were taken in coordination with a NASA-provided MRR and the NOAA NSSL Total trailer (NOAA National Severe Storms Laboratory (2025c)) by placing these instruments near the Horus site, as it was communicated to our team that Horus was expected to achieve polarimetric variable performance to a few hundred meters from the radar, enabling a repeat of the PX-1000-style measurement taken over 360° at closer ranges, which may have helped to capture more localized and heavier rainfall returns at the microscale than PX-1000 was able to achieve on March 9, 2024. The PX-1000 data taken on March 9th, 2024 was used to show a large improvement in rain rate estimator performance through the use of horizontal and vertical derivatives of radar variables, as detailed in 4.5.0.0.2. Likely due to a total blind range of 1.75 km, the improvements were most evident for stratiform precipitation. An intention with the test setup on June 3, 2025 was for the same experiment to be repeated for Horus with a much smaller blind range, capable of capturing the microscale, to show how the use of PAR pseudo-3D data could help to improve both stratiform and convective precipitation. As shown in Figure 2.5, the true blind range for the measurement ended up close to 691 m from the radar. As was noted in Figure 2.1, the microscale is typically characterized by spatial scales less than 1 km

making a 2*691 m = 1382 m analysis diameter likely too large to capture microscale dynamics. The same test setup was thus analyzed in a different way to reveal insights at a fine spatiotemporal scale made possible with both 3D volume scans and 3D wind estimates, which are discussed in Chapter 4.

Our team pursued PROWEX objectives at all stages Horus integration. Recall that PROWEX began with a student-facilitator led planning meeting where relevant science stakeholders (including the graduate students working on Horus science investigations) were called to evaluate test scenario options and provide inputs about whether they would work for their desired science outcomes. Tasks, roles, and metrics for success for the experiment were discussed as well as a project timeline that worked around Horus integration tasks. Organizational and project administrators were present and able to provide feedback, as were outside collaborator representatives from NSSL. Meeting science stakeholders were queried in an open sign-up format for their interest in taking part in radar operation tasks, which may aid their learning and development as well as ensure that their science priorities are appropriately executed. At the time of the PROWEX meeting, however, some stakeholder desired scanning features were not available with Horus, such as sector scans of hail, which were eventually available in 2025 when azimuthal rotation and RHI imaging were implemented. The next step in the September 2023 PROWEX planning process would have been for the facilitator to assign roles for field campaign deployment and to help oversee the project execution.

The execution of PROWEX according to the planned sequence with the Horus radar initially required administrative support and close collaboration with the PROWEX experiment facilitator. Following the inclusive planning meeting, a new directive redefined the timing and execution protocol for all Horus measurements and introduced a newly designated lead. Despite this change that impacted the PROWEX planning, the PROWEX team adapted to the revised Horus measurement protocol and priori-

ties, maintaining communication with external collaborators and stakeholders to ensure the successful completion of the experiment's science objectives. A proposed outline for the administration and coordination of future field campaigns built to minimize inefficiencies is provided in Appendix 10.

2.4 Polarimetric Radar Variables

Having detailed how the Horus PAR was incrementally advanced during the field campaign deployments, how the PROWEX campaign was developed, and a vision for improved field campaigns in the future, we now focus on the practical outcomes from these efforts. Horus, PX-1000, and RaXPol are all dual-polarized Doppler radars that produce polarimetric variables with appropriate postprocessing of I/Q data. No matter the project management framework, scientific advancement in the field of radar QPE is built on a Doppler and polarimetric radar variable foundation for the science being performed. Thus we transition here to talking about background definitions that help to answer the science questions in this work. The instrument and its outputs are a fundamental physical basis for the microphysical retrievals and model comparisons analyzed within this document.

Polarimetric variables are products derived from radar-returned power and phase shifts of a transmitted signal after it is modified and reflected back to the antenna by the environment within the radar's field of view. The radar illuminates only parts of the atmosphere within the radar transmit beamwidth and detects scattered energy from this only within the receive beamwidth. For dish radar systems, transmit and receive beamwidths are typically the same and collocated, but all-digital PAR systems may employ different schemes for transmit and receive. In the measurements considered herein, we can be assured that the energy transmitted illuminates the full beamwidth

of the energy received, though gain and sensitivity may be impacted depending on the chosen transmit scheme. Radar variables are post-processed outputs. The radar variables of equivalent reflectivity (Z), backscatter differential phase (ϕ_{dp}), specific attenuation (A), differential reflectivity (Z_{dr}), specific differential phase (K_{dp}), and correlation coefficient (ρ_{hv}) are summarized at the end of this section in Figure 2.7. Polarimetric weather radar differs from its predecessor, the single-polarized radar, by integrating an orthogonal antenna polarization into the system. This dual-polarimetry allows for the expansion to all the listed variables beyond Z. Even A, a theoretically single-polarized variable is commonly estimated with the use of the dual-polarized variable ϕ_{dp} (Ryzhkov et al. (2014)). No matter the polarization, any radar can also be designed as a Doppler radar using a pulsed transmit and receive scheme such that they return radial velocity, v_r, and spectrum width, σ_v.

2.4.1 Equivalent Reflectivity Factor (Z)

The most commonly used radar variable is Z which is derived for an ideal volume of hydrometeors, assuming spherical particles, illuminated by a radar beam in Appendix 7. Equation (2.3) indicates that ideally the equivalent reflectivity factor, most often referred to simply as "reflectivity," is proportional to the sixth power of particle diameter, so this variable is greatly impacted by larger particles present in an illuminated radar bin. Equation (2.3) shows how the reflectivity is indeed related to the received power, P_r, scattered back to the antenna by hydrometeors in the environment and is most sensitive to the sixth moment of the particle diameter. Z can be derived for any polarization of the radar system, but for ground radar most commonly refers to the horizontally polarized Z_h such that, for example, the major axis of liquid drops that tend to become more oblate with size is captured. Z_v, in a low-turbulence environment, would be most impacted by the minor axis of oblate raindrops. Typical Z values range

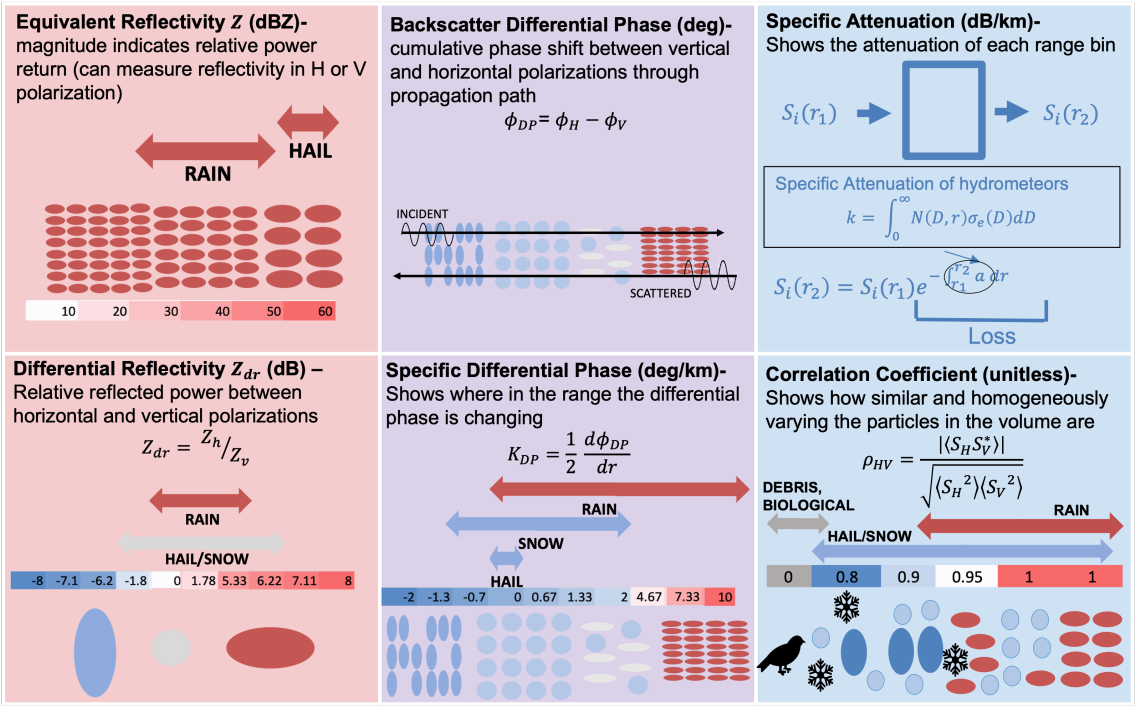


Figure 2.7: The radar variables of Z, ϕ_{dp}, A, Z_{dr}, K_{dp}, and ρ_{hv} are conceptually summarized. Z is sensitive to the size of the drops, as this impacts the magnitude of the power scattered to the radar. ϕ_{dp} is impacted by the cumulative size and concentration through the whole path of travel of the radar wave. A practically provides the attenuation of the radar signal by each radar bin. Z_{dr} is impacted by the size and shape of hydrometeors, as these variables depend on power reflected back for two antenna polarizations. K_{dp} is the range derivative of ϕ_{dp} showing how ϕ_{dp} changes for each radar bin. ρ_{hv} is close to a value of 1 for volumes with particle homogeneity in returns for both polarizations. (Content from this figure has been adapted from material in Basara (2022))

from 0 to 60 dBZ when the linear scale Equation (2.3) to is transformed to log scale. Rainfall tends to be between 0 and 50 dBZ, while hail returns up to 60 dBZ are not uncommon (University Corporation for Atmospheric Research (UCAR) (2012–2017)).

2.4.2 Differential Reflectivity (Z_{dr})

Z_{dr} is the relative reflected power between horizontal and vertical polarizations. In linear scale this is

$$Z_{dr,linear} = Z_{h,linear}/Z_{v,linear} \tag{2.7}$$

but Z_{dr} is most commonly considered to range between -8 and 8 dB in the log scale, as

$$Z_{dr} = Z_h - Z_v. \tag{2.8}$$

Negative values of Z_{dr} are uncommon in snowfall, as most ice crystals and aggregates preferentially orient with their major axis horizontally, producing slightly positive Z_{dr}. Negative Z_{dr} values may occur in limited cases, such as with conical graupel or when particles become preferentially vertically oriented. In contrast, Z_{dr} tends to be positive in heavy rainfall when raindrops become increasingly oblate and horizontally oriented. For snow, hail, and light rainfall, when drops tend to be more spherical, Z_{dr}, can exhibit low magnitudes close to 0 dB. Thus Z_{dr} expresses information about the size, shape, and orientation of hydrometeors, with larger values indicating larger, more oblate drops or melting ice and values near zero indicating more spherical particles. It is a polarimetric radar variable commonly used in hydrometeor classification algorithms (Ryzhkov et al. (2007)) in addition to ϕ_{dp} and K_{dp}.

2.4.3 Correlation Coefficient (ρ_{hv})

ρ_{hv} is the co-polar correlation coefficient between horizontally and vertically polarized radar returns from the same resolution volume (Figure 2.7). It measures how similarly the horizontally and vertically polarized signals vary and is therefore a useful indicator of hydrometeor uniformity within the radar sampling volume. High values (near 1) indicate homogeneous hydrometeors with consistent sizes and shapes, whereas inhomogeneous volumes, such as those containing mixed-phase particles, strong nonuniform beam filling (NUBF), or other variability in particle properties, tend to reduce ρ_{hv} below about 0.9. Very low values (e.g., below ~ 0.5) often indicate non-meteorological scatterers such as debris, birds, or insects. Because low ρ_{hv} values frequently occur in regions where radar echoes are unreliable for quantitative precipitation estimation (QPE), including the melting layer (bright band), mixed-phase precipitation, or rain contaminated by hail, ρ_{hv} is widely used as a quality-control variable in QPE algorithms. In practice, thresholds (e.g., $\rho_{hv} > 0.97$) are applied to retain only homogeneous resolution volumes and to filter out data affected by the melting layer or other sources of inhomogeneity (Ryzhkov et al. (2022)).

2.4.4 Backscatter Differential Phase (ϕ_{dp}) and Specific Differential Phase (K_{dp})

ϕ_{dp}, which has units of degrees, is the cumulative phase shift between vertical and horizontal polarizations through the entire propagation path of the vertically and horizontally polarized radar pulses. "Cumulative" here means that the incident electromagnetic wave travels through and is scattered back by all the hydrometeors in its path.

K_{dp} shows where in range the differential phase is changing because it is proportional

to the range derivative of ϕ_{dp} as

$$K_{dp} = \frac{1}{2}\frac{d\phi_{dp}}{dr}. \tag{2.9}$$

This provides even more information about hydrometeor shape to further expand on the shape information available through differential reflectivity Z_{dr}. Since it K_{dp} is a range derivative that is nearly linearly proportional to A, it is also sometimes used to help estimate radar attenuation corrections because it captures how ϕ_{dp} accumulates with range, so it reflects the continuous buildup of propagation effects (e.g., attenuation) along the radar beam (Bringi et al. (1990)). K_{dp} is valued for its proportionality to liquid water content, making it especially useful for QPE (Zrnić and Ryzhkov (1996)). A challenge with the estimation of K_{dp} is the wide breadth of methods used for its computation, typically varying in their handling of often noisy ϕ_{dp} estimates. As will be seen, K_{dp} has been calculated as a part of this work, but likely due to integrative calibration steps, ϕ_{dp} had unpredictable and noisy storm behavior that made it unreliable for QPE estimation. Most early analyses before the advent of dual-polarization have relied on Z as a primary QPE estimator due to its independence from these effects.

2.4.5 Specific Attenuation (A) and Differential Specific Attenuation (A_{dp})

Specific attenuation, A, for a given polarization is the attenuation of each range bin and is normally expressed in units of dB/km. The difference between horizontal attenuation and vertical attenuation, expressed by the differential specific attenuation A_{dp}, can provide information that is similar to specific phase in that its value increases with drop oblateness.

Path integrated attenuation (PIA) is estimated from the slope of phi_{dp} accumulation

over a storm system with a multiplicative tuning factor applied, derived from the slope of the magnitude trend between Z and Z_{dr}:

$$PIA = \alpha \Delta \phi_{dp} \tag{2.10}$$

where the change in ϕ_{dp} is taken over range and α is typically determined dynamically from a slope between Z and Z_{dr} magnitudes. A and A_{dp} are temperature dependent, and the dynamic tuning of α poses a complexity to their real-time use for QPE. Still, A is used in many QPE products due to its excellence in estimating LWC, of which rain rate is a flux.

2.4.6 Non-polarimetric variables: radial velocity (v_r) and spectrum width (σ_v)

v_r is the Doppler velocity of meteorological scatterers observed by a radar. It is detectable because radars are pulsed systems, and within the comparison between two consecutive pulses, a phase shift can be detected if the illuminated target is in motion away from or towards the radar. Because many particles within a radar resolution volume have different associated v_r, the spectrum width, σ_v can describe the spread of v_r values within the resolution volume.

2.5 Spectral Bin Microphysics Model

The 1D SBM model used in parts of this study is designed to simulate vertical interactions of hydrometeors within a single atmospheric column (Ryzhkov et al. (2013b)). Originally developed to analyze the melting of hail with bi-exponential distributions, the model is versatile and capable of representing the evolution of liquid water dis-

tributions modeled with an initial gamma distribution aloft. It tracks the vertical motion and transformation of hydrometeors, such as graupel, hail, and rain, using a bin-resolved representation of PSDs rather than manipulating terms of predefined distributions like bulk microphysics models. For this reason it is computationally intensive relative to bulk models but allows for the specific parameterization of particle-level processes that depend on the size of the particle as well as the environmental changes that occur in reaction to a particle's morphology. The model begins with an initial distribution of graupel and hail at a defined altitude and temperature, e.g. 4 km and the freezing level (0°C), and simulates their descent toward the surface, calculating terminal velocities based on particle mass, ambient air density, air viscosity, and drag coefficients (Ryzhkov et al. (2013b)). This approach captures size-sorting effects in both updraft and downdraft scenarios. A key feature of the model is its treatment of hail melting, which employs heat transfer equations that account for particle volume, density, and environmental temperature (Ryzhkov et al. (2013b)). As hail descends through temperatures below the 0° C isotherm, it becomes water-coated. Once the amount of meltwater on a hailstone exceeds a critical threshold, water shedding begins and continues throughout the melting process (Ryzhkov et al. (2013b)). The melting rate, and thus the rate of diameter reduction, depends on the size and density of the hail. For example, smaller hail melts more quickly (Ryzhkov et al. (2013b)). The model accounts for three primary mechanisms of raindrop formation, which include direct melting of hail, shedding of water droplets from melting hail, and breakup of drops larger than about 8 mm in diameter during descent (Ryzhkov et al. (2013b)). These processes are used to update the liquid water mass within each particle size bin, making the model highly applicable for studying warm rain microphysical processes (excluding collision coalescence) and associated particle size distributions. The processes of melting, sublimation, and evaporation also occur in the model, changing the

size of the drops in the distribution.

As the particles are modified in the model, the environment is impacted. For example, evaporation, melting, and sublimation all cause cooling of the atmosphere as energy is absorbed from the hydrometeor's surroundings to engage a phase transformation of the particles from solid to liquid or gas. Besides reducing the environmental temperature, all the processes typically increase the relative humidity in the atmosphere, noting that melting usually occurs simultaneously with evaporation in temperatures above freezing. A faster reduction in temperature with increasing altitude is indicative of an unstable environment and a higher lapse rate. Air parcels near the surface may have a tendency to buoyantly rise in this scenario, but in the case of descending precipitation with precipitation loading and precipitation process-induced cooling, the descending air will tend to be denser and colder than its surroundings, causing it to sink more rapidly in a downdraft, which, by increasing the vertical air motion, increases the vertical velocity of hydrometeors and their precipitation rate. The controls on downdraft formation have to do with the initial environmental temperature, pressure, and vertical wind profiles that control stability as well as the altitude and composition/makeup of the distribution of hydrometeors that descend to the surface. As this is a 1D model, it does not include the effects of advection.

While originally focused on mixed-phase processes such as melting hail (Ryzhkov et al. (2013a)), the model is particularly well-suited for examining the microphysics of rain formation and size sorting of liquid droplets in stratiform and convective precipitation. For example, it has been used in case studies involving downdrafts initiated at the melting level (Ryzhkov et al. (2013a)). To connect the microphysics to remote sensing observations, the model includes a radar operator that converts the spectral bin hydrometeor distributions into vertical profiles of radar polarimetric variables. This operator uses scattering theory based on hydrometeor size, shape, composition (ice/water

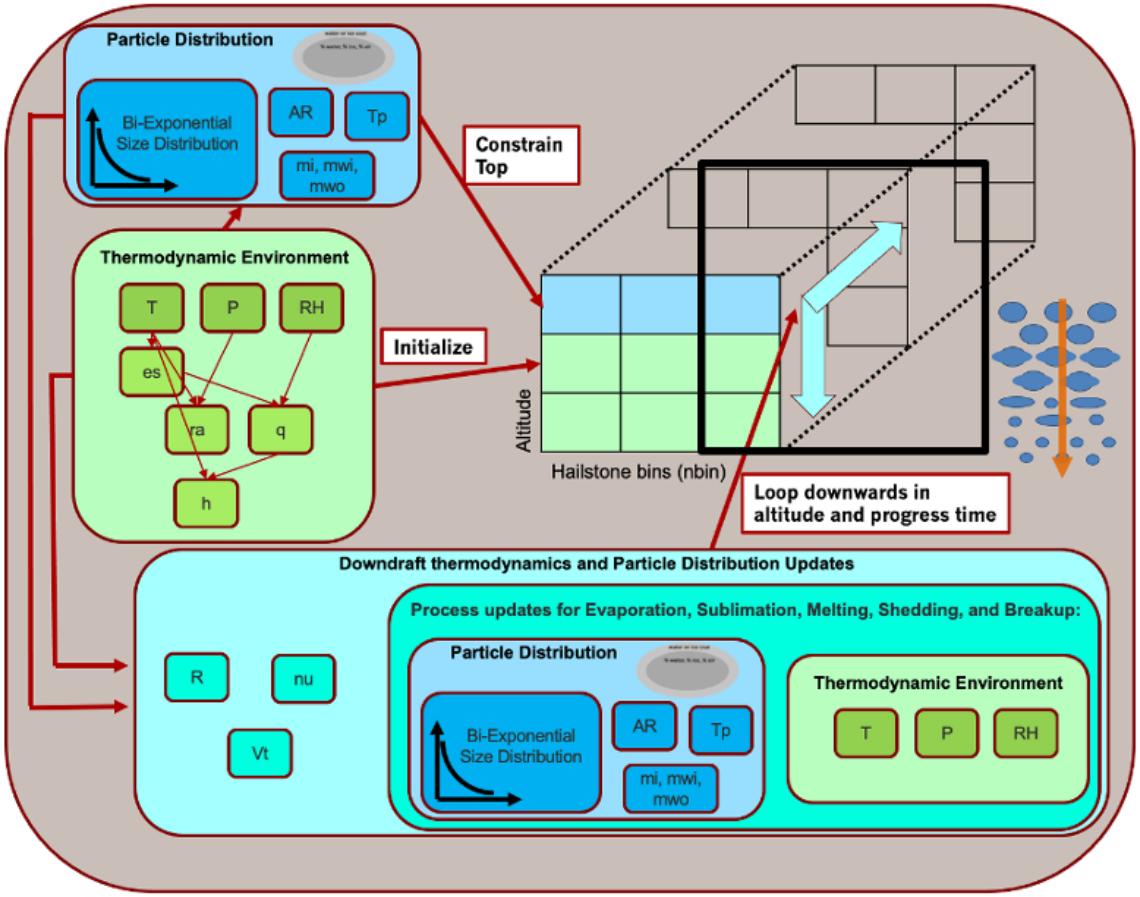


Figure 2.8: Microphysical processes evolve as a function of time and height. For the 1D SBM model, a distribution of hydrometeors is set at some altitude in an initial thermodynamic environment defined by temperature (T), pressure (P), and relative humidity (RH). Then the model steps forward in time and progresses downwards in altitude as the particles fall. At each altitude and time step the distribution and thermodynamic environment are updated as the particles undergo processes like evaporation, sublimation, melting, shedding, and drop breakup. These processes evolve as a function of time and height. Symbol Key: Axial Ratio (AR), Particle Temperature (T_p), Mass of ice (mi), Mass of water inside the particle (mwi), Mass of water on the outside of the particle (mwo), density of moist air (ra), heat (h), saturation vapor pressure (es), mixing ratio (q), Reynolds number (R), Kinematic viscosity of air (nu), Particle terminal velocity (V_t)

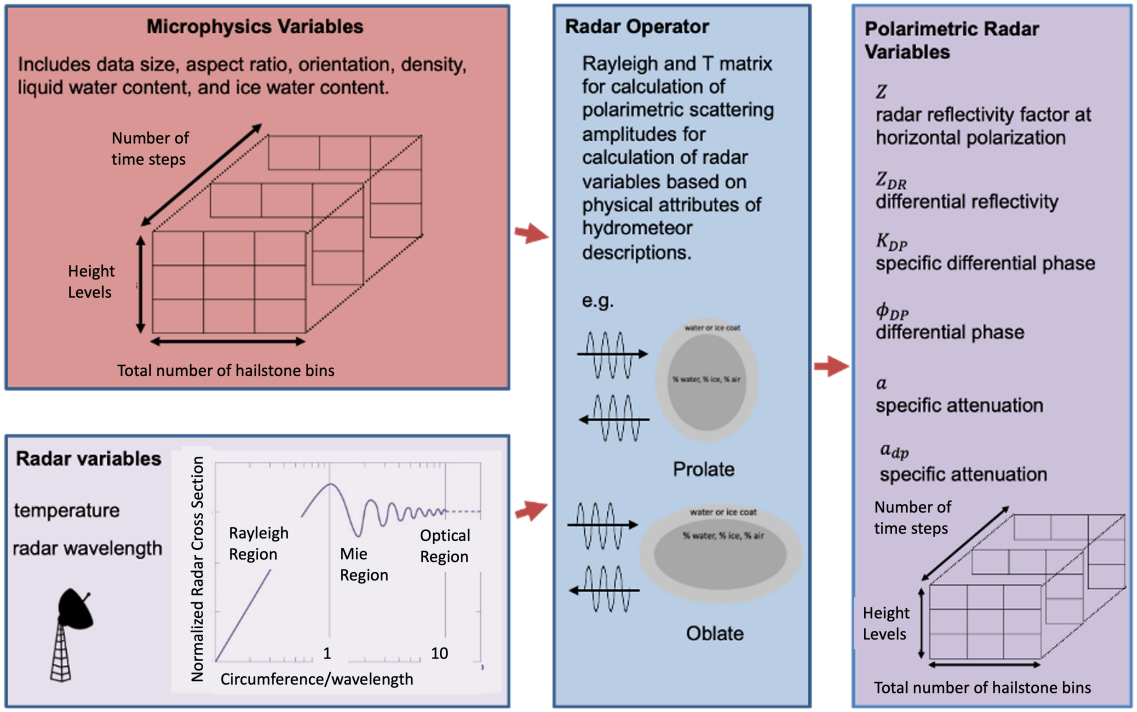


Figure 2.9: The 1D SBM model generates microphysics particle properties like particle aspect ratio, orientation, density, liquid water content, and ice water content. These, as well as radar-influencing variables like temperature and radar wavelength, are fed into the radar operator, which performs T-matrix calculations to produce simulated polarimetric radar variables.

composition), and dielectric properties, which are influenced by environmental temperature and radar wavelength (Ryzhkov et al. (2013b)).

Figure 2.9 shows a plot of normalized radar cross section, proportional to the power scattered back to the radar for different hydrometeor sizes relative to circumference divided by wavelength. This is shown in the "Radar Variables" panel in the figure. Radar wavelength is an important input to the radar operator. For particle sizes outside the Rayleigh regime, the Rayleigh approximation, which assumes a linear relationship between normalized radar cross section and the ratio of particle circumference to wavelength, is no longer valid. In the Mie region, backscattering must be estimated by directly solving Maxwell's equations (Matsuyama (2006)). Maintaining operations within the Rayleigh regime is one reason S-band frequencies are commonly used for

weather radars in the United States, as operation in the Mie or optical regimes leads to higher absorption and greater attenuation.

The scattered field components from an individual hydrometeor are related to the incident field via an amplitude scattering matrix or a T-matrix, which is an alternative form of the scattering matrix (Matsuyama (2006)). In other words, knowing a particle's T-matrix and the incident electric field allows calculation of the backscattered electric field (Spurr et al. (2012)). Conveniently, the T-matrix can be computed from the particle's shape, size, orientation, incident wavelength, and refractive index (Leinonen (2014)). For an ensemble of hydrometeors, the ensemble T-matrix is obtained by superposing the individual T-matrices, accounting for averaged orientations.

For small particles relative to the radar wavelength, Rayleigh scattering approximations are sufficient (Ryzhkov et al. (2011)). For larger particles or shorter wavelengths, the T-matrix method is required to capture resonance effects and complex scattering behavior (Ryzhkov (2001), Ryzhkov et al. (2013b)). Within the radar operator, frozen hydrometeors can be modeled as two-layer spheroids (e.g., water-coated hail) or as single spheroids when fully melted; they may be prolate or oblate depending on environmental conditions and hydrometeor motion (Ryzhkov et al. (2013b)). Forward and backward scattering amplitudes derived from these models are then used to compute radar polarimetric variables (Ryzhkov et al. (2013b)).

In summary, the 1D spectral bin microphysics model is a powerful tool for studying the vertical evolution of hydrometeor populations, particularly for warm-rain processes and melting layer dynamics. Although originally developed to study hail melting, its flexibility makes it valuable for analyzing pure liquid water distributions across varied environmental conditions.

2.6 Microphysical Retrievals from Radar Data

Remote sensing instruments do not directly measure physical properties; rather, they provide signatures of microphysical characteristics, including particle size, distribution, phase, and composition. These retrievals are critical for understanding cloud processes and improving model parameterizations, but they must be inferred from available radar returns, which, in the case of polarimetric radar, are typically expressed as polarimetric radar variables. The NEXRAD radars in the United States, as well as the prototype PAR called Horus, are equipped with Doppler capabilities, enabling the measurement of v_r and σ_v of the observed hydrometeors.

2.6.1 Traditional Approaches and Metrics

Traditional approaches for rain rate estimation have involved reflectivity since this is readily produced by single-polarimetric radar systems. As we have seen in the definition of Z in Appendix 7, there is a theoretical link between the PSD and reflectivity. Because reflectivity and rain rate are both moments of the PSD, we expect these two variables to be linked. The most fundamental historical relation involving reflectivity to estimate rain rate at the surface is the marshall-palmer Z-R relation Marshall and Palmer (1948) which takes a power law form to define Z in units of mm^6m^{-3} as:

$$Z = aR^b. \tag{2.11}$$

where a and b are constants. Many of these relationships linking Z to R exist in the literature. Other relationships exist linking reflectivity more broadly to snow and hail rates (Ryzhkov et al. (2013b), Matrosov (1992)).

Metrics typically used to quantify the performance of all QPE estimates, including

the performance of the Z-R relationships, are the correlation coefficient (ρ), bias, the mean absolute error (MAE), and fractional mean absolute error ($fMAE$). The linear Pearson correlation coefficient considers the trend of how changes in one variable relative to its mean relate to changes in another variable relative to its mean, e.g. the estimated precipitation rate values (O_i) and the "true" in-situ reference precipitation rate values (R_i). The bias conveys the sign (overestimation or underestimation) and magnitude of systematic discrepancies, as defined in e.g., Habib et al. (2001) as:

$$\rho = \frac{\sum_i (R_i - \bar{R})(O_i - \bar{O})}{\sqrt{\sum_i (R_i - \bar{R})^2 \sum_i (O_i - \bar{O})^2}} \tag{2.12}$$

$$\text{Bias} = \frac{1}{N} \sum_i (O_i - R_i) \tag{2.13}$$

The MAE represents the magnitude of the difference between the observation and the reference.

$$\text{MAE} = \frac{1}{N} \sum_i |O_i - R_i| \tag{2.14}$$

For all metrics, it is important to consider the time scale over which measurements are accumulated. Precipitation variability is a function of spatial and temporal scale, and it impacts evaluation metrics. For example, while Ryzhkov et al. (2022) reports that for 24 hr rainfall accumulations, the correlation coefficient ρ typically exceeds 0.9, with biases below 10% when comparing rain rate estimators based on WSR-88D reflectivity to surface gauge rain rate accumulations over the same time period, other studies have shown lower correlations for shorter accumulation periods (Peleg et al. (2013), Pöschmann et al. (2020), Wang and Wolff (2010)). As another example, Wang and Wolff (2010) provides a clear example of how radar rain rate correlations between NASA Tropical Rainfall Measuring Mission (TRMM) satellite radar rainfall estimates of radar resolution volumes (1–4 km spatial scale associated with the radar footprint)

and collocated surface rain-gauge measurements (point measurements) increase with accumulation time: $\rho = 0.60$ for 5 min accumulations, $\rho = 0.80$ for 30 min accumulations, and $\rho = 0.93$ for 24 hr accumulations.

Reflectivity sampled aloft by ground-based radars may not always accurately represent surface precipitation. Reflectivity fluctuates with height due to various microphysical processes, including melting, aggregation, collision, coalescence, evaporation, and drop breakup. Advection can also modify the precipitation measured aloft before it reaches the surface. Additionally, the radar beam's elevation increases with distance, while its width degrades the vertical sampling of the precipitation's vertical structure. This representativeness issue can be exacerbated in complex terrain, where ground radars must sample precipitating systems at higher elevation angles. Vertical variations in reflectivity are a major source of error in estimating surface precipitation using weather radar. They can potentially double the estimation error when not accounted for (e.g., Kitchen et al. (1994)). The vertical variations of the radar reflectivity factor in the atmosphere are typically represented by the vertical profile of reflectivity (VPR)Correcting the error due to the VPR requires its determination, which enables the projection of reflectivity measured aloft onto the ground before it is converted into a precipitation rate. Despite the progress made in recent decades, determining the VPR remains an open research topic (e.g., Kirstetter et al. (2013)). One of the most significant vertical variations of Z is around the melting layer in stratiform situations. After quality control, radar returns above and below the freezing level can be used to detect Z enhancements caused by melting hydrometeors. This enhancement, called the bright band, typically occurs near the 0°C isotherm. Reflectivity increases in the melting layer as ice becomes water-coated or forms wet aggregates, and reflectivity can increase by 5–10 dBZ. Once fully melted, drops have lower sizes and may break apart, causing a significant decrease in reflectivity below the melting layer. Using R–Z

relationships to estimate rain rate (R) in the melting layer can therefore lead to substantial overestimations. The bright band impact on QPE can be mitigated if correctly estimated.

In general, the correlation between surface precipitation estimated with polarimetric variables and in situ surface measurements may decrease with distance from the radar due to beam broadening, signal attenuation, and increasing altitude separation between the surface and the radar resolution volume. The same effect can occur for R estimates, although this also depends on the empirical conditions used to fit the relationships; for example, Rosenfeld et al. (1993) and Llort (2010) found strong range dependence in $Z - R$ relationships.

A radar-based precipitation estimator is generally assumed to represent the full vertical structure of a precipitating column and all volume-averaged sizes. For NEXRAD, the resolution volume depth can reach up to $D = 4$ km at its maximum range of $r = 230$ km, for example, estimating the beam diameter as $D = 2r \tan\left(\frac{\theta}{2}\right)$ Doviak and Zrnić (1993). The altitude of the lowest beam, typically 0.5° in elevation, ranges from a few hundred meters near the radar to above 5 km far from the radar, occasionally intersecting the 0° isotherm.

The cross-polar correlation coefficient, ρ_{HV}, is used for quality control. In cases where ρ_{HV} is too low for a given bin, neighboring values may be interpolated to represent the precipitation in that bin, as implemented in MRMS. Z-R relationships are empirical, and their accuracy in a particular storm depends on how representative the relationship is of the observed precipitation. Localized tuning of Z-R relationships can improve their performance (Ryzhkov et al. (2022)), with benefits in developing distinct relationships for different types of rainfall, such as tropical versus continental. All rainfall relationships must also be calibrated for the specific radar operating frequency.

2.6.2 Polarimetric Approaches

Z indirectly represents the precipitation rate which is a vertical flux of liquid water content. Combinations of Z, Z_{dr}, K_{dp}, and A can be used to improve the accuracy of rain rate estimation They can also be used for hydrometeor classification and drop size distribution estimation. By observation of efficacy in different situations, logic trees have been built to determine when a radar variable is most appropriate to use. For example, the combination of Z_{dr} and Z for rain rate estimation has shown improved performance over Z alone (Seliga et al. (1981)). By analyzing errors from three WSR-88D radars, Simpson and Fox (2018) showed that $R(Z, Z_{dr})$ improved MAE with near 0 bias over $R(Z)$, but that $R(K_{dp})$ was the most robust over range (while other estimates had degraded performance with range) with a low MAE and high correlation.

Both K_{dp} and A, in theory, promise lower sensitivity to PSD variability, attenuation, calibration, and partial beam blockage (Wang et al. (2019)). $R(A)$, with a dynamically tuned multiplicative factor, α, has excellent metric scores relative to in-situ references for low- to mid-magnitude rain rate, but $R(K_{dp})$ must be chosen in cases where hail is detected by classification (Cocks et al. (2019)). This is because hail is a strong scatterer of energy composed of ice, which has a lower dielectric constant (Wang et al. (2019)). Despite the advances A brought to QPE estimation, uncertainty is associated with dynamic tuning due in part to temperature sensitivity. Despite these challenges, MRMS takes advantage of A and K_{dp} in its 2-minute real-time merged radar product for R. MRMS, after hydrometeor classification, uses $R(A)$ for rain, $R(K_{dp})$ for hail or rain-hail mixed precipitation, and a VPR-corrected $R(Z)$ in areas with frozen and mixed-phase precipitation (Zhang et al. (2016a)).

Polarimetric radar is particularly effective from the ground due to its favorable angle of incidence with precipitation, which allows it to capture returns that characterize

the horizontal structure of hydrometeors. In contrast, spaceborne radars generally do not utilize polarimetry because their top-down viewing geometry limits their ability to resolve such horizontal features. While polarimetric techniques have significantly advanced QPE by providing additional microphysical information, ground-based radar remains constrained to terrestrial networks. It is not a viable solution for global QPE, particularly over oceans or regions with sparse radar coverage, and its performance is further limited in areas with complex terrain due to beam blockage. To achieve spatially comprehensive QPE, research is underway on observations from low-Earth orbiting (LEO) satellites, led by agencies such as NASA. Satellites offer the potential to fill observational gaps where ground-based radar networks and in situ measurements are unavailable.

2.6.3 Detecting Processes in the Atmosphere

Another advantage of polarimetric radars, according to Kumjian et al. (2022) and Brauer (2022), is that dominant microphysical processes can be identified for vertical variations of polarimetric variables estimated with the slope of the Z and Z_{dr} profiles below the melting layer. These differences in microphysics occur in part due to environmental conditions driven by large-scale processes that influence atmospheric water content and temperature lapse rates. In the process of collision-coalescence as raindrops collide to form larger drops, the power reflected back to the radar is increased. At the same time, Z_{dr} increases also occur because larger drops become more oblate as they fall. Under a collision-coalescence/breakup balance, the increase in Z is expected to be smaller than collision coalescence alone and with a slightly negative Z_{dr} slope because broken-up smaller drops are more spherical than larger drops. Size sorting occurs as heavier drops fall faster than smaller drops. When larger drops are closer to the surface than smaller drops, an initial increase in Z_{dr} is expected towards the sur-

face, followed by a likely decrease. Evaporation reduces the size of drops, also reducing Z and Z_{dr}. Continued breakup reduces the size of drops and thus naturally causes a negative slope in both Z and Z_{dr}.

Dolan et al. (2018) further extended these theories by applying principal component analysis to disdrometer measurements using drop size distribution parameters, R, LWC, and total drop number to classify precipitation into six distinct groups that together explain 88% of rain rate variability across three northern hemisphere latitude bands. She linked these groups to radar profiles of Z and Z_{dr}. Two of the groups represented convective and stratiform rain specifically: Group 1 represented convective precipitation with broad drop size distributions, large drops, high liquid water content, and profiles indicative of strong updrafts and oblate drops. Group 2 characterized stratiform rain with weak vertical motion, small drops, low liquid water content, and profiles showing low Z and weak Z_{dr}. These profile-based distinctions complement the microphysical measurements in defining the precipitation processes.

All of the aforementioned processes may occur in both convective and stratiform rain to different degrees depending on the associated updrafts, particle distributions, and environmental conditions. However, it is important to note that Dolan et al. (2018) showed that profiles of convection exhibit higher Z and Z_{dr} values than the stratiform group and that both groups show a clear separation in PSD shape. This aligns with studies from space that have shown that convective and stratiform types have clear separation in mass-weighted mean diameter and resulting rain rates (Chase et al. (2020)).

Dolan et al. (2018) also showed vertical profiles of Z which revealed a stronger slope of increase of Z towards the surface in convection, which may be contributed to by efficient collision-coalescence processes occurring for convection. As will be seen in Chapter 4, analyzed by a 1D SBM model, polarimetric variables and horizontal

derivatives of polarimetric variables distribute themselves differently depending on the dominant processes that are occurring, making them useful for process identification.

Vertical changes to hydrometeors allude to one of the main topics of this work, which is the spatial contributions that can be afforded to QPE and process rate estimation. Beyond vertical changes, we consider changes in 3D in Chapter 4 to capture effects of advection in addition to vertical changes, a unique capability afforded by rapidly scanning ground radars and PAR, which can provide extremely high horizontal resolutions at fast update times.

Ground radars, as has been evidenced by the mentioned literature, also have the ability to produce vertical profiles. Another instrument that, especially at mid-to-far ranges from the ground radar, produces even higher vertical resolutions is satellite radar. Ground-based weather radars have much to offer for the science and applications of space-based precipitation and convection. The vantage point of satellite radars provides a finer depiction of the vertical structure than ground radars, which is essential for documenting the atmospheric components of the Earth's water cycle and associated extremes, though observation gaps exist with low-level mid-/high-latitude precipitation and convective motions.

Historically, R estimation for both stratiform and convective precipitation using single-frequency spaceborne radars relied on power-law relationships dependent on Z that were tuned using ground-reference measurements. However, the availability of dual-frequency returns from DPR (Ka- and Ku-bands) allows for more accurate R estimates by estimating mass-weighted mean diameter, D_m, and normalized intercept parameter, N_w, which is related to the concentration of precipitation particles based on assumed gamma PSDs, as demonstrated in recent studies (Nakamura (2021)). As we have mentioned, researchers have confirmed clear separations between stratiform and convective precipitation in the D_m and N_w parameter space, indicating their iso-

lation as largely unique precipitation regimes (Dolan et al. (2018)). The same regime classification can be done with polarimetric radar from the surface.

Ground-based radars provide a complementary insight through their finer horizontal, time-continuous sampling that probes into the microphysics and dynamics of storms. Ground radar also has much to offer space radar for benchmarking and validation, especially considering new satellite missions such as INCUS, which relies on time-separated Z observations to estimate vertical mass flux. The temporal sampling advantage of PAR can be used to validate the suitability of this sampling scheme for dynamic convective systems.

2.7 Spaceborne Radar QPE and Convective Fluxes

2.7.1 Bridging Satellite Spatial Limitations with Ground-Based Radar

With the rising trend in extreme precipitation under various global warming scenarios 9Dai (2011)), there is a pressing need not only for global coverage but also for highly precise rainfall retrieval algorithms.

The joint NASA and Japan Aerospace Exploration Agency (JAXA) Global Precipitation Measurement (GPM) mission has developed a high-resolution multi-sensor merged precipitation product updated every half hour called IMERG (NASA (2020)). This initiative leverages data from the GPM core satellite's Dual-Frequency Precipitation Radar (GPM-DPR) and GPM-Microwave Imager (GMI), with accuracy evaluated by ground validation from radar and rain gauge measurements, as well as high-spatial and temporal resolution data from geostationary satellite imagery (about 5 km horizontal resolution). This effort aims to advance the understanding of microscale cloud

and precipitation microphysics, planetary-scale weather patterns including teleconnections, climatology, and the global water cycle. While infrared imagery provides cloud top information but cannot penetrate cloud cover (Hou et al. (2008), Upadhyaya et al. (2021)), microwave radiometers like the GMI, although with lower spatial and temporal resolution than infrared sensors, sample brightness temperatures representative of in-cloud properties to infer surface precipitation (Hou et al. (2008)). The evolution of infrared and microwave radiometer technologies has been substantial, with earlier precipitation-focused missions like the NASA TRMM (launched in 1997) focusing on tropical rainfall and hurricanes using radar and radiometer measurements. GPM aims to enhance TRMM's capabilities by deploying a dual-frequency radar concept capable of computing microphysical parameters such as the mass-weighted mean diameter, D_m. A critical piece of this merged-observation ecosystem is the improvement of DPR rain estimates with ground validation information content. As will be shown in Chapter 5, ground radar can reduce errors for convective precipitation by utilizing precipitation variability information available via ground validation. Chapter 5 shows an opportunity for this in the form of enhancements observed by NEXRAD, but Chapter 3 shows how the NEXRAD WSR-88Ds do not sample the atmosphere quickly enough to appropriately capture convective storm dynamics, so PAR can play an important role for benchmarking satellite operations in convection.

2.7.2 Bridging Satellite Temporal Limitations with Ground-Based Radar

Opportunities for the enhancement of spaceborne radar observations using PAR's high-temporal sampling are also highlighted in this work. Specifically, temporal changes in ground-radar polarimetric variables and near-earth S-band observations provide sup-

plemental views of convective storms during the satellite overpass. As an important single-observation example, polarimetric radar decorrelation times are demonstrated to validate the time-dependent satellite observations proposed for the upcoming spaceborne missions such as INCUS. With complementary frequency bands, sensitivity, resolutions, polarimetric and fast-sampling capabilities, and polarimetric PAR, it offers insight into precipitation and convection that complements and enhances spaceborne radar observations. The INCUS mission is especially interesting in its pursuit of vertical mass flux estimates using 30 s time-separated radar reflectivity measurements and its observation of a relationship between vertical mass transport and the time derivative of Z from space.

Haddad et al. (2022) breaks down the method concisely. Considering that an empirical relation can be made between reflectivity and mass or the condensed-water-mixing-ratio Q above the melting layer,

$$Z = aQ^b. \tag{2.15}$$

where a and b are constants, then the continuity equation can be solved for the vertical motion w in terms of the temporal (t), horizontal (x, y), and vertical (h) derivatives of Q as

$$w = \frac{\frac{dQ}{dt} + u\frac{dQ}{dx} + v\frac{dQ}{dy}}{\alpha_p - \frac{dQ}{dh}}. \tag{2.16}$$

where α_p is related to the mass entering or leaving the system, which is assumed to be proportional to w and influenced by temperature. Advection terms, $u\frac{dQ}{dx} + v\frac{dQ}{dy}$ have to be estimated from, for example, the local correlation between consecutive images, taking into account the satellite motion. Our work hypothesizes that similar approaches can be pursued from the ground because PAR provides faster temporal update times that allow a ground-based system to mimic the INCUS sampling and to validate it.

Thus, the next two chapters highlight the spatiotemporal benefits of PAR, considering first the required sampling time for precipitation systems and then the separation of flux terms, including advective terms to improve QPE.

Chapter 3

Time Continuity: QPE and Radar Variable Improvements

Traditional QPE retrieval methods have advanced our understanding of precipitation regimes and variability, aiding model development and assimilation for forecasting, but all QPE retrievals carry errors arising from discontinuous sampling, instrument errors, differences in spatiotemporal averaging between the remotely sensed data and the reference instrument used for training, and misaligned observations relative to the target prediction point. These tradeoffs limit the reliability of QPE estimates, especially in dynamic or heterogeneous environments. Considering the specific source of error due to discontinuous sampling in highly dynamic environments, this chapter seeks to demonstrate the use of a framework to characterize the QPE uncertainty that arises for different sampling schemes. Giving this chapter broader significance to the weather radar community that relies on radar returns for a multitude of applications, we show how temporal errors also impact the reliability of the radar variables, like reflectivity Z, which are used in the estimation of QPE. We consider key improvements over traditional methods with the use of block kriging to characterize errors.

Temporal errors are important to study because they impact the applications of weather radars, such as numerical weather prediction, nowcasting, reanalysis, and merged instrument products, that stand to gain accuracy when temporal sampling

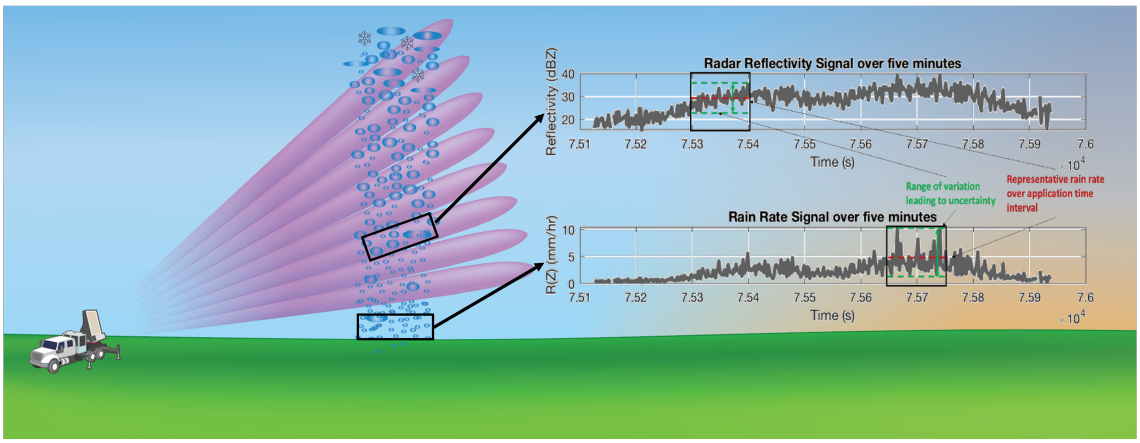


Figure 3.1: RHI observation depiction showing five minutes of radar reflectivity data collected every 0.76 s by the Horus phased array radar on July 7, 2024. Applications like QPE or validation with in-situ instruments require averaging the true underlying continuous signal over an application time domain, depicted by a box surrounding 30 s of data. Within this application interval, a representative value is shown with a red dashed line along with an uncertainty range delineated with dashed green lines. Any instantaneous observation taken to represent the interval may lack representativeness due to the underlying signal's range of variation within this time domain.

errors are minimized. Figure 3.1 shows a visual example from real phased array radar data of how the dynamic range of a reflectivity or rain rate signal can vary, leading to observed estimates unequal to the desired representative value of the variable over an application interval. Analysis of the temporal sampling errors of an observation over the application time domain (T), such as 2 min or 5 min, for key phenomena like deep convection can aid in the optimization of radar scanning strategies and networks.

Radar variables and retrievals require the estimation of both their expected values and associated errors. Since QPE estimates depend on input polarimetric variables like Z, Z_{dr}, K_{dp}, and specific attenuation (A), these polarimetric variables must come along with uncertainty metrics that characterize the QPE estimator. There is currently no standard approach for reporting radar system errors produced by meteorological signal fluctuations that are not captured by the observing instrument, in part because these errors vary depending on the spatiotemporal sampling density of the radar and the

temporal fluctuations of the atmosphere at small temporal scales. Importantly, WSR-88D specifications state that the standard deviation of Z collected over 6-64 pulses (4.71 microseconds for a long pulse or 1.57 microseconds for a short pulse) due to meteorological signal fluctuations should be within 1 dB for given a signal at 10 dB signal-to-noise ratio, without taking into account the temporal scale of the considered application ((Center, 2001)). This specification refers to a pseudo-instantaneous error, tunable through calibration, which does not account for the use of scanning radar revisit times for meteorological analyses and application use. While calibration is important, more important is the spatiotemporal representativeness of the radar variable over the domain of interest. Uncertainty is characteristic of geophysical variables derived from radar observations. The ingestion of radar derived QPE data by applications requires uncertainty estimates in the estimated R in order to assess risk (e.g., Kirstetter et al. (2015a)). For example, flash flood monitoring and forecasting requires QPE estimates within an uncertainty of 10-15 % within the temporal domain of 2 min for flash flood forecasting (Gourley et al. (2017a)). Specifically addressed in this chapter is the question of the representativeness of radar observations over a temporal domain, which is illustrated in Figure 3.1. Two examples of 5-min time-series Z measurements are shown for two radar resolution volumes, that are captured by a phased array radar (PAR) sampling the atmosphere in fast-range height indicator (RHI) mode and producing RHIs every 0.76 s. The two time series display large dynamic ranges of Z values within 5 min, i.e., 0 - 10 dBZ for the radar resolution volume near the ground and 18 - 40 dBZ aloft. Any instantaneous observation randomly sampled within this T by a slower dish radar (e.g. the WSR-88D VCP-12) to represent the interval is associated with uncertainty that can far exceed the expected 1 dB accuracy over T. Because R estimates depend on polarimetric variables (Ryzhkov et al. (2022)), errors associated with too sparse sampling of a highly dynamic precipitation event trickle down to QPE.

R is often estimated from an instantaneous measurement at some location aloft and validated by a time-integrated observation at the surface (e.g., with a rain gauge). With the emergence of faster scanning radars or PARs, more frequent observations are becoming available within temporal domains relevant for science and applications of weather radar. For the first time, by accounting for the temporal fluctuations of radar observations with fast-revisit times of the atmosphere, the temporal structure of radar variables is robustly analyzed and their uncertainty is quantified for various application Ts. Decorrelation times computed from fast-scanning radar measurements are also demonstrated with the intent that they may be used to develop weather radar sampling specifications. The purpose of this chapter is to demonstrate a quantitative approach for defining radar temporal sampling requirements and to show their downstream impact on precipitation estimation. It will be shown that PAR can provide the required dense temporal information content and that temporal uncertainties can be characterized. A geostatistical framework is used to compute decorrelation times and expected errors for radar Z associated with temporal meteorological variability for two cases of convection observed by a PAR on July 7, 2024 and on May 12, 2023 with different radar beam designs. To extend the analysis to a level closer to the application space, rain rate values and their associated errors will also be computed using empirical Z-R relationships. While the heaviest focus of this chapter is on PAR observations, the usefulness of the geostatistical framework for estimating rain rate uncertainties depending on temporal sampling density will further be vetted by comparison of Micro-rain radar (MRR) Z to collocated 2DVD disdrometer measurements at the surface.

Temporal sampling errors from weather radar observations are provided in Chapter 3 along with recommendations for sampling requirements of precipitation for atmospheric science and hydrometeorological applications. First, the temporal structure of precipitation is analyzed with high-resolution Phased-Array Radar (PAR) measure-

ments for two typical convective events. The uncertainty in equivalent radar reflectivity is investigated using geostatistics over different temporal domains from 30 s to 5 min. Then, the uncertainty in precipitation estimates is quantified and studied as a function of the temporal resolution of radar sampling and precipitation rate intensity. Finally, the impact of temporal resolution on estimation accuracy is confirmed with a micro-rain radar (MRR) and a 2-DVD disdrometer. The required time resolution for radar quantitative precipitation estimation (QPE) is estimated as a function of the uncertainty on the radar observations and derived precipitation rates. According to the results, equivalent radar reflectivity requires temporal resolutions below 30 s, that common operational radars cannot provide. Quantitative precipitation estimates up to 5 mm/h require temporal resolutions below 1 minute. Quantitative precipitation estimates above 5 mm/h require temporal resolutions below 30 s. The results support the sparse collection of recommendations for weather radar revisit frequency for hydrometeorology reported in the literature.

3.1 Impact of Enhanced Temporal Sampling on Radar Reflectivity Accuracy within Fixed Resolution Volumes

3.1.1 Data

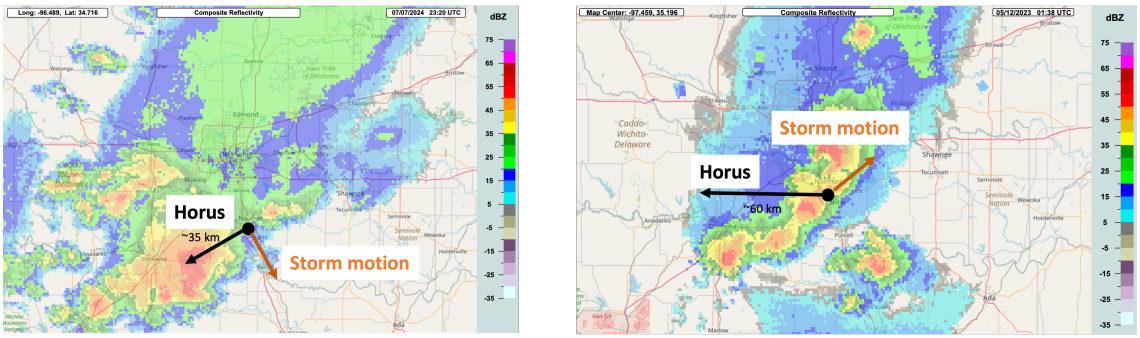
With support from NOAA/NSSL and OU/ARRC, this research builds on observations from a mobile S-band scanning polarimetric PAR called Horus (Palmer et al. (2023a)). Horus observed two precipitating weather systems using range-height-indicator (RHI) mode scans. The first event was captured on July 7, 2024, using Horus' nominal 2.58

degree beamwidth in azimuth and elevation. The second event was on May 12, 2023 collected with a wide fan-beam of 6.7 degrees in azimuth while the elevation was at the nominal radar beamwidth. The Horus RHI scan specifications for the two events are summarized in Table 1. Both events are convective in nature with hail, which is notable because severe weather with hail tends to evolve rapidly. The difference in the two events beam characteristics is used to investigate the impact of beamwidth on radar temporal uncertainty.

Table 3.1: Horus PAR settings and observed event information. Horus is located at 35.18 Latitude ,-97.45 Longitude operating in an RHI mode. (Palmer et al. (2023b) and `https://arrc.ou.edu/radar_horus.html`)

Observed Event	Event 1	Event 2
Observation Date	07-07-2024	05-12-2023
3 dB azimuth beamwidth (degrees)	2.6	6.7
3 dB elevation beamwidth (degrees)	2.6	
Range resolution (meters)	19.2	
Elevation extent (degrees)	0.83-29.17 in steps of 1.67	0.5-32 in steps of 0.5
Duration (UTC)	23:19 - 23:59 (about 40 min)	1:38-2:48 (about 70 min)
Revisit time (s)	0.76	2.0
Azimuth Pointing (degrees from North)	230	270
Approximate storm motion	Northwesterly	Southeasterly
Precipitation Type	Convective, Hail	Convective, Hail
Maximum Range (km)	30	65
Freezing Level (km)	4.6 km at 0 UTC on July 8th	4.5 km at 0 UTC on May 12th

Figure 3.2 shows the horizontal context at the start time of both events from the Multi-Radar Multi-Sensor System (MRMS) Operational Product Viewer, with arrows indicating the azimuthal pointing direction and horizontal extent of the Horus RHI storm-cross sections relative to the storm motions. The MRMS precipitation type classifier reports that both events involve convective precipitation and hail (Zhang et al. (2011)). While Horus is a polarimetric PAR, Z is the most fundamental radar variable that is chosen for study in this chapter. The calibration of polarimetric variables such as Z_{dr}, K_{dp},and A with PAR is a current challenge that warrants on-going research, so these variables are excluded. As they are used for QPE (Ryzhkov et al. (2022)), they



(a) (b)

Figure 3.2: (a) Event 1 on July 7, 2024 at 23:20 UTC (b) Event 2 on May 12, 2023 at 1:38 UTC

will be investigated in a future study.

On July 7, 2024, Horus was pointing at an angle of 230 degrees relative to north, and the convective system was moving to the southeast as shown in Figure 3.2(a). The melting layer at 00 UTC on July 8, 2024 reported from the nearest sounding is located about 4.6 km in altitude (University of Wyoming Department of Atmospheric Science (2023); Lat.: 35.181, Long.: -97.438)). On May 12 at 00 UTC, the a melting layer was located at about 4.5 km in altitude.

In addition to Horus data, four 24-hour events were collected by a MRR collocated with a 2D Video Disdrometer (2DVD) at the Kessler Atmospheric and Ecological Field Station (KAEFS; `https://www.ou.edu/kaefs`). MRRs have been commercially available since the 1990s, and are well known to produce reliable rainfall characteristics and disdrometers have long been considered ground reference measurements in the field of precipitation (Klugmann et al. (1996), Chen et al. (2015), Tokay et al. (2020)). The MRR is a frequency modulated continuous-wave (FM-CW) radar that operates at 24 GHz (`https://data.eol.ucar.edu/datafile/nph-get/612.018/METEK-MRR-physical-basics.pdf`). Though it operates continuously, a repeated frequency modulation pattern can be used to extract both distance and veloc-

ity information of the hydrometeors in the radar resolution volume within the vertical column above the MRR up to about 5 km in altitude. With range resolution dependent on its bandwidth, the range of falling precipitation is captured by the MRR by a frequency difference between transmission and reception. As Z is related to the size of the falling drops, and because the relationship between the terminal fall velocity and the diameter of the drop is empirically understood, this is used to estimate the drop size distributions with the assumption that additional vertical wind contributions are neglibible (`https://data.eol.ucar.edu/datafile/nph-get/612.018/METEK-MRR-physical-basics.pdf`). The four events observed with the MRR are detailed in Table 2 and have a one-minute time resolution corresponding to the R measurements of the collocated 2DVD.

Table 3.2: MRR Settings and event information for the considered MRR data located at 34.98 Latitude, -97.53 Longitude

Observed Event	Event 1	Event 2	Event 3	Event 4
Observation Date	10-04-2023	09-30-2021	04-13-2019	10-25-2019
3 dB beamwidth (degrees)	1.5			
Range resolution (meters)	200			
Duration (hours)	24			
Revisit time (s)	10 (60 s with downscaling)			
Pointing	vertical			
Approximate storm motion	Southwesterly	Northwesterly	Southwesterly	Southwesterly
Precipitation Type	Convective, Hail	Convective, Hail	Stratiform, Convective	Stratiform, Convective
Freezing Level (km)	3 km	4 km	2.5 km	2.5 km

3.1.2 Methods

This section presents a framework for quantifying uncertainties in weather radar observations and derived precipitation rates that can be used to help define radar temporal sampling requirements for observed convective systems. The densest temporal sampling available from Horus is used to establish a reference for time periods (blocks) of 30 s, 2 min, and 5 min. This section begins with a presentation of the problem at hand and an introduction to the geostatistical tools used. The block kriging technique

estimates radar observations and derived R values along with the associated estimation standard deviations over the considered blocks.

3.1.2.1 Estimating Observation Uncertainty using Kriging

The objective is to compare a radar estimated variable $Z'(A,T)$ from discrete instantaneous observations to the true, typically unknown, variable to characterize the accuracy of radar observations for various time periods T and spatial domains A. The estimated equivalent radar reflectivity over T and within A is denoted as $Z'(A,T)$, although the approach could be applied to any observed radar variable. Precipitation rates ($R(A,T)$) derived from radar observations $Z'(A,T)$ are also analyzed following the same approach. The spatial domains considered are Horus radar resolution volumes which increase in size (and volume) with the distance from the radar and the radar beamwidth, and MRR resolution volumes. These spatial domains offer the finest spatial resolution available from the measurements. Several application block durations (T) are considered that are representative of current operational radar sampling and applications. $T = 2$ min and $T = 5$ min correspond to representative sampling intervals for operational WSR-88D radars in SAILS mode and for comprehensive coverage plans, respectively (Kurdzo et al. (2024)). As WSR-88D radars typically revisit a given radar resolution volume about every 2 to 5 min, their observations are practically assumed to be representative over the same time period. This assumption is investigated as part of this study. Besides, automatic systems that integrate data streams from multiple radars, such as the NOAA Multi-Radar/Multi-Sensor System (MRMS; Zhang et al. (2016a)), operate with temporal domains of 2 min that meet the needs for flash flood monitoring and prediction (Gourley et al. (2017b)). A third time period of 30 s is also considered, as it is relevant to spaceborne time-delayed observations of convective transport in the atmosphere for which PAR may be a validation instrument candidate

(e.g., INCUS mission; Van den Heever et al. (2022)). The collocated 2DVD and MRR observations, which will be considered in brief in 3.2.4 will be analyzed for block sizes ranging from 2 to 60 min.

For any radar resolution volume, the true time-averaged Z, denoted $Z(A,T)$, is written as: $Z(A,T) = \frac{1}{T}\frac{1}{A}\iint Z(x,t)\,dxdt$ where x is the location vector and t is time. The radar-estimated Z may be written as: $Z'(A,T) = \frac{1}{T}\int Z'(A,t)\,dt$, where $Z'(A,t)$ is a single radar observation at time t over the resolution volume A. The reference used to evaluate the radar estimates should match the corresponding true values averaged over the same volume A and time interval T. This reference, noted Z_{ref}, is proposed to be the temporally averaged $Z'(A,t)$ from all available Horus (or MRR) observations over T, provided that its associated uncertainty is sufficiently low. A single radar observation $Z'(A,t)$ is nearly instantaneous as a given resolution volume is illuminated by the radar wave for a few microseconds, and it has limited temporal representativeness over a time interval T that can range from the order of ten s to several minutes. The temporal variability of hydrometeor scatterers at small scales over T and the large resolution difference between each radar observation and T (as much as five orders of magnitude in duration) may cause large differences in the statistical sampling properties of the extremely variable precipitation process and add statistical noise when comparing the two quantities. The temporal representativeness of radar observations must be evaluated to determine whether the sampling over the intervals T is sufficiently frequent, i.e., whether the sampling time interval is below the decorrelation time of Z (and R) within a given resolution volume A, and whether $Z_{ref}(A,T)$ is associated with sufficiently low uncertainty. In this study, two sampled dataset of RHI observations from Horus (with RHIs separated by 0.76 s and 2 s) and four events captured by a vertically pointing MRR with one minute sampling resolution are considered. The block kriging linear interpolation estimator (Journel and

Huijbregts, 1978; Olea (2000)) is used to (1) analyze the temporal structure of the observed reflectivity, $Z(A,t)$, and determine the decorrelation times over resolution volumes comprising Horus RHIs and MRR profiles to assess the suitability of radar sampling, and (2) estimate the expected $Z_{ref}(A,T)$ (and $R_{ref}(A,T)$) and associated uncertainty in the form of estimation standard deviation from radar observations at nearby sampling times.

In the following section the block kriging framework is introduced taking the example of $Z(A,t)$. Assuming the $Z(A,t)$ to be a realization of a random function, the kriging technique uses a structure function given by the variogram $\gamma(h)$, which represents the temporal correlation of the Z time-series as a function of temporal lag h between the radar observation times:

$$\gamma(h) = \frac{1}{2}E(Z(A,t) - Z(A,t+h))^2 \tag{3.1}$$

where E is the expectation operator. The set of $\gamma(h)$ values can be computed from temporally distributed radar observations for all h to infer an empirical variogram. A standard variogram model is fitted to the empirical variogram. Among the set of classical models, the Gaussian model was chosen for its better fit to the radar data overall:

$$\gamma(h) = \begin{cases} C_0 + (C - C_0)(1 - e^{\frac{-h^2}{a^2}}) & h < a \\ C & h \geq a. \end{cases} \tag{3.2}$$

where the three parameters are the nugget (C_0), the sill (C) and the distance parameter (a). The sill is theoretically equal to the field variance. The distance parameter is related to the mean decorrelation lag of the measurements called the range given by $\sqrt{3}a$ when the variogram function reaches 95% of the sill variance. Neighboring radar samples separated by a time lag larger than the range are decorrelated. The nugget

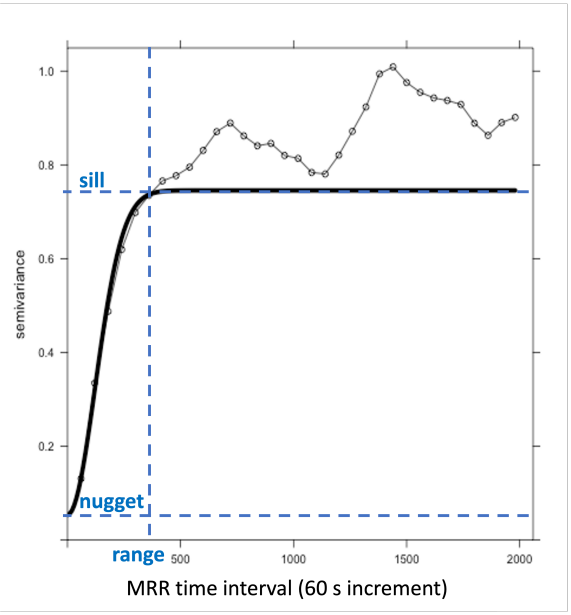


Figure 3.3: An example of a gaussian variogram model fit (bold line) to an emperical variogram compiled from a single radar range gate from MRR observations separated by interdistances from 60 s to 2000 s. The variogram metrics discussed in this chapter are marked: sill, range, and nugget.

parameter can be used to describe a possible discontinuity of the variogram at the origin that may be due to: (i) process variability at small temporal scales unresolved by the radar observations and/or (ii) radar observation errors. Figure 3.3 shows an example of an empirical variogram computed from MRR observations and a fitted gaussian model to highlight the three parameters. Variograms are computed with rapid updates from Horus and MRR observations to analyze the temporal structure of $Z(A,t)$ (and $R(A,t)$) and to determine the decorrelation times and assess the suitability of radar sampling.

The block kriging linear interpolation estimator makes use of the variogram to determine the reference $Z_{ref}(A,T)$ and other estimates $Z'(A,T)$ from radar observations $Z(A,t)$:

$$Z_{ref}(A,T) = \sum_{i=1}^{N_r} \lambda_i Z(A,t) \tag{3.3}$$

where N_r is the number of radar observations available at adjacent times t; $\{\lambda_i, i = 1, Nr\}$ are the block kriging weights. The block kriging estimator is unbiased and minimizes the estimation variance. The estimation variance allows assessment of the estimation quality as a function of the temporal structure of the Z field and the relative lag of the radar observations versus the temporal domain of interest T. Its expression is:

$$V_{ref}(A,T) = Var(Z_{ref}(A,T) - Z(A,T))$$
$$= -\frac{1}{T^2}\int_T\int_T \gamma(t,t')\,dt\,dt' + 2\sum_{i=1}^{N_r}\lambda_i(\frac{1}{T}\int_T \gamma(t,t_i)\,dt) - \sum_{i=1}^{N_r}\sum_{j=1}^{N_r}\lambda_i\lambda_j\gamma(t_i,t_j) \tag{3.4}$$

$\gamma(t,t')$ is the variogram function computed on the time lag between the two times t and t'. The first term denotes the block-to-block computation of the variogram function over the temporal domain T with t and t' belonging to T. The second term computes the variogram function between each radar measurement time t_i and temporal domain T with t belonging to T. Finally the last term is the in-between radar measurement times variogram computation. The estimation variance depends on the variogram characteristics and the temporal domain T.

In short, taking into account the temporal structure of Z (associated with storm variability) through the variogram, the Z is computed over temporal domains T representative of current operational radar sampling and weather radar applications. The temporal domains T are sampled at various frequencies. The estimation variance $V_{ref}(A,T)$ of the reference $Z_{ref}(A,T)$ is assessed from all available radar observations (i.e., with the densest temporal sampling) to verify it is sufficiently low so the reference estimates are deemed reliable and representative. Other estimates $Z'(A,T)$ are estimated with block kriging using more sparsely sampled observations $Z'(A,t)$, thus increasing the associated estimation variance $V'(A,T)$.

3.1.2.2 Error Analysis

The objective of this section is to quantify the temporal observation uncertainty to (1) assess its significance over time periods representative of current operational radar sampling and (2) identify required temporal sampling for the types of events considered that support weather radar applications. In the field of weather radar QPE, various error modeling approaches have been developed and used to represent the error of R products, such as the characterization and superposition of errors from different sources, analyzing the mean and variance of residuals, space-time correlated error fields, and Monte Carlo inputs to a given application (see Mandapaka and Germann (2010) for a review). Errors in radar observations can be systematic in nature, implying that they can be corrected (e.g., mean field bias). Systematic errors have been studied extensively in the literature (e.g., radar calibration, vertical structure of precipitation, precipitation types), and the reader is referred to Anagnostou et al. (2001), Seo et al. (2000), Delrieu et al. (2009), and Zhang et al. (2008). Errors can also be random (e.g., Kirstetter et al. (2010), Maggioni et al. (2016)). Random errors are more elusive than systematic errors. They are contributed to by intermittent and noncontinuous sampling of the atmosphere and the use of radar observations and retrievals in applications defined over spatio-temporal grids coarser than the characteristic scales of the observed phenomena. Spatiotemporal sampling errors arise from such mismatch and depend on the precipitation spatial and temporal variability at all scales. For example, a five-minute duration volume coverage pattern may not produce a representative depiction of a fast-evolving storm that generates different features within the radar's field of view over the five-minute period. The random observation error E_o has two contributing error sources: spatial $E_{o,s}$ and temporal $E_{o,t}$. By computing a reference Z_{ref} from all available radar observations (retrievals) over temporal domains

T, and by estimating Z' from more sparsely sampled observations, this study focuses on random errors attributed to non-stationary factors and transient weather features intermittently captured in radar resolution volumes: $E_{o,t}$. It is estimated with the estimation standard deviation $\sqrt{V'(A,T)}$ as a function of temporal sampling. Systematic errors are ignored by assuming that the radar calibration is stable over the course of the storm event and by considering each resolution volume A to be independent.

The radar variable Z in linear scale has historically been used to estimate precipitation rate at the surface using empirical relations such as the Marshall-Palmer Z-R power-law relation (Marshall and Palmer (1948)). An empirical $R(Z)$ rain relation is utilized to convert reflectivity reference values Z_{ref} and estimates Z' into precipitation rate estimates R_{ref} and R' to investigate the impact of Horus PAR temporal sampling density on estimated rainfall estimates. This relationship, optimized for a large drop size distribution data set collected in Oklahoma for the S-band, is $R(Z) = 1.9410^{-2}Z^{0.694}$ (Ryzhkov et al. (2022)). The uncertainty of R depends on magnitude and displays an asymmetric distribution (e.g., Kirstetter et al. (2015b)). It is analyzed through residuals that are defined as the difference $\epsilon_R = (R' - R_{ref})_{(A,T)})$. This empirical error analysis is specific to the radar instruments, storms, and data processing implemented. The distributions of ϵ_R sub-samples defined by parameters like Z and R magnitude and distance from the radar must be considered to highlight their influence. Indeed, radar resolution volumes increase in size with distance from the radar along with the potential for unresolved microphysical process variations and NUBF.

Note that sampling errors may also arise from the reference E_r and compound with E_o. Yet these are considered negligible because the MRR and the 2DVD observations are matched in space and time.

3.2 Integrating Application-Driven Temporal Resolution Requirements with Radar Sampling Strategies

3.2.1 Variogram Analysis

The temporal structure of PAR observations is used to evaluate the suitability of the radar sampling. Meteorological and hydrological applications often require time series of radar observations or radar-derived Rs. The underlying variability of these signals, when observed with high temporal resolution observations, can be described by the variogram which is closely related to the autocorrelation of the signal. The decorrelation times (range), maximum variability (sill), and variability at very close time steps (nugget) are all impacted by processes, advection, and vertical motions of the hydrometeors observed in the atmosphere. These hydrometeor fluctuations are furthermore indirectly interpreted through the lens of Z observed in an Eulerian sense. The Horus RHI scans collected on May 12 and July 7 were processed to generate variograms at each radar resolution volume for all range gates and elevation angles. Generated variogram metrics for all cases show a clear structure in time.

Figure 3.4 displays the distributions of variogram parameters. The range parameter is an indication of the decorrelation time of an observed temporal series. It can be seen as the maximum temporal interval beyond which two consecutive radar scans will not yield correlated observations that are useful for predicting the underlying structure of the sampled signal. The range parameter indicates that decorrelation times vary between 6 and 1500 s (25 min) for the two events, with median values of 196 and 423 s for the May 12$^{\text{th}}$ and July 7$^{\text{th}}$ events, respectively. The Horus sampling rate falls well

below the reported range values, so it is sufficient to capture the temporal structure of the storms. A radar sampling every 30 s is below 95% (99%) of the decorrelation times, while a radar sampling every 120 s is below 72% (96%) of the decorrelation times, and a radar sampling every 300 s is below 29% (67%) of the decorrelation times for the May 12$^{\text{th}}$ (July 7$^{\text{th}}$) event. Overall, this suggests that WSR-88D temporal sampling of the atmosphere near 5 min is too infrequent and only partly captures storms' temporal evolution for these convective cases. While these case studies do involve convective storms, to make a general radar sampling specification, an assessment would be required with a more numerous and diverse pool of storms to represent the variability expected to be captured by the intended radar applications. Note that accurate radar estimations for applications call for more frequent sampling than the variogram decorrelation times, as is explored in the next section. Since the temporal domains T are typically smaller than the reported variogram decorrelation times (range values), a low nugget parameter is essential for the reliability and representativeness of radar estimates and derived quantities. As the nugget increases, the standard deviation associated with block kriged $Z_{ref}(A,T)$ and $Z'(A,T)$ (and by derivation, $R_{ref}(A,T)$ and $R'(A,T)$ for rainfall) increases. Note that the nugget parameter is expressed as a percentage of the sill value in Figure 3.4 to allow comparison the field of view. The nugget values are generally low, with median values of 8.1% and 7.7% for the May 12$^{\text{th}}$ and July 7$^{\text{th}}$ events, respectively. About 60% (80%) of nugget values are within 10% (20%) of the sill value for both events, suggesting that limited variability occurs at scales finer than the Horus sampling intervals and that measurement uncertainty is also limited. Note that the nugget tends to be consistently larger with the larger Horus beamwidth used during the May 12$^{\text{th}}$ event, which is more prone to NUBF.

Figure 3.5 displays the spatial distribution of variogram parameters estimated over the course of the two events sampled by Horus. All parameters, estimated indepen-

dently for each resolution volume, display a spatial pattern that reflects the impact of microphysical and dynamical processes (e.g., vertical transport of hydrometeors) and advection.

On July 7$^{\text{th}}$, as shown in Figure 3.2(a), the northwesterly storm motion is nearly perpendicular to Horus's azimuth, so advection strongly influences the variogram structure. Storm-relative winds are reported by the NOAA Storm Prediction Center's (SPC) mesoscale analysis to be up to about 10 m/s (Center (2015)). On May 12$^{\text{th}}$, as shown in Figure 3.2(b) the southwesterly storm motion, 45 degrees from perpendicular to Horus's azimuth, suggests horizontal advection significantly contributes to observed storm variability, with storm-relative winds reported by NOAA-SPC's mesoscale analysis to be up to about 10 m/s (Center (2015)). Higher maximum variability in the July 7$^{\text{th}}$ Horus RHI, compared to May 12$^{\text{th}}$, is evident from the greater variogram sill in the liquid phase below 5 km (Figure 3.4(a) vs. (d)). This contrast partly reflects stronger advection aligned with Horus's orientation on July 7$^{\text{th}}$. Along with higher semivariance, the July 7$^{\text{th}}$ event shows longer liquid-phase decorrelation times, up to 20 min, compared to 10 min on May 12$^{\text{th}}$. On May 12$^{\text{th}}$, Z exhibits lower overall variability and more transient fluctuations over the 70-minute period, likely due to the smaller, localized cell structure (Figure 3.2(b)).

3.2.2 Uncertainty of Radar Reflectivity

Taking into account the variogram temporal structure, Z_{ref} and Z' values are computed with block kriging for $T = 5$ min, 2 min, and 30 s. Z_{ref} is computed using all available radar observations. Z' is computed using sparser sampling via multiples of the actual Horus temporal sampling interval (i.e., 0.76 s and 2 s for the July 7$^{\text{th}}$ and May 12$^{\text{th}}$ events, respectively) so that $Z_{ref} = Z'(0)$ where the index 0 indicates the actual Horus sampling interval. The estimation standard deviation depends on the

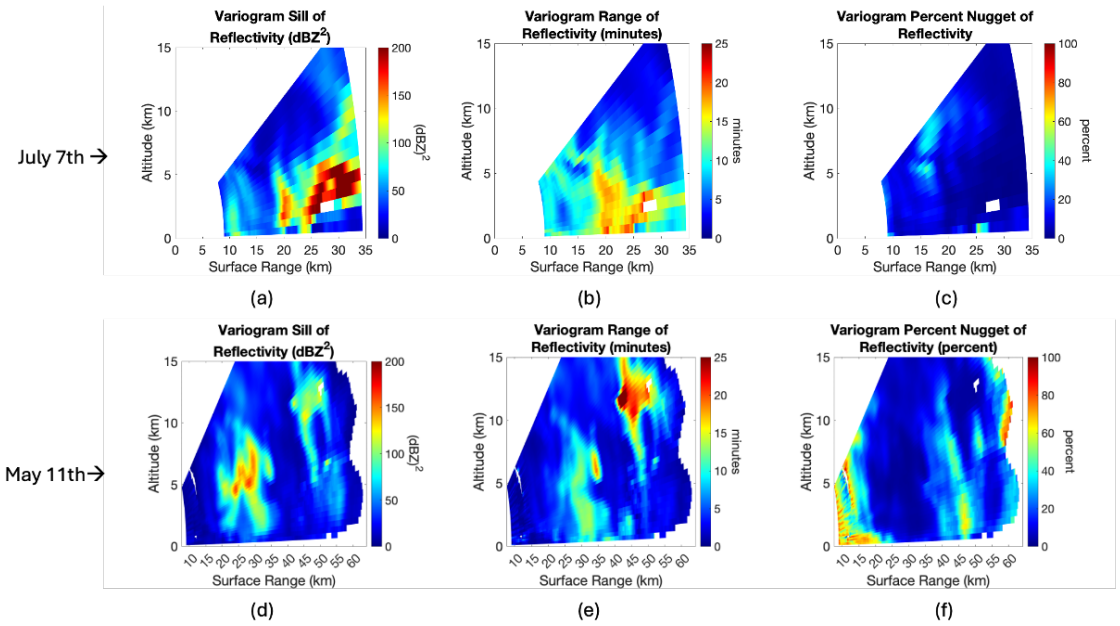


Figure 3.4: July 7, 2024 (a) temporal range (decorrelation time), (b) sill, and (c) percent nugget and the May 12, 2023 (d) temporal range, (e) sill, and (f) percent nugget.

variogram characteristics, T, and t (Eq.4). The sparsest temporal sampling (i.e., the largest sampling interval, or time between observations Δt) that is considered is the duration T which corresponds to one radar sample per analysis block. For each event and time domain T, the Horus RHI time series provide datasets exceeding 35 million samples, enabling robust statistical analysis.

Figure 3.6 shows the distributions of Z' uncertainty, or $E_{o,t}$, as functions of sampling interval for the different temporal domains T. The 50%, 25–75%, and 10–90% quantiles are plotted for the uncertainty distributions. Figures 3.6(a)-(f) show a shift toward higher uncertainty as the sampling interval increases, as expected. The rate of uncertainty increase is higher for shorter T. For example, at Δt= 20 s for July 7$^{\text{th}}$, the median uncertainty is 0.52 dBZ for $T = 5$ min (Figure 3.6(a)), 0.78 dBZ for $T = 2$ min (Figure 3.6(b)), and 1.51 dBZ for $T = 30$ s (Figure 3.6(c)). Distribution spread increases with Δt, reflecting greater uncertainty due to a wider range of temporal changes

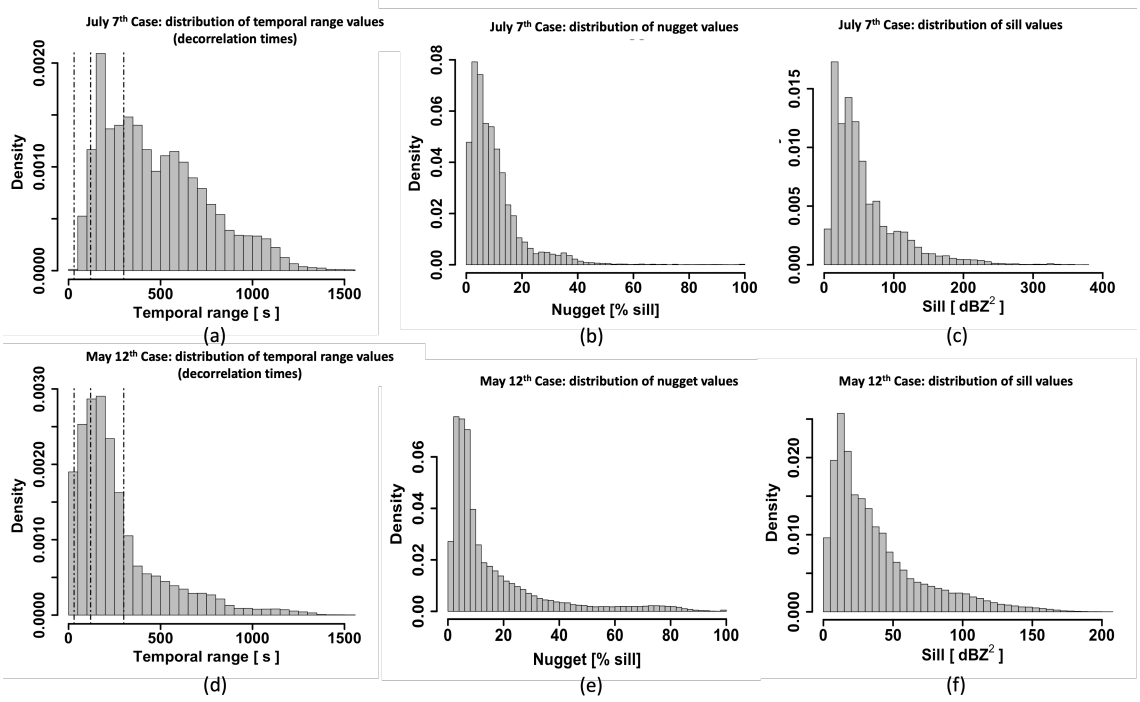


Figure 3.5: Histograms depicting the distribution of variogram parameters are shown for July 7, 2024 (a)temporal range (decorrelation time), (b) sill, and (c) percent nugget and the May 12, 2023 (d) temporal range, (e) sill, and (f) percent nugget. The temporal lag of 30 s, 2 min and 5 min are highlighted with the temporal range histograms (a, d)

between samples.

As expected, Z_{ref} is systematically associated with lower uncertainty. For example, at sampling interval 0.76 s for July 7$^{\text{th}}$, 80% of the uncertainty values are below 0.14 dBZ for $T = 5$ min (Figure 3.6(a)), 0.20 dBZ for $T = 2$ min (Figure 3.6(b)), and 0.38 dBZ for $T = 30$ s (Figure 3.6(c)). The highest sampling rate (smallest Δt) provides the most information content within each temporal domain T, leading to the most representative reflectivity value associated with the lowest uncertainty. Note that Z_{ref} meets the WSR-88D system specifications, establishing uncertainty of ± 1 dBZ for reflectivity. According to Figure 3.6(a), a sampling every 20 s or less is required for reflectivity uncertainty within ± 1 dBZ with Horus for $T = 5$ min.

In contrast, sampling only once over T (Δt=T) leads to significant uncertainty. For example with the July 7, 2024 event, $T = 5$ min sampled every 300 s yields a median uncertainty value of 2.6 dBZ (Figure 3.6(a)), a median value of 2 dBZ for $T = 2$ min sampled every 120 s (Figure 3.6(b)), and a median value of 1.8 dBZ for $T = 30$ s sampled for 5 min (Figure 3.6(c)). In particular, if the Next Generation Weather Radar (NEXRAD) system was sampling this event with a typical VCP update-time of 5 min, reflectivity $E_{o,t}$ values ranging from 1.9 dBZ (quantile 10%) to 4.2 dBZ (quantile 90%) would be expected. These values are outside the range of WSR-88D uncertainty specifications. Assuming that nearby WSR-88D are out of phase in the merging of multiple radar observations, MRMS produces gridded-reflectivity products every 2 min. For the July 7$^{\text{th}}$ observation, a radar sample used to represent reflectivity at a given location in space over $T = 2$ min would be associated with $E_{o,t}$ values ranging from 1.5 dBZ (quantile 10%) to 2.5 dBZ (quantile 90%) as shown in Figure 3.6(b). If we relate the temporal uncertainty of the INCUS satellite mission to these ground radar measurements, computing observed temporal differences over 30 s, a ground radar measurement sampling the atmosphere for the July 7$^{\text{th}}$ event with a revisit time

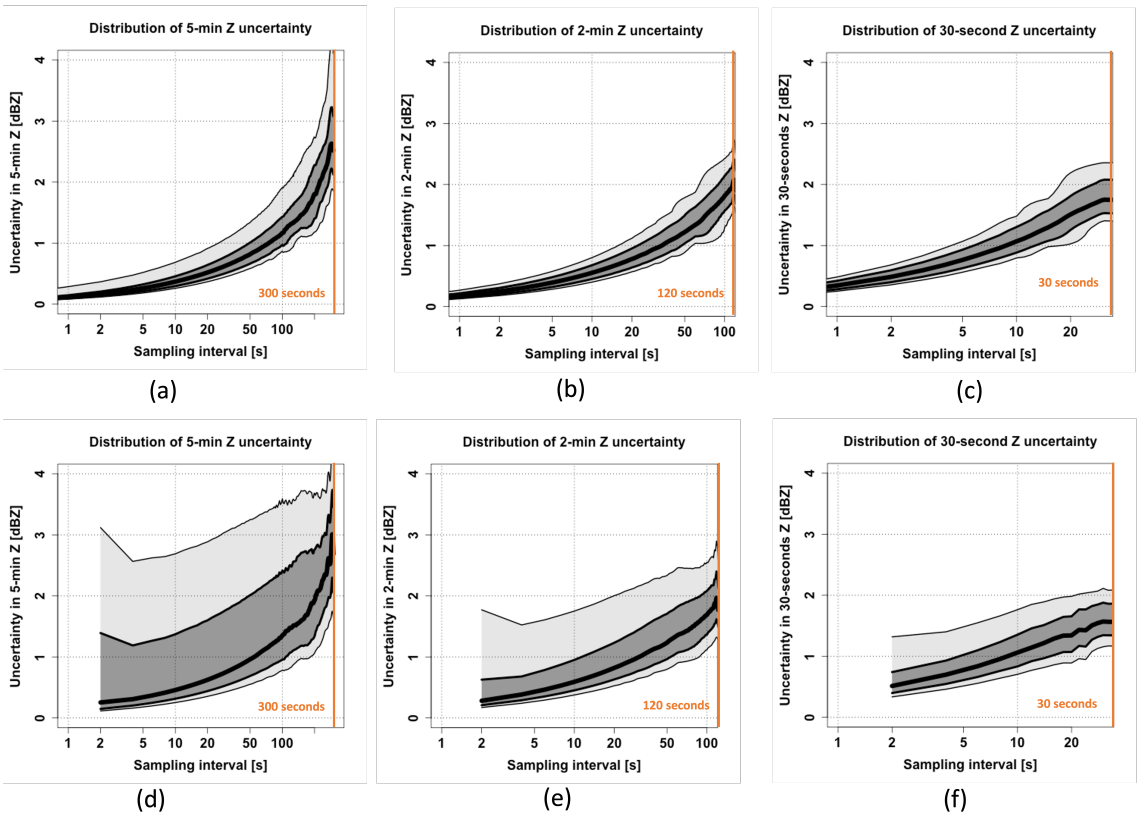


Figure 3.6: Estimates of Z uncertainty, or expected temporal observation error $E_{o,t}$, are shown for July 7$^{\text{th}}$ over various temporal domains, T = (a) 5 min, (b) 2 min, and (c) 30 s. Estimates of Z are shown for May 12$^{\text{th}}$ for T = (d) 5 min, (e) 2 min, and (f) 30 s. Shaded areas represent the 25/75th percentiles and 10/90th percentiles of the uncertainty values for all the blocks in the considered dataset.

of 30 s would yield a mean $E_{o,t}$ of about 1.8 dBZ with possible uncertainties greater than 1.3 dBZ 90% of the time as shown by the 90th percentile line in Figure 3.6(c).

The May 12$^{\text{th}}$ RHI observations tell a complimentary story. The wider beamwidth exhibits higher 75% and 90% quantiles of $E_{o,t}$, Δt, and T, likely due to the presence of more NUBF. The median uncertainty increases with increasing Δt, and the rate of increase is higher with lower T.

For the $T = 5$ min block shown in Figure 3.6(d), median $E_{o,t}$ for Z_{ref} 0.2 dBZ while $E_{o,t}$ for Z' sampled only once in the block is 3 dBZ. For the $T = 2$-minute block shown in Figure 3.6(e), median $E_{o,t}$ for Z_{ref} 0.3 dBZ while $E_{o,t}$ for Z' sampled only once in the

block is 2 dBZ. Median $E_{o,t}$ meets the WSR-88D specification when the 5 minute block is sampled every 50 s and when the 2 minute block is sampled every 35 s. Neither the 5- nor 2-minute blocks meet the 1 dBZ WSR-88D uncertainty specification by median value; high quantiles exceed it by 3 and 2 dBZ, respectively. The 30-second block has a median reference Z' uncertainty of 0.5 dBZ, raising to 1.4 dBZ as the sampling interval is increased from 2 to 30 s.

3.2.3 Uncertainty for Quantitative Precipitation Estimation

In this section, the uncertainty associated with Horus estimated $R'(Z)$ is analyzed as a function of the radar sampling interval Δt and the R magnitude.

At a given Δt and T, fast-evolving convective storms and slower stratiform regions contribute differently to rain rate uncertainty due to their contrasting rain rates and evolution speeds. (Dolan et al. (2018),Niu et al. (2010)). Figure 3.7 and 3.8 show the R magnitude error (e_m) and relative error (e_p) as functions of R_{ref} and Δt. The magnitude error $e_m = |R_{ref} - R'|$ highlights magnitude differences between R' and R_{ref} (overestimates or underestimates) and it is shown in the color scale in units of mm/hr. The relative error $e_p = \frac{|R_{ref} - R'|}{R_{ref}}$ conveys the significance of the error relative to the magnitude and highlights the comparative significance across magnitudes. e_p is expressed in percent and marked with labeled contour lines. Each combination of R_{ref} and Δt is associated with a population of e_m and e_p pairs. The populations e_m and e_p are analyzed by their medians (Figure 3.8) and extreme values via their 90th percentiles (Figure 3.7).

Both Figures 3.7 and 3.8 display similar behavior for the magnitude error e_m across events and temporal domains. Consistent with findings in 3.2.2, e_m increases with Δt at a given R_{ref}. For any given Δt, e_m also consistently increases with R_{ref} (above 0.3 $mm.hr^{-1}$). Thus R extremes typically associated with more vigorous convection

and rapid storm evolution tend to have higher e_m. e_m varies in the ranges [0.01 - 9.2] $mm.hr^{-1}$ and [0.01 - 22] $mm.hr^{-1}$ for the quantiles 50% and 90%, respectively, with values below 1 $mm.hr^{-1}$ being generally found for sampling intervals lower than 20 s or reference rain rates below 0.5 $mm.hr^{-1}$, and larger values are systematically associated with larger R_{ref} and Δt. Various R_{ref} and Δt combinations result in similar values of e_m and e_p. As an example with the e_m quantile 50% for May 12$^{\text{th}}$ for $T = 2$ min (Figure 3.8(e)), a moderate 2 $mm.hr^{-1}$ rain rate sampled every 100 s e_m(2 $mm.hr^{-1}$, 100 s) = 0.5 $mm.hr^{-1}$ is the same error as a high R of 10 $mm.hr^{-1}$ sampled every 10 s over the same temporal interval e_m(10 $mm.hr^{-1}$, 10 s)= 0.5 $mm.hr^{-1}$. The relative error e_p ranges from 0% to over 100% and shows varying dependence on Δt and R_{ref}. As expected, e_p is higher when R_{ref} is low. Above 2 mm/hr, e_p often increases with Δt (e.g., Figure 3.7(a)). Consistent with 3.2.2, e_m and e_p approach zero as Δt decreases. For a given Δt, errors increase with shorter T due to fewer samples per block. For example, considering the range of all rain rate magnitudes on July 7$^{\text{th}}$ at Δt=10 s, 90% of e_m (e_p) values are typically below 0.4 $mm.hr^{-1}$ (8.4%), 0.54 $mm.hr^{-1}$ (10%), and 1.02 $mm.hr^{-1}$ (18.8%) for $T = 5$ min, 2 min, and 30 s, respectively. At Δt= 30-s, 90% of e_m (e_p) values are below 0.7 $mm.hr^{-1}$ (14.3%), 0.97 $mm.hr^{-1}$ (17.9%), and 1.8 $mm.hr^{-1}$ (32%) for the $T = 5$ min, 2 min, and 30 s respectively. Increases in e_m and e_p can also be seen for a given Δt at a given magnitude as T is decreased in Figures 3.7 and 3.8 for both Horus observations.

Figures 3.7 and 3.8 can be used to estimate the expected error at various R_{ref} and Δt values, and to identify the required Δt to meet the accuracy requirements of any weather radar application with defined T for the two events. If specifications are required for more dynamic and variable atmospheric phenomena (e.g., tornados, derechos, or convective systems with rain rates exceeding 50 $mm.hr^{-1}$) than those captured on July 7$^{\text{th}}$ and May 12$^{\text{th}}$, the geostatistical analysis framework described in

Section 3.1.2 should be applied to a set of representative observations that capture the variability required to be observed by the intended application.

For July 7$^{\text{th}}$ and $T = 5$ min, a Δt= 5 min is associated with e_p median uncertainties that range from [18-25]% (Figure 3.8(a)) and can reach [50-65]% (Figure 3.7(a)). The median error magnitude for $R_{ref} = 10\ mm.hr^{-1}$ is $e_m(10mm/hr, 300s, 50\%) = 2.26\ mm.hr^{-1}$ and 90% of error magnitudes are below $e_m(10mm/hr, 300s, 90\%) = 7\ mm.hr^{-1}$, while for $R_{ref} = 20\ mm.hr^{-1}$, $e_m(20mm/hr, 300s, 50\%) = 4mm.hr^{-1}$, and $e_m(20mm/hr, 300s, 90\%) = 11\ mm.hr^{-1}$. This means that extreme R observed on the temporal scale of the WSR-88D VCPs (Δt= T= 5 min) can be associated with e_p greater than 50%. Similar considerations apply when Δt is reduced to 2 min associated with the merged MRMS products, as the rain rate error can exceed 40% for the same reference magnitudes. For a 30 second sampling interval, the error is about 30%. These observations on the impact of magnitude on rain rate error carry through to the May 12$^{\text{th}}$ case in Figure 3.7(a)-(c).

Figure 3.8 shows the median error. Importantly, for both the July 7$^{\text{th}}$ and May 12$^{\text{th}}$ cases, the errors are reduced when moving from $T = 5$ min to 30 s, and are reduced further to near-zero as the Δt approaches its minimum value. Evidenced by the curves generated by PAR observations in Figures 3.6-3.8, PAR observations can be utilized to characterize weather system sampling needs which vary depending on the storm being observed. PAR can also enable an error analysis associated with radar variables and R errors so that they can be accounted for within end-use application spaces like numerical weather prediction or flood forecasting. The use of PAR data in this work to characterize sampling errors also motivates the need for faster sampling of the atmosphere as faster sampling equates to more accurate radar variable estimates over application temporal domains.

To analyze the dependency of R error with resolution volume size, Figure 3.9 shows a

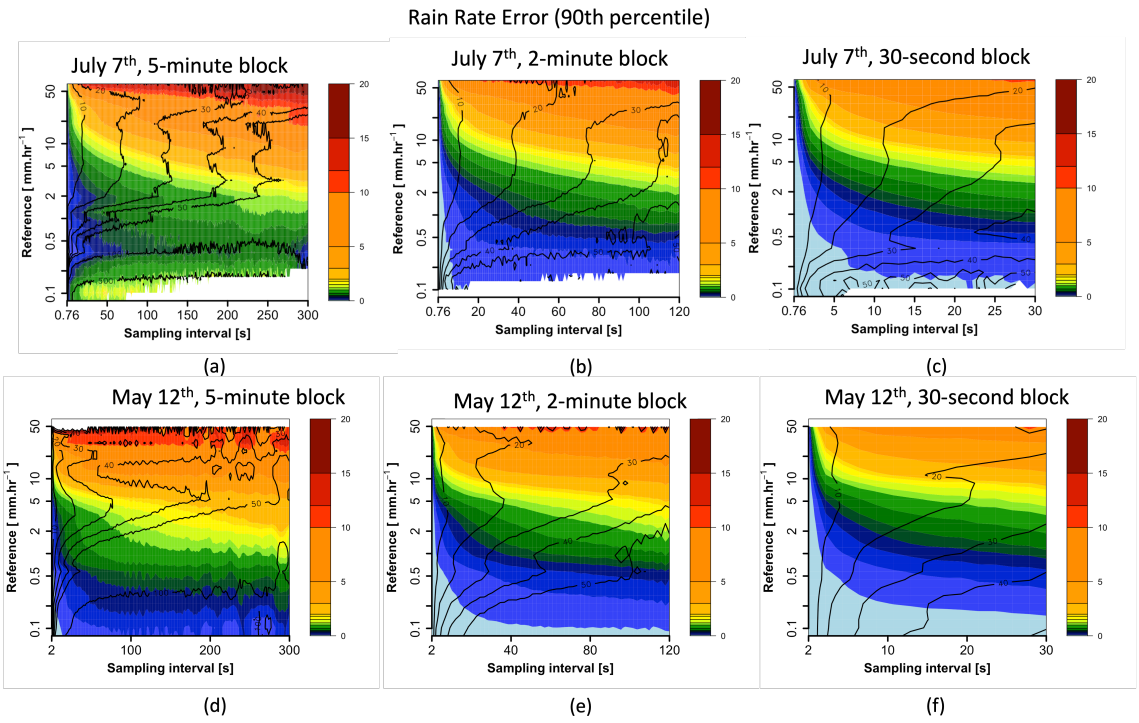


Figure 3.7: 90th percentile of the population of additive rain rate error $|R_{ref} - R|$ with contours indicating the percent error $\frac{|R_{ref}-R|}{R_{ref}}$ plotted verses R_{ref} (y-axis) and sampling interval Δt (x-axis).

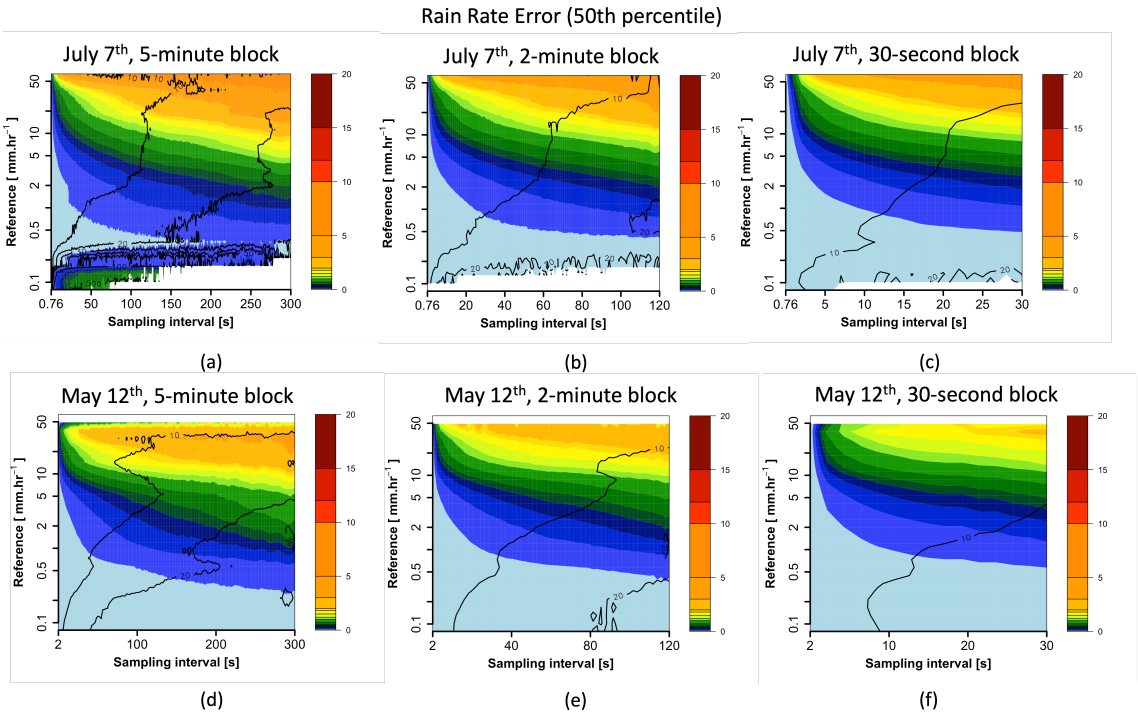


Figure 3.8: 50th percentile of the population of additive rain rate error $|R_{reftrue} - R|$ with contours indicating the percent error $\frac{|R_{ref}-R|}{R_{ref}}$ plotted verses R_{ref} (y-axis) and sampling interval Δt (x-axis).

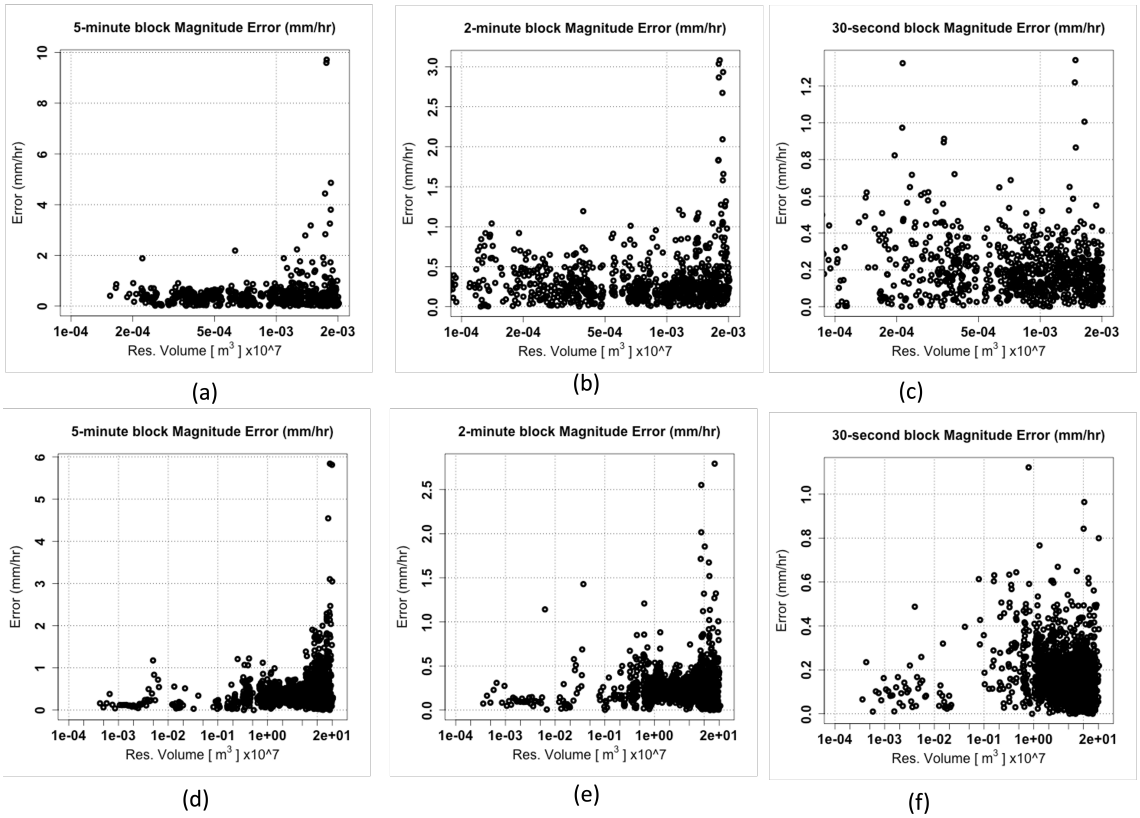


Figure 3.9: 50th percentile of rain rate magnitude error (mm/hr, y-axis) versus resolution volume ($m^3 * 10^7$, x-axis in log-scale). July 7^{th} with T = (a) 5 min, (b) 2 min, and (c) 30 s. The rain rate error for the observed event on May 12^{th} is also shown for T = (d) 5 min, (e) 2 min, and (f) 30 s.

representative example of the 50th percentile values of R magnitude error e_m associated with $R = 1mm.h^{-1}$ versus the radar resolution volume size. Errors tend to increase with resolution volume size, as evidenced in Figure 3.9(a,b,d,e) for T= 5 min and 2 min. The 30-second e_m increase is evident for the May 12th case in Figure 3.9(f). This trend is not as prominent in Figure 3.9(c), which can be attributed to smaller resolution volumes for the July 7th. A useful rule of thumb is that radar systems should be designed such that their largest resolution volumes comply with imposed error thresholds for the largest expected rain rates that will be encountered by the system.

Weather radar QPE is often assessed using statistical bias and correlation metrics to compare estimates with reference values (e.g., Delrieu et al. (2009), Kirstetter et al. (2010)). Since we assume the Horus data (section 3.1.2.2) excludes systematic biases, Figure 3.10 shows how temporal sampling affects the coefficient of determination (r^2) between R_{ref} and R'. The r^2 value, representing the variance in R_{ref} explained by R', is calculated across Δts for each temporal domain T. For a given T, considered sampling intervals vary from the shortest (densely sampled temporal domains) to the duration of T (sparsely sampled temporal domains with one sample only). As expected, r^2 values are maximum (1) for the densely sampled T and decrease with larger Δt. For the July 7th case event, r^2 values remain high and larger than 0.95 for $\Delta t < 100$ s then decrease sharply. For the May 12th case, the r^2 decrease with Δt is immediate and more significant, which is attributed to NUBF in the fan beam. For sparsely sampled temporal domains, r^2 values decrease with T. For example with the July 7th case event r^2 equals 0.97, 0.89, and 0.76 for $T = 30$ s, 2 min, and 5 min, respectively. These results highlight the impact of temporal radar-revisit frequency, the time it takes for the radar to revisit the same atmospheric volume, on QPE performance.

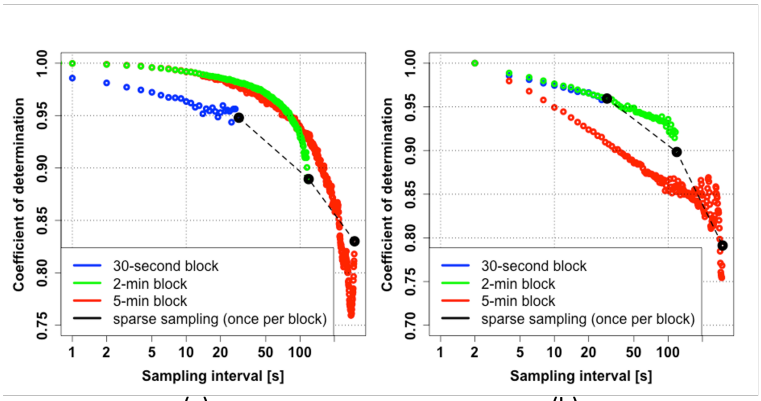


Figure 3.10: Correlation between the reference rain rate sampled at the minimum sampling interval (e.g. 0.76 s or 2 s) over $T = 30$ s (blue), 2 min (green), and 5 min (red) for (a) the July 7, 2024 case with a minimum sampling interval of 0.76 s and (b) the May 12, 2023 case with a minimum sampling interval of 2 s

3.2.4 Micro-Rain Radar Validation Study

This section supports the previous PAR findings with a comparison to MRR data analyzed with the same approach and bolstered by independent rain rate reference data collected from a collocated disdrometer at the surface.

Table 3.2 in section 3.1.1 describes the MRR dataset and provides an overview of the instrument specifications. The operating principle for Z and R estimation is different between the MRR and the PAR as is the frequency, range resolution, and pointing angle. The MRR samples a single vertical column at a temporal resolution of 1-minute. Despite these differences, both Horus and MRR Z values relate to the size of falling drops and can thus be used to estimate R vertical columns. While MRR measurements have a lower temporal resolution, they cover longer observation periods of 24 hours providing a statistically significant sample size. MRR observations below the 0 degree isotherm are considered in the analysis. MRR observations are downscaled from their native 10-second resolution to a 60-second temporal resolution to align with the 1-minute resolution disdrometer 2DVD measurements collocated with the MRR at

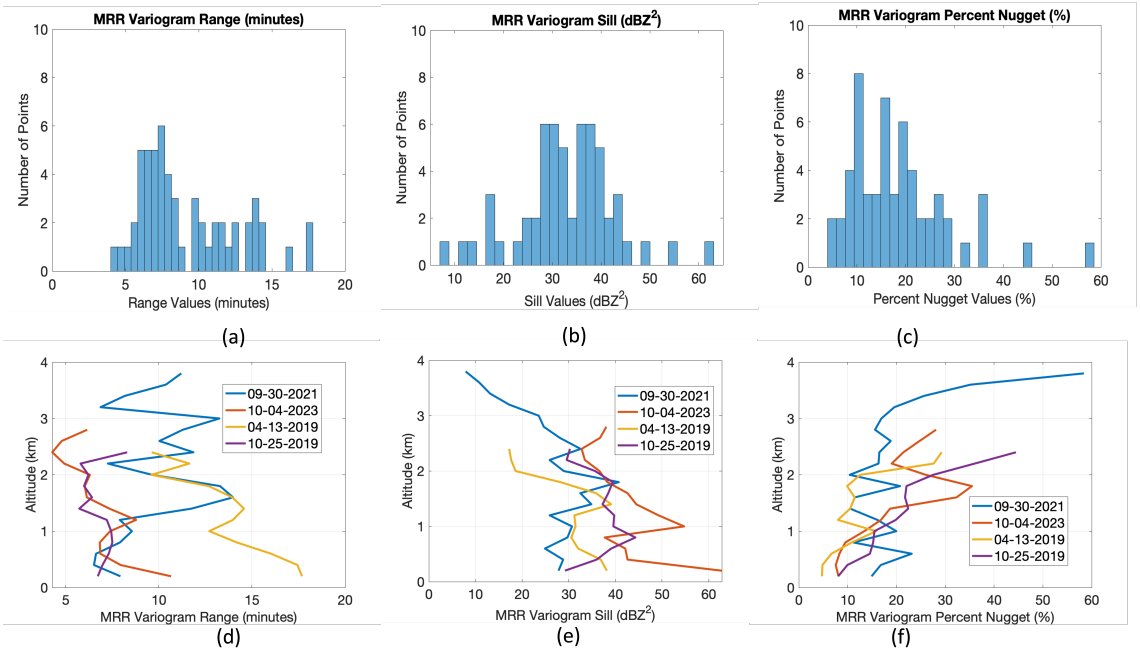


Figure 3.11: MRR key variogram metrics for all four events in table 3.2 taken at the KAEFS observation site are combined into histograms showing the number of observation points for values of (a) range (minutes), (b) sill (dBZ^2), and (c) nugget (percent of sill). These metric values are shown versus altitude for each individual observation case for (d) range, (e) sill, and (f) nugget where the blue curves are variogram metrics estimated on September 30, 2021, the red curves on October 4, 2023, the yellow curves on April 13, 2019, and the purple curves on October 25, 2019.

the surface.

Figure 3.11 shows the MRR variograms parameters for each observation day (Table 3.2) at levels below the 0 degree isotherm determined according to the nearby OUN site (University of Wyoming Department of Atmospheric Science (2023)). The parameter histograms (Figure 3.11(a)-(c)) show decorrelation times in the [5-10] minute range, a sill (maximum variability) in the range [30-40] dBZ^2, and a percent nugget between 5% and 30%. Such values are consistent with the Horus RHI variogram parameter values (Figure 3.5) as Horus range values are mostly below 600 s (10 min) and percent nugget values fall well below 30%. The Horus sill values are slightly higher than the MRR values, which requires further study but may be hypothesized to be due to the

higher temporal resolution of Horus as well as the larger resolution volume sizes of Horus causing the data to be impacted by more NUBF at far ranges.

The variogram range profiles shown in Figure 3.11(d) exhibit varied range behaviors between events. Below 1 km in altitude, the September 30, 2021, October 4, 2023, and October 25, 2019 events stand out with their lower range values, which can be explained by their convective nature according to table 3.2. The profile with the largest range, or longest decorrelation time, occurs on April 13, 2019. This event involves a mix of stratiform and convective precipitating types. It exhibits decreasing range values with altitude from the surface up to the 0 degree isotherm at 2.5 km. This behavior combined with the comparatively low nugget values suggests increased homogeneity in the liquid phase as expected in primarily stratiform systems. From Figures 3.11(d-f), all events display relatively consistent range and sill values and increasing percent nugget values with altitude. The later might be explained because MRR errors tend to increase in height due to signal attenuation, beam spreading, and changing particle types relative to rain rate retrieval assumptions.

Temporal block kriging is applied to MRR rain estimates for the four events over various temporal domains T ranging from 2-60 min. Kriged estimates are compared to the 2DVD distrometer in-situ surface rain values over the same T by computing coefficients of determination that are shown in Figure 3.12. Blue markers indicate MRR estimates from densely sampled T (sampled every minute) and red markers indicate sparsely sampled T (one sample only). The reference rain rate values are computed via kriging using the full 1-minute sampling density of the 2DVD in-situ observations over T. It is immediately clear from the Figure that the r^2 with dense sampling maintain higher values for all T. Note that deviations from the maximum value (1) can also be attributed to other error sources than temporal sampling. In contrast, r^2 values obtained with the sparsely sampled temporal domains are lower than with the densely

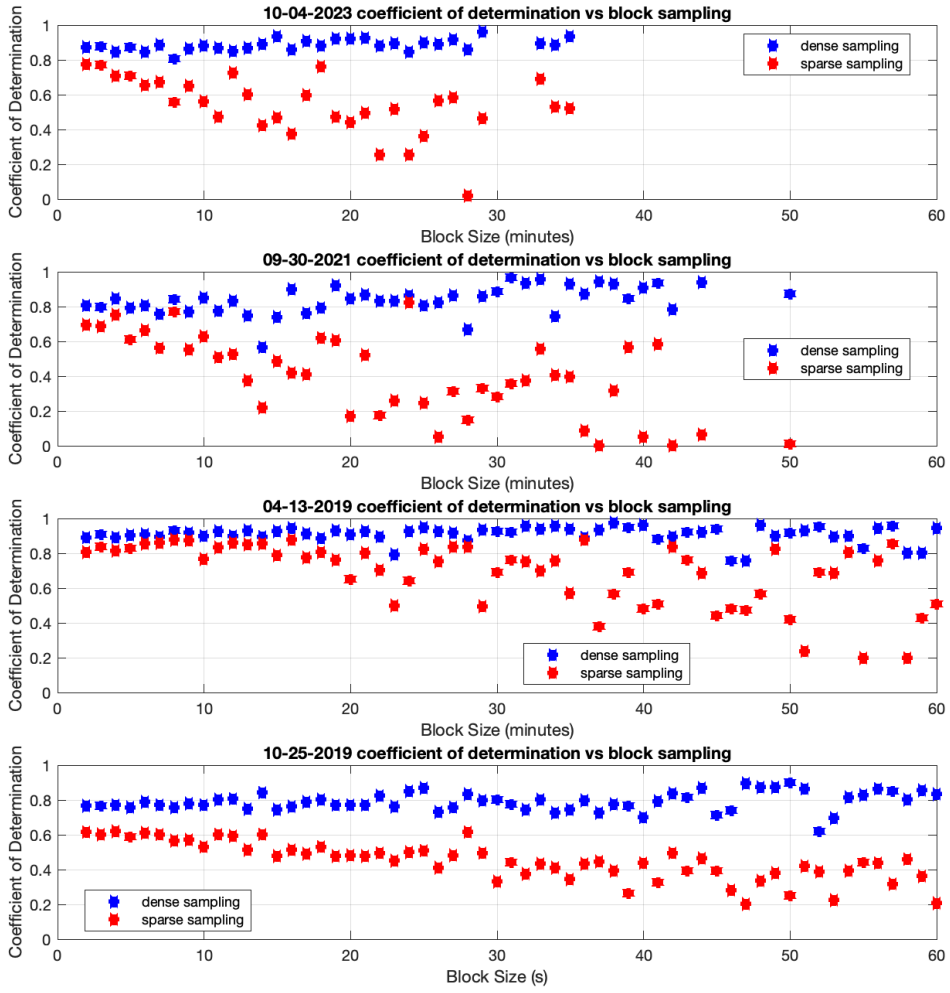


Figure 3.12: MRR estimates of r^2, square of the pearson correlation, between kriging estimated rain rates and in-situ 2DVD distrometer rain rates over various block sizes. Densely sampled kriging blocks (sampling every one minute) are indicated by blue markers and sparsely sampled blocks (sampling over one minute per block) indicated by red markers. This result is shown for 24-hour MRR observations over the days of October 4, 2023 (first plot), September 30, 2021 (second plot), April 13, 2019 (third plot), and October 25, 2019 (fourth plot).

sampled domains, and they further decrease with larger T. This is consistent with the findings with Horus measurements (Figure 3.10) where the r^2 values with sparse sampling (outlined with three black markers at the largest sampling interval) decrease with T. These results, obtained with a different instrument from Horus and with an independent precipitation reference, help confirm the impact of temporal radar-revisit frequency on QPE performance of weather radar.

3.3 Conclusions for Balancing Data Quality and Atmospheric Revisit Time

Accurate observation of the atmosphere with weather radar depends on the revisit frequency applied to capture the multiscale evolution of microphysical processes and atmospheric dynamics. This chapter addresses the fundamental question of how frequently radars must sample the atmosphere for atmospheric science and applications with a focus on QPE. This analysis also sheds light on an important source of random errors associated with the revisit frequency of the atmosphere. The objective was to quantify the characteristic temporal scales relevant to describe precipitating systems and to estimate the minimum sampling intervals of radar observations required for QPE. High-resolution datasets were considered including PAR RHIs with unprecedented fast sampling, MRR and 2DVD disdrometer data. Using variograms within a geostatistics framework, the temporal structure of radar reflectivity was studied over the radars field of view and its uncertainty was linked to the sampling interval Δt over various temporal domains T related to applications, namely 5 min, 2 min and 30 s. These temporal domains were considered to assess the completion time of the WSR-88D volume coverage plan, MRMS mosaicked precipitation products and flash flood forecasting, and spaceborne observations of convective fluxes. The analysis was per-

formed for two different cases of convective precipitation observed by the Horus PAR with two different radar beamwidth settings. The uncertainty was shown to increase with the Δt, the magnitude of the rain rate, and the and the radar resolution volume size. Variogram analysis revealed that a significant portion of reflectivity decorrelation times below the melting layer fall below the sampling revisit intervals used for operational WSR-88D volume coverage plans and MRMS. The variability of reflectivity within Δt is therefore a significant source of uncertainty that can exceed the ± 1 dBZ specification for operational WSR-88D systems. Sampling intervals under 30 s are generally needed to keep reflectivity uncertainty below 15%. Since QPE in this work relies on a power-law relationship with reflectivity, QPE uncertainty depends on both sampling interval and precipitation intensity. This uncertainty can help benchmark the minimum radar revisit frequency needed for hydrometeorological applications. Overall, QPE up to 5 mm/hr requires sampling intervals less than 1 minute, while QPE above 5 mm/hr requires sampling intervals below 30 s. The impact of temporal sampling uncertainty on QPE performance through the coefficient of determination was examined with PAR data and further confirmed using MRR observations collocated with an exogenous precipitation reference from the 2DVD disdrometer.

The analysis framework described in this chapter can be applied to any application of weather radar data. A novel aspect is the use of temporal domains that are defined by applications instead of instrument sampling characteristics and limitations. It allows us to identify trade-offs between instrument volume coverage plans and applications that have error requirements on radar variables or derived quantities such as precipitation rates. A temporal analysis is particularly useful to define system specifications in general and as replacement options are being considered for the next generation of weather radars in the U.S. in particular. Preliminary results from this analysis suggest the need for faster sampling of the atmosphere than NEXRAD achieves.

This chapter focused on the fundamental radar variable Z. Future work will consider other polarimetric radar variables such as Z_{dr}, K_{dp}, and A which have been shown to improve precipitation rate estimation (Ryzhkov et al. (2022)). Also, it is essential that events are representative of the expected variability, both in terms of dynamical behavior and hydrometeorological diversity. While the convective events considered are characterized by relevant variability, the approach in this study will be applied to more cases to increase the representativeness of the results.

While this chapter has focused on the uncertainties introduced by discontinuous temporal sampling, another key limitation of traditional QPE approaches lies in their spatial representation of precipitation. In heterogeneous or rapidly evolving weather systems, coarse spatial resolution and inconsistencies in observation coverage can obscure localized extremes or introduce spatial biases. These biases are reduced with the added sampling provided by phased array observations of the atmosphere. Furthermore the pseudo-continuous spatial continuity from phased array offers the opportunity for flux observations, previously unresolvable, to enhance QPE by the consideration of advection in 3D and enables direct estimates of process rates in the atmosphere. This is especially useful in regions with strong spatial gradients in precipitation and heavy process influence such as convective storm environments. The following chapter explores these spatial enhancements to QPE and process rate estimation, examining how improved spatial sampling can be utilized to reduce spatial uncertainty and yield more accurate and reliable precipitation estimates.

Chapter 4

Space Continuity:

QPE Improvements

4.1 Continuity Equation for Radar-Estimated Mass

The central scientific question guiding the PROWEX field campaign is whether high-temporal-resolution, 3D observations of polarimetric radar variables, together with radial velocity estimates derived from PAR data or other instruments, can be combined to achieve an approximate closure of the continuity equation for radar-observed condensed water mass. Addressing this question carries important implications for precipitation science, hydrometeorology, and hydrology. In particular, it offers potential improvements to QPE by accounting for wind-driven advection effects, and it supports deeper insight into microscale atmospheric processes through the quantification of process rates (p), defined here as the sources and sinks of condensed hydrometeor mass within the radar-sampled atmosphere. The continuity equation, stemming from mass conservation, underpins many models that describe motion across synoptic, mesoscale, and microscale regimes (Adamiec-Wójcik et al. (2022)). A derivation of this equation for a finite volume representative of a radar resolution volume is provided in Appendix 8.1 to formalize its application to radar-detectable condensed water. For context it should be noted that the NASA INCUS satellite project, which will attempt to ob-

serve temporal changes in reflectivity through a train of satellites, assumes that process rates are a constant (Stephens et al. (2019)). This work attempts to estimate process rates, p, at high temporal resolution rather than assuming them to be constant.

As discussed in Section 2.4, current operational dish radars such as the WSR-88Ds sample the atmosphere only intermittently in space and time. The resulting polarimetric variables provide indirect information about the shape, size, composition, and number concentration of hydrometeors within the grid of radar resolution volumes covered by the VCP. These quantities are measured as integrated values within the illuminated resolution volume. The dimensions of each resolution volume depend on sampling parameters, including elevation angle, beamwidth, atmospheric refraction, and distance from the radar.

For QPE applications, the radar variables measured aloft within the VCP grid are empirically related to surface precipitation rates, such as rain or snow rate, through established retrieval relationships (e.g., Ryzhkov et al. (2022)). In practice, however, the observations collected aloft are more directly tied to hydrometeor water content than to precipitation rate because hydrometeor vertical velocities and effects of wind advection are unknown, making the connection to surface precipitation necessarily indirect. Moreover, due to the intermittent spatial and temporal sampling of dish radars, each radar resolution volume is treated independently of others for QPE.

PARs, owing to their rapid electronic beam steering, provide much higher temporal and spatial VCP sampling densities within evolving weather systems than legacy operational radars. Because all-digital PARs can generate high-quality, simultaneous vertical profiles of polarimetric variables and radial velocity independent of the pedestal's azimuthal rotation rate, they eliminate the time normally required to reposition the radar to a new elevation after each azimuthal sweep in a volume scan. This enhanced sampling capability opens the possibility of detecting previously unobserv-

able microphysical signatures and fluxes—namely, rates of change in time, altitude, and horizontal space. Such signatures may be represented as temporal, vertical, or horizontal derivatives of radar variables, or as derivatives of mass retrievals derived from those variables.

These unique derivatives of radar variables obtainable from PAR, hereafter referred to as PAR variables, are hypothesized to contain distinctive signatures of microphysical processes that can be leveraged to improve QPE, both as predictive inputs and through process classification. A process-informed estimation approach, grounded in the continuity equation, can further refine QPE by classifying the atmospheric processes in play. This extends QPE improvements beyond those achieved through hydrometeor classification alone. For example, Paulitsch et al. (2009) improved QPE by selecting different Z–R relationships based on the identified hydrometeor class (e.g., snow, rain, or hail). We will demonstrate a similar approach by selecting different rain rate estimators based on the identified process regime (e.g., collision-coalescence, drop breakup, or evaporation).

Due to the Horus development timeline described in Section 2.3.1, the initial exploration of the usefulness of the PAR-derived variables for QPE was conducted using vertical profiling techniques. This exploration began with the use of a MRR to observe radar reflectivity profiles, followed by fast-scanning RHIs collected by Horus. Both observation strategies enable the derivation of PAR variables from the temporal ($\frac{d}{dt}$) and vertical ($\frac{d}{dh}$) derivatives of radar-observed quantities, which are then related to surface precipitation rates. Because QPE ultimately aims to estimate precipitation at the ground, where hydrological applications, flood forecasting, and validation datasets are defined, it is essential to understand how these PAR variables translate to surface rates. Using the profiling techniques, how strongly the derived variables correspond to surface precipitation is examined, and the extent to which incorporating their temporal

and vertical variability into R estimation techniques improves QPE is assessed using correlation and bias metrics.

Recognizing that PAR systems may not become operationally widespread for another 10 to 15 years, as was highlighted in Chapter 1, profiling techniques are alternative observational strategies that could enable derivative-based approaches to study atmospheric processes and enhance QPE in the interim. Finally, Building upon the demonstrated efficacy of PAR-derived variables for improving QPE, we next present results from the final PROWEX observations collected on June 3, 2025, which address the core scientific objectives of the field campaign.

4.2 Evaluating Continuity-Based Observables for QPE

This section investigates how measurable components of the atmospheric continuity equation can inform and improve QPE by using derivatives of radar variables dZ/dt, dZ/dh, dZ_{dr}/dt, dZ_{dr}/dh, dK_{dp}/dt, or dK_{dp}/dh as fingerprints dm/dt and dm/dh, which were derivatives used in the continuity equation in Appendix 8.1. Two complementary studies are presented that rely on measurements of vertical profiles.

The first study uses MRR data to examine how temporal and vertical derivatives of radar reflectivity relate to surface precipitation rates, demonstrating, via vertical profiles, the benefits of pseudo-PAR variables for QPE. We use the term pseudo-PAR variables for the MRR because its observations differ fundamentally from Horus in both look angle (vertical for the MRR versus 20° elevation for Horus) and operating frequency (K-band versus S-band) but are also comparable because an ideal PAR system would provide very fast RHI observations over the volume, or in other words, would provide vertical column measurements within the field of view of the radar.

The vertical-profile analysis is also qualitatively compared with an S-band SBM model run to verify that derivatives of radar variables exhibit a consistent relationship with surface precipitation rates in both observations and simulations.

The second study, using PAR observations from Horus, extends the PAR variable demonstration to S-band RHIs, using $\frac{d}{dt}$ and $\frac{d}{dz}$ derivatives of reflectivity for vertical columns along the range in the radar's field of view. These are also used to demonstrate QPE enhancement as well as process classification according to existing literature mapping slopes within the vertical column to processes occurring in the atmosphere (e.g., Kumjian et al. (2022)). Together, these analyses evaluate the practical value of PAR variables for improving precipitation estimation.

4.2.0.1 Radar Measurements and Derived Continuity Observables

4.2.0.1.1 MRR Observations and 1D SBM Simulations To investigate the potential of derivative-based radar observables for QPE, data from the 1D NOAA/CIWRO SBM model and a vertically pointing MRR were examined. Limited availability of Horus PAR data, under development at the time of this study, motivated the use of a simulation and the MRR as a proxy for PAR. This approach enabled the exploration of QPE improvement through vertical and temporal derivatives d/dt and d/dz. This study is motivated by the following guiding questions:

1. Is there a visible relationship between R and time and height derivatives of radar observables, since these derivatives are indirect contributors to surface rain rate according to the continuity equation?

2. Can R estimation be improved by considering time and height derivatives of radar observables in addition to or alongside traditional polarimetric radar returns?

To obtain evidence to address these questions, we consider both the 1D SBM simulation

and the MRR observations. The simulation includes tunable parameters for temporal and vertical resolution; for this study, we use a time resolution of 1 s and a vertical resolution of 200 m. The MRR provides high temporal and vertical continuity at K-band using a vertically pointing beam with a 200 m range resolution to match the resolution of the simulation, but a 1-min temporal resolution after standard post-processing. It also has a narrow 3 dB beamwidth of about 1.5°, such that the horizontal diameter of the considered volume of space at 600 m, for example, is approximately 16 m, increasing with distance from the radar (Basics (2009)). Both the simulation output and the MRR measurements are vertical profiles, and examples of pseudo-PAR measurements.

The MRR is a frequency-modulated continuous-wave (FMCW) radar operating at 24 GHz (Basics (2009)). Its modulation scheme enables discrimination of both the velocity and linearly polarized reflectivity of falling hydrometeors in a vertical column above the radar.

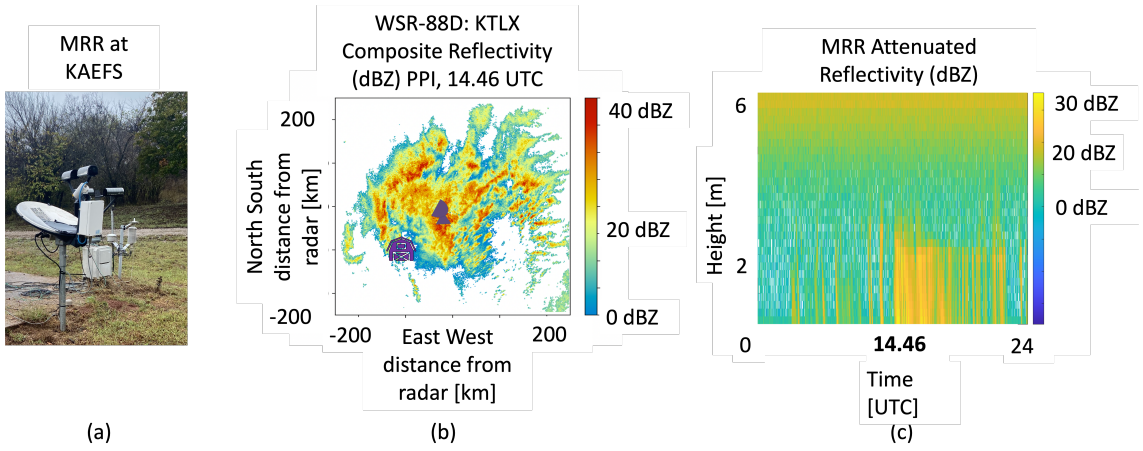


Figure 4.1: A pseudo-PAR case study conducted on October 25, 2019, using a 24 GHz FMCW Micro Rain Radar co-located with a 2DVD disdrometer and two Parsivel2 disdrometers at KAEFS. The time-resolution of both measurements was 1-minute. (a) Photograph of the measurement site, (b) KAEFS location (farm icon) on WSR-88D composite reflectivity plot with radar site shown by a radar icon, and (c) 24-hour MRR attenuated reflectivity time–height plot.

The simulation with the SBM model considers hail falling and melting in a downdraft starting at a defined 4 km altitude 0° C isotherm. Microphysical fields, including the PSD, R, and polarimetric radar variables (at S-band), were simulated over altitude and time and extracted at 600 m altitude above the surface. Because the focus of the later analysis is on Z-based estimators, only the simulated Z is retained for comparison with the MRR observations. Figure 4.2 shows the simulated Z field in several forms: contours of Z versus altitude and time (Figure 4.2d), the time series of Z and R at 600 m (Figure 4.2e), and a CFAD summarizing the mean, 25th, and 75th percentiles of reflectivity over the first 800 s of the simulation of falling and melting hail before it converges to steady-state profile behavior (Figure 4.2f). Figures 4.2e–f serve to indicate which dimensions PAR variables (derivatives) are derived over; for example, Figure 4.2e has an arrow along the time dimension over which it dZ/dt is derived, and Figure 4.2e shows a dashed line along the slope of the Z profile, the slope of which is dZ/dh at the altitude indicated by the dashed line. These same estimation procedures will be applied to the MRR observations; however, no direct one-to-one comparison between the two datasets is intended. Rather, each dataset is examined independently to determine whether both exhibit a relationship between rain rate and the Z derivatives.

For the observational MRR component, a warm-rain case from October 25, 2019, taken at KAEFS, was selected wherein the MRR was co-located with a Parsivel2 disdrometer (NOAA Physical Sciences Laboratory). Figure 4.1a shows a picture of the MRR instrument with disdrometers pictured behind it. Figure 4.1b shows the measurement site, with KAEFS marked by a farm icon and the WSR-88D KTLX radar 45 km northeast indicated by a radar icon. A 24 hr time–height plot of MRR Z is also provided in Figure 4.1c to illustrate the vertical structure of precipitation over the course of the day in 1-min increments. As with the simulation output, the MRR

Z field serves as the basis for applying Zgradient estimation techniques, enabling an assessment of whether similar qualitative relationships emerge in both simulated and observed conditions, without implying that they can be compared in a consistent or quantitative manner.

The spatial and temporal continuity of the MRR allows the extraction of pseudo-PAR variables: dZ/dt and dZ/dh. These were derived for the full day of MRR observations at an altitude of 600 m to examine their utility for R estimation. Figure 4.2 presents Z extracted at 600 m altitude (Figure 4.2a), an overlay of MRR Z and disdrometer-observed R over the 24 hr period (Figure 4.2b), and a CFAD of reflectivity showing the mean, 25th, and 75th percentiles (Figure 4.2c). Note that the MRR observations and the 1D SBM simulation differ widely in terms of microphysics and radar frequencies.

For both the simulation and the MRR observations, $Z - R$ relationships were consistently established using the probabilistic QPE approach described in Kirstetter et al. (2015a). Probabilistic QPEs such as these are modeled from the conditional distribution of R for combinations of the predictors Z, dZ/dt and/or dZ/dh. For each tested combination of predictors, the conditional distribution is estimated within a simple supervised learning model to derive a temporally continuous mean and standard deviation. The distribution is assumed to have the same parametric form for all predictor values within a given set of predictors using the generalized additive models for location, scale, and shape approach (GAMLSS) as the supervised learning approach (Rigby and Stasinopoulos (2005)). It should be noted that this supervised learning approach performs a The most appropriate probabilistic model for the estimator is identified by investigating different parametric density fits (e.g., normal, lognormal, gamma, Weibull, logistic, etc.) with a goodness of fit. Consistent with Kirstetter et al. (2015a), the lognormal distribution was selected as the most appropriate for estimating

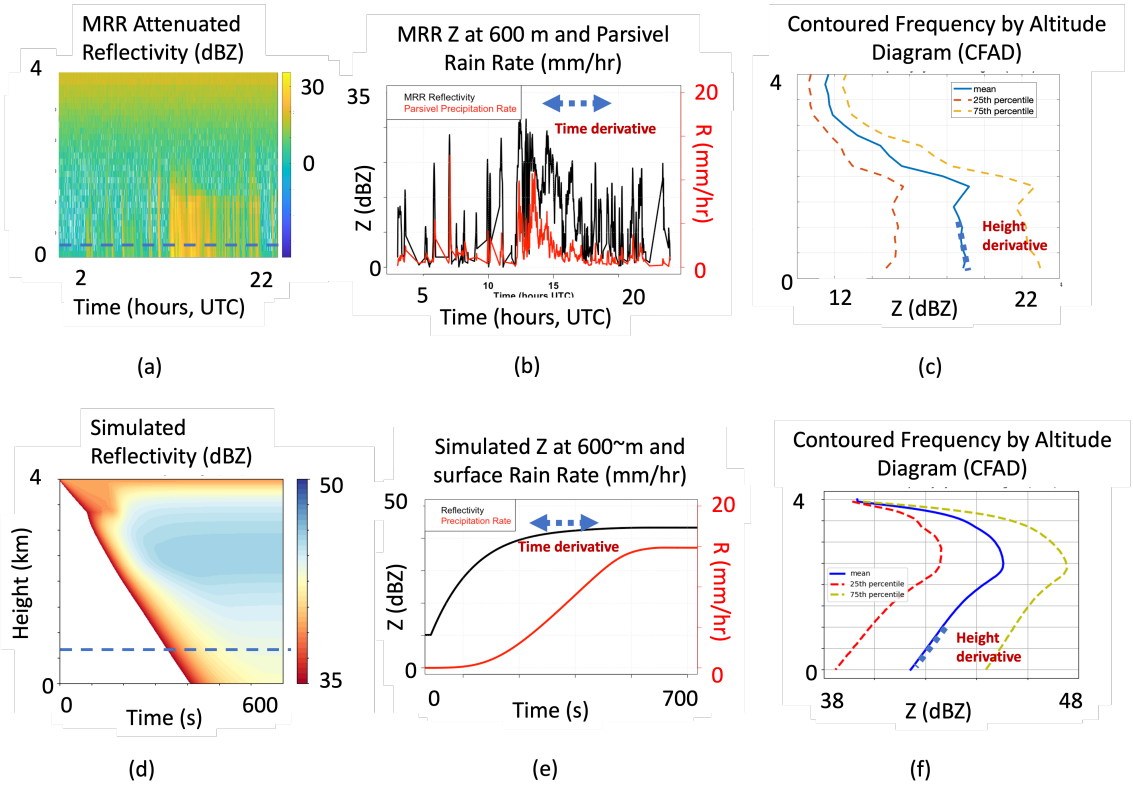


Figure 4.2: (a) The 600 m altitude at which MRR reflectivity values are extracted. (b) Overlay of MRR reflectivity and disdrometer-observed R over 24 hours. (c) CFAD showing mean, 25th, and 75th percentiles of reflectivity for the day, illustrating precipitation behavior in the time and altitude derivatives of Z. (d) Horizontally incident T-matrix–derived Z outputs at S-band from the 1D SBM for hail melting in a downdraft from 4 km to the surface over 700 s. (e) Comparison of Z extracted at 600 m with ideal surface rain rate values, and CFAD of simulated Z over 700 s.

precipitation. Various probabilistic regression models, corresponding to different sets of predictors, were fit to create R estimators from observed MRR and simulated Z derivatives. Once a probabilistic model is fitted for the MRR or simulated data, the expectation value is computed as a function of predictors for comparison with surface R. Four metrics were computed: bias, defined as the normalized difference between the expected value of the estimator and the true R; the correlation between estimated and true R; the explained variance, defined to be the square of the correlation coefficient; and an uncertainty variable, Δ, defined as the normalized difference between the 75th

and 25th percentiles of the probabilistic estimate, following the method of Kirstetter et al. (2015a). Note that for the simulated case, the rain relations exhibited a nearly deterministic character, as is shown in Table 4.1, yielding perfect correlation with rain rate values and low bias, variance, and uncertainty.

Using the MRR dataset, R estimators were derived from Z, dZ/dt, and/or dZ/dh. A quantitative summary of estimator performance for all predictor combinations is provided in Table 4.1. Each row corresponds to a distinct regression configuration, showing bias, correlation, explained variance, and uncertainty for both simulated and observed cases. Various studies have examined radar and gauge rainfall at high temporal resolution, reporting correlations at the 1-minute timescale typically ranging from 0.6 to 0.85, depending on rainfall type and spatial sampling (e.g., Brommundt and Bárdossy, 2007; Mandapaka et al., 2009). Here it is shown that the inclusion of derivative terms clearly improves model performance in terms of the metrics of correlation, explained variance, and uncertainty. Including the height derivative reduced estimator bias and uncertainty while increasing correlation and explained variance compared to using Z as the only estimator predictor. Incorporating the time derivative further improved correlation and reduced estimator uncertainty, though a slight underestimation bias was observed. This analysis demonstrates that for the considered MRR observations, derivative-based predictors capture meaningful information about precipitation evolution that is not present in instantaneous Z measurements alone.

To further suggest the benefit of derivatives, Figure 4.3 shows the relationship between dZ/dh (x-axis) and MRR estimated R (y-axis) for both the observed and simulated datasets representing distinct environmental conditions and radar operating bands. The black dots in the figure represent collocated MRR R estimates with height derivatives of MRR Z for October 25, 2019. The blue curve corresponds to a supervised learning fit with GAMLSS to the collocated measurements represented by black

Table 4.1: Performance of MRR R estimators using different combinations of Z the temporal and vertical derivatives of Z.

Estimator Variables	**Bias**	**Correlation**	**Explained Variance**	**Uncertainty (Δ) [%]**
Z only	0.24	0.67	0.45	70.78
$Z + \frac{dZ}{dh}$	0.03	0.72	0.52	66.17
$Z + \frac{dZ}{dt}$	0.61	0.68	0.46	69.42
$Z + \frac{dZ}{dt} + \frac{dZ}{dh}$	-0.28	0.73	0.53	64.92
Z_{sim} (SBM reference)	0.00	1.00	1.00	0.00

dots for the warm-rain event observed at KAEFS. The red curve is plotted for comparison, representing a similar GAMLSS fit for the simulated hail-melting downdraft case from the spectral bin microphysics model, though the collocated measurements for this simulated case are not included in the black scatter plot within the figure. Both curves exhibit a decreasing power-law dependence between R and dZ/dh. This preliminary result suggests a physical consistency between the derivative-based estimators across contrasting precipitation regimes. The agreement between observed and simulated relationships also suggests the potential transferability of derivative-based QPE approaches.

Taken together, these findings show that a relationship does exist between precipitation rate and the time and height derivatives of radar observables, consistent with their role as indirect contributors to surface R through the continuity equation. However, the observations and simulations do not display close quantitative agreement, nor should they be expected to: the simulation represents melting hail within a downdraft, whereas the observational case is a warm-rain process. Because these environments and microphysical regimes differ, the derivatives of reflectivity naturally exhibit different magnitudes and shapes; for example, the simulated melting hail case produces sharper vertical reflectivity decreases associated with phase change and drop shedding. Even so, both cases exhibit qualitatively similar behavior in how height derivative signatures

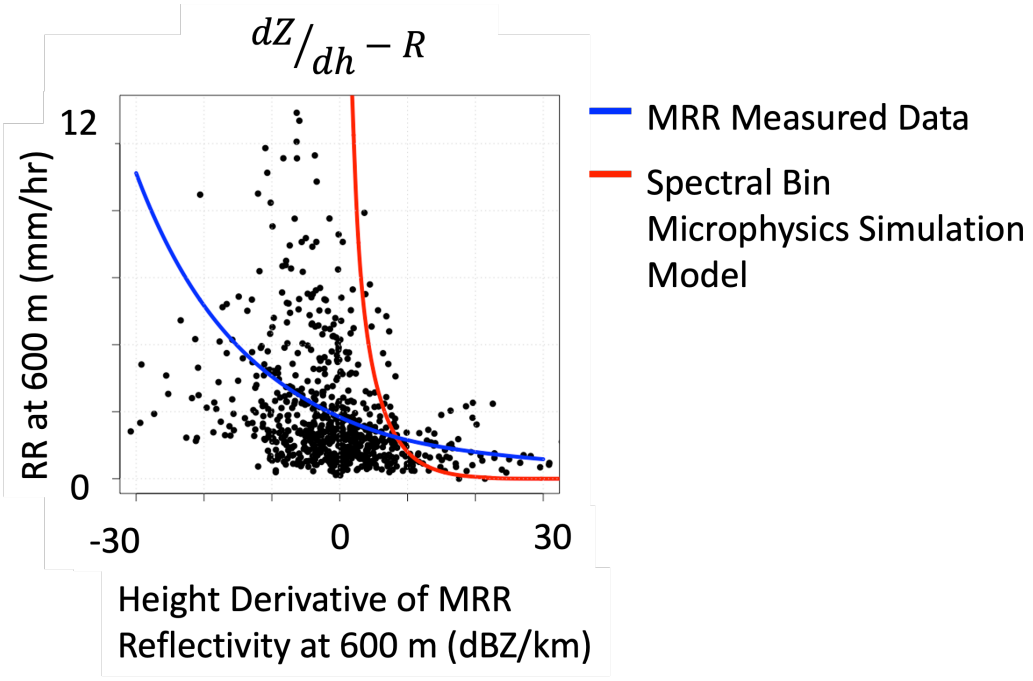


Figure 4.3: Comparison of the relationship between reflectivity height derivatives and R for observed (blue) and simulated (red) datasets. Both exhibit a power-law dependence, illustrating the consistent physical relationship between reflectivity gradients and rainfall intensity across distinct regimes. The observed curve corresponds to the warm-rain event at KAEFS, while the simulated curve corresponds to the hail-melting downdraft case from the SBM model.

relate to changes in rain rate, suggesting an underlying physical link even when the cases differ. Precipitation estimation can be improved by incorporating Z derivatives, but the degree of improvement and the specific derivative–R relationship will depend on the storm structure and environment which influence precipitation microphysics. This also implies that extending pseudo-PAR methods like these to PAR systems is promising, provided that environmental variability and microphysics are considered when developing and applying operational predictors.

Variable	Symbol	Units	Type
Reflectivity	Z	dBZ	Polarimetric Variable
Time derivative of reflectivity	$dZ/_{dt}$	dBZ/s	Time Derivative (PAR Variable)
Altitude derivative of reflectivity	$dZ/_{dh}$	dBZ/km	Altitude Derivative (PAR Variable)
Differential Reflectivity	Z_{DR}	dB	Polarimetric Variable
Time derivative of differential reflectivity	$dZ_{DR}/_{dt}$	dB/s	Time Derivative (PAR Variable)
Altitude derivative of differential reflectivity	$dZ_{DR}/_{dh}$	dB/km	Altitude Derivative (PAR Variable)
Specific differential phase	K_{DP}	degree/km	Polarimetric Variable
Time derivative of specific differential phase	$d\mathrm{K}_{DP}/_{dt}$	degree/(km*s)	Time Derivative (PAR Variable)
Altitude derivative of specific differential phase	$d\mathrm{K}_{DP}/_{dh}$	degree/km^2	Altitude Derivative (PAR Variable)
Precipitation Rate or Rain Rate	RR	mm/hr	Surface in-situ measurement

Figure 4.4: Table listing the PAR variables referenced in this section and their notations

4.2.0.1.2 PAR RHI Measurements Building on the vertical profiling analysis with the MRR, data from OU's prototype all-digital PAR, Horus, were analyzed when the radar had 13 panels and conducted experiments in a single-azimuth-RHI mode on August 8, 2023. While the MRR provided vertically continuous profiles at a single location, these PAR data enable sampling in both space (range and altitude) and time at one azimuth pointing angle. In addition to polarimetric variables, the time and altitude derivatives of polarimetric variables can be obtained, making up a set of unique PAR variables. This work analyzes the efficacy of these variables for predicting R using the first pencil-beam RHI observations collected by a ground-based PAR and probabilistic R estimators to show that precipitation prediction can be improved with PAR observations.

4.2.0.1.3 Microphysical Process Classification with Phased Array Radar A new set of PAR variables are proposed here for QPE that are derived from the

radar Z, Z_{DR}, and K_{DP}. These polarimetric and radar observations carry information about hydrometeor shapes, sizes, orientations, and phase. Z is proportional to the returned power of the horizontally polarized wave from the radar because hydrometeor size changes occur more visibly in the horizontal dimension, i.e., raindrops become more oblate as they become larger. In the radar sampling volume, Z is measured as the sum of all particles scattering so Z depends on the particles' number density, as has been described in Appendix 7. Yet it is most sensitive towards the larger particles that dominate the backscattering of the radar signal, because backscattering's dependency on size is higher than its dependency on the total number of particles. Z_{DR} provides an indication of the raindrops' shapes (hence sizes). Z_{DR} is positive for a population of oblate (large) raindrops with their maximum dimension oriented in the horizontal on average. Z_{DR} is near 0 dB for spherical (small) particles or non-spherical particles randomly oriented in the radar resolution volume. Note that as for Z, the contribution to Z_{DR} is dominated by larger particles in the radar volume. Unlike ϕ_{DP} which is cumulative along the radial path from the radar, K_{DP} involves is non-cumulative along the path since it is a range derivative of ϕ_{DP}. K_{DP} is positive for a population of oblate raindrops with their maximum dimension oriented in the horizontal on average. Small spherical particles have no contribution to K_{DP} unless their concentrations within the resolution volume are polarized to favor one dimension over another.

The evolution of polarimetric variables in vertical sets of radar resolution volumes (i.e., over a few kilometers in altitude) has been used to infer the occurrence of precipitation processes influencing populations of scattering particles falling towards Earth's surface (e.g., Ryzhkov et al. (2008), Kumjian et al. (2012), Carr et al. (2017), Porcacchia et al. (2017), Porcacchia et al. (2019), Kumjian et al. (2022)). Microphysical processes modify particle sizes and shapes, number densities, phase, and compositions, to which the polarimetric radar variables are sensitive and translate into signatures in

terms of vertical modifications. Hence, changes in the vertical profiles of polarimetric variables can be related to liquid and solid phase processes. For example in warm rain, size sorting and evaporation are both indicated by an increasing Z_{DR} and decreasing Z and K_{DP} towards the surface. Both processes lower the number densities of smaller drops, hence a mass shift toward larger drops in a given PSD, which leads to an upward shift in the mean drop size and Z_{DR}, while the water content loss lowers Z and K_{DP}. Drop breakup is indicated by a decrease in Z_{DR}, Z, and K_{DP} towards the surface as a result of large drops breaking apart into smaller drops (i.e., lower Z given its higher dependency on larger drops) that are also more spherical (i.e., lower Z_{DR} and K_{DP}). Collision-coalescence is indicated by increasing Z, Z_{DR} and K_{DP} towards the surface because an initial PSD characterized by a higher concentration of smaller drops sees drops collide and coalesce to form larger drops as they fall. While the total number of raindrops (number of concentration) decreases and the mass content is preserved in the PSD, the occurrence of larger and more oblate drops shift Z, Z_{DR} and K_{DP} towards higher values (Kumjian (2012)).

It is hypothesized that altitude derivatives of radar variables, which can be uniquely derived from dense PAR observations, capture signatures of evolving PSDs under the influence of precipitation microphysical processes: dZ/dh, dZ_{DR}/dh, and dK_{DP}/dh. These PAR variables are listed in Table 4.4 alongside standard radar variables Z, Z_{DR}, and K_{DP}.

Note that in reality microphysical processes in the atmosphere occur simultaneously and are often mixed within a radar resolution volume. In some precipitation regimes a process can be dominant and identifiable through its signatures (e.g., collision-coalescence in tropical cyclones (Brauer et al. (2022), Brauer et al. (2024))), while in other cases the signatures of simultaneous processes can be obscured in the vertical changes of radar variables. It can be expected that such signatures depend on the spa-

tial and temporal domain over which the vertical changes are computed and assessed. Thanks to denser spatio-temporal sampling, PAR offers the opportunity for researchers to identify signatures over smaller domains than dish radars. Significant averaging or toleration of sample time separation is required to extract process signatures from discontinuous observations of dish radars, for example, via a quasi-vertical profile (QVP) or a columnar vertical profile (CVP) (Murphy et al. (2020), Ryzhkov et al. (2016)). The QVP is composed of altitude samples formed from azimuthal averages for each range gate of a radar beam. It requires an assumption of horizontal hydrometeor characteristics and process homogeneity when considering vertical variations in the atmosphere. The CVP is formed utilizing aligned range gates at a given horizontal location from azimuthal revolutions at various elevation angles collected during the course of a VCP. Because a VCP for currently operational radars like the WSR-88Ds can take on the order of 5 min to complete, there is also an assumption that processes are nearly static within the VCP coverage time. In short, with QVP or CVP methods, the evolution of a given radar variable as a function of the altitude requires collecting data over a space–time domain that is typically hundreds of square kilometers in area and tens of minutes in duration, along with an assumption of homogeneous precipitation physics within the considered field of view and over the temporal sampling period, so variability around the profile may be masked. It has been a major limitation of vertical profiles of reflectivity techniques over the last three decades (Kirstetter et al. (2013)). Averaged vertical profiles capture large-scale microphysical and dynamic processes but lack the temporal and spatial resolution required to understand fine-scale processes, particularly for high-impact or convective weather events.

Building from PAR's dense vertical sampling, height derivatives of polarimetric radar variables such as dZ/dh, dZ_{DR}/dh, dK_{DP}/dh can capture signatures of microphysical processes at scales that are several orders of magnitude finer than with dish

radars, i.e., typically 0.25 square kilometers in area and less than 10 s in duration. Their sign and magnitude are hypothesized to provide relevant information for QPE. For example, as mentioned previously, negative dZ/dh, dZ_{DR}/dh, and dK_{DP}/dh can indicate the occurrence of collision-coalescence, as these values increase towards the surface, especially when observed along with moderate values of Z, Z_{DR}, and K_{DP} that are typically observed for PSDs with a higher concentration of smaller drops (Carr et al. (2017)). This process can be captured by a PAR even when the process is highly localized in area and rapidly changing. Furthermore, PAR can provide insight into time tendencies and microphysical fluxes through the capture of time derivatives of observed radar variables.

Precipitation rates computed from mechanically scanning radar observations over coarse temporal domains are also subject to uncertainties due to unobserved atmospheric evolution and horizontal wind advection because precipitation rates are determined from radar returns aloft and mapped to a value for R at the surface using empirical relations. In particular, they do not provide the pseudo-instantaneous depiction of the vertical structure required to capture rapidly evolving processes that can be associated with extreme weather events and that work to modify the PSD below the observation altitude of the radar. This can explain part of the discrepancies noticed between radar QPE and rain gauges at short time steps as mentioned in Chapter 3. While temporal changes of radar variables have not been as extensively explored as their spatial changes, Stephens et al. (2019) recently investigated how changes in Z over time periods Δt ranging from 30 s to 120 s relate to fluxes of water and air in deep convection.

This concept has been a scientific basis for the launch of NASA's INCUS mission (Dolan et al. (2023)). By extension, it is postulated in this work that rates of changes of radar variables measured in a radar sampling volume provide information about PSD

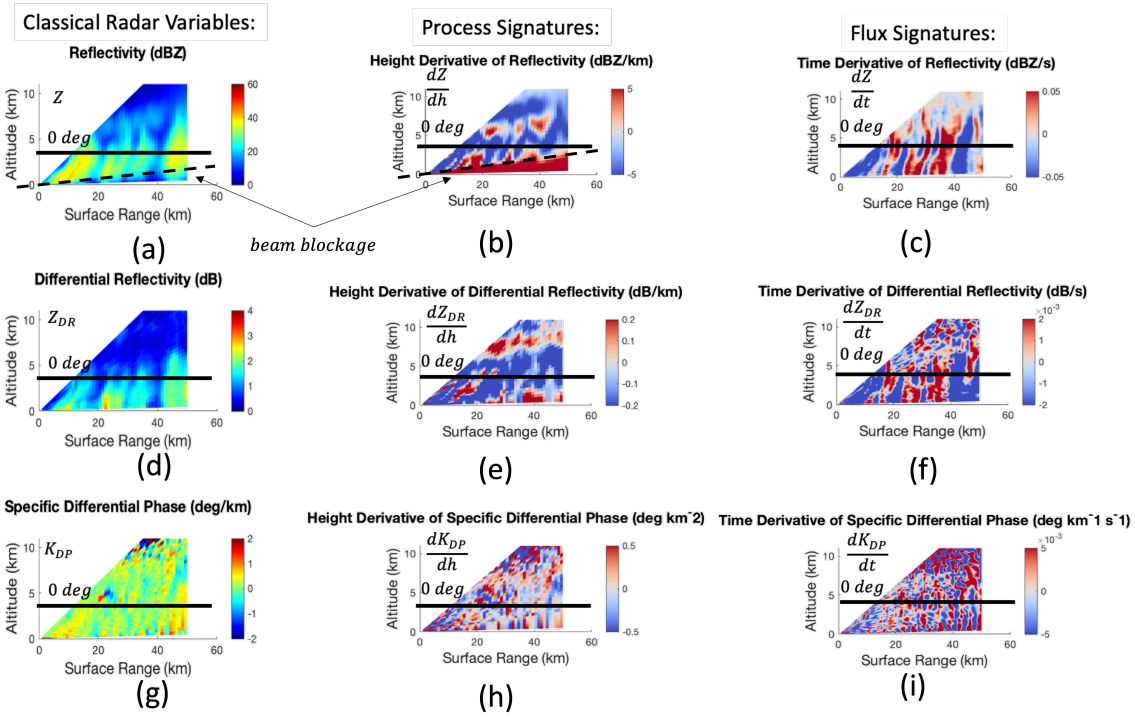


Figure 4.5: Radar variables (a) Z, (d) Z_{DR}, and (g) K_{DP} (left column) as well as their altitude derivatives (center column; (b) dZ/dh, (e) dZ_{DR}/dh, and (h) dK_{DP}/dh) and their time derivatives (right column; (c) dZ/dt, (f), and (i) dK_{DP}/dt) from time 10:19:61 UTC on August 8, 2023 near Norman, Oklahoma. The 0° C isotherm is marked by a horizontal black line at 4.5 km in altitude. An angled dashed black line marks a zone of near-surface beam blockage in sub-figures a and b. All variables are considered to be quasi-continuous in space and time; each RHI scan is completed within 16 s.

rates of change from advection (flux) through the volume and precipitation processes acting within the volume to change the observed PSD. PAR time derivatives of polarimetric variables, dZ/dt, dZ_{DR}/dt, and dK_{DP}/dt, computed over time intervals shorter than 30 s, are also hypothesized to capture the occurrence of rapidly evolving processes and mass fluxes. For example, dZ_{DR}/dt relates to the rate of change of particle shapes and sizes in the radar volume.

Figure 4.5 shows polarimetric variables and their derivatives collected by the Horus radar on August 8, 2023, near Norman, Oklahoma. A columnization technique was developed to generate these plots such that radar variables are averaged within a chosen

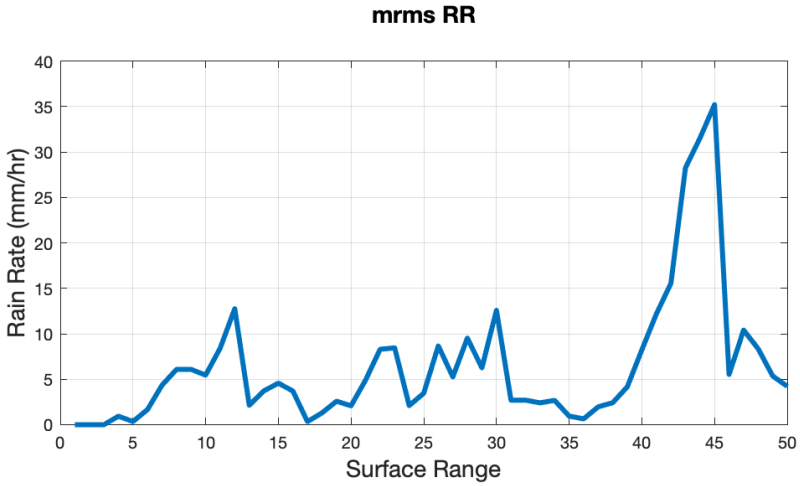


Figure 4.6: MRMS surface precipitation rate collocated with the radar variables and their derivatives is shown in Figure 4.5 at 10:18 UTC.

spatial distance at a discrete number of points from the radar. The variables were columnized in 1 km steps from 0 to 50 km in range from the radar. This provides vertical columns over which the altitude derivative and time derivative are taken. A notable takeaway from Figure 4.5 is that altitude and time derivatives of radar variables can be quasi-continuously computed in space and time as new PAR variables. Horus RHI scans were collected with 60 elevation angles ranging from 0.5 to 31.5 °every 16 s over a measurement period of 18 min. Altitude derivatives are computed over radar resolution volumes separated by about 0.3 km in altitude at a range of 30 km from the radar. Time derivatives are computed over moving time windows of 80 s updated every 16 s. The leftmost column of Figure 4.5 shows a snapshot of the radar variables within the full considered measurement time period for a Horus RHI taken at 10:19:61 UTC. Figure 4.5a is a plot of Z over the altitude and range showing values up to 40 dBZ,

indicative of moderate rainfall (Austin (1987)). It is confirmed with collocated MRMS precipitation rates shown in Figure 4.6, which show maximum R values between 5 and 10 mm/hr for precipitation cells between 0 and 35 km from the radar. A heavier R maximum, up to nearly 35 mm/hr, is observed about 45 km from the radar. Z_{DR} in Figure 4.5d shows columns, albeit with values less than 3 dB, indicating moderately sized drops, that align with the local maxima in the collocated R values. In particular, the tallest Z_{DR} column is associated with the global R maximum noted at about 45 km from the radar in Figure 4.6. K_{DP}, shown in Figure 4.5(g), is derived by taking the range derivative of smoothed differential phase and shows vertical columns with values in the range 0.5–1 °/km that align with range values from the radar where the maxima in surface R occur.

An undesirable feature indicating partial beam blockage is present in this measurement and is visible below 2 km in altitude in Figures 4.5a and 4.5b (see the black dotted line). The region of partial beam blockage displays inconsistently low values of Z, high dZ/dh (decreasing Z toward the surface). Other observations are not impacted, e.g., Fig.4.5c, 4.5d, 4.5e, 4.5f, 4.5g, 4.5h, and 4.5i, because these measurements rely on measurement ratios or phase in range or time that mitigate the effect of partial blockage. For example, because the time derivatives of reflectivity dZ/dt are computed as differences in dBZ (equivalent to a ratio in natural scale), the impact of partial beam blockage is filtered out. This is a further advantage of the time resolution offered by PAR sampling.

Center panels in Figure 4.5 show the height derivatives of polarimetric variables. Each panel displays a spatial structure distinct from random noise that can be qualitatively interpreted in terms of signatures of precipitation processes. In particular, the sign of the altitude (height) derivatives of the radar variables can be used to infer microphysical processes occurring within the atmosphere, although caution is recom-

mended near the surface. A positive altitude derivative in Figures 4.5b, 4.5e, and 4.5h indicates that the corresponding radar variable is decreasing towards the surface, while a negative altitude derivative indicates that the radar variable is increasing in value towards the surface. For example, considering the liquid phase below the melting layer (assumed to be located near the 0° C isotherm) and above the partial beam blocking region, Figure 4.5b shows regions of negative dZ/dh indicating that reflectivity is increasing toward the surface. Figure 4.5h shows an RHI plot of dZ_{DR}/dh that also displays collocated negative values, which can be interpreted to mean that collision-coalescence is the dominant liquid-phase process (e.g., Kumjian et al. (2022)). Conversely, positive dZ_{DR}/dh, e.g., between 40 and 45 km in range where the maximum precipitation occurs as shown in Figure 4.6, indicates that Z_{DR} is decreasing towards the surface. As it is collocated with Z increasing towards the surface, it suggests that drop-breakup balances the effect of collision-coalescence. The dominant process of collision-coalescence is likely to occur for low-level convective conditions where the cloud base is low, limiting ice processes(Gupta et al. (2023)). The precipitation maximum at 10:18 UTC is located between 40 and 45 km in range from the radar (Figure 4.6) and collocated with the tallest Z, Z_{DR}, and K_{DP} columns in Figure 4.5. This is likely a convective and localized precipitation maximum where drops in the convective column grow large enough for drop breakup to contribute considerably alongside collision-coalescence. Following K_{DP} in Figure 4.5g, dK_{DP}/dh in Figure 4.5h shows higher spatial variability in vertical trends than the other PAR altitude derivatives. dK_{DP}/dh is also an in indicator of microphysical processes (Kumjian et al. (2022)). If advection is assumed to have a negligible effect, increasing values toward the surface (negative dK_{DP}/dh) can indicate that drops are becoming larger towards the surface, while a positive dK_{DP}/dh may indicate drops are becoming smaller under the influence of breakup. K_{DP} derivative variability helps to expose the presence of a mixture of pro-

cesses and process rates contributing to the final observed precipitation at the surface. It should be noted that K_{dp} estimation is challenging because ϕ_{dp} is a noisy radar return, not always monotonically increasing in range from the radar, leading researchers to develop nonstandard approaches for its computation (Aldana et al. (2025)). K_{dp} can then be noisy and subject to error as it is a derivative along range of ϕ_{dp}. Similarly, vertical and temporal derivatives of K_{dp} may also further propagate K_{dp} noise and errors. Thus, the interpretations of K_{dp} and associated derivative implications should be understood to be subject to uncertainty and should be interpreted judiciously.

The right panels in Figure 4.5 show the time derivatives of polarimetric variables. As with height derivatives, these variables also display organized structures that may reflect precipitation processes and fluxes as well as advection in the RHI plane. The sign of the time derivatives of the polarimetric radar variables indicates how the variables change with time as signatures of fluxes in the atmosphere. Figures 4.5c and 4.5f show the RHI of dZ/dt and dZ_{DR}/dt. Note that time derivatives display less impact from the partial beam blockage near the surface, especially dZ/dt. Consistent with convection, time derivatives display vertical structures that match surface precipitation. For example, if one considers the approximate local maxima of collocated precipitation in Figure 4.6, at 12 km, 30 km, and 45 km from the radar, and the local minima at 5 km, 20 km, and 40 km, zones of positive dZ/dt and dZ_{dr}/dt (increasing Z and Z_{DR} and associated precipitation fluxes) approximately align with local precipitation maxima, and zones of negative dZ/dt and dZ_{dr}/dt align with precipitation minima. dK_{DP}/dt in Figure 4.5i shows shorter scales of variations that are consistent with K_{DP} and its height derivatives. This indicates, for radar variables, that time derivative maxima may correspond to a maxima in precipitation, while time derivative minima may correspond to a precipitation minima. Considering the continuity equation, this may be true if advective wind components u and v are small relative to temporal

changes such that Equation (8.9) becomes

$$\frac{d}{dz}R = p - \frac{d}{dt}LWC. \tag{4.1}$$

Further neglecting the impact of p, this equation shows that a positive time derivative of LWC should be associated with a negative $\frac{d}{dz}R$, indicating that R increases towards the surface of the earth. It also indicates that a negative time derivative of LWC should be associated with a positive $\frac{d}{dz}R$, indicating that R decreases towards the surface of the earth. Since Z, Z_{dr}, and K_{dp} are related to LWC, the alignment of precipitation minima and maxima with these radar variables' minima and maxima may tend to correlate as long as the influence of advection and process rates on the minima and maxima have near-constant or small relative contributions in Equation (8.9).

4.2.0.1.4 Framework for QPE retrievals This work is motivated by the high spatiotemporal information content afforded by PAR and posits that new time and altitude derivatives of radar polarimetric variables have the potential to improve the accuracy of R estimates at the surface because they are fingerprints of microphysical processes and fluxes aloft. Quantitatively mapping radar variables to R should also quantify associated uncertainties, as weather radars provide indirect information on precipitation processes and fluxes (Neuper and Ehret (2019),Kirstetter et al. (2015a)). Following Kirstetter et al. (2015a), a probabilistic approach is used to describe the range and likelihood of possible surface R that are associated with radar returns. A probabilistic estimation conveys a most likely estimate of R along with the spread of possible values and likely extremes that are being observed based on the variability of the training dataset. This section outlines a framework for PAR probabilistic R retrievals, including a technique selected to objectively identify unique PAR variables for QPE. Probabilistic QPEs computed in this study are modeled to fit the distribution

of predictand values (R values) that align with a combination of PAR variables as predictors. For the sake of efficiency, the conditional distribution of R, given a set of PAR variables, is assumed to have the same parametric form for all PAR variables. Among various machine learning techniques, the generalized additive models for location, scale, and shape approach (GAMLSS) (Rigby and Stasinopoulos (2005)) is explored as the supervised learning technique used to build a framework for PAR QPE, providing the inputs of radar variables as well as their time and altitude derivatives as predictors. GAMLSS is a regression framework used to fit nonlinear probabilistic models between the distribution of a dependent variable, R, and a series of PAR radar variables as independent variables (Stasinopoulos and Rigby (2008)).

GAMLSS models the predictand distribution, R, with the following assumptions: (1) R is a random variable following a known distribution with density f($R \mid \mu$,σ) conditional on the parameters μ (location) and σ (scale) and (2) the observations R used for training are mutually independent given the parameter vectors μ and σ. Each parameter is a function of PAR variables using monotonic (linear or nonlinear) link functions. This work uses the package GAMLSS (Stasinopoulos and Rigby (2008)) in R (Team (2021)). The precipitation trends for each parameter of the distribution are fitted using penalized splines. To evaluate the most appropriate distribution model for R, a variety of two-parameter distributional forms (e.g., normal, lognormal, gamma, Weibull, logistic, etc.) were tested. The goodness of fit on the whole data set has been checked for each of the density fits by investigating the Akaike information criteria (AIC), computing the residuals, the first four moments, their Filliben correlation coefficient, and quantile plots (Stasinopoulos and Rigby (2008)). In accordance with previously observed precipitation properties (Kirstetter et al. (2015a)), the lognormal was consistently found to be the best overall distribution for surface Rs that ensures positive Rs when generating ensembles of precipitation and achieves a balance between

model complexity, accuracy, and efficiency:

$$R\left(R|\mu,\sigma\right) = \frac{1}{R\sqrt{2\pi}\sigma} e^{-\frac{\left(\ln R_{ref} - \mu\right)^2}{2\sigma^2}} \tag{4.2}$$

where $f(R)$ is the lognormal distribution and R is the predictand assumed to be a random variable with the mean μ and standard deviation σ of the random variables' natural logarithm.

Using the distributions, the location parameter μ is related to the deterministic component of the relationship between R and PAR variables, and the scale σ is related to the variability of this relationship. Both depend on the PAR variables. These models are compact and described with simple mathematical expressions, which minimizes computational costs.

Finally, a feature selection algorithm is implemented within an additive regression model that extracts from radar variables and their PAR-enabled time and altitude derivatives to select independent variables used in a final GAMLSS precipitation rate estimation model. A bidirectional stepwise GAMLSS regression is run across the dataset to construct a model step-by-step by the successive addition of PAR variables, testing the predictands estimated with various groups of predictors (PAR variables) for statistical significance after each iteration. Variable addition iterates until any further predictor addition leads to a detriment in the model performance. Thus the feature selection (or predictor selection) chooses the predictors that are the most important for estimating the predictand. This method of selecting a subset of PAR variables for the R estimator is shown to improve the estimation of R over the use of polarimetric variables on their own via a case study using PAR measurements.

Figure 4.7 illustrates the relationship between the rainfall rate R and PAR variables. This relationship is best characterized as a *gray box* rather than a black box,

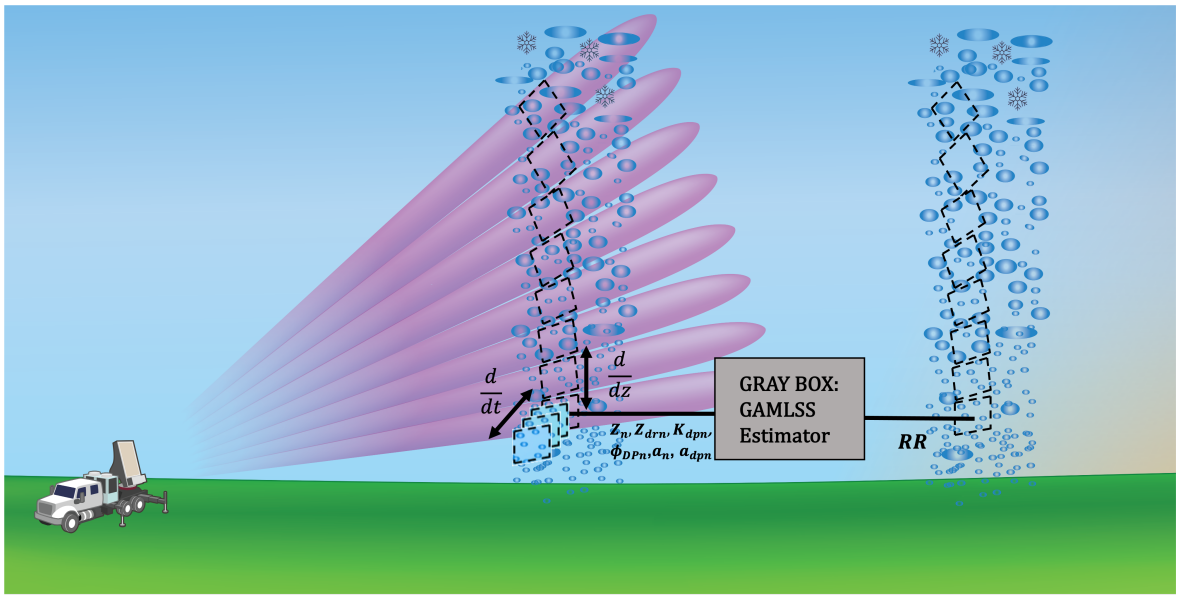


Figure 4.7: R can be derived at every range bin from PAR returns using an algorithm of choice. This work considers a probabilistic R estimate using an additive regression model to predict R from unique polarimetric PAR variables.

because the links between polarimetric radar variables and hydrometeor physical properties are reasonably well understood. Currently, even the sign of altitude derivatives is often interpreted intuitively to diagnose physical processes such as evaporation and drop breakup. Through feature selection, the GAMLSS estimator quantitatively identifies which PAR variables are significant for a given training dataset. In the GAMLSS framework, R is modeled as a sum of penalized splines involving the chosen predictors, which can be examined for consistency with physical expectations, making the approach a form of explainable machine learning. This analysis demonstrates, through a case study, that incorporating PAR polarimetric variables—specifically, the time and altitude derivatives of polarimetric radar returns—improves the estimation of R compared to using standard polarimetric variables (Z, Z_{DR}, K_{DP}, and ρ) alone.

The continuity equation, e.g., Equation (8.9), indicates that there is a clear relationship between R and fluxes of LWC. Using radar variables and derivatives of radar variables to estimate R is an indirect approach to the calculation of R because radar

variables are only fingerprints of the true LWC in the atmosphere. The approach taken in this section for estimating R also lacks wind information content to approximate a closure of the continuity equation. This makes the relationship between R and PAR variables a *gray box* relationship and makes the use of supervised learning techniques a useful proxy when the full information is lacking.

4.2.0.1.5 Case study: first Horus observations The derived estimators are conditioned by Horus instrument constraints (e.g., PAR calibration) and R_{ref} spatial and temporal offsets relative to the radar. These measurements represent some of the first Horus observations of a convective storm using a pencil beam about 3°in azimuth and elevation. To provide context for the considered event that is analyzed within a cross-section, Figure 4.8 shows the composite reflectivity extracted from MRMS (Zhang et al. (2016a)) of a precipitation system with a convective core near Norman, Oklahoma (USA) on August 8, 2023, at 10:16 UTC. As indicated by Figure 4.11, Horus sampled this convective event with polarimetric radar observations in the range of $10 < Z < 40$ dBZ, $0.6 < Z_{\mathrm{DR}} < 2.6$ dB, $0.7 < K_{\mathrm{DP}} < 4.8$ deg/km. These values are indicative of moderate rain possibly mixed with graupel/hail (Bringi et al. (2003)). Offering a supplementary perspective, the MRMS product viewer classifies hail within the convective core to the immediate southeast of the PAR RHI measurement that moves further southeast away from the PAR RHI from 10:16 UTC to 10:34 UTC (National Severe Storms Laboratory, National Oceanic and Atmospheric Administration (2023)). The weather system moves to the southeast as the measurement time lapses. Horus RHI measurements with a 3° beamwidth in azimuth and elevation were taken through the storm at an azimuthal angle of 60 degrees from North, as is depicted with a black arrow in Figure 4.8(a) starting at 10:16 UTC and (b) ending at 10:34 UTC. A single RHI pass covering 60 elevation angles from 0.5°to 31.5° was retrieved every 16 s

with a pulse repetition time of 2 ms, allowing for the calculation of vertical and time derivatives of radar variables.

The Skew-T diagram on Figure 4.8(c) shows a sounding taken a couple of hours after the Horus RHIs. The freezing level is near 4.5 km. This sounding and the sounding at 00 UTC on the same day indicate a highly turbulent environment with low convective available potential energy but high precipitable water at 44.7 mm, which contributed to the observed frontal precipitation at 10 UTC.

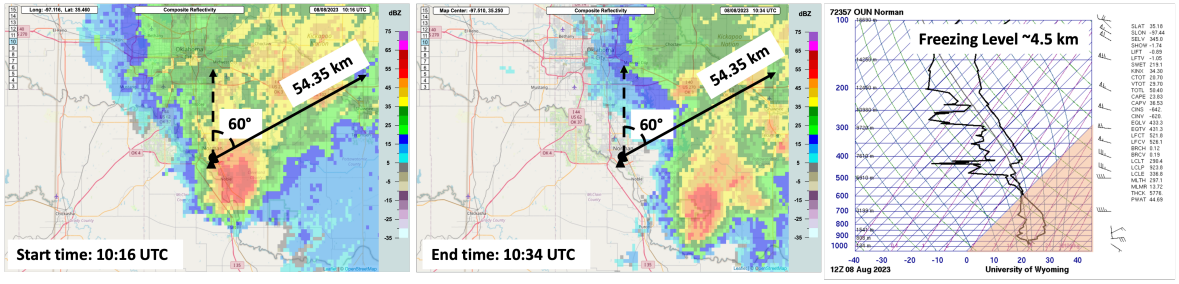


Figure 4.8: A composite Z extracted from the MRMS operational product viewer shows the spatial coverage of the frontal system near Norman, Oklahoma (USA), on August 8, 2023, that contained localized hail at (a) the measurement start time of 10:16 UTC, (b) the measurement end time of 10:34 UTC (National Severe Storms Laboratory, NOAA (2024)), and (c) a sounding taken at 12 UTC in Norman revealing a freezing level near 4.5 km (University of Wyoming Department of Atmospheric Science (2023)).

The pseudo-continuous PAR measurement in altitude and time, a snapshot of which is shown in Figure 4.5 for a single time step, allows for the development of a GAMLSS-based rain rate estimator, $R_{\text{est}}(\mu,\sigma)$. The training data for the estimation algorithms $R_{\text{est}}(\mu,\sigma)$ consists of a time series of PAR variables at the radar bins closest to the surface that remain above beam blockage at the lowest altitudes of the radar scan. These data are discretized into 1 km surface range steps from the radar (1 to 50 km from the radar) that are collocated with gauge-corrected R surface values derived from MRMS grid points. Figure 4.9 shows the horizontal difference between the center of the MRMS grid and the target latitude/longitude along the Horus RHI path. The maximum location error is about 0.005 degrees (about 500 m) in both latitude and

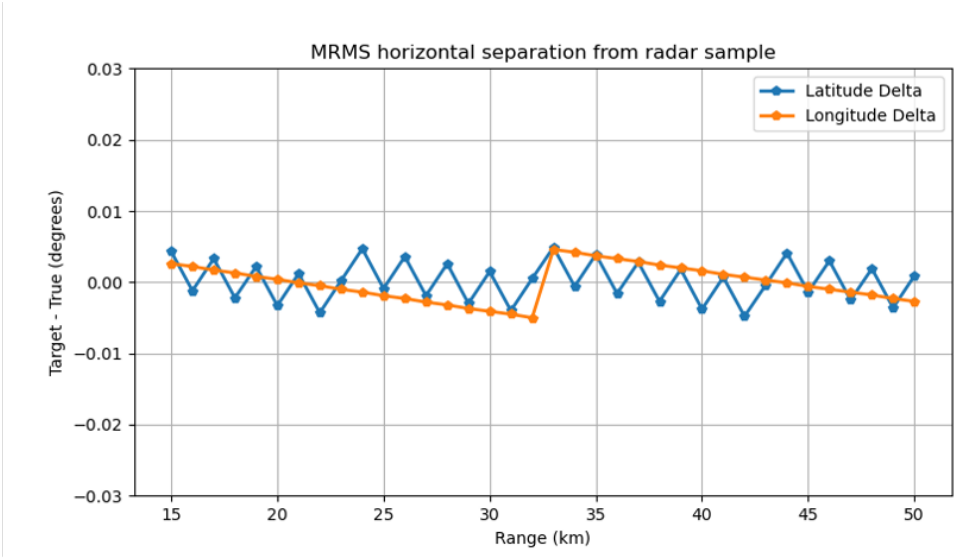


Figure 4.9: Target PAR horizontal latitude/longitude samples relative to MRMS latitude/longitude locations.

longitude. As the estimator training data set, it is also important to note that MRMS precipitation is a combined product of ground radars within the NEXRAD network. As such, the samples provided at a given MRMS time increment of 2 min may come from the preceding or following 2 min of the recorded time step. This is in part due to the temporal revisit time of the NEXRAD VCPs, which may take up to 5 min to complete a scan. Despite the horizontal and temporal uncertainties of this training dataset, MRMS was chosen due to its availability along the path of interest and because it incorporates gauge-based corrections. The MRMS gauge-corrected precipitation rate is provided on an hourly basis, while the MRMS radar-only precipitation rate is provided every 2 min. In this work we apply the gauge correction to the R at each distance from the radar by multiplying the 2-min MRMS extracted precipitation rate by a correction factor equal to the hourly gauge-corrected precipitation rate divided by the radar-only precipitation rate (Kirstetter et al. (2015a)). The PAR variables sampled aloft serve as the predictors, and the gauge-corrected MRMS R values serve as the predictand for $R_{\text{est}}(\mu,\sigma)$, the GAMLSS-based estimator considered in this study.

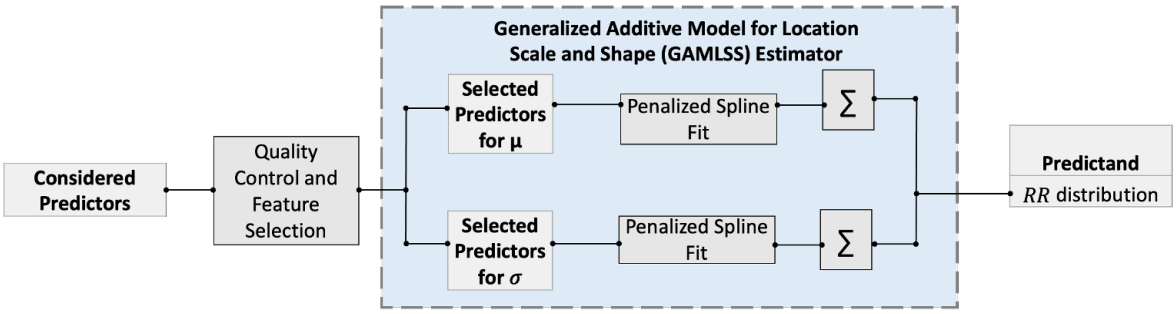


Figure 4.10: Logic flow diagram for training and estimating the predictand (R) given an input set of PAR variable predictors (PAR variables). The predictors are first quality controlled to remove extreme outliers and redundant variables or variables with negligible correlation to the predictand by referencing a rank correlation matrix. A GAMLSS feature selection is performed to down-select important variables for predicting R. The selected variables for the mean and the standard deviation σ, are trained to fit the predictand as a summation of penalized splines. The resulting predictand represents both the expected value and the variability of the R.

4.3 Association of Rain Rate with PAR Polarimetric Radar Variables and Derivatives

PAR variables and collocated MRMS gauge-corrected precipitation rates were extracted to generate an estimator. Data are composed of PAR variables horizontally collocated with MRMS R that are sampled in altitude above regions of beam blockage. The training variables are summarized in Figure 4.10 including PAR variables considered as potential predictors for the estimator and the predictand, R. While the estimator optimally sums penalized splines fit to these predictors to determine a value for R, it is instructive to examine for physical explainability the individual relationships between the PAR variables and the R.

Probabilistic relationships between the observed Horus PAR variables and the MRMS derived R are shown in Figure 4.11, by using conditional distributions of the MRMS R values relative to the PAR variables in the form of quantiles (10th, 25th,

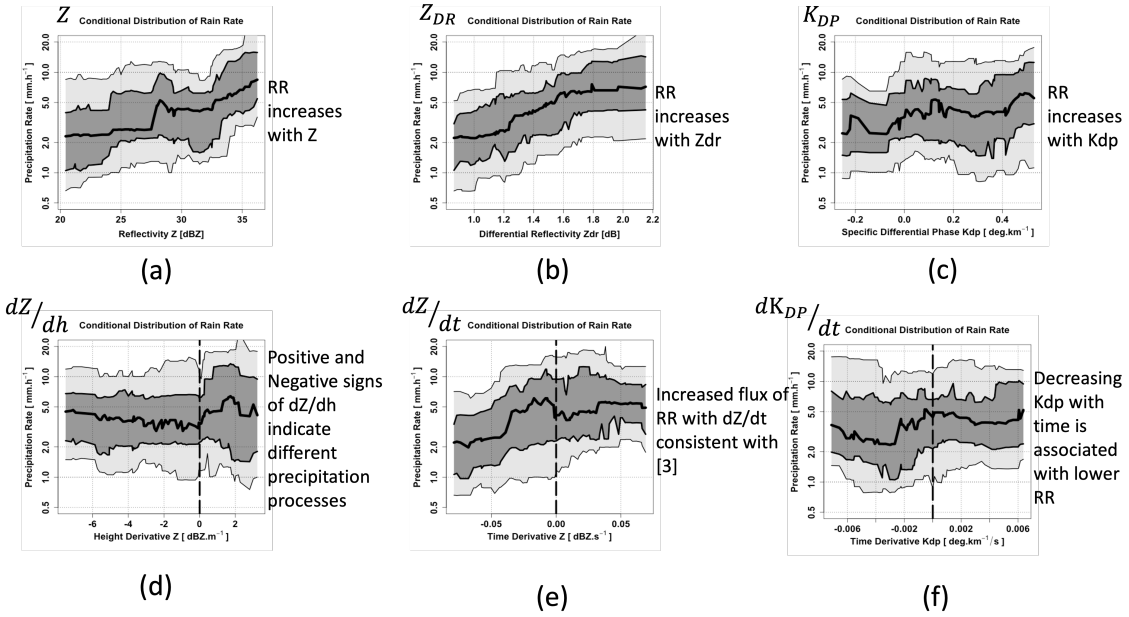


Figure 4.11: Conditional distributions of MRMS R values in the y-axis relative to the radar variables in the x-axis (first column), the time derivative of radar variables in the x-axis (second column), and the altitude derivative of the radar variables in the x-axis (third column). In each panel, the thick black line represents the median (50th percentile), the dark gray-shaded region represents the area between the 25th and 75th percentiles, and the light gray-shaded region represents the area between the 10th and 90th percentiles.

50th, 75th, and 90th percentiles). For each radar variable, the conditional median (center line in Figure 4.11) describes the trend of R relative to the PAR variable, while the interquantile area (dark shaded area) estimates the heterogeneity in the relationship, and the 10th and 90th percentiles (outer bounds of light shaded area) describe the conditional extreme values of R observed on August 8, 2023, during the time frame of this case study. Quantile plots with standard polarimetric variables are used for estimator quantification Z, Z_{DR}, and K_{DP} make up the x-axis values for the plots in the top row of Figure 4.11 while R is shown on a logarithmic scale on the y-axis. Radar variables have been increasingly used in QPE since the first Z-R relationships (Marshall and Palmer (1948)). Z, Z_{DR}, and K_{DP} are now common polarimetric variables used for QPE (Ryzhkov et al. (2022)), and numerous QPE relationships have been proposed in literature that involve one or more polarimetric variables.

Figure 4.11(a) shows the quantile plots of R as a function of Horus reflectivity and displays an increasing trend in R with Z, as expected. For example, the median (75th percentile) increases from about 2 (5) mm/hr at 20 dBZ to 7 (15) mm/hr at 35 dBZ. The spread between quantiles also increases, e.g., the 75th-25th percentile difference increases from about 4 mm/hr at 20 dBZ to 11 mm/hr at 35 dBZ, which conveys increasing uncertainty in estimating higher rain rates (Kirstetter et al. (2015a)).

Z_{DR} is used in QPE to capture the effects of PSD variability as it provides information on the median volume diameter of hydrometers in the radar resolution volume. Figure 4.11(b) consistently indicates that the distribution of MRMS R shifts toward higher values with Horus, Z_{DR} and this relationship displays similar dynamics as reflectivity, as expected. For example, the median rain rate (75th percentile) increases from 2 (4) mm/hr at Z_{DR}=1 dB to 7 (15) mm/hr at Z_{DR}=2 dB. Consistent with the reflectivity relationship is the increasing spread between R quantiles with Z_{DR}, e.g., the interquantile range increases from about 3 mm/hr at Z_{DR}=1 dB to 11 mm/hr at

Z_{DR}=2 dBZ, also conveying increasing uncertainty in estimating higher rain rates.

While both Z and Z_{DR} require precise calibration and can be affected by attenuation and, in some circumstances, by partial beam blockage, K_{DP} is largely immune to these error sources (Ryzhkov et al. (2002)). The relationship to R is less sensitive to the PSD variability because K_{DP} is related to a moment of the PSD of similar order to R, and K_{DP} can be indicative of the shape and concentration of hydrometers. However, K_{DP} is historically noisy for light rain (Ryzhkov et al. (2002)). For this case event, Figure 4.11(j) shows an increasing trend in the R distributions with K_{DP} as expected, with an overall increase of mean R from K_{DP}=0 deg/km to 0.6 deg/km of about 2.5 mm/hr.

Quantile plots with some examples of time and height derivatives of radar variables are shown in the second row of Figure 4.11. Time derivatives of radar variables provide information both about rates of change of condensed water mass as well as precipitation fluxes. Figure 4.11(e) shows a positive relation between different rain rate quantiles and the time derivative of reflectivity dZ/dt with similar features in terms of dynamic range, uncertainty, and extremes as the relation obtained with Z (see Fig. 4.11(a)). For example, the median R increases from about 2 mm/hr at -0.05 dBZ s^{-1} to just below 5 mm/hr at 0.05 dBZ s^{-1}. Such a relationship presents some consistency with previous works from Stephens et al. (2019) and Dolan et al. (2023) who report that the time difference of radar measurements contains information about the vertical movement of water mass in storms. Relationships between convective mass fluxes (typically associated with higher R values) and changes in reflectivity over time intervals of 30, 90, and 120 s are used to design the INCUS space-borne mission (Kim et al. (2023)). The current work is the first time that time differences of radar reflectivity over intervals of a few seconds are linked to surface precipitation fluxes.

Quantile plots with PAR reflectivity derivatives are shown in Figure 4.11(d). Variations of radar variables with height help to signal the occurrence of precipitation

processes that may be relevant for QPE. While the quantile plots do not portray monotonic and dynamic quantitative relationships between the altitude derivatives and the R distributions, the signs and magnitude of height derivatives seem to be associated with distinct distributions. For example, a shift toward higher R values can be noted with increasingly negative dZ/dh (e.g., below -4 dBZ km^{-1}) and dZ_{DR}/dh (e.g., below -0.3 dB km^{-1}) values, as might be expected in collision-coalescence process conditions, as noted in 4.2.0.1.2. Looking at the positive side, median R values increase from around 3 mm/hr to 5 mm/hr with dZ/dh up to 2 dBZ km^{-1} and with dZ_{DR}/dh up to 0.1 dB km^{-1}, highlighting separate trends in the negative and positive domains of these altitude derivatives. It suggests that process regimes and rates may be distinguished by considering radar signatures in PAR height derivatives of radar variables. While they lack a direct proportionality to R and may not be sufficient to quantify precipitation when considered in isolation, altitude derivatives rather provide curve-shaping information to R estimators.

Although the individual trends of R with the PAR variables are shown via the quantile plots, multiple PAR variables are needed to capture the concomitant influence of various microphysical processes and fluxes. This calls for a multivariate quantification approach. Thus, a multidimensional modeling approach is used in the next section to account for the collective relationships of the PAR variables with R, to uncover the relative impact of different variables on QPE, and to improve precipitation estimates.

4.4 Rank Correlation and Feature Selection for PAR Predictors of Rain Rate

An efficient multivariate R estimator should involve only the most significant predictors listed in Figure 4.4. Redundant and highly correlated variables with low correlation

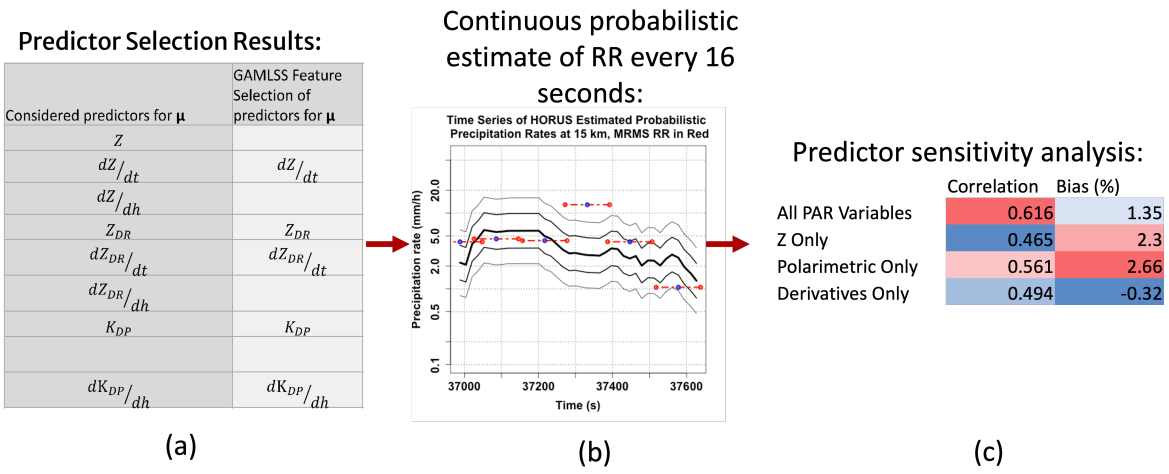


Figure 4.12: Considered and selected predictors for the estimation of mean R resulting in a trained probabilistic estimator with terms $\mu(dZ/dt,\ Z_{\mathrm{DR}},\ dZ_{\mathrm{DR}}/dt,\ K_{\mathrm{DP}},\ dK_{\mathrm{DP}}/dh)$. (a) GAMLSS is used to select these predictors and (b) generate continuous probabilistic R estimates every 16 s. (c) A predictor sensitivity analysis shows the highest correlation to be with the inclusion of all selected PAR variables. It is compared to correlations and bias metrics for estimators using predictors of Z only polarimetric variables, and derivatives only from the set of considered predictors.

to R are identified and removed before performing the feature selection for predictor terms that help to fit the best rain rate relationship for the observed events.

A GAMLSS supervised learning feature selection is performed for parameters μ and σ. The results of this feature selection for the parameter μ of the probabilistic estimator for R is shown in Figure 4.12(a) and Figure 4.12(b), respectively. The estimate of the mean of R for this case is determined to be a multivariate function of PAR variables with the terms $\mu(dZ/dt,\ Z_{\mathrm{DR}},\ dZ_{\mathrm{DR}}/dt,\ K_{\mathrm{DP}},\ dK_{\mathrm{DP}}/dh)$.

4.5 Probabilistic Rain Rate Estimates at Fine Scales and Comparative Estimator Analysis

Probabilistic estimators trained using data with variability representative of the variability expected of the predictors and the predictand can be used to estimate R given new predictors. Probabilistic estimators provide both an estimated mean, μ, and and estimated variability, σ. A probabilistic estimate of R can now be obtained from PAR observations at their revisit time resolution, in this case 16 s. This is demonstrated by computing time series of GAMLSS-estimated probabilistic surface R values shown in Figure 4.13. At each time step, a distribution of precipitation rates is computed according to likelihood including uncertainty bounds (e.g., 25th and 75th percentiles) and extreme values (e.g., 90th percentiles). Overlayed are R predictand training data at 15, 20, 25, 30, 35, 40, 45, and 50 km from the radar, shown as dots. The red training data points depict the collocated MRMS R values, while the dashed lines represent training-data temporal uncertainty bounds. MRMS forms radar-based precipitation products in increments of 2 min utilizing NEXRAD's approximately 5 min VCPs (Crum and Alberty (1993)). For this reason, there is a timing uncertainty for each QPE measurement of +/- 2 min for each scan (Zhang et al. (2016a)). As expected, the training dataset (including its temporal uncertainty) oftentimes falls within the uncertainty bounds of the probabilistic estimator. Despite the presence of outliers, the R estimator demonstrates efficacy.

To provide insight on the added quantitative value of PAR variables, the probabilistic R estimator utilizing all PAR variables (standard radar variables and their time and altitude derivatives, f_{PAR}) is compared to estimators utilizing (1) only reflectivity (f_Z), (2) only standard radar variables (e.g. f_s= f(Z, Z_{dr}, K_{dp})), and (3) only the

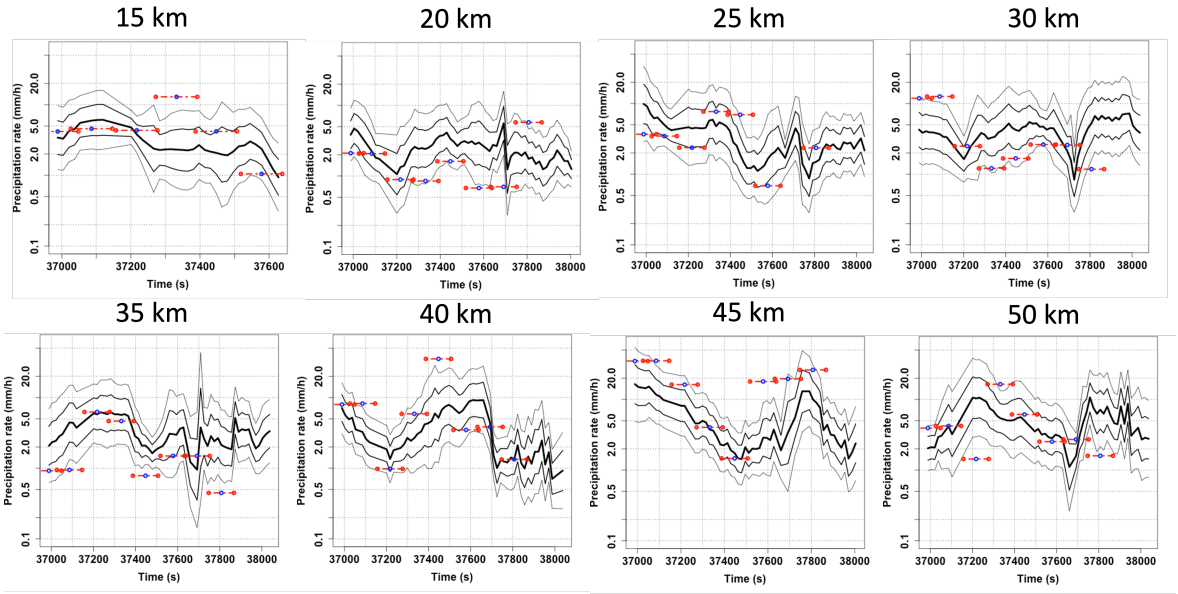


Figure 4.13: Time series of Horus estimated probabilistic QPE at various distances from the radar, including the estimated median (center black curve), 25th and 75th percentiles (inner curves), and 90th and 10th percentiles (outer curves). The included training data (MRMS gauge corrected Rs) at each distance from the radar is marked in red and constitutes 14 percent of the total continuous MRMS data set. Error bars are overlaid on the MRMS Rs to indicate the potential for time errors by the MRMS data capture.

derivatives of radar variables (f_d).

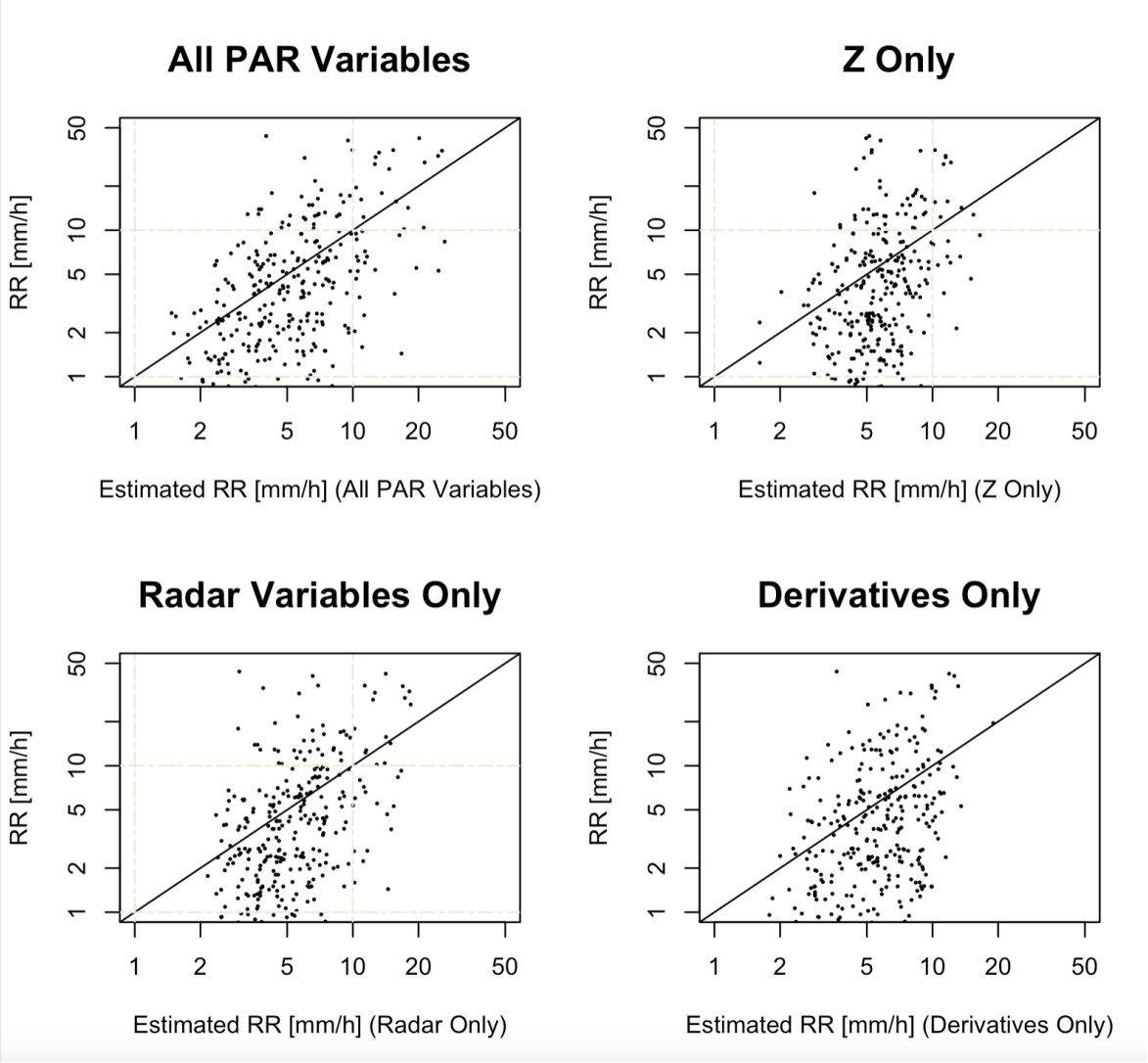


Figure 4.14: Scatter plot of MRMS R vs. estimated R for various GAMLSS-based estimators.

This model comparison is performed first by comparing the systematic part of the probabilistic models, which is represented by the first moment of the distribution, i.e., the expected value E($R \mid \mu,\sigma$), with the reference. Figure 4.14 shows scatter plots comparing the MRMS R dataset to the systematic part of the probabilistic estimates. The model f_{PAR} displays closer alignment with the 1:1 line, hence a higher dynamic

	Correlation	Explained Variance	Bias (%)
All	0.52	0.27	0.37
Z Only	0.31	0.09	-1.06
Radar Only	0.45	0.20	-1.41
Derivatives Only	0.37	0.14	0.01

Figure 4.15: Linear correlation, explained variance, and bias table for various GAMLSS-based estimators relative to R

range than the other models f_Z, f_s, and f_d, highlighting the contribution of PAR variables.

Along the scatterplots, performance metrics for each probabilistic model f_{PAR}, f_Z, f_s, and f_d are summarized in Figure 4.15 with the correlation, the corresponding explained variance, and the relative bias values. The explained variance is defined to be the square of the correlation, which is the correlation between the mean estimated R and the training R. The bias is defined to be the mean difference between the estimated versus the reference R values normalized to the mean of the reference R values. Note that given the limited sample size associated with this case study, the presentation of the result metrics focuses on the training data set as opposed to an independent verification set. This approach is both necessary to provide an evaluation within the constraints of the available data, and to give a preliminary understanding of model performance and potential areas for improvement. Figure 4.15 shows that as expected, all probabilistic models display low systematic bias, i.e., well within typically accepted values of 10 percent bias for R estimators (see Table 3 and Fig.4 in Kirstetter et al. (2015a)). The correlation values vary from 0.31 (Z model) to 0.52 (PAR model) which is good given the variability of precipitation at 16-s timescale and that correlations at short time scales are lower than at 24 hr time scales. The best performer is overall $f_{AllPARVariables}$ with a correlation of 0.52. Following are $f_{RadarVariablesOnly}$ with a correlation of 0.45, $f_{DerivativesOnly}$ with a correlation of 0.37, and f_{ZOnly} with a correlation

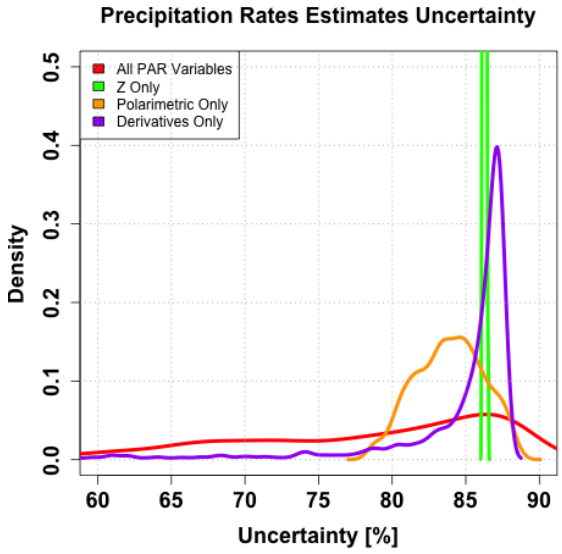


Figure 4.16: Density plot of uncertainty values for various GAMLSS-based estimators: (red) an estimator including all chosen PAR variables as listed in Figure 4.12, (green) an estimator only including Z as a predictor, (orange) an estimator only considering the standard radar variables from 4.12, and (purple) an estimator only considering the altitude and time derivative predictors from 4.12

of 0.31. It confirms the potential value of PAR variables for QPE.

Probabilistic models can also be compared in terms of their conditional spread, represented by the relative uncertainty computed as a percentage defined to be the difference between the 75th and 25th quantiles of the estimated R normalized by the mean of the R distribution (Kirstetter et al. (2015b)). Lower relative uncertainties indicate a more precise estimator. Density distributions of the relative uncertainties of f_{PAR}, f_Z, f_s, and f_d are shown in Figure 4.16. For each model, relative uncertainty values are computed from the test data set composed of radar variables sampled at Horus temporal sampling between 15 and 50 km in range from the radar (i.e., not from the training data set). Figure 4.16 shows the density distribution of relative uncertainties associated with each probabilistic model trained with the different subsets of radar variables. Relative uncertainties of the f_Z model (in green) are concentrated around

87%, while the relative uncertainties obtained with the f_d model (in purple) display similar uncertainty distributions with values primarily above 85 percent. f_s improves upon these with a wider uncertainty distribution centered around 84%. Improving further upon other estimators, the estimator that provides the lowest uncertainty values is the estimator that utilizes a combination of radar variables and their time and altitude derivatives; f_{PAR} distinguishes itself as the foremost example of an estimator with lower uncertainty values than the other considered estimators with its large spread of uncertainty values over the range of 55% to 100% uncertainty.

The representative dynamic range displayed in Figure 4.14, the ranked performance of estimators shown in Figure 4.15, and the comparative uncertainty analysis provided via Figure 4.12 provide preliminary support toward an affirmative answer to the primary science question posed in Section 4.2: Does the inclusion of PAR variables that provide signatures of processes and fluxes in the atmosphere in R probabilistic estimators improve QPE?

4.5.0.0.1 PAR RHI Measurement Takeaways This work exploits the dense vertical sampling and high temporal resolution provided by PAR measurements to derive fingerprints of microphysical processes and fluxes as new PAR variables that inform multivariate probabilistic rain rate retrievals.

In the context of a case study with PAR fast-scanning RHI cross-sectioning a convective storm in Norman, Oklahoma, on August 8, 2023, signatures of processes and fluxes observed with PAR were introduced and discussed, along with a QPE framework that utilizes time and altitude derivatives of radar variables. The probabilistic framework was used to show the improvement to QPE allotted by the use of time and altitude derivatives over the classical radar variables alone. These preliminary results suggest that the inclusion of signatures of processes and fluxes improves QPE.

Overall this study illustrates the benefit of PAR spatiotemporal sampling density over more standard estimation techniques that rely on intermittent and discontinuous radar sampling of the atmosphere. A disclaimer is that for this case study has limited representativeness; hence, more data should be analyzed as they become available. Also, Horus radar beam-pointing inaccuracies of up to 5° were reported due to the development stage of Horus at the time these measurements were taken. Thus the results in the tables and diagrams presented must be somewhat interpreted qualitatively rather than quantitatively.

Nevertheless, through these combined analyses, the study confirms that incorporating time and altitude derivatives of radar polarimetric variables enhances both the accuracy and reliability of probabilistic QPE. The derived framework demonstrates how advanced data handling, methodological rigor, and statistical modeling converge to extract physically meaningful insights from high-resolution radar data. This integration of process-level understanding and computational inference represents a substantial step toward next-generation radar-based precipitation estimation capable of resolving convective variability at operationally relevant scales.

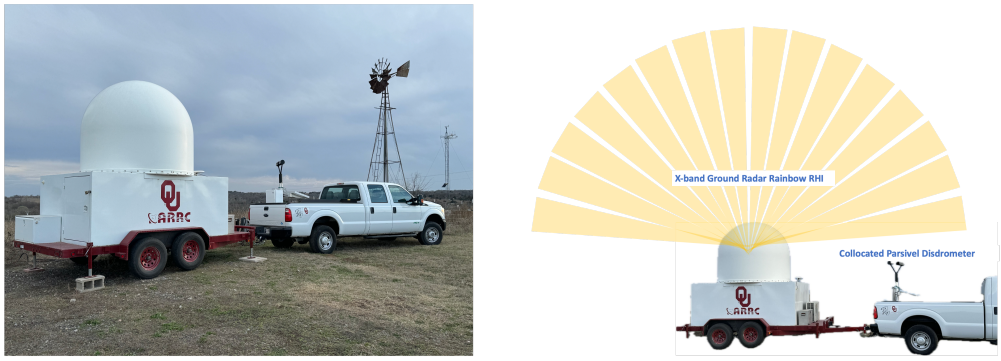


Figure 4.17: The PX-1000 X-band polarimetric radar system is used for high-resolution precipitation observations.

4.5.0.0.2 Crossed RHI Measurements with PX-1000

Building on the previous Horus study of vertical and temporal derivatives, we now consider crossed range-height indicator (RHI) measurements to further explore the utility of PAR variables for improving QPE. While Horus focused on vertical profiles, crossed RHI scans provide additional information on horizontal variability, allowing for a more complete assessment of the continuity-based framework for QPE.

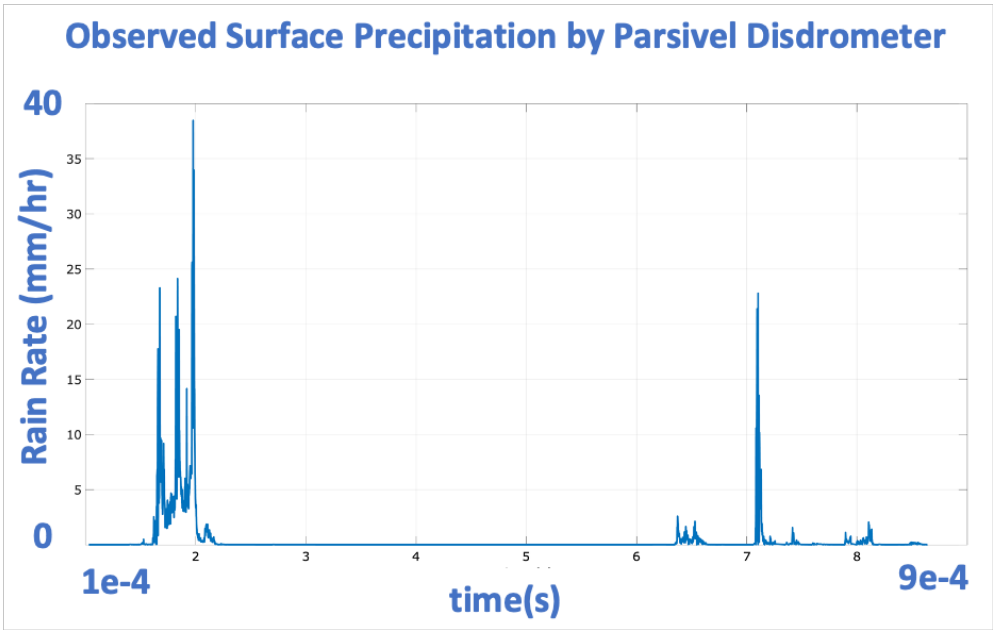


Figure 4.18: Observed precipitation structure and intensity during the study period, as measured by the PX-1000 radar.

Precipitation measurements were collected on March 8, 2024, at the Kessler Atmospheric and Ecological Field Station (KAEFS) in Oklahoma, USA (34.98° N, 97.52° W) from 05:33:53 UTC to 20:36:01 UTC, using the Polarimetric X-band 1000 (PX-1000) radar (ARRC (2025)), collocated with a Parsivel disdrometer at the surface. At 12:00 UTC, the 0 ° C isotherm was located approximately 2.8 km above the surface, with a relative humidity of 69%, and the surface temperature was 11.2 °C, with 93% relative humidity. Crossed RHI measurements captured orthogonal components of polarimetric

variable variations, enabling analysis of multidimensional spatial and temporal changes in hydrometeor properties.

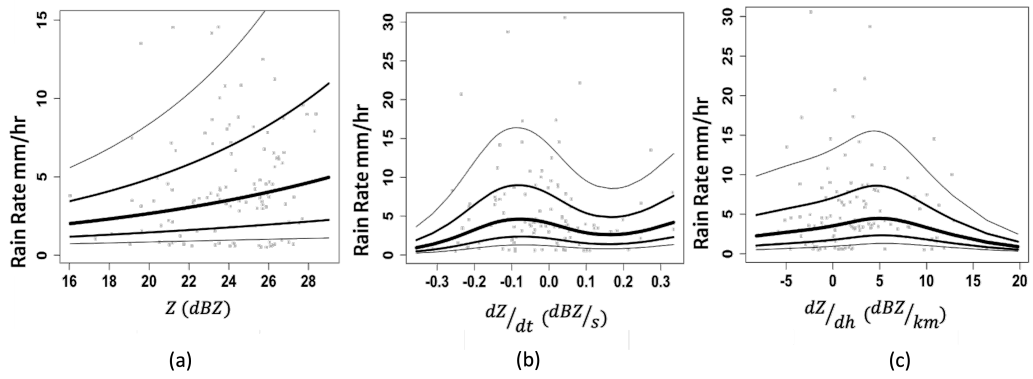


Figure 4.19: Reflectivity (Z), the time derivative of reflectivity (dZ/dt), and the height derivative of reflectivity (dZ/dh) are derived from PX-1000 radar profiles.

Polarimetric variables such as reflectivity (Z), differential reflectivity (Z_{DR}), and specific differential phase (K_{DP}) provide information on the size, shape, and phase of hydrometeors. While traditional QPE approaches empirically map these variables to surface rain rate, their time and spatial derivatives contain additional information relevant to precipitation flux. Altitude derivatives of polarimetric variables have been documented as fingerprints of microphysical processes (Kumjian et al. (2022)), and by considering full spatial derivatives within the continuity equation framework, we can extract more information to improve QPE.

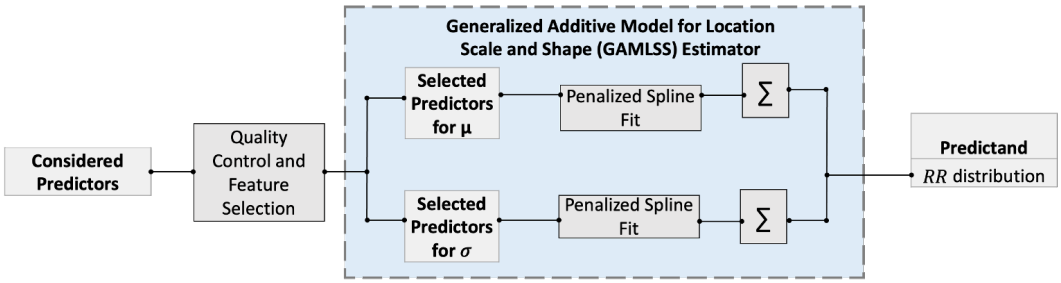


Figure 4.20: Example of the GAMLSS (Generalized Additive Model for Location, Scale, and Shape) regression fit used to estimate rain rate from derivative-based predictors.

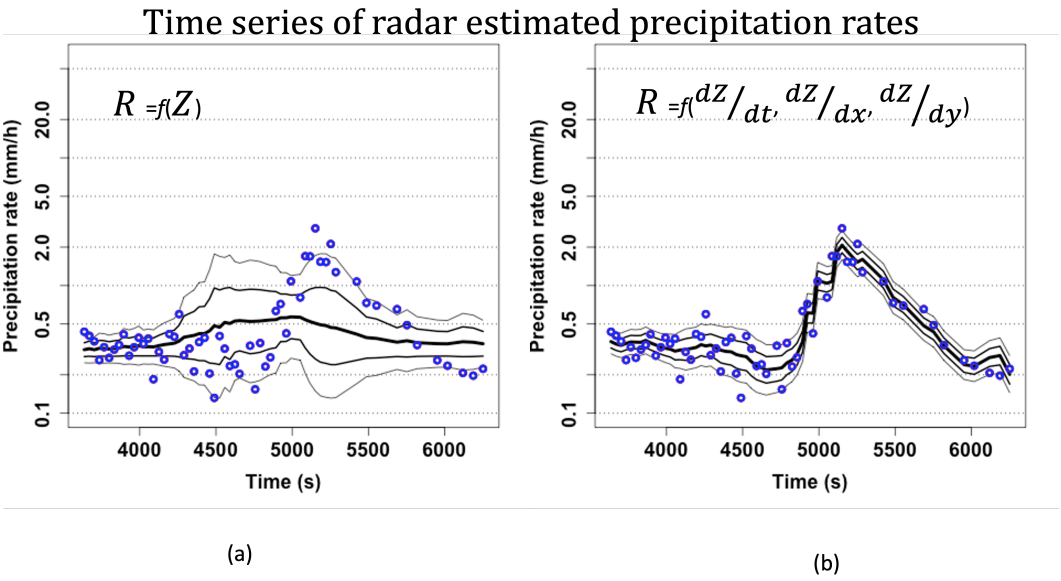


Figure 4.21: Time series of rain rate estimation results showing observed and modeled values over the study period.

GAMLSS was used to quantify the relationship between PAR-derived observables and surface precipitation. Predictors included time and spatial derivatives of reflectivity (Z) and horizontal derivatives of differential reflectivity (Z_{DR}). These predictors were used to estimate parameters of a lognormal distribution for rain rate at the surface (Kirstetter et al. (2015a)). Correlation and bias between the GAMLSS-estimated rain rate and measurements from the collocated Parsivel disdrometer are summarized in Table 4.2. At sub-minute time scales, correlation is naturally lower than for coarser temporal aggregations (Ryzhkov et al. (2022)), yet all models show low bias, indicating that they capture the conditional variability of precipitation effectively.

The results demonstrate that temporal and spatial derivatives of polarimetric variables improve QPE accuracy at the surface. Multidimensional PAR variables derived from crossed RHI scans provide enhanced signatures of microphysical processes compared to 1D vertical profiles. Moreover, supervised learning models that incorporate both standard polarimetric variables and their derivatives yield higher correlation and

Table 4.2: Performance metrics (correlation and bias) for rain rate estimators using different linear combinations of predictors for the mean (μ) and standard deviation (σ) components of the GAMLSS model.

Selected linear combination of predictors for μ	**Selected linear combination of predictors for σ**	**Rain rate correlation**	**Rain rate bias (%)**
Z	Z	0.24	5.9
dZ/dt	dZ/dt	0.24	1.7
$dZ/dt + dZ/dr + dZ/dx$	$dZ/dt + dZ/dy$	0.32	4.8
$Z + dZ/dt + dZ/dh$	$Z + dZ/dt + dZ/dh$	0.35	1.7

lower bias than models relying solely on reflectivity or individual derivatives. These findings reinforce the value of fast-scanning PAR systems for continuity-based QPE and highlight the potential of multidimensional derivative observables to inform process-aware precipitation estimation frameworks.

4.6 Application of the Continuity Equation in Convection

While the findings thus far support the capability of fast-scanning PAR systems to capture the microphysical and dynamical signatures needed for continuity-based QPE, completing the PROWEX analysis requires combining these derivative approaches with 3D wind field estimates to test a full continuity framework under real atmospheric conditions. This section investigates continuity-equation closure using Horus combined with 3D wind measurements from passive receivers, as has been demonstrated by Emmerson (2022).

To culminate the PROWEX experiment, the observation of a convective storm moving through Norman, Oklahoma, on June 3, 2025, between 22 and 23 UTC is considered. According to reports, a "tornado developed about a mile east of US-62

to the north of Southeast 23rd Street and moved generally east, dissipating in a tree line near the Canadian River. One home suffered roof damage, a barn collapsed, and numerous large trees were snapped" (Compilations (2025)). Photos of the tornado are shown in Figure 4.22. An EF1 tornado with maximum winds between 86 and 110 mph (approximately 38 to 49 m/s) formed at 23:00 UTC and remained on the ground for about 5 min, dissipating at 23:05 UTC. It reached a maximum width of 125 yards (114.3 m) and fortunately caused no casualties. Environmental conditions reported by the Norman Mesonet station at 35.23° N, 97.46° W included a relative humidity of 95%, an air temperature of 20.5° C, and a station pressure of 966.28 mb (Oklahoma Mesonet, Oklahoma Climatological Survey (2025)).



Figure 4.22: Photographs of the EF1 tornado observed near Norman, Oklahoma, on June 3, 2025. Panels (a) and (b) show two views of the same tornado as it moved east toward the Canadian River. (Media (2025),Compilations (2025)).

During this event, Horus and NSSL's Telemetry of Observed Total Accumulated Liquid (TOTAL) trailer were deployed in the parking lot of Lloyd Noble Center in Norman, OK (NOAA National Severe Storms Laboratory (2025c)). Figure 4.23a shows the approximate tornado path, situated about 9.5 km northwest of Horus and the TOTAL trailer. Figure 4.23b provides a closer view of the instrument deployment, showing the disdrometer on the TOTAL trailer and Horus near 35.19° N, 97.45° W.

Horus scanned the atmosphere using a spoiled transmit beam and 13 simultaneous receive beams from 0.54° to 13.46° in elevation, with a reduced blind-zone radius of approximately 921 m due to the use of PPC+.

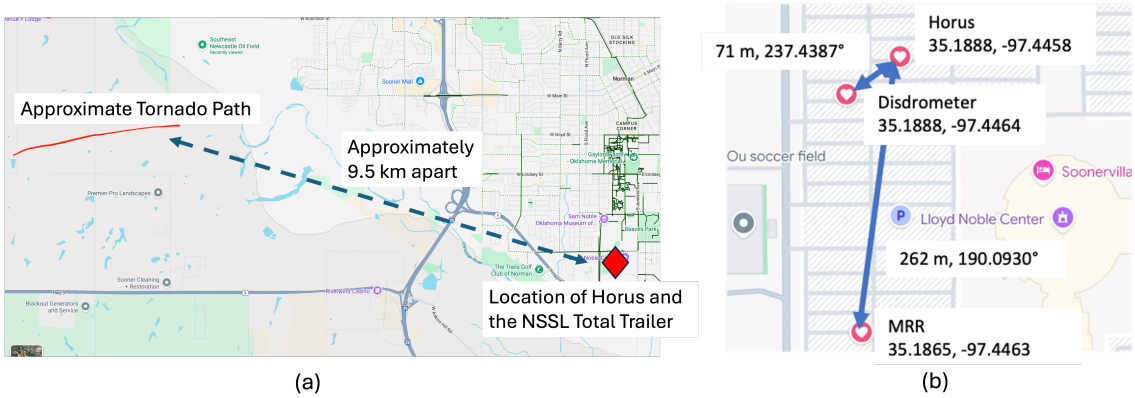


Figure 4.23: (a) Approximate path of the June 3, 2025, Norman, OK, tornado relative to the Horus radar and NSSL's TOTAL trailer at the Lloyd Noble Center. (b) Zoomed view of the instrument deployment showing the locations of Horus and the TOTAL disdrometer. (Compilations (2025)).

Figure 4.24a shows a photograph of Horus taken just prior to the observed convection on 3 June. Figure 4.24b shows disdrometer-derived rain rates, which reached up to 150 mm/hr, classifying the event as torrential (World Meteorological Organization (2024)).

Figure 4.25 presents MRMS Operational Product Viewer results. Heavy Low-Level Rotation exceeding 0.014 s^{-1} is shown in Figure 4.25a at 22:00 UTC near the tornado path from Figure 4.23a. Figure 4.25b shows composite reflectivity at 22:26 UTC, with Z values up to 55 dBZ consistent with heavy rainfall (NOAA National Severe Storms Laboratory (2025a)).

Figure 4.26 shows the radial Doppler velocity measured by Horus at 22:26 UTC, indicating primarily westerly winds exceeding 20 m/s.

The Storm Prediction Center (SPC) Mesoscale Analysis Archive combines surface and upper-air observations with numerical weather prediction models such as RAP

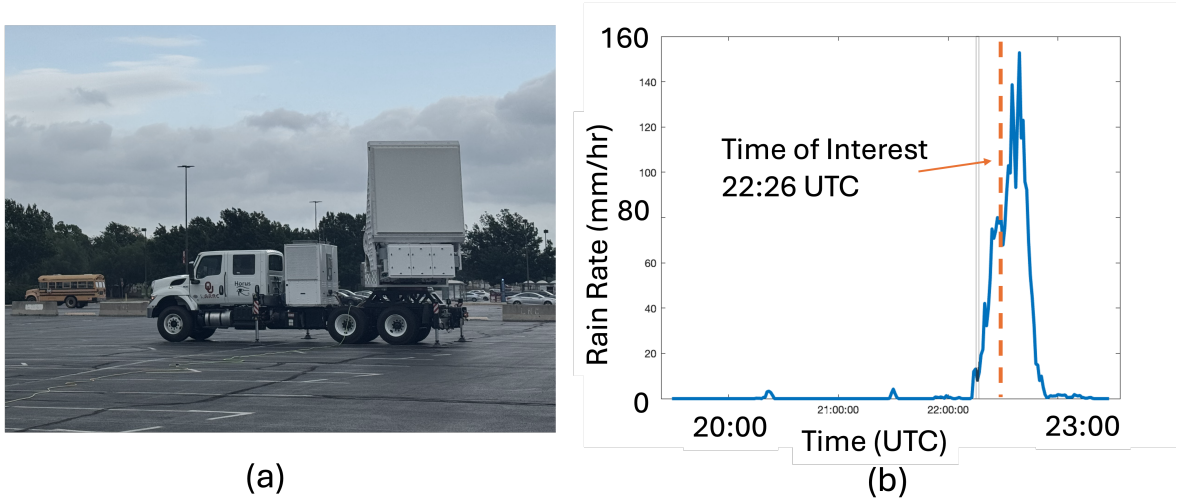


Figure 4.24: (a) Photograph of the Horus mobile radar taken prior to the June 3, 2025 convective event. (b) Disdrometer-derived rain rates during the event, which reached values up to 150 mm/hr.

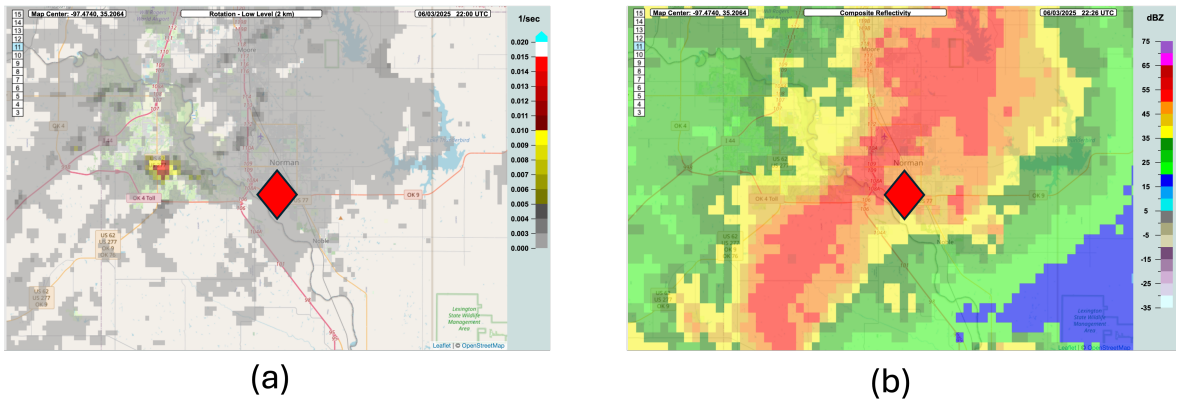


Figure 4.25: MRMS observations during the June 3, 2025 event. (a) Low-Level Rotation (LLR) exceeding 0.014 at 22:00 UTC near the tornado path. (b) Composite reflectivity at 22:26 UTC, showing maximum values up to 55 dBZ, indicative of heavy rainfall.

and HRRR to derive fields including CAPE, moisture convergence, and precipitable water (NOAA Storm Prediction Center (2025)). For this event, the SPC analysis indicates high moisture convergence near Norman, 2000 J/kg surface-based CAPE, and 48.26 mm of precipitable water, highlighting a highly unstable environment.

Simultaneously, a network of passive receivers was deployed to capture 3D wind

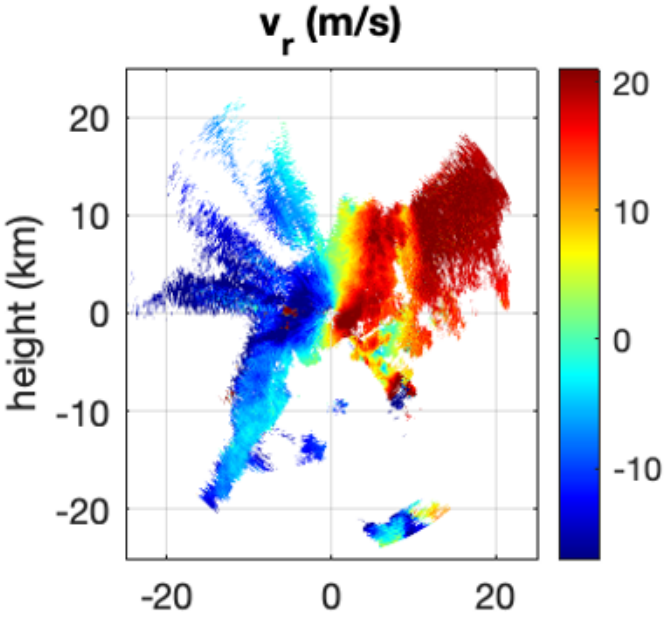


Figure 4.26: Radial Doppler velocity from Horus at 22:26 UTC, showing mainly westerly winds exceeding 20 m/s.

components relative to the nearby KTLX WSR-88D Radar as part of an OU-developed multistatic weather radar system (Emmerson (2022), Emmerson et al. (2025)). The resulting 3D winds at 22:26 UTC are shown in Figure 4.27. Horizontal U-winds exceed 10 m/s near Horus, and vertical W-winds indicate an updraft that could contribute to the heavy rainfall measured by the disdrometer. The combination of Horus radar returns and 3D wind measurements enables evaluation of continuity-equation closure.

The continuity equation is derived in Appendix 8.1. Equation (8.2) shows the continuity equation for condensed hydrometeor mass observable by the radar in Cartesian coordinates. For convenience with the implementation of the continuity equation relative to Horus, and to reduce regridding errors that would come from regridding both the 3D winds on the KTLX spherical grid and the Horus data on the Horus spherical grid to Cartesian coordinates, the 3D winds are regridded to the Horus grid using the PyART package in Python (Helmus and Collis (2016)). Then the continuity equation

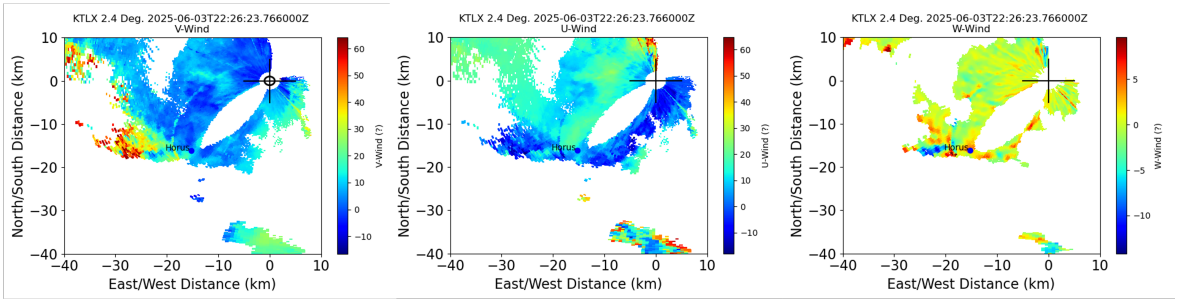


Figure 4.27: 3D wind components measured at 22:26 UTC on June 3, 2025, with respect to the KTLX WSR-88D Radar using a multistatic retrieval technique. Panels show (a) U (east–west), (b) V (north–south), and (c) W (vertical) wind velocities.

can be applied in spherical coordinates relative to the Horus grid, assuming that there are sources and sinks of mass, p (in units of kg/s) to be

$$p = \frac{dm}{dt} + \frac{1}{r^2}\frac{d(r^2 m V_r)}{dr} + \frac{1}{r\sin\theta}\frac{dmV_\phi}{d\phi} + \frac{1}{r\sin\theta}\frac{dmV_\theta sin\theta}{d\theta} \tag{4.3}$$

where V_r is the radial Doppler velocity observed by Horus, θ is the elevation pointing angle, ϕ is the azimuthal pointing angle. V_θ is the velocity along the elevation, which is assumed to be equal to an estimated fall velocity of the hydrometeors W_{tot} that combines the hydrometeor terminal velocity (V_t) with the W-wind (W) as $W_{tot} = W - V_t$. And V_ϕ is the azimuthal velocity computed as a combination of U and V winds tangent to the Horus radial as

$$V_{phi} = -U sin\phi + V sin\phi. \tag{4.4}$$

As a shorthand, the flux components in Equation (4.3) will be referred to as

- $flux_a = \frac{dm}{dt}$ describes temporal mass changes
- $flux_b = \frac{1}{r\sin\theta}\frac{dmV_\theta sin\theta}{d\theta}$ describes vertical mass flux

- $flux_c = \frac{1}{r \sin\theta} \frac{dmV_\phi}{d\phi}$ describes advective azimuthal mass fluxes
- $flux_d = \frac{1}{r^2} \frac{d(r^2 m V_r)}{dr}$ describes advective radial mass fluxes

As Horus does not directly return a mass variable, it must be estimated from the radar variables. The condensed precipitation mass is considered as a grams-per-meter-cubed quantity, such as LWC, used in place of m. The LWC is retrieved based on an empirical power law proposed by Bringi and Chandrasekar (2001) at S-band, assuming that the particles fall within the Rayleigh scattering regime:

$$LWC = \rho_l W = \rho_l 3.4 Z^{4/7}. \tag{4.5}$$

according to a relation from Hagen and Yuter (2003) where W has units of $mm^3\ m^{-3}$, Z is in linear scale, and $\rho_l = 0.001\ g/mm^3$. The terminal velocity is estimated according to Gunn and Kinzer (1949), to be used as a component of the representative fall velocity of the PSD, as follows:

$$V_t = 9.65 - 10.3 * e^{-0.6 * D_0} \tag{4.6}$$

where D_0 is the diameter of an individual water droplet in millimeters and V_t typically has units of $m.s^{-1}$. Since Horus illuminates volumes of drops at S-band, the diameter used is a median drop diameter estimated to be the median drop diameter according to Bringi et al. (2002) in relation to Z_{dr} in linear scale as

$$D_0 = 1.619 (Z_{dr})^{0.485}. \tag{4.7}$$

Figure 4.28a shows a PPI map of Horus estimated LWC at 3.78° elevation in units of $g.m^{-3}$. A histogram of the drop diameters estimated for the same elevation angle according to Equation (4.7) is shown in Figure 4.28b. Figure 4.28c shows a histogram of the terminal velocities estimated according to Equation (4.6) indicating that drop

terminal velocities fall within the range of 4 $m.s^{-1}$ to 8 $m.s^{-1}$.

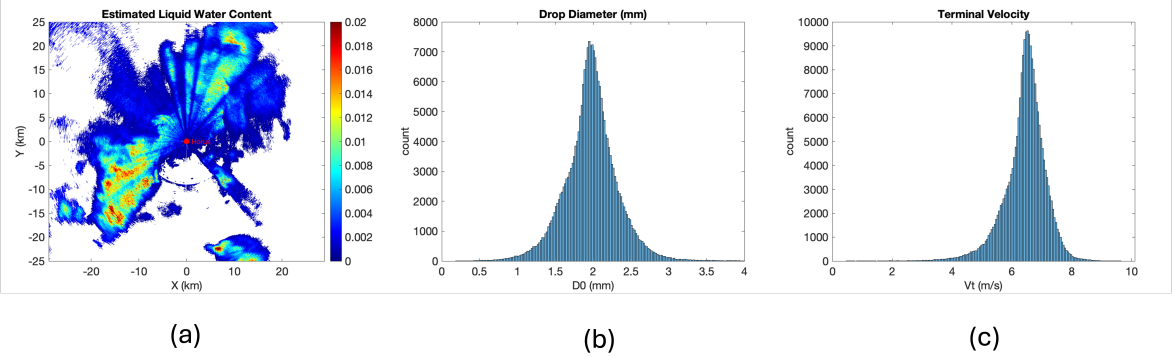


Figure 4.28: Microphysical measurement estimates derived from Horus Z and Z_{dr} at 3.78° elevation on June 3, 2025. (a) PPI map of estimated liquid water content (LWC, g/m^3). (b) Histogram of drop diameters calculated using Equation (4.7). (c) Histogram of estimated drop terminal velocities from Equation (4.6).

In order to analyze process rates, a sector of the Z field was considered between 273.9° from north and 240.8° from north as shown in Figure 4.29a for an elevation angle of 4.85°. Locations of visible beam blockage were isolated manually for each elevation (lower elevation angles are more impacted). Figure 4.29b shows the case at the lowest elevation angle considered, 2.69°, which includes two regions excluded from the analysis, indicated by the red dashed sectors.

This data was used to analyze the magnitudes of various flux terms. Figure 4.30 shows $flux_a$ terms ranging in magnitude from about 0 to $1 * 10^{-6}$ $kg.s^{-1}.m^{-3}$), $flux_b$ terms reaching higher magnitudes that extend from 0 to $4 * 10^{-6}$ $kg.s^{-1}.m^{-3}$), $flux_c$ terms at an order of magnitude higher extending from less than 0 to $10 * 10^{-5}$ $kg.s^{-1}.m^{-3}$), and $flux_d$ terms ranging from 0 to beyond $6 * 10^{-6}$ $kg.s^{-1}.m^{-3}$). Thus, $flux_c$, the azimuthal flux has a dominant impact on the process rate (Eq. (4.3)), meaning that advection has a strong impact on the creation of mass in this area in the storm. This makes physical sense; for example, Grabowski and Morrison (2017) demonstrated that horizontal advection continuously supplies moisture to the storm

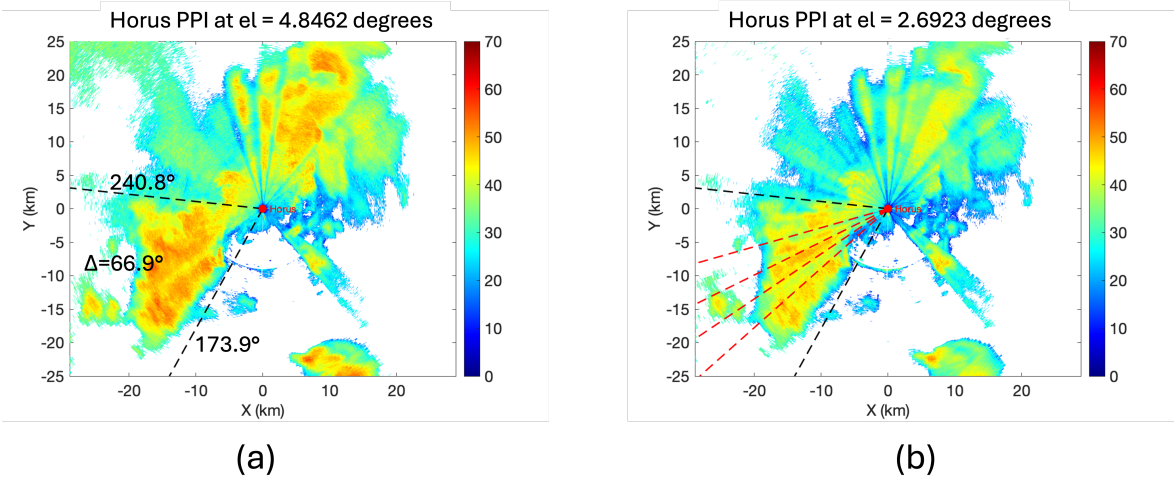


Figure 4.29: (a) Sector of the Z field between 273.9° and 240.8° from north used for process rate analysis at 4.85° elevation. Beam-blocked regions were manually removed for each elevation. (b) Example at 2.69° showing two excluded sectors (red dashed outlines).

environment, providing the vapor necessary to maintain supersaturation and ongoing condensation, i.e., a positive process rate. The resulting enhancement of latent heating reinforces buoyancy and intensifies updrafts, which further reinforce condensation and deposition as the air cools (Houze (1993)).

Furthermore, mass convergence at fine spatial scales can impact the generation of LWC. For example, studies of torrential rainstorms in China have highlighted the importance of accretion of cloud water by both raindrops and graupel, in producing extreme rainfall (e.g., Huang and Cui (2015); Zhao et al. (2025)). This is investigated in Figure 4.31 showing p as a function of the divergence of the 3D wind field. It can be noted on the figure that a reduction in LWC is noted with positive divergence, as signified by a negative p value, whereas negative divergence (convergence) is associated with positive p values indicating generation of mass. This preliminary result is physically consistent and may have implications for helping to better understand storm processes at a fine scale. Future work should consider more heavy rainfall observations

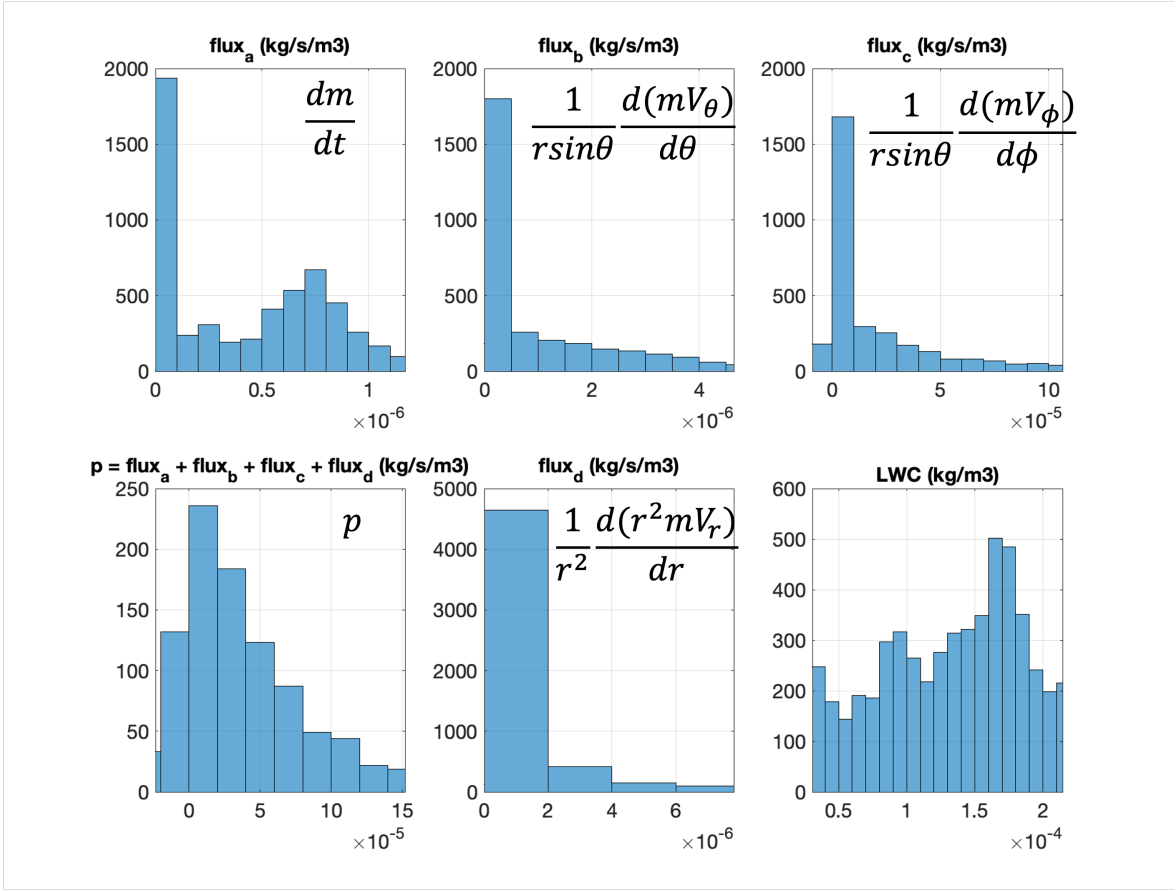


Figure 4.30: Distributions of the four flux terms used in the analysis.

to confirm the influence of small-scale convergence on process rates. It is a promising line of inquiry because other researchers have noted that small-scale convergence can locally enhance vertical motion and moisture accumulation. This effect has been noted in cloud-resolving modeling studies (e.g., Morrison (2012); Pinsky et al. (2008)), and could lead to increased microphysical process rates.

The divergence is computed from the 3D wind field (U, V, W), which has Cartesian coordinates but is laid out on a spherical grid. The wind terms, originally estimated from passive radar returns relative to and on the grid of the KTLX WSR-88D, are regridded, as has been mentioned, to the grid of the Horus radar. Then the divergence is computed from spatial derivatives of the winds.

In order to compute spatial derivatives, we must first convert each grid point from spherical coordinates (θ, r, ϕ) to Cartesian coordinates (x, y, z) using the standard relations

$$x(\theta, r, \phi) = r \cos\phi \cos\theta, \tag{4.8}$$

$$y(\theta, r, \phi) = r \cos\phi \sin\theta, \tag{4.9}$$

$$z(\theta, r, \phi) = r \sin\phi. \tag{4.10}$$

This yields three arrays, X, Y, and, Z defined on the same grid as the vector components.

Since u, v, and w are defined in Cartesian coordinates, the divergence of the vector field is given by the Cartesian expression

$$\nabla \cdot \mathbf{V} = \frac{\partial u}{\partial x} + \frac{\partial v}{\partial y} + \frac{\partial w}{\partial z}. \tag{4.11}$$

Substituting the derivatives into Eq. (4.11) yields the divergence field

$$\mathrm{div}(\mathbf{V})(\theta_i, r_j, \phi_k) = \frac{\partial u}{\partial x} + \frac{\partial v}{\partial y} + \frac{\partial w}{\partial z},$$

expressed at each of the original spherical points of the Horus grid.

Further investigation suggests that the relation between p and the wind field divergence depends on the liquid water content magnitude, as shown in Figure 4.31. Figure 4.32 breaks down the data by showing the relationship for various LWC magnitudes (with units of kg/m^3) magnitude ranges: (a) $0.1e-5 < LWC < 2e-5$, (b) $2e-5 < LWC < 4e-5$, (c) $0.1e-5 < LWC < 2e-5$, and (d) $8e-5 < LWC < 20e-5$. This indicates that there is a relationship between the magnitude of the LWC and the process rate.

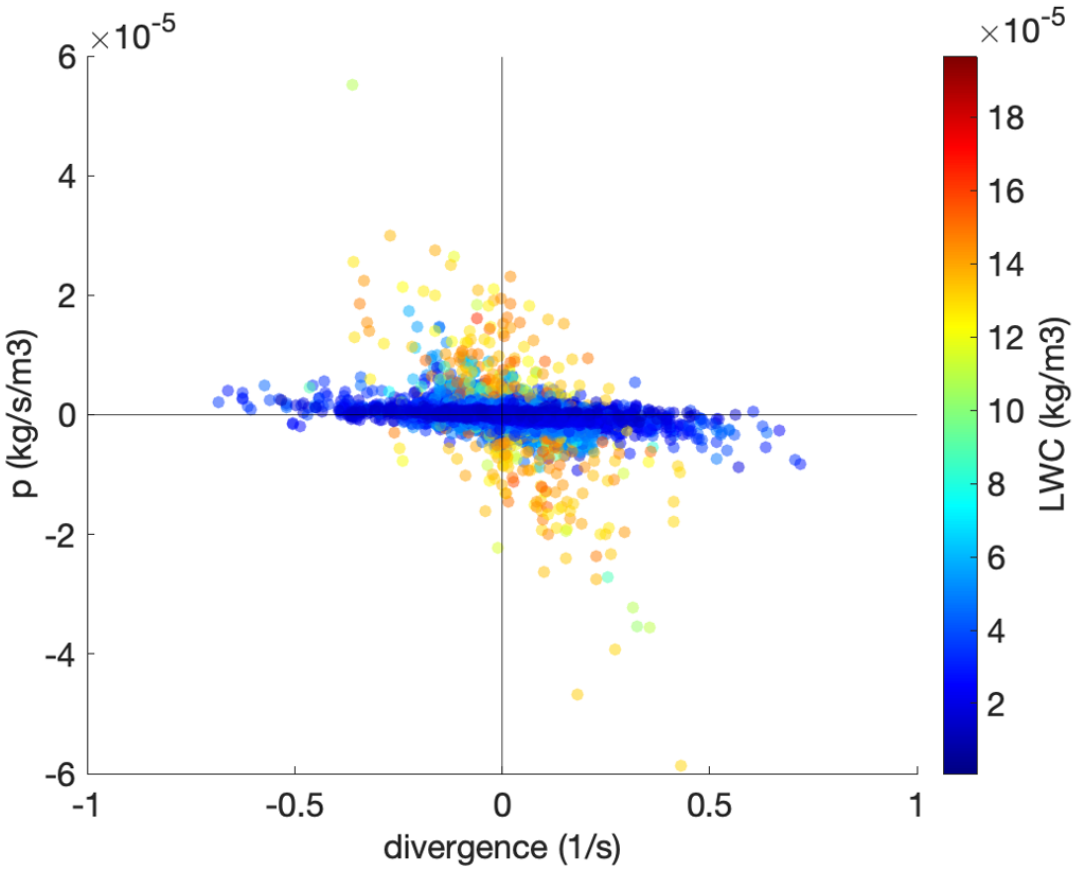


Figure 4.31: Relationship between p and the divergence of the 3D wind field. Positive divergence generally corresponds to reductions in LWC (negative p), while negative divergence (convergence) is associated with LWC generation within the storm.

There is also a dependency on the magnitude of the wind, as is shown in Figure 4.33. Strong positive horizontal winds and small/near-zero vertical winds in combination are associated with high process rate magnitudes. This aligns with the results from Figures 4.30a and b which show advection as having a dominant contribution to the process rates, and it is specifically the horizontal U winds that are contributing the most. The vertical W-winds, especially strong downdrafts, also appear to have an impact, as is shown in Figure 4.30c.

Fluxes have now been shown to have a contribution on sources and sinks of mass within convection, and they also impact R at the surface. Figure 4.34 shows the rela-

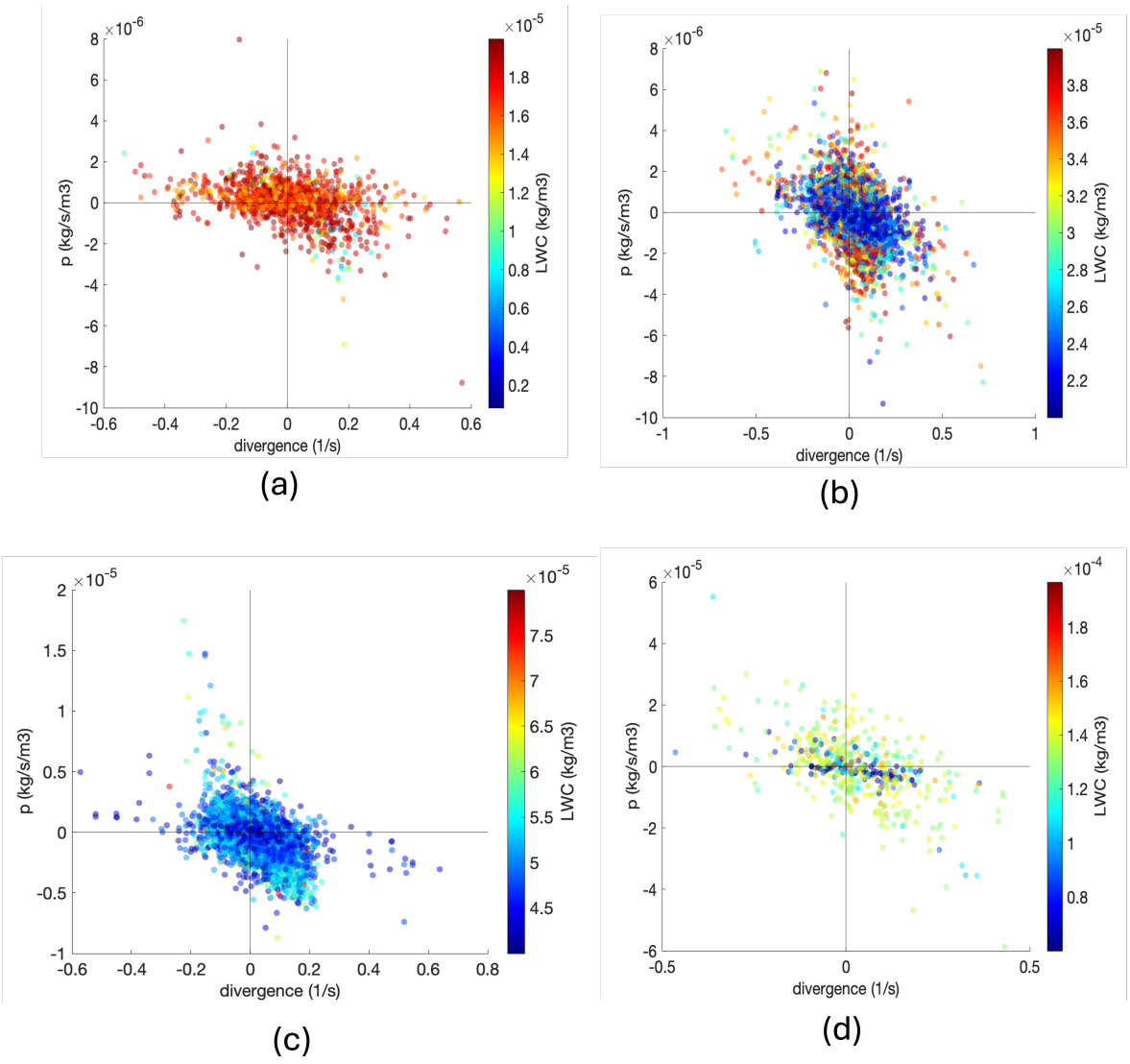


Figure 4.32: Dependence of the p–divergence relationship on liquid water content (LWC). Panels show the relationship for different LWC ranges (kg/m): (a) $0.1\times10^{-5} <$ LWC $< 2\times10^{-5}$, (b) $2\times10^{-5} <$ LWC $< 4\times10^{-5}$, (c) $4\times10^{-5} <$ LWC $< 8\times10^{-5}$, and (d) $8\times10^{-5} <$ LWC $< 20\times10^{-5}$. These subsets illustrate that the mass generation trend varies with LWC magnitude.

tionship between the surface R and the continuity equation flux terms. R is computed with the S-band $R-Z$ relationship $R(Z) = 1.9410^{-2}Z^{0.694}$ (Ryzhkov et al. (2022)). The correlation coefficients between R and the flux terms were also computed. Figures 4.34a, 4.34b, 4.34c, and 4.34d show the relationship between R and $flux_a$ (correla-

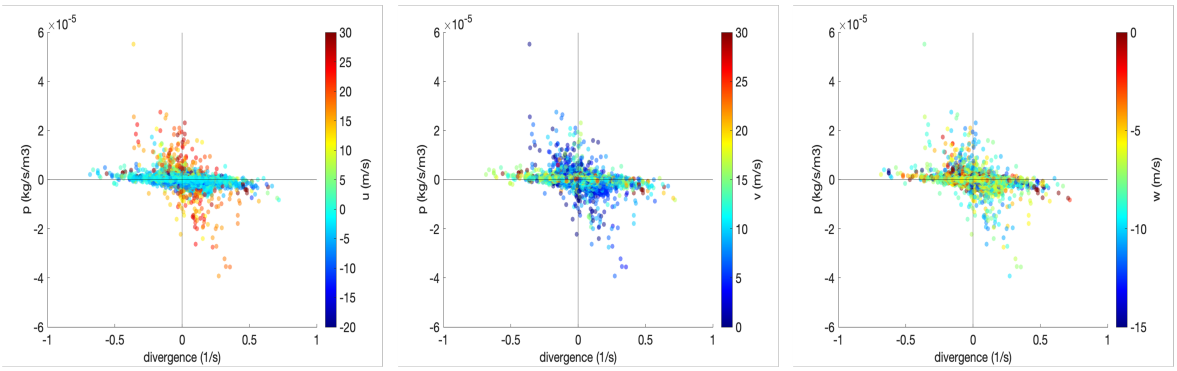


Figure 4.33: Dependence of p on wind magnitude. Strong positive horizontal winds combined with small or near-zero vertical winds are associated with large process rate magnitudes. This is consistent with the flux analysis in Figure 4.30a,b, which shows horizontal advection as the dominant contributor, while vertical motions (especially strong downdrafts) also influence the process rates, as seen in Figure 4.30c.

tion = 0.204), $flux_b$ (correlation = 0.5006), $flux_c$ (correlation = 0.0376), and $flux_d$ (correlation = 0.1312), respectively. The correlation between LWC and R remains the highest of these at 0.885, which may be expected since both LWC and R are derived from Z. Figure 4.34 reveals that $flux_b$ may be the most linearly significant flux impacting, R which is expected since $flux_b$ is the vertical flux of LWC, which is closely related to the vertical derivative of R as indicated in 8.8.

While ground-based PAR systems offer high-resolution insights into microphysical and dynamical precipitation processes, their spatial coverage is inherently limited. Expanding these derivative-based methodologies to satellite platforms presents an opportunity to bridge this gap, enabling global, continuous observation of precipitation structures and evolution. The integration of multidimensional polarimetric concepts with satellite remote sensing could further enhance QPE capabilities by linking surface-based process understanding with broad-scale atmospheric observations. The following chapter explores how emerging satellite missions and observation strategies can extend these principles to spaceborne sensing, highlighting synergistic pathways for improving

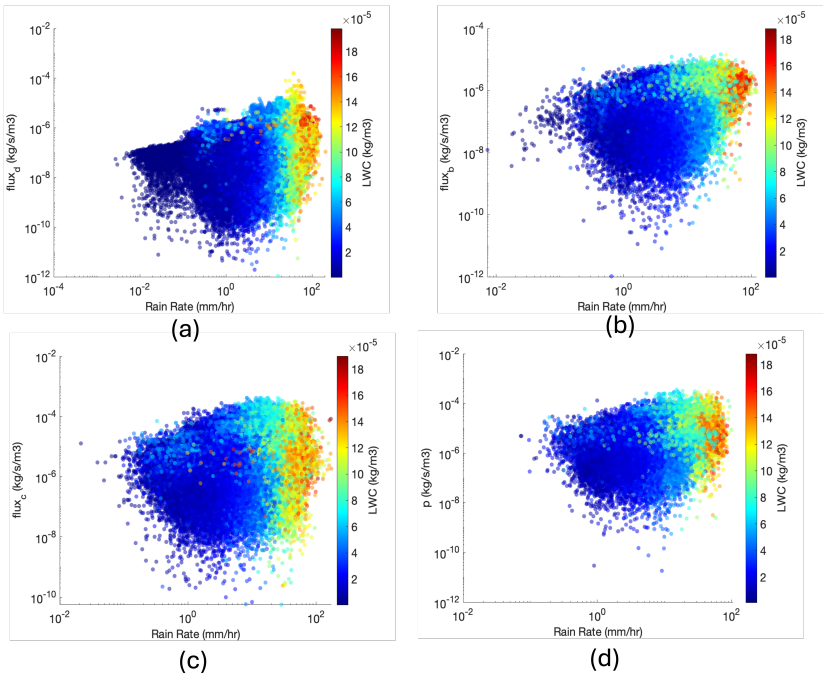


Figure 4.34: The relationship between surface rain rate R and the continuity-equation flux terms. R is estimated using the S-band R–Z relation $R(Z) = 1.94 \times 10^{-2} Z^{0.694}$ (Ryzhkov et al. (2022)). Panels (a–d) show R versus $flux_a$, $flux_b$, $flux_c$, and $flux_d$, with $flux_b$ exhibiting the strongest linear relationship. LWC remains most strongly correlated with R, reflecting their shared dependence on reflectivity.

precipitation retrievals through combined radar and satellite perspectives.

Chapter 5

Satellite Opportunities: Enhancing the Continuity Framework

5.1 Temporal Bridging of Satellite Gaps with Phased Array Radar

Building on the discussion of spatial and temporal advancements that PAR brings to ground radar observational capabilities, the following chapter explore their applications to the enhancement of satellite radar retrievals of precipitation and convection through uniquely collocated ground and satellite radar observations of convection. A separate study presenting an analysis of ground variability enhancements for satellite radar observations with the use of MRMS data is explicated in Appendix 9. In this section, by examining a real-world event through the complementary perspectives of two radars, this case demonstrates how spatial and temporal enhancements potentially offer a more comprehensive understanding of atmospheric processes of dynamic weather systems. The following analysis not only showcases the distinct contributions of each radar but also highlights the opportunity for synergistic insights through their integration, insights that neither could achieve alone. This case study serves as a steppingstone to the final section in this chapter, which proposes a path forward for expanding the joint application of satellite- and ground-based radars. By identifying key opportunities for

coordinated use, we propose a framework for future research, data integration strategies, and methodological innovations that aim to maximize the scientific return from combined observational assets and target some current key leading science objectives in the field of hydrometeorology.

The last 20 years have seen an increasing convergence between space- and ground-based weather radar observations to study precipitation and convection. Spearheaded with the Tropical Rainfall Measuring Mission (TRMM; Kummerow et al. (2000)) Ground Validation initiative (GV; `https://trmm-fc.gsfc.nasa.gov/trmm_gv/links.php/`) and expanded through the Global Precipitation Measurement GV program (GPM; (Hou et al. (2014), Hou et al. (2014)), Petersen et al. (2020b)), sub-orbital radar observations support orbital objectives for accurate precipitation science and applications (Kirstetter et al. (2013); Gatlin et al. (2020); Porcacchia et al. (2019)). While their profiling capabilities provide unique information on the vertical distribution of precipitation and convective storms, spaceborne radars have observation gaps when it comes to probing key characteristics and processes, including accurate quantification of precipitation and convective motions (Battaglia et al. (2020), Valdivia et al. (2022)). Ground-based radars are well-established assets for assessing space-based retrieval performance (e.g., Kirstetter et al. (2020)) but they also address critical science objectives that the orbital radars cannot achieve, like documenting detailed processes that occur on small horizontal spatial scales, have a significant temporal component, or are beyond the reach of orbital measurements.

Ten years ago, concomitant weather radar technological advances on space-based (dual-frequency) and ground-based (dual-polarization) platforms both targeted the characterization of hydrometeor species and distributions, leading to improved quantitative estimation of precipitation (e.g., Ryzhkov et al. (2014); Liao and Meneghini (2022); Iguchi et al. (2012)). We are currently witnessing another convergence of space-

borne and ground-based technology that aims at shedding light on dynamical processes in precipitation and convection that link 3D air motions, cloud microphysics, and storm dynamics, in line with the Decadal Survey's recommendations on the central theme of convection and heavy precipitation and the question, "Why do convective storms, heavy precipitation, and clouds occur exactly when and where they do?" (National Academies of Sciences, Engineering, and Medicine (2019)). Snapshots from satellite radars in orbit today do not offer the temporal continuity that is critical for assessing stormwater and energy transport. Recent and planned satellite missions target vertical motions and water fluxes in storms by using Doppler technology (e.g., EarthCare; Illingworth et al. (2015)) and time-separated radar reflectivity measurements of the same convective cloud to capture the time evolution of radar reflectivity (e.g., NASA's Investigation of Convective Updrafts (INCUS) mission; Dolan et al. (2023), Van den Heever et al. (2022), Haddad and Sy (2024); Stephens et al. (2019)). On the ground, PAR enables rapid sampling of polarimetric radar variables to capture transient, fast-evolving signatures of updraft and downdraft structures by means of rapid radar variable capture in precipitation and convection and enables dense horizontal sampling, especially above 5–6 km altitude, wherein lies an opportunity for the capture of the characteristics of deep convection. In particular, PARs can be used to benchmark time-spaced sampling satellite missions via the capture of storm radar signature decorrelation times. Through the rare capture of PAR profiling of a storm at the same time as a Ku-Ka-band spaceborne radar overpass, decorrelation time capture is demonstrated with the Horus ground-based polarimetric PAR collocated with the GPM Dual-frequency Precipitation Radar (DPR). The advantage of high-horizontal resolution S-band observations is also demonstrated. Future opportunities for the enhancement of spaceborne radar observations using PAR's high-temporal sampling are highlighted.

Section 2 presents the setup of this unique case study involving a single PAR collocated with the GPM overpass. Section 3 analyzes the ground-based temporal characteristics of the radar observations in the times immediately around the time of the DPR overpass. Conclusions are made by discussing opportunities offered by ground-based polarimetric PAR observation decorrelation times for space-based missions.

5.1.1 Convective Weather Demonstration

On July 7, 2024, at 23:38:18 UTC, the GPM-DPR captured a precipitating convective system in central Oklahoma (Figure 5.1(a)). Concomitantly, the "Horus" S-band polarimetric PAR (Palmer et al. (2023b)) sampled the storm with a series of range-height-indicator (RHI) scans separated by 0.76 s within the swath of the DPR to capture collocated storm cross-section measurements (Figure 5.1(b)). GPM-DPR specifications are compared to Horus in Table 3.1. The DPR observes single-polarization radar reflectivity profiles using Ku- and Ka-band frequencies from the vantage point of space and with a surface footprint size of about 5 km (3 km for INCUS with a 9 km swath) (NASA (2023a), Dolan et al. (2023)). Horus samples storms at S-band from the ground, covering a significant horizontal extent with a maximum elevation angle of 17°, a nominal 2.58°beamwidth, and a range resolution of 19.2 meters (resolution along the quasi-horizontal radial). The size of the Horus beam tangent to its radial direction (along the quasi-vertical dimension) is about 0.68 km at a range of 15 km from Horus and about 1.35 km at a range of 30 km from the radar. With a 250 m range resolution, the DPR samples profiles of reflectivity at a higher vertical resolution than Horus, especially at far ranges, while Horus maintains a higher horizontal resolution.

Figure 5.1(a) shows the observed DPR swath of attenuation-corrected Ku-band reflectivity values estimated at the surface. The black star indicates the starting point of the DPR cross-section shown in Figures 5.1(c-d). The blue dot in Figures 5.1(a-b)

Table 5.1: Radar Specifications for the considered data (NASA (2023a), Palmer et al. (2023b), Masaki et al. (2020), and `https://arrc.ou.edu/radar_horus.html`)

Radar	Horus	GPM KuPR	GPM KaPR (matched-scan)
Space or Ground	Ground-based	Space-based	Space-based
Polarimetric	Yes	No	No
Operating Frequency	2.7–3.1 GHz	13.6 GHz	35.5 GHz
Horizontal Field of View	50 km from the radar (fixed azimuth RHI 230°from North)	245 km swath	245 km swath
Vertical Field of View	0-29.17°elevation (e.g. 15 km altitude at 30 km from the radar)	above 1.62 km (blind zone)	above 1.62 km (blind zone)
Nominal Beamwidth	2.58°	0.701°	0.701°
Peak Transmit Power	8.32 kW (each polarization for 832 active elements)	1030 W	146 W
Max Pulse Width	100 μs at 10% duty cycle	two 1.667 μs pulses	two 1.667 μs pulses
Range/Vertical Resolution	19.2 m (with pulse compression)	250 m vertical resolution	250 m vertical resolution
Temporal Resolution	0.76 s (between RHIs)	None (moving platform)	None (moving platform)
Sensitivity (1 pulse)	4.3 dBZ at 50 km	15.5 dBZ	19.2 dBZ

indicates the surface position of Horus in Norman, Oklahoma. The horizontal extent of the GPM cross-section is shown in Figure 5.1(b) leading from the black star marker as a dotted line, along with a blue-dashed line indicating the horizontal extent of the Horus RHI measurement. Figures 5.1(c) and 5.1(d) show the DPR attenuation-corrected

Ka- and Ku-band observed reflectivity profiles, respectively. The DPR profiles are associated with moderate to deep convection, with Ku-band 30 dBZ echo tops between 6 and 13 km in altitude. Accordingly, the DPR hydrometeor distribution retrievals suggest large mass-weighted mean diameter D_m values (close to 3 mm) in the ranges of 20 to 30 km along the track where stronger Ku-band echoes are observed. The corresponding normalized intercept parameter N_w retrievals are noticeably lower around 2.5 $m^{-3}.mm^{-1}$. Note that the DPR retrieval estimates D_m are N_w within each radar resolution volume and cap D_m values at 3 mm to prevent retrieval instabilities; hence, this area of the storm might test the limits of DPR microphysical retrieval. Figures 5.1(g) and 5.1(h) show corresponding Horus S-band reflectivity profiles at native resolution and resampled to the GPM resolution, respectively, and illustrate how storm structural information is degraded when transitioning from the Horus native resolution to the DPR's resolution. Consistent with DPR, Horus displays high reflectivity values between 20 and 30 km along-track. Horus S-band reflectivity profiles at native resolution (Figure 5.1(g)) display finer structures in the along-track path than the GPM profiles (Figures 5.1(c) and 5.1(d)). In addition, resampled Horus profiles in Figure 5.1(h) show structure within the DPR blind zone (about 1.2 km above the surface). The GPM-DPR provides high vertical resolution ($\sim 250m$) but suffers from poor horizontal resolution ($\sim 5km$), that struggles to resolve convective cell structure. Horus offers both high vertical and horizontal resolution close to the radar, though the vertical resolution decreases because beam width increases with distance.

Figure 5.2 shows the collocated cross-section of Horus horizontal reflectivity (Z), differential reflectivity (Z_{DR}), and specific differential phase (K_{DP}) at the time of the GPM overpass. While not discussed here, a major benefit of ground-based polarimetric variables is their insight into hydrometeor classification and precipitation microphysics (e.g., particle size distribution; Cao et al. (2010)). Z is a radar variable proportional to

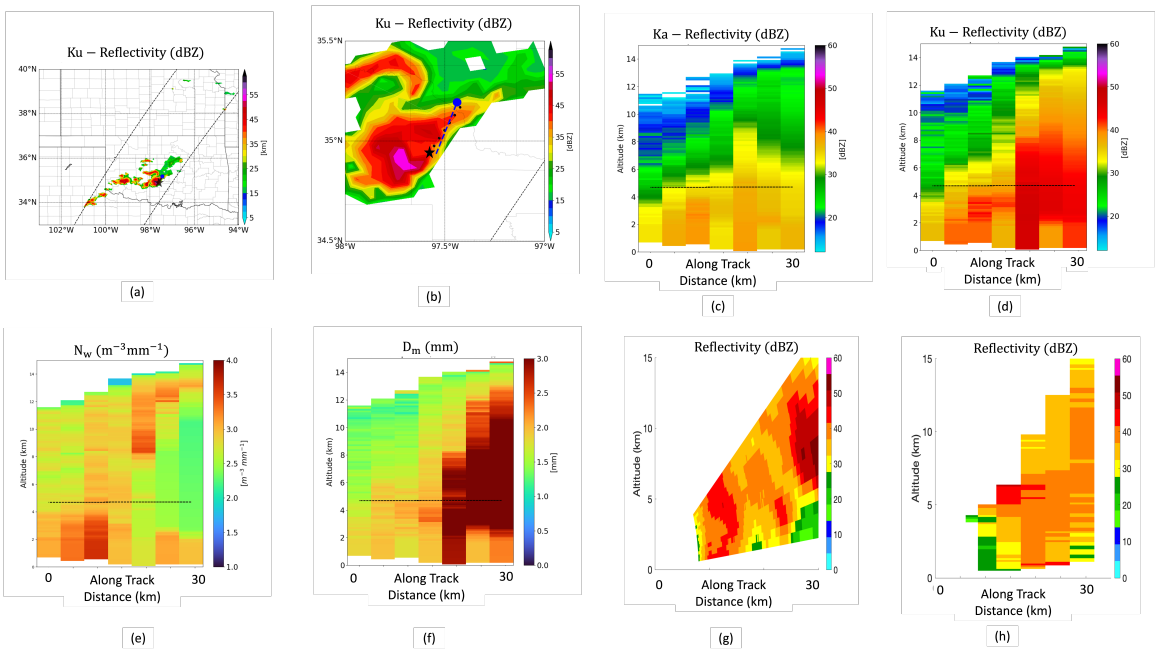


Figure 5.1: DPR attenuation-corrected Ku-band estimated surface reflectivity at 23:38:18 UTC on July 7, 2024, over (a) the DPR swath and (b) zoomed in on the location of Horus (blue dot) along with the Horus RHI extent (blue dashed line); DPR cross sections of attenuation-corrected reflectivity along the black dotted line in (b) for (c) Ka-band and (d) Ku-band; Cross sections of DPR estimated hydrometeor distribution parameters: (e) the log of the normalized intercept parameter N_w and (f) the mass-weighted mean diameter; Collocated Horus RHI S-band reflectivity (g) at native resolution and (h) resampled to the resolution of the GPM-DPR; In panels (c) to (f), the horizontal dotted lines figure the isotherm 0° C altitude.

the particle number density and the volume-integrated horizontal return power from hydrometeors in a radar resolution volume where large particles dominate the backscattered signal. Z_{DR} is the ratio between horizontal and vertical reflectivity that provides an indication of the hydrometeors' shapes (and sizes in the case of raindrops). K_{DP} is a range derivative of the differential phase between received horizontal and vertical signals, positive for oblate raindrops. While there are different approaches to calculating K_{DP}, the Horus K_{DP} shown in Figure 5.2 is computed via a direct range derivative of a smoothed differential phase signal along range using a 200-range bin moving average window. Figure 5.2 also displays the height of the isotherm 0° C at an altitude of 4.6

km (sounding information from the University of Wyoming Department of Atmospheric Science: `https://weather.uwyo.edu/upperair/sounding.html`). Qualitatively interpreting these polarimetric variables provides insight into the storm characteristics. Signatures of heavy rainfall are apparent in the liquid zone at a surface range of 25 km from the radar with a K_{DP} core along with $Z_{\mathrm{DR}} \geq$ of 2 dB and $Z \geq$ of 40 dBZ. Such large values of Z_{DR} indicate large hydrometeors, which is expected by the DPR retrievals showing large mass-weighted mean diameter D_m values in the corresponding columns (see Fig. 5.1(f)). Some altitude discrepancies are expected because of a small misalignment between the Horus and DPR vertical cross sections (Fig. 5.1(b)). At 10 km from Horus, located at 0 km, $Z \geq 40$ dBZ along with lower values of Z_{DR} and K_{DP} than at 35 km indicate a high concentration of small drops, which is also consistent with the GPM-DPR retrieved number concentration (N_{w}) and mean drop diameter (D_{m}) measurements shown in Figures 5.1(e) and (f).

Radar systems from the ground and space have different limitations and also complementary advantages for understanding precipitating and convective systems. One limitation of space-based radars is that they operate on moving low earth orbit (LEO) platforms and capture single spatiotemporal snapshots of a storm. Time-separated concepts for upcoming space missions such as INCUS aim to capture water and energy transport in storms by observing reflectivity profiles offset in time. For example, INCUS will fly a train of three time-separated Ka-band radars to capture along-track Ka-band radar reflectivity profiles at 30, 60, and 90 second intervals (Van den Heever et al. (2022)). The sampling interval (or interval time) is the revisit time between two radar observations of the same volume of atmosphere. Since Ka-band is heavily attenuated in heavy precipitation, key storm features hidden to the satellite observations are revealed from the surface level to the top with PAR S-band returns that penetrate into the core of the precipitating storm system. Analyzed in the next section, PAR

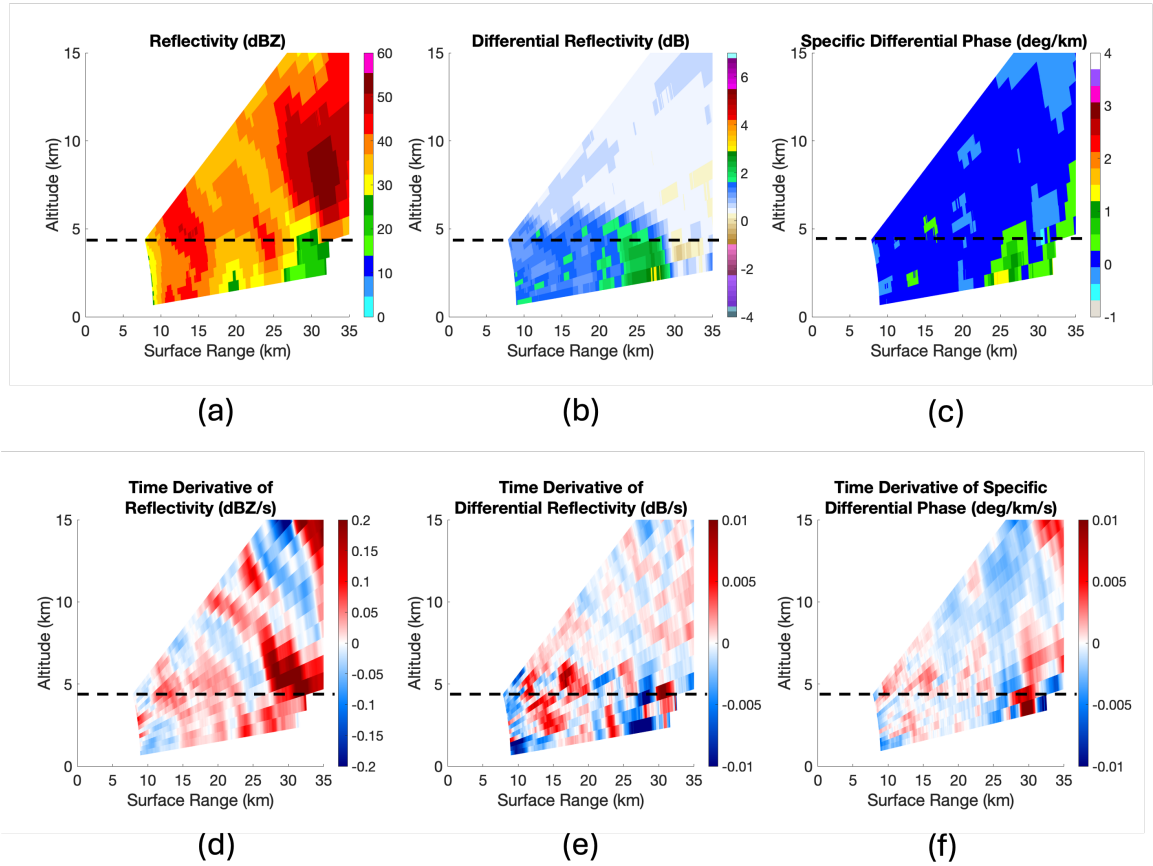


Figure 5.2: Horus snapshot of (a) Z, (b) Z_{DR}, and (c) K_{DP} as well as (d) dZ/dt, (e) dZ_{DR}/dt, and (f) dK_{DP}/dt at 23:38:18 UTC on July 7, 2024. The horizontal dotted line indicates the isotherm 0°C altitude.

can observe a storm's temporal evolution within the space-based radar footprint with its finer temporal sampling (1 s) over longer time periods than the snapshot provided from space.

5.1.2 Analysis

Temporal changes in storms are observables targeted by ground-based and spaceborne PAR radar technologies. The reader is referred to Stephens et al. (2019) which describes the principles of estimating vertical momentum and velocity in convective storms from temporal changes to satellite observed Z. On the ground, PAR technology

observes temporal changes in storms that are typically missed by single sensors onboard LEO platforms and only sparsely documented by trains of satellite pairs. Specifically, ground-based PARs can sample temporal changes over shorter time intervals (e.g., 0.76s for Horus versus 30s for INCUS) and over longer time periods (e.g., the storm was sampled for 40 min by Horus, while a satellite overpass is quasi-instantaneous). Ground-based polarimetric PAR detects temporal changes of more variables than from space with Z, Z_{DR} and K_{DP}. For the July 7, 2024 storm, these temporal changes are expressed as time derivatives dZ/dt, dZ_{DR}/dt, and dK_{DP}/dt and are plotted in Figure 5.2(d,e,f), respectively. Time derivatives are computed using a regression fit 30 s around the DPR overpass time (consistent with the finest INCUS time separation). With a sampling rate of ∼0.76 s, the fitting sample size (∼40) is significantly larger than the satellite sample (2) and deemed large enough to provide statistically more reliable and accurate results over the same time period. Time derivatives provide signs and rates of change of polarimetric radar variables. These changes are contributed to by microphysical processes, storm horizontal advection, and vertical transport Dolan et al. (2023). Note that horizontal advection is significant because the storm traveled at an estimated 40 $km.h^{-1}$ orthogonal to the RHI plane. A few features can be noted from these panels. First, all time derivatives display coherent structures in space, information that can be used to characterize underlying microphysical processes and dynamics (Dolan et al. (2023)). One can infer changes in the storm. For example, at ∼30 km from Horus, a positive dZ/dt from altitudes 3 to 8 km ($dZ/dt \geq 0.2$ $dBZ.s^{-1}$, i.e., Z increasing by more than 6 dBZ over 30 s) coupled with a decreasing Z aloft from altitude [8-12]km ($dZ/dt \leq$ -0.05 $dBZ.s^{-1}$) suggests an intensification toward the surface associated with descending hail and rain associated with the large Z core (∼55 dBZ; see Figure 5.2(a)) (Williams (2016)). This temporal derivative signature is likely associated with a descending hail core and a downburst (with some contribution

of advection). Note that a spaceborne Ka-band radar has usable reflectivity returns to a depth of ∼5 km from the storm echo top height, allowing for reflectivity changes by INCUS to be observed in the upper part of highly convective storms (Chase et al. (2025)). The behavior of the storm at lower levels that is necessary for determining the causes of the increase or decrease aloft evades Ka-band radar observations. Regarding other ground-based polarimetric observations, the same location has also increasing Z_{DR} and K_{DP} in the liquid phase, confirming the intensification of precipitation toward the surface. Overall the time derivatives indicate rapid temporal changes near convective activity, as expected. Besides their usefulness for scientific studies, PAR temporal derivatives show promise for ground validation of satellite systems aimed at capturing storm dynamics.

Through their continuous temporal sampling of storms, fast-scanning ground-based radars uniquely provide the characteristic time evolution of radar variables that can benchmark spaceborne sampling. It is demonstrated with this case study and with using the INCUS planned along-track sampling of 30, 60, and 90 s sampling intervals. Note that more such observations are recommended for a statistically significant validation effort. Thanks to their high temporal resolution (Table 3.1), PAR observations offer unique insights into the temporal structure of precipitation and convection. The decorrelation times of the Horus polarimetric variables computed using geostatistics are a useful benchmarking metric (Howarth (1979)). Note that while satellite and ground radar operate at different frequencies and vantage points, S-band and Ka-band reflectivity returns trend monotonically (Biswas and Chandrasekar (2018),Mroz et al. (2023),Baldini et al. (2012),Heymsfield et al. (2023),Leinonen et al. (2011)), which results in comparable decorrelation times. A variogram analysis is applied to the 40 min time series of Horus observations at each elevation and gate following a procedure described in Kirstetter et al. (2010). A standard Gaussian variogram model of the form

of Equation (3.2) is fit to the empirical variogram analyzed at each location over time

Figure 5.3 shows temporal variogram ranges for Z, Z_{DR}, and K_{DP} derived from the series of Horus RHI observations taken at 0.76-s intervals between 23:19:21 UTC to 23:59:59 UTC. Notably, variogram range values display spatial structures within the RHI plane despite having been estimated independently at each spatial location. Below the freezing level (5 km altitude), decorrelation times tend to be larger (>12 min) than above (<8 min). This suggests that the ice and liquid phases of the storm involve processes with different dynamics, and/or that temporal changes in the size distributions and scattering properties of hydrometeors impact the radar variables differently according to the phase. Given that ice has more variable scattering properties than liquid hydrometeors, it is expected that temporal changes in the ice phase are reflected by shorter deccorelation times. The INCUS sampling intervals are shorter than the decorrelation times of reflectivity observed by PAR, which makes them suitable to estimate the temporal changes of reflectivity in this case. Decorrelation times are smaller for K_{DP} and Z_{DR} than Z because each variable is sensitive to different characteristics of the particle size distribution. For example, temporal changes in Z_{DR} can reflect temporal changes in the mean size of hydrometeors, while K_{DP} changes relate to changes in both the mean size and the concentration of hydrometeors in the radar resolution volume. Z is primarily impacted by the larger scattering particles of the distribution. This suggests that temporal changes in mean particle sizes and/or number concentrations occur over shorter time intervals than temporal changes in Z.

Fast-sampling PAR systems enhance data richness by offering temporal derivatives and facilitating weather characterization through decorrelation times. These insights pave the way for innovative ground validation and weather lifetime studies.

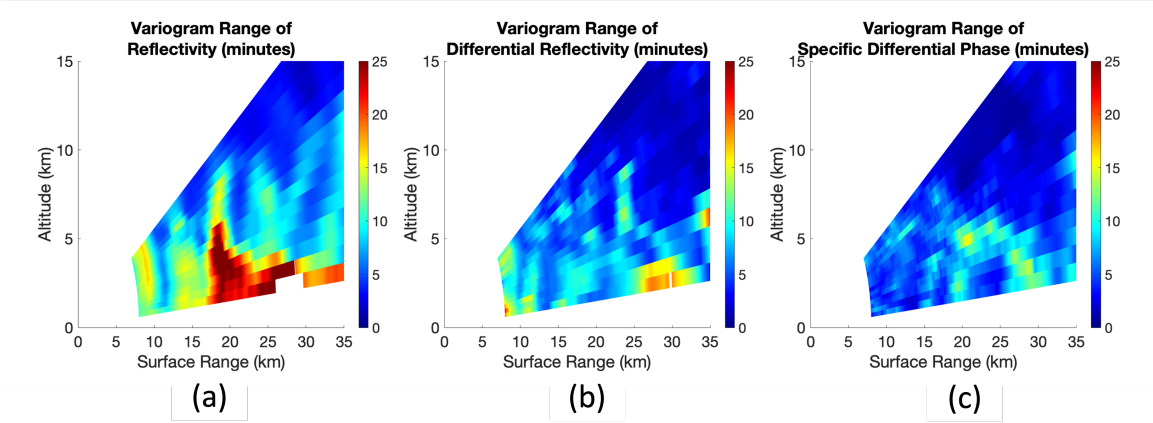


Figure 5.3: Horus decorrelation time of (a) Z, (b) Z_{DR}, and (c) K_{DP} over a variogram fit in time from 23:19:21 UTC to 23:59:59 UTC

5.1.3 Conclusions

A convective storm concomitantly observed by the GPM-DPR and Horus, serving as an example of the complementarity between ground and space radars in observing temporal changes in storms has been shown. It highlights the benefits from less attenuated ground-based radars that can peruse into storms by combining dual-polarized signal (insight into microphysics) and fast-scanning capabilities (insight into storm evolution). This case illustrate the relevance to upcoming time-separated satellite mission concepts with statistically robust estimates of temporal changes of reflectivity, and with radar observations decorrelation times used as a benchmark for INCUS fixed sampling intervals.

LEO satellite concepts are being developed that expand on current snapshot sampling capabilities of precipitation to capture precipitation and convection changes. The dynamics and processes that these satellite missions seek to observe benefit from their synergy with ground-based radars, particularly for scientific studies and validation. Rapid polarimetric PAR data can be used to compute storm decorrelation times, provide a temporal context to satellite observations, help to identify condensed hydrom-

eteor mass flux structures, and may be used for satellite uncertainty characterization. An integrated interpretation of satellite/PAR hydrometeor analysis is possible through their complementary vantage points, frequencies, and vertical/horizontal resolution advantages. In the context of NASA Decadal Survey's recommendations on precipitation and convection, these capabilities are necessary for assessing space-based estimates of dynamical processes and for addressing science objectives that the orbital radars cannot achieve such as documenting detailed processes that occur on small spatial scales, have a significant horizontal advection component, or are beyond the reach of attenuated Ka-band measurements. While the combination of spaceborne and ground-based weather radars have much to offer our understanding of precipitation and convection, the exploration of their complementary insights is still in its infancy.

5.2 NASA FINESST Proposal: Combining Radar Observations from Ground and Space

This chapter has demonstrated, through the capture of a rare overpass between the GPM DPR and a fast-scanning PAR, some of the potential value provided by ground radars that can help to enhance satellite only radar observations of precipitation. In this work, PAR provided less attenuated S-band polarimetric information about the precipitation near the surface at high temporal and horizontal resolution, while satellite radar offered a complementary view of the precipitation from Ku- and Ka-band with a vertical perspective highlighting precipitation aloft with a very high vertical resolution. Together, these relative platform advantages can help to reveal dynamics that may remain undetected using either instrument alone. However, the demonstration focused on a single convective event and did not explore the full range of potential configurations or applications of this dual-instrument approach. Building on these promising results,

the following proposed work was submitted to NASA to the Future Investigators in NASA Earth and Space Science and Technology (FINESST) program and details an approach for expanding this line of inquiry by systematically exploring new joint instrument retrievals using the combination of satellite and ground radar. The goal is to develop a more generalized understanding of how the synergistic use of these instruments can enhance insight across broader applications, potentially informing future workflows and instrument design in the field of radar meteorology.

5.2.0.1 Background

The coupled process continuum of clouds, convection and precipitation is a priority "designated observable" identified in the 2017 Earth Science Decadal Survey. In the coming decades there is an enhanced risk for extreme events including flooding and drought which also impacts agriculture, water resources including freshwater, public health, and mortality (Basara (2022)). Improved QPE and process understanding aids in improving weather and climate models which serve as warning and risk reduction planning tools (Basara (2022)). NASA's work to improve weather forecasts and climate models extends to the Atmosphere Observing System (AOS) composed of a constellation of satellites and including the use of Ka–band, W–band, and Ku–band Doppler Radars (NASA (2023b)). This is an efficient step towards improving model representations of cloud, precipitation, and convection which have been recognized to be one of the largest sources of uncertainty in future projections of climate change. Current and future NASA missions such as the Global Precipitation Measurement (GPM), the INvestigation of Convective UpdraftS (INCUS; planned in 2026) and the Atmosphere Observing System (AOS; planned in 2028) aim at improving the physical understanding of these atmospheric processes, quantifying associated fluxes such as precipitation, and representing them in global cloud resolving models (e.g., Hou et al.

(2014), Skofronick-Jackson et al. (2018)).

All these missions rely in-part on weather radar observations. Because atmospheric microphysical observations associated with clouds, convection, and precipitation are constrained by the capabilities of the instruments used to measure them, there is a need to understand the process and flux information content that can be extracted from ground-based/suborbital and spaceborne radars. The proposed work will explore this information content by using a simulation framework involving multiple spaceborne and ground-based radar instruments: the GPM Dual-frequency Precipitation Radar (DPR; Ku– and Ka–band) targeting precipitation, the INCUS train of three scanning Ka–band radars designed for convective mass fluxes, the AOS Ku–band Doppler radar for precipitation processes within convection, and the ground-based S–band 1988 Doppler Weather Surveillance Radar (WSR-88D) and future phased-array radar (PAR, e.g., Kumjian et al. (2022)). By quantifying the observation capability differences (e.g., resolution, frequency, sensitivity, and orientation) as applied to microphysical properties (e.g., hydrometeor size, shape, phase) and processes (e.g. evaporation, melting, drop-breakup, and collision-coalescence) from the instruments and their synergistic use, this work will address a need to understand and optimize our capability to characterize atmospheric processes from current and future ground- and spaceborne instruments. Probabilistic retrievals of microphysical fluxes, process rates, and precipitation rates that account for uncertainty will be developed to quantify the information from radar returns from both individual instruments and joint instrument observations at their beam intersections. It will also address the important need to quantify the contribution of suborbital observations to address science objectives which cannot be adequately resolved from space. It will help to quantify the contribution of suborbital observations to supplementing space-based observations. On the ground, PAR technology is an identified solution to provide more spatially and temporally continuous suborbital observa-

tions of the atmosphere.. From space, current radars on low-orbiting platforms (e.g., GPM DPR) only provide discontinuous snapshots of atmospheric processes that miss convective and precipitation fluxes. The planned INCUS design attempts to capture time-varying observations (https://eospso.nasa.gov/missions/investigation-convective-updrafts-evm-3) and/or vertical motions (e.g., The Earth Cloud Aerosol and Radiation Explorer (EarthCare), Atmospheric Observing System (AOS)). Questions remain open (1) on the optimal time increments, spatial resolution, and sensitivity required to capture the spectrum of precipitation and convective fluxes from space, and (2) on the role of suborbital platforms and their implementation strategies to address orbital science objectives, such as documenting detailed cloud-convection-precipitation interaction processes that occur on small spatial scales, have a significant temporal component, or are beyond the reach of the orbital measurements (e.g., blind zones , see https://aos.gsfc.nasa.gov/suborbital.htm).

My current PhD work is poised to answer the question: "How can PAR technology aid in the improvement of Quantitative Precipitation Estimation (QPE)?" Fast scanning ground-based radars offer dense sampling of the atmosphere that provide insight into vertical and temporal changes in polarimetric variables. These changes over unprecedented fine scales are hypothesized to characterize and quantify microphysical processes and precipitation fluxes. Altitude derivatives of polarimetric variables are related to process occurrence by the sign of the change in altitude and process rates by the magnitude of the change in altitude of condensed water mass. Time derivatives of radar variables are related to vertical velocities (Palmer et al. (2023b)) and fluxes of condensed water mass, e.g., precipitation rate, or convective mass fluxes.

I have proposed novel height and time derivatives of polarimetric variables and have applied them to PAR observations collected during a convective case in August 2023 in Norman, OK. These new PAR variables were successfully used to classify domi-

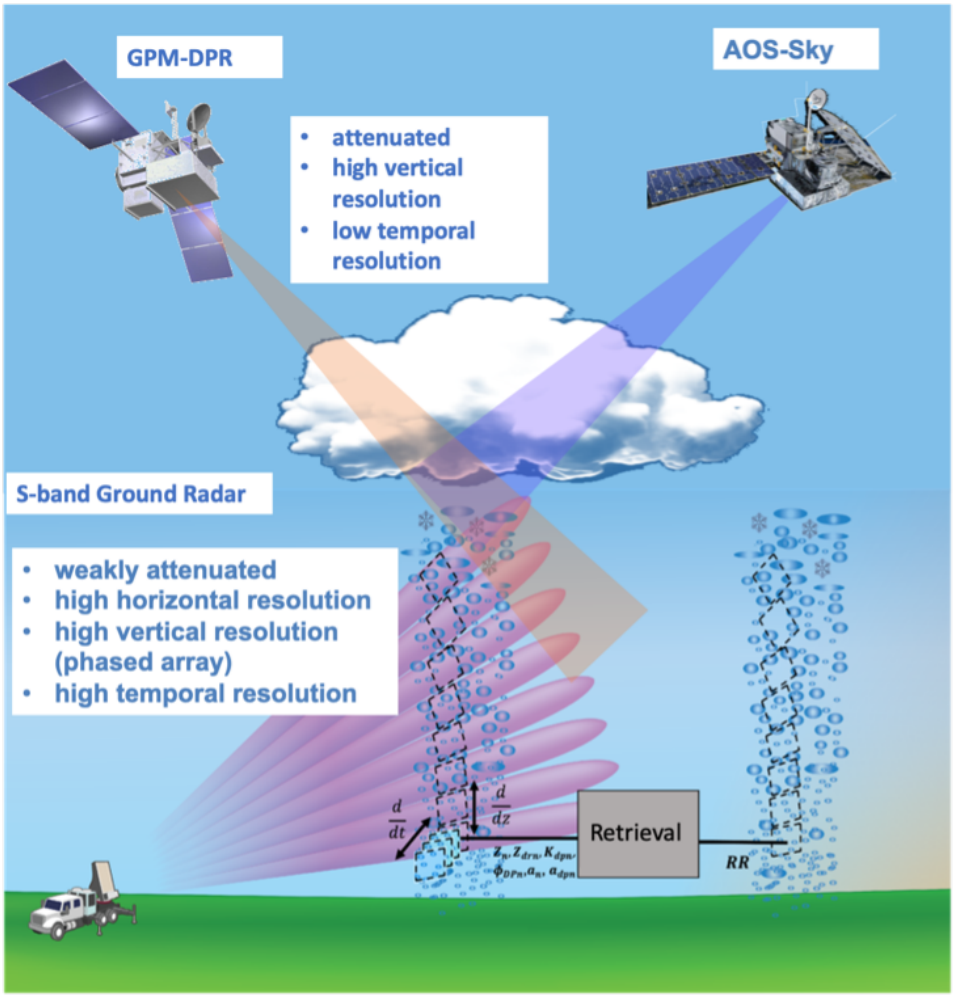


Figure 5.4: This work will develop retrievals predicting precipitation process-rates, fluxes, and vertical motion from simulated radar returns from individual and combined instruments that builds upon current work on PAR precipitation rate retrievals. (Note: Figure not to scale)

nant processes of collision-coalescence (CC) and break-up (BU) and improve QPE over conventional dish (slower) radar-based estimates (Fig. 2). It was found that QPE conditioned by process signatures improved QPE accuracy (Fig. 2 and Stephens et al. (2019)). I have used probabilistic precipitation rate (PR) estimators (Dixon et al. (2024b)) enable the quantification of uncertainty. This working estimation framework can be applied to study precipitation processes and fluxes signatures in spaceborne radar observations. Hurricane Ian (2023) provided a unique opportunity to analyze

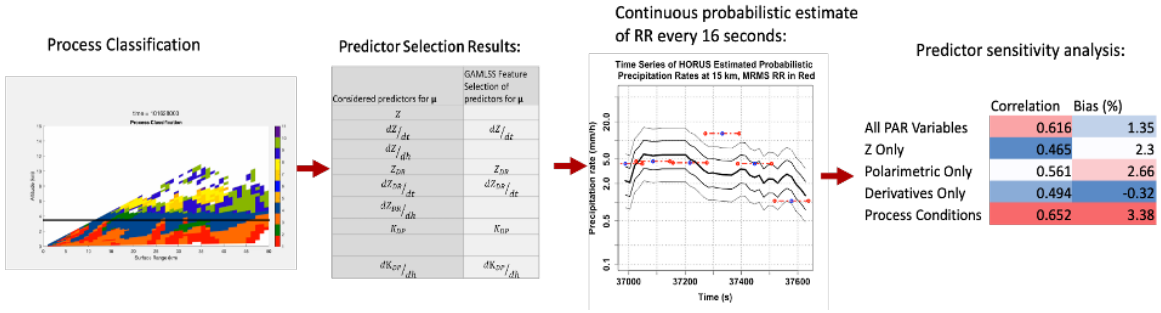


Figure 5.5: Process classification improves probabilistic precipitation rate estimation performance, allowing for continuous PAR estimates of precipitation in time and space (from Stephens et al. (2019).)

process rates in the bind zone of the GPM DPR with a the RaXPol fast-scanning radar. Due to the unique combination of instruments that were used during this event, ground and space-borne radar retrievals were applied to quantify and compare inferred precipitation processes. Signatures of CC and BU processes (as expected in a landfalling hurricane) were consistently found across RaXPol and DPR observations. Process rates were quantified by altitude derivatives of numbers of concentration and mean diameter of the particle size distribution (PSD; Kirstetter et al. (2015a)). It was shown that the resolution of the DPR observation significantly reduces the range of estimated process rates relative to the resolution of RaXPol. Such analysis offers potential solutions for satellite blind-zone filling techniques by extending observed processes into the blind-zone region (Kirstetter et al. (2015a)).

To study precipitation microphysical processes and fluxes, a 1D spectral bin microphysics (SBM) model developed at NOAA/CIWRO has been used to track the evolution of microphysical parameters, including the PSD of hydrometeors, as processes of evaporation, sublimation, melting, shedding, and breakup occur. A forward radar operator based in Rayleigh and Mie theory estimates corresponding polarimetric radar variables from physical descriptors of hydrometeors . The model is adapted to include radar beam effects and PAR sampling to allow for the study of QPE retrievals,

process rate estimation, and process characterization/delineation through the lens of instrument constraints (Searls (2022)). I am currently in the process of extending this analysis framework in 3D with collaborators Jacob Shpund (Hebrew University of Jerusalem) and Pavlos Kollias (Stony Brook University) by using the Weather Research and Forecasting Model spectral-bin cloud microphysics model (WRF-SBM) coupled with an existing S-band radar simulator.

5.2.1 Objectives

The proposed work builds on my previously developed analysis frameworks and available tools to investigate precipitation and convective process and flux signatures in orbital and suborbital weather radar observations to advance their retrievals. A simulation framework involving WRF-SBM and a weather radar simulator that accounts for the beam geometry, nonuniform beam-filling, and signal integration effects is applied on representative precipitation cases to simulate observations from orbital and suborbital weather radars: Outputs from Ka, Ku, and W-band satellite radar simulators and S-band ground radar simulators within a WRF-SBM simulation of convection will be used to analyze the vertical information from space to ground. Analysis of processes, process rates, and fluxes within the convective lifecycle will be performed for existing systems: GPM DPR (Ku-Ka band), the INCUS train of three Ka-band radars, the AOS Ku-band Doppler radar, the ground-based S-band WSR-88D radar (providing horizontal information closer to the surface; see Fig. 1) and the future polarimetric doppler phased-array radar (PAR) systems (providing high resolution horizontal and vertical information close to the surface).

I aim to extend my current work on hydrometeor processes and QPE study to spaceborne radars to show how radar process rates and vertical motion sensed from space can be used alongside the process information and fluxes estimated by ground-

based radars to create a seamless column describing the evolution of precipitation processes from clouds to the surface. In addition, my current work uses a simulation framework to compute probabilistic time and height derivative retrievals from radar measurements. This proposal expands on this concept to test relations at much larger scales using spaceborne active sensors and ground-based active sensors. The key goals of this FINESST proposal are: Goal 1: Build emulators for orbital and suborbital radar by creating RF system models based on the operating metrics of the considered active radars and utilizing existing ground radar and satellite radar simulators for WRF-SBM (Dixon et al. (2024a), Dixon and coauthors (2023), Shpund et al. (2019), and Oue et al. (2020)). Goal 2: Develop estimators for process rates, fluxes, and vertical motions occurring within SBM models from the perspective of spaceborne W- and Ku/Ka-band satellite radar and ground-based S-band radar simulators utilizing probabilistic supervised machine learning techniques (Dixon et al. (2024b)). Estimate uncertainties in the estimator, including limitations introduced by each radar system.

Because my current work involves integrating existing ground-based simulators with WRF-SBM run on the OSCER supercomputer at the University of Oklahoma Kollias et al. (2014). Task 1 involves training ground-based radar estimator(s) to the process rates (e.g., evaporation, melting, drop breakup, and collision-coalescence) and fluxes (including QPE) and vertical motions using the same probabilistic supervised learning technique I employ in my current work. The estimates will be verified by an independent subset of simulated data within the model using only parameters that translate to real-world measurement techniques (e.g., drop size distribution measured with disdrometers, vertical winds, or drop size distributions measured with vertically pointing radars Kollias et al. (2022)). Furthermore, Task 1 will be an evaluation over the course of a case of the convective lifetime, cataloging the simulated instrument-estimated process information within the vertical field of view of the WSR-88D and PAR radars.

5.2.1.1 Task 2 (Goal 1 and Goal 2): Evaluating spaceborne radar emulator's capability to observe processes and fluxes

This task will require the integration of an existing spaceborne simulator to be released by the Kollias group by summer 2024 (Dixon and coauthors (2023), Shpund et al. (2019), and Oue et al. (2020)) within the identified convective WRF-SBM simulation of (Task 1) to capture simulated spaceborne W-, Ku-, and Ka-band process returns. Satellite radar estimators will be trained using the probabilistic framework from my current work for process rates and fluxes. The satellite systems considered for this analysis are AOS-Sky's W-band doppler radar, the Global Precipitation Measurement Mission's (GPM) Dual-frequency Precipitation Radar (DPR), and the INCUS train of three Ka-band radars (Donovan et al. (2023)). These systems have different observation capabilities. AOS-Sky is best poised to measure clouds with its highest operating frequency of 94 GHz (Neeman et al. (2013)). GPM-DPR houses radars at two frequencies: Ku band with an operating frequency of 13.6 GHz and Ka band with an operating frequency of 35.5 GHz allowing GPM-DPR to produce vertical profiles of the dual-frequency ratio DFR enhancing the information content available to prescribe microphysics retrievals (Williams and Giangrande (2023), and Kim et al. (2023)). The INCUS mission involves radar measurements with time separations of 30, 60, and 90 s meaning that it can estimate vertical motions and fluxes (Donovan et al. (2023)). These satellite radars and ground-based S-band radars operating near 3 GHz have tradeoffs in resolution, frequency, sensitivity, and orientation when it comes to measuring the microphysical properties of precipitation, such as size, shape, phase, process rates, and fluxes. Task 2 will be an evaluation over the course of the case of the convective lifetime from Task 1, cataloging the modeled process information alongside simulated instrument-estimated process information within the vertical field of view of

each considered radar.

5.2.1.2 Task 3 (Goal 2): Satellite-to-ground-radar estimation moments of opportunity

Within regions of satellite-to-ground-radar overlap, capture differences between the process estimates and their uncertainty metrics from the utilization of their respective independent process estimators. Within the region of overlap, tune the individual process estimators using supplemental additional information available during the time of overlap, e.g., tune vertical motion estimated by the ground-based radar using Doppler-from-space and project missing process rate extremes due to the low resolution of the satellite radars to their estimates using the ground-based radar estimates. Evaluate the case of the convective lifetime from Task 1 and the benefit derived from estimation tuning within satellite-to-ground measurement overlaps. Based on the results of Task 3, recommendations will be made for how to improve model parameterizations using observations

5.2.2 Potential Sources of Uncertainty

This work focuses on the development of instrument-constrained process estimators within WRF-SBM. Instrument constraints are built into the simulators. This enhanced information content will be used to document, describe, and quantify the uncertainty in radar returns. This work will limit the considered instrument errors creating variability in the radar-variable data set to instrument resolution, instrument noise, PAR calibration, and nonuniform beam filling.

The proposed project addresses several high-priority science objectives identified across NASA and the broader scientific community. From the 2017–2027 Decadal Survey, it responds directly to Science Question H1-b—quantifying global precipita-

tion rates and phase at convective and orographic scales—by using vertical profiles of W-, Ku-, and Ka-band radar variables, along with GPM DPR retrievals of D_m and $log_{10}(N_w)$, to reveal drop growth, breakup processes, and gradients indicative of collision–coalescence, supported by S-band suborbital radar for intercomparison. It also addresses Science Question W-9a, which calls for characterizing hydrometeor microphysical processes and precipitation rates within 5%. This is achieved through combined ground-based and spaceborne multi-frequency radar observations that track temporal and spatial evolution of precipitation and drop size distributions throughout convective life cycles, while probabilistic estimators quantify uncertainty in precipitation-rate retrievals. In alignment with NASA's 2022 Strategic Plan—specifically Earth Science Research Strategic Objective 1.1—the project strengthens understanding of Earth system processes by improving global storm-resolving models and clarifying how instrument constraints affect model accuracy, thereby bolstering confidence in both modeled and measured data. Although focused on active instruments and convection, the underlying framework could also be extended to passive sensors, broadening its relevance across atmospheric science. The work further supports NASA SMD leadership priorities, exploration and scientific discovery, innovation, and interconnectivity and partnerships by producing a publicly accessible community tool that can inform future instrument and network design and through collaborations spanning UTokyo, the University of Wisconsin–Madison, the University of Oklahoma, CIMSS, NOAA, CIWRO, and OU's ARRC. It also contributes to SMD's science focus areas of reducing climate uncertainty, informing societal response, and addressing surface dynamics, hazards, and disasters, especially through advancements to global storm-resolving and high-resolution weather models (e.g., GEOS-5 and WRF) that strengthen understanding of water–energy cycle coupling. Finally, the project responds to challenges highlighted by WCRP and GEWEX under the Clouds and Circulation Grand Challenge by emphasizing convec-

tive process analysis and model improvement through observations.

5.2.3 Future Applications

The applications of this work extend across a wide range of scientific and engineering pursuits, highlighting its potential to advance both observational capabilities and theoretical understanding. This approach can support future expansion of the GPM Ground Validation Network (Cecil et al. (2023)), enable more robust intercomparisons between measured and modeled data, and contribute to algorithm development that exploits crossed path measurements. It also offers valuable guidance for designing future satellite constellations and ground-based networks, while strengthening the intercomparison of satellite and ground-based observations more broadly. By incorporating multiple observing perspectives and instrument configurations, this framework deepens our understanding of the underlying physics and informs the development of methods to mitigate satellite blind zones. Ultimately, the insights gained here can improve quantitative precipitation estimation for hydrological models and enhance the process parameterizations used in global climate models, making this work a meaningful step toward more accurate and resilient Earth system observations.

Chapter 6

Conclusions and Future Work

This dissertation has examined how enhanced spatiotemporal sampling from PAR can address long-standing limitations in ground-based QPE, particularly in convective environments where precipitation evolves rapidly in both time and space. While dual-polarization has significantly advanced operational QPE over the past two decades through the enhanced dimensionality of radar returns, conventional mechanically scanning radars remain constrained by limits to their revisit time. This constraint limits the radar's ability to resolve precipitation variability due to undersampling, or sampling below the decorrelation time of the storm. This dissertation has demonstrated how PAR can be used to diagnose required storm sampling revisit times. Furthermore, this work has demonstrated how PAR can be used to identify microphysical processes, including sources and sinks of condensed water mass that have been previously unobservable with ground radars, and how it can be used to quantify temporal sampling uncertainties in both radar variables and rain rate estimates. By leveraging preliminary PAR observations collected between 2021 and 2025, this work demonstrates that fast, flexible radar sampling enables new observational capabilities that directly improve QPE and expand its physical interpretability. A central contribution of this research is the systematic evaluation of temporal continuity in radar observations and its implications for QPE accuracy. Using high-temporal-resolution observations from micro-rain radar and PAR RHI scans with revisit times as short as 0.76 s, this work quantified decorrelation times, temporal sampling errors, and uncertainty in radar reflectivity and

derived rainfall rates. These analyses show that precipitation variability in convective storms often occurs on timescales shorter than those resolved by current operational radars, leading to non-negligible sampling error in QPE products. The results provide guidance on temporal sampling requirements for radar-based precipitation estimation and reinforce the value of PAR's rapid-update capability for meeting and being used to define radar quality requirements across a range of meteorological applications.

Beyond temporal considerations, this dissertation advanced QPE through the incorporation of advective terms derived from PAR radar returns. These are the spatiotemporal derivatives of radar variables. Backed by the continuity equation to radar-observed condensed water content, a supervised learning framework was developed to relate radar variables and their spatial and temporal derivatives to precipitation rates. Feature selection and probabilistic modeling showed that these PAR variables provide complementary information beyond traditional radar observables, improving fine temporal-scale rain rate estimation. The use of a spectral bin microphysics model allowed these retrievals to be evaluated in a controlled setting, highlighting both their physical relevance and the impact of processes on rain relation applicability that builds upon past work looking into distinct estimators for different rain regimes (Ryzhkov et al. (2005)). Through the use of both PAR returns and emerging 3D-wind estimate research, this work has demonstrated that the continuity equation can be used to derive process rates (source and sink rates of mass) at a fine scale. Dense PAR sampling enables, for the first time, a new view of processes occurring within convective storms, quantities that are not accessible with traditional scanning strategies. The ability to estimate these process rates represents a shift from purely diagnostic QPE toward a more physically informed interpretation of precipitation evolution, linking radar observations to underlying microphysical and dynamical processes.

The 2017 decadal survey, a bottom-up survey, defined the following priorities: to

quantify rates of precipitation and its phase (rain and snow/ice) worldwide at convective and orographic scales suitable to capture flash floods and beyond and to characterize the microphysical processes and interactions of hydrometeors by measuring hydrometeor distribution and precipitation rate to within five percent (National Academies of Sciences, Engineering, and Medicine (2019)). Towards this end, this work has demonstrated frameworks for improved quantification of precipitation at convective scales relevant to flash flooding, improved radar variable estimation at various meteorological temporal scales, has demonstrated a method for microphysical process rate retrieval and a method for quantifying the uncertainty in both radar variable and rain rate estimations. The decadal survey target of precipitation rate quantification to within five percent is in the context of satellite observations and does not directly translate to the resolution volume of ground-based radar; therefore, a discussion of the satellite and ground scale mismatch is warranted, including how uncertainty information can be used across observation scales, which could be addressed in part using PAR measurements within the proposed geostatistical framework. This is suggested as a future research direction relevant to the convergence of ground-based and spaceborne observations of precipitation and convection.

This work does explore ground-based PAR as a candidate to bridge spaceborne radar observations, which would help to extend benefits of PAR to spaceborne systems that have worldwide reach. By proposing methods for how PAR can temporally and spatially supplement satellite measurements, this work highlights opportunities to mitigate known satellite limitations related to revisit time and footprint size. Demonstrations using convective cases and a proposed NASA FINESST framework are forward-looking directions for how coordinated ground- and space-based radar observations can enhance precipitation estimates and support the development and evaluation of satellite retrieval algorithms.

Overall, this dissertation shows that the primary advantage of PAR for QPE lies not only in faster updates but also in the multidimensional density of information content that fast, adaptive sampling provides. The ability to resolve temporal variability, estimate fluxes, and quantify process rates opens a pathway toward closer integration of radar observations with numerical weather prediction and hydrologic models. These findings can directly inform the design and scientific priorities of future observing systems, including the resulting system from the Radar Next program, by establishing observational requirements that account for both horizontal and vertical atmospheric transport.

Future work should broaden these analyses to encompass a wider spectrum of storm types, precipitation regimes, and environmental conditions in order to better generalize sampling strategies and assess retrieval performance. Continued advances in process-rate estimation techniques, including rigorous uncertainty quantification and formulations suitable for data assimilation, will be critical for successful operational implementation. In addition, stronger coordination among the scientific communities engaged in PAR development and deployment, satellite missions, and modeling efforts through distributed and collaborative leadership presents a valuable opportunity to advance precipitation science and to build a next-generation QPE framework that more effectively serves societally relevant needs.

Chapter 7

Appendix A:

Derivation of Radar Equivalent Reflectivity

An antenna has properties of gain (G) and effective aperture area (A_e). Power transmitted to an antenna is amplified multiplicatively by the gain as it is converted into a plane wave traveling into the atmosphere, spreading energy over a sphere of radius R. The power density in units of watts per meter squared (W/m^2) arriving at a distance (d) to a target such as a volume of hydrometeors is then

$$P_d = \frac{P_t G}{4\pi R^2} \tag{7.1}$$

The power reflected from the target depends on the target's radar cross-section (σ) so that the power density reflected from the target is $P_d\sigma$ and the power density reflected back to the antenna from the target with units W/m^2 is

$$P_{d,r} = \frac{P_t G \sigma}{(4\pi R^2)^2} \tag{7.2}$$

The power received by the antenna is augmented by the antenna effective aperture (A_e) to be $P_{d,r}A_e$ so that the total received power in units of W by the radar at the

output terminals of the antenna is

$$P_r = \frac{P_t G \sigma}{(4\pi R^2)^2} A_e \tag{7.3}$$

where A_e represents the power density captured by the antenna with units of m^2 defined to be

$$A_e = \frac{G\lambda^2}{4\pi}. \tag{7.4}$$

If the target being observed is a volume of hydrometeors, then each hydrometeor in the target volume contributes a portion of the scattered power that is reflected back to the radar. Typically in atmospheric sciences this radar cross section for the number of drops in the target volume is derived assuming that the radar operating wavelength (λ) relative to the diameter of the hydrometeor (D) lies within the Rayleigh regime, which is true for S-band, such that

$$\sigma = \frac{\pi^5}{\lambda^4} \left| \frac{m^2 - 1}{m^2 + 2} \right|^2 \int_0^\infty D^6 N(D) dD \tag{7.5}$$

assuming that D meets the condition for the Rayleigh regime of $\frac{2\pi D}{\lambda} << 1$ (Cavallo (2021b)). k is the complex refractive index of the hydrometeors, and N(D) is the number concentration for each particle of size D in the volume.

If we define the equivalent reflectivity (Z) in units of $mm^6 m^{-3}$ to be

$$Z = \int_0^\infty D^6 N(D) dD \tag{7.6}$$

and consider the volume of space over which the reflectivity is being collected to occur for the transmit pulse length, τ causing a distance of $\frac{c\tau}{2}$ to be traversed in the forward and backwards directions (velocity is the distance traversed divided by

the time) and the focusing of power over a hemisphere (Ω) as defined by the two-way antenna pattern (f^4) can be approximated using an assumed symmetric 3 dB Beamwidth (θ) by

$$\int_{\Omega} f^4 d\Omega = \frac{\pi\theta^2}{8ln(2)} \tag{7.7}$$

Then if Equation (7.4), Equation (7.5), and Equation (2.3) are substituted into Equation (7.3), it becomes

$$P_r = \frac{P_t G \sigma}{(4\pi R^2)^2} \frac{G\lambda^2}{4\pi} \frac{\pi^5}{\lambda^4} \left|\frac{m^2-1}{m^2+2}\right|^2 Z \tag{7.8}$$

which can be rewritten to define equivalent radar reflectivity to be

$$Z = \frac{P_r (4\pi)^3 R^2 \lambda^2}{\left|\frac{m^2-1}{m^2+2}\right|^2 G^2 \pi^2 P_t L} \tag{7.9}$$

This form of the definition Z includes an added path loss, L, of the signal by vapor in the atmosphere, which may indeed be present, and it aligns with the definition presented in Hong and Gourley (2017).

Chapter 8

Appendix B: Derivation of Continuity Equation for spherical hydrometeors

8.1 Radar Sensitivity to Hydrometeor Size

Radar resolution volumes associated with observed volumes of space as S-, X-, and C-band in the atmosphere are most sensitive to condensed liquid (e.g., rain) and ice (e.g., snow) hydrometeors in the Rayleigh regime with diameters of approximately 0.5–8 mm for liquid rain (National Oceanic and Atmospheric Administration, 2000; Battan, 1973; Matrosov et al., 2022; Bohren and Huffman, 1983).

Sensitivity depends on both microphysical and electromagnetic factors because hydrometeors in the ice phase can grow larger than raindrops, and because the dielectric constant of ice ($|K|^2 \approx 0.197$) is about five times smaller than that of liquid water ($|K|^2 \approx 0.93$), meaning that larger ice particles are required to produce equivalent radar reflectivity; and complex, non-spherical shapes of snow and graupel lead to weaker backscatter efficiency per unit size compared to liquid drops. As a result, radar systems in the S-, C-, and X-band range exhibit the strongest backscatter sensitivity for raindrops of order 1–3 mm and ice particles of order 1–8 mm in diameter, depending

on wavelength and hydrometeor composition.

If we consider the condensed hydrometeor mass detected by a radar to be m, then, assuming that there are no sources and sinks of mass in the atmosphere, the conservation of mass dictates that

$$\frac{D}{Dt}m = 0 \tag{8.1}$$

within the volume, where $\frac{D}{Dt}$ is the total derivative. Expanding the total derivative puts the equation in terms of local directional derivatives in a three-dimensional Cartesian coordinate system defined by the horizontal axes x and y and the vertical axis z:

$$\frac{d}{dt}m + u\frac{d}{dx}m + v\frac{d}{dy}m + w\frac{d}{dz}m = 0 \tag{8.2}$$

assuming that u, v, and w are the mass-weighted mean velocities in the considered volume in the x, y, and w directions, respectively.

Considering the simplified case of an ideal spherical raindrop (with liquid water density ρ_l with a volume, V, defined by its diameter, D, to have a volume defined as

$$V_{drop} = \frac{\pi}{6}D^3\rho_l, \tag{8.3}$$

then the total m in an observed volume of spherical drops depends on V_{drop}, the particle size distribution, $N(D)$. It is defined as

$$V_{drop} = \frac{\pi}{6}\rho_l \int D^3 N(D) dD, \tag{8.4}$$

and Equation (8.2) can be rewritten as

$$\frac{d}{dt}\frac{\pi}{6}\rho_l \int D^3 N(D) dD + \frac{d}{dx}\frac{\pi}{6}\rho_l \int D^3 N(D) u(D) dD + \frac{d}{dy}\frac{\pi}{6}\rho_l \int D^3 N(D) v(D) dD + \frac{d}{dz}\frac{\pi}{6}\rho_l \int D^3 N(D) w(D) dD = 0. \tag{8.5}$$

Now, because processes like evaporation, sublimation, and vapor deposition are actively involved in storm development and evolution, it cannot be assumed that there are no sources and sinks of hydrometeor mass within the volume. For example, Tao et al. (2022) indicates that for convective systems condensation, deposition, and freezing primarily happen in updrafts, while evaporation and sublimation occur in downdrafts. There is a process rate, p, that is positive when mass is added to the observed hydrometeor distribution in the volume (e.g., during vapor deposition) and is positive when mass is removed (e.g., during evaporation or sublimation). Including the process rate, p, Equation (8.5) becomes

$$\frac{d}{dt}\frac{\pi}{6}\rho_l \int D^3 N(D) dD + \frac{d}{dx}\frac{\pi}{6}\rho_l \int D^3 N(D) u(D) dD + \frac{d}{dy}\frac{\pi}{6}\rho_l \int D^3 N(D) v(D) dD + \frac{d}{dz}\frac{\pi}{6}\rho_l \int D^3 N(D) w(D) dD = p. \tag{8.6}$$

where $u(D)$, $v(D)$, and $w(D)$ represent the velocity terms associated with each D within the volume. If the mass-weighted mean velocity is considered, then the velocity terms may be pulled out of the integral equation:

$$\frac{d}{dt}\frac{\pi}{6}\rho_l \int D^3 N(D) dD + u\frac{d}{dx}\frac{\pi}{6}\rho_l \int D^3 N(D) dD + v\frac{d}{dy}\frac{\pi}{6}\rho_l \int D^3 N(D) dD + w\frac{d}{dz}\frac{\pi}{6}\rho_l \int D^3 N(D) dD = p. \tag{8.7}$$

Recall the rain rate, R, and the liquid water content, LWC, as defined in Chapter 2 in Equation (2.2) and Equation (2.4), respectively. The vertical term in 8.6 is directly

related to R.

$$\frac{d}{dz}\frac{\pi}{6}\rho_l \int D^3 N(D) w(D) dD = \frac{d}{dz} R. \tag{8.8}$$

Thus, rearranging 8.6 to be

$$\begin{aligned} &\frac{d}{dz}R \\ &= p - \frac{d}{dt}\frac{\pi}{6}\rho_l \int D^3 N(D) dD - u\frac{d}{dx}\frac{\pi}{6}\rho_l \int D^3 N(D) dD - v\frac{d}{dy}\frac{\pi}{6}\rho_l \int D^3 N(D) dD \\ &= p - \frac{d}{dt} LWC - u\frac{d}{dx} LWC - v\frac{d}{dy} LWC. \end{aligned} \tag{8.9}$$

which indicates that the evolution of rain rate within the vertical column, $\frac{d}{dz}R$, is influenced by process rates, p, changes to the LWC in time, $\frac{d}{dt}LWC$, and through advection, $u\frac{d}{dx}LWC$, $v\frac{d}{dy}LWC$.

Chapter 9

Appendix C: Analysis and Enhancement of GPM's Dual-Frequency Precipitation Algorithm Through Ground-Radar Variability Insights

9.1 Introduction

In the coming decades, there is an increased risk of extreme weather events such as floods and droughts, significantly impacting agriculture, freshwater resources, public health, and mortality. Accurate quantification of rainfall accumulation is crucial for enhancing weather and climate models, which serve as vital tools for warning systems and risk reduction planning (Basara (2022)). With the rising trend in extreme precipitation under various global warming scenarios (Dai (2011)), there is a pressing need not only for global coverage but also for highly precise rainfall retrieval algorithms.

The joint National Aeronautics and Space Administration (NASA) and Japan Aerospace Exploration Agency (JAXA) Global Precipitation Measurement (GPM) mission has developed a high-resolution multi-sensor merged precipitation product updated

every half hour called Integrated Multi-Satellite Retrievals for GPM (IMERG) (Pradhan et al. (2022b), Hou et al. (2008)). This initiative leverages data from the GPM core satellite's Dual-Frequency Precipitation Radar (GPM-DPR) and GPM-Microwave Imager (GMI), with accuracy evaluated by ground validation from radar and rain gauge measurements, as well as high-spatial and temporal resolution data from geostationary satellite imagery (km-scale horizontally). This effort aims to advance the understanding of cloud and precipitation microphysics, large-scale weather patterns including teleconnections, climatology, and the global water cycle. While infrared imagery provides cloud top information but cannot penetrate cloud cover (Hou et al. (2008), Upadhyaya et al. (2021)), microwave radiometers like the GMI, although with lower resolution than infrared, can penetrate clouds and detect precipitation by converting brightness temperatures into temperature and water vapor content profiles as well as inferring surface precipitation (Hou et al. (2008)). The evolution of infrared and microwave radiometer technologies has been substantial, with earlier precipitation-focused missions like TRMM (launched in 1997) focusing on tropical rainfall and hurricanes using radar and radiometer measurements. GPM aims to enhance TRMM's capabilities by deploying a dual-frequency radar concept capable of computing microphysical parameters such as the mass-weighted mean diameter D_m. A critical piece of this merged-observation ecosystem is the improvement of DPR rain estimates with ground validation information content. As will be shown in this appendix, a critical part of this is reducing errors for convective precipitation by utilizing precipitation variability information available via ground validation.

The merging of multi-satellite data involves constructing microphysical databases to connect observations from different sensors via methods such as forward radiative transfer models (Hou et al. (2008)). This process adjusts cloud and background parameters to align with DPR and GMI observations, capturing estimated vertical profile

variability crucial for scientific investigations. Gauge-corrected radar ground validation serves as the surface precipitation reference and plays a pivotal role in calibrating and developing precipitation products for various satellite instruments and providing microscale insights into surface-level microphysical variations (Hou et al. (2008)). Historically, R estimation for both stratiform and convective precipitation using single-frequency radars relied on power-law relationships dependent on equivalent reflectivity that were tuned using ground-reference measurements. However, the availability of dual-frequency returns from DPR (Ka- and Ku-bands) allows for more accurate rain rate estimates by estimating mass-weighted mean diameter D_m and normalized intercept parameter N_w based on assumed gamma drop size distributions (DSDs), as demonstrated in recent studies (Nakamura (2021)). Researchers, by employing clustering analysis techniques, have confirmed clear separations between stratiform and convective precipitation in the D_m and N_w parameter space, indicating their isolation as largely unique precipitation regimes (Dolan et al. (2018)). Though some overlap is possible, the assumption of unique stratiform and convective regimes will be assumed in this work.

Stratiform precipitation occurs with weaker vertical air motion, frequently found in frontal boundaries within low-pressure systems, where stable conditions favor the formation of cloud layers that accumulate mass until precipitation occurs through vapor deposition or warm advection (Munchak et al. (2012)). While stratiform precipitation may not initiate extreme events and tends to exhibit relatively uniform behavior, it contributes significantly to total accumulated precipitation globally (Munchak et al. (2012)). In contrast, convective precipitation results from less dense air rising with strong vertical motion, allowing condensed particles to grow into large drops before falling as precipitation. This type of precipitation can lead to localized or widespread areas of heavy rainfall, often associated with isolated cells or larger systems such as

mesoscale convective systems (Houze Jr (1997b)).

Organized convective precipitation (e.g., thunderstorms) can fall within the mesoscale scale of motion with a time evolution of one hour to one day and a spatial scale of 1 km to 1000 km, but it is also common for convection to be at the microscale with convective cells evolving in time resolutions between 1 s and 1 min and a spatial scale of less than 1 km (Cavallo (2021b)). The GPM-DPR with a footprint of 5 km and a scan swath of 245 km does not resolve the full spatial scale of convective motion. As shown in Figure 9.1 relative to the DPR footprint, the multi-radar multi-sensor system (MRMS) built to merge the Next Generation Radar Network (NEXRAD) and a network of gauge observations covering CONUS has about a 1 km x 1 km resolution. From a horizontal perspective, MRMS covers mesoscale motions that are not captured by the DPR.

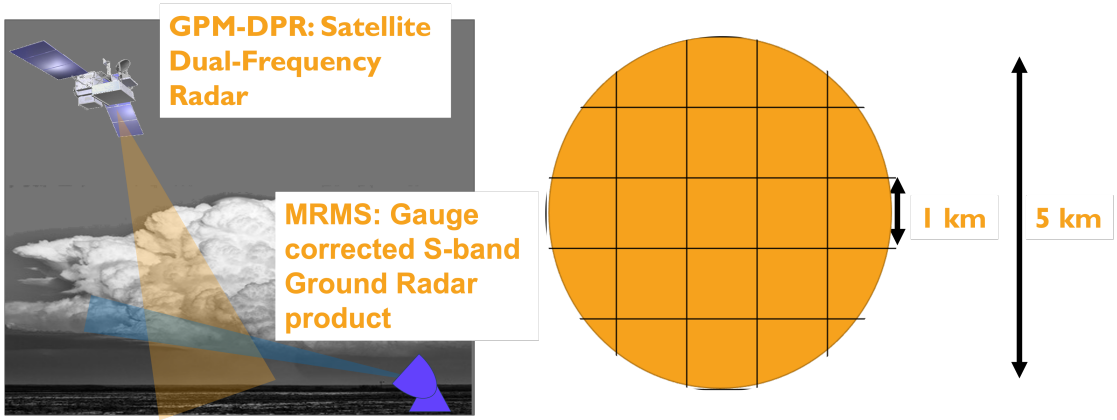


Figure 9.1: The dataset analyzed in this appendix is composed of variables calculated from an MRMS grid (about 1 km square) matched to the 5 km diameter DPR footprints (depends on local zenith angle) captured over CONUS from June 2014 to October 2016, as well as associated DPR Level-2 products.

This appendix hypothesizes that biases in DPR precipitation estimates are largely influenced by unobserved variability within the DPR footprint. To test this hypothesis, a 2-year dataset of DPR products will be analyzed alongside MRMS rain retrievals over CONUS. Clustering relevant DPR products based on bias and MRMS-observed

rain variability within each footprint will identify parameters associated with high-magnitude bias (overestimation or underestimation) for various rain regimes. K-means clustering is employed to cluster the data, an effective statistical technique for revealing trends in large multidimensional datasets by identifying regions of similarity. Subsequently, improvements for high-bias regimes will be proposed, aiming for generalized enhancements applicable to an improved R-D_m relationship over CONUS.

This study presents the outcomes of applying K-means clustering to a two-year-long dataset of Level-2 rain rate estimates from the GPM-DPR over the CONUS matched to gauge-corrected MRMS surface rain rates. Section 2 outlines the utilized dataset and the K-means clustering methodology. Section 3 presents the K-means clustering results. Physical factors contributing to the biases observed in three high-bias convective clusters are considered, and suggestions for R-Dm algorithm improvements are made. Section 4 concludes with the overall findings of the study and lists considerations for future work.

9.2 Methodology

9.2.1 Dataset

A matched DPR-MRMS dataset is used to analyze the bias associated with the DPR rainfall estimates relative to the MRMS ground reference rainfall. MRMS delivers a quantitative precipitation estimate (QPE) utilizing ground radar observations and in situ gauge measurements. MRMS covers CONUS with a grid 1.11 km north-to-south and 0.6 km-1 km east-to-west (Zhang et al. (2016b)). The GPM Core Observatory hosts onboard the DPR: a Ku- and a Ka-band radar with matched beam footprints where the radar beam intersects the surface. The DPR footprint is about 5 km in

Table 9.1: MRMS Variables derived from a horizontal 1 km x 1 km grid matched to each 5 km diameter GPM-DPR beam surface footprint provided alongside DPR variables listed in Table 9.2 for the 2-year dataset covered in this study

Variable	Description	Units
ref	Gauge-corrected and quality-controlled mean rain rate	mm/hr
stdpix	Standard deviation of MRMS rain rate pixels within the footprint (Kirstetter et al. (2012))	mm/hr

diameter with 25 beams covering a 120 km swath horizontal to the satellite direction of motion (Liao and Meneghini (2022)). Due to its relatively coarse size with respect to the MRMS grid, within each frequency-matched DPR footprint is a grid of MRMS ground-based precipitation data. The dataset utilized in this study contains variables associated with 255,586 DPR footprints, their location, and their associated MRMS precipitation data for precipitation types classified by the DPR to be both stratiform (51,025 footprints with no bright band and 143,259 containing a bright band) and convective (61,302 footprints). For each footprint, Table 9.1 provides a list of considered variables associated with the MRMS ground-reference data matched to each DPR footprint.

The dataset contains values taken over CONUS from June 2014 to October 2016. It is a quality-controlled version of a subset of the full suite of available DPR variables [18]. Quality controls include the assumption that a DPR reflectivity echo is detected, total input data quality is high [GPM/DPR TRMM/PR L2/3 Product Format Documentation Version 5.3], a precipitation type is detected, measurement is taken over land, the mean MRMS rain rate and standard deviation are non-negative, all MRMS grid cells within the footprint are precipitating, and the DPR precipitation has a liquid phase. Table 9.2 provides a list of considered DPR level-2 products, which are provided alongside the latitude and longitude values associated with the center of each surface

footprint. All variables, though they may take different names, are described in Iguchi et al. (2010). The dataset includes the DPR estimated surface rainfall rate (rse). The storm top height (STH) defines the peak altitude containing precipitation and the altitude below which drop size distribution (DSD) parameters are calculated. The freezing level height (FLH) is determined from ancillary environmental data. The bright band is detected based on differences between Ku- and Ka-band vertical profiles of reflectivity or by examination of nearby horizontal pixels when the features are smeared by observation via an off-nadir beam. The height (bbh) and width (bbw) of the bright band are then determined based on characteristic changes in vertical profile slope. A heavy ice flag characterizes ice above the 10°C isotherm (as determined by models) by the value of the Ku-band reflectivity, Ka-band reflectivity, or dual-frequency ratio defined to be equal to the difference in magnitude between the Ku- and Ka-band reflectivities. In general, an increasing value of the heavy ice flag is associated with heavier ice aloft, indicated by the value of the Ku- and Ka-band reflectivities. The normalized surface cross-section (sigma) is calculated by solving the radar range equation for the target radar cross-section at the surface. The path integrated attenuation (PIA) can be calculated using a surface reference technique by the difference between sigms within and outside the rain area, where the rain-free sigms is based on a spatial and temporal average. The pians and piams variables are finalized attenuation products from the DPR dual-frequency algorithm, taking into consideration a mass-weighted mean diameter ($D_m$derived) and the surface reference technique PIA.

The DPR algorithm estimates rain rate utilizing an R-D_m relationship where R is the rain rate and D_m is the mean drop diameter for melted particles, assumed to be spheres (Liao and Meneghini (2022)). The R-D_m relationship inherently includes an estimate of the normalized intercept parameter N_w because the DSD is assumed to take the form of a gamma distribution (Seto et al. (2021)). D_m can be estimated

Table 9.2: DPR Level-2 products were included for each footprint provided alongside their associated footprint-centered latitude and longitude for the 2-year dataset covered in this study. Variables are analogous to those discussed in Iguchi et al. (2010) and the DPR L2/3 Product Format Documentation Version 5.3

Variable	*Description*	*Units*
rse	Rainfall rate estimated at the surface	mm/hr
hst	Storm top height	meters
flh	Freezing level height	meters
bbh	Bright band height	meters
bbw	Bright band width	meters
fip	Heavy ice flag	flag
sigms	Normalized surface cross-section	dB
pians	Path Integrated Attenuation (Normal Scan)	dB
piams	Path Integrated Attenuation (matched scan)	dB
elt	Terrain elevation	meters
lza	Local zenith angle	degrees

using the dual-frequency ratio where the Ku-band reflectivity (Z_{Ku}) and the Ka-band reflectivity (Z_{Ka}) are known because they are measured quantities for each resolution volume in the DPR ray. This is possible because, for drops assumed to be spherical, the backscatter cross-section for incident waves hitting the drops at Ka-band is higher than the backscatter cross-section at Ku-band, meaning that a D_m mapping can be made between the differential observed Z between Ku- and Ka-band in logarithmic scale, dependent on their respective backscatter cross-sections, called the DFR, that tends to increase in value with increased drop diameter. Specifically,

$$DFR = 10\log_{10}[Z_{Ku}(r)] - 10\log_{10}[Z_{Ka}(r)], \tag{9.1}$$

where r is the distance from the radar to each range gate. For each range gate at wavelength λ,

$$\frac{Z_\lambda}{N_m} = \frac{\lambda_\lambda^4}{\pi^5 |K_\lambda|^2} \int_{D_{min}}^{D_{max}} \sigma_\lambda(D) D^\mu e^{-\frac{(4+\mu)D}{D_m}} \, dD, \tag{9.2}$$

where K is a constant calculated from the complex refractive index, σ_λ is the backscatter cross-section at a given frequency, D is the drop diameter, the shape factor for the assumed gamma DSD μ is assumed to be 3, and D_m is the mass-weighted mean diameter that is then calculated given an observed DFR on the left-hand side of Equation (9.1) (Iguchi et al. (2010)). Once D_m is solved for, an estimated PIA can be computed using D_m the surface reference technique (Iguchi et al. (2010)), and then N_w computed at the surface using the measured Ku-band reflectivity

$$10log_{10}[Z_{Ku}] = 10log_{10}[N_w] + 10log_{10}[\frac{Z_\lambda}{N_w}] - PIA. \tag{9.3}$$

The R-D_m relation is derived from the assumption of a gamma DSD, a particle velocity defined by Ulbrich and Atlas (1978), and an assumed specific-attenuation to reflectivity relationship, k-Z (Seto et al. (2021)). The final R-D_m relationship for convective rain rate (mm/hr) used in the DPR algorithm is

$$R = 1.370\epsilon^{4.258} D_m^{5.420} \tag{9.4}$$

and for stratiform rain is

$$R = 0.401\epsilon^{4.649} D_m^{6.131}. \tag{9.5}$$

where ϵ is a critical tunable adjustment factor is determined gate-by-gate along the radar field of view to the surface by choosing one ϵ parameter from a series of tested potential values that optimizes a cost function.

The ϵselection is a critical step in the GPM-DPR R-D_m relation that makes it

adaptable to specific observed DSDs. Each initial guess of the ϵ value can be used to compute an apparent specific attenuation (and apparent PIA) via the assumed k-Z relation tuned for observations taken in the Tropics [15]. Following this, D_m can be determined using an observed Z_{Ku}. During the optimization of ϵ, a cost function minimizes the difference between the apparent Z_{Ka} and observed Z_{Ka} and the difference between the apparent PIA and PIA determined by the surface reference technique.

Despite the adaptability of the DPR algorithm relative to static algorithms used in the past (e.g., Iguchi et al. (2000)), underestimation and overestimation of reference rain rate can still occur (Liao et al. (2014)). The dataset introduced in this section will be used to elucidate sources of underestimation and overestimation in the DPR algorithm. The use of MRMS data will be proposed to improve these errors over CONUS, a presumption that is realistic due to the MRMS rain rates' relatively lower latency compared to DPR rain rate latency statistics. MRMS produces precipitation estimates every two minutes, and the DPR has historically produced its Level 2 precipitation estimates with a latency of 76.2 minutes (Skofronick-Jackson et al. (2018)).

9.2.2 K-means Clustering

K-means clustering is frequently employed in atmospheric science to group multivariate datasets by defining features (e.g., Derin and Faure (2023), Carvalho et al. (2016), Houssos et al. (2008)). Essentially, the clustering approach works by collecting clusters of points with membership defined by a sample's distance to center points within the multidimensional space formed by the variables in the dataset. This allows neighborhoods of points with similar features to be defined. K-means clustering is different from principal component analysis, which explains the simultaneous covariance of parameters (e.g., Dolan et al. (2018)).

To prepare the matched DPR/MRMS dataset for K-means clustering, the data as-

sociated with each variable is standardized and normalized, meaning that each variable is scaled to have a mean of 0 and unit variance and then that the variables in the whole dataset are normalized (scikit-learn contributors (2024b)). These steps are taken so that no variable dominates the separation of variables simply due to its inherent magnitude and dynamic range. Then a number of K-means clusters is selected using the "elbow technique," wherein K-means clustering is exercised for an increasing number of cluster values on the prepared dataset, and the sum of squared distances of all samples to their nearest cluster center is recorded (scikit-learn contributors (2024a)). When plotted, a visible "elbow" point where the sum of squared distances decreases with increased cluster count slowly indicates an appropriate number of clusters (Kumar et al. (2011)). The variables considered alongside the rain rate bias in a first (and second) application of clustering, whose results will be shared in Section 3, were stdpix, elt, lst, lza, hst, flh, bbh, bbw, fip, piams, and sigms (and stdpix, elt, hst, fip, and piams). The variables for the first application of clustering applied to the full dataset, which included both stratiform and convective DPR observations, were chosen because they represent physical and environmental impacts influencing the observed precipitation. The variables used in the second, convective-only, application of clustering were down-selected from the first set due to their tendency to show separability between the high- and low-bias clusters to be defined in the next section. Once the cluster selection converges from a random starting point to a finalized set of data clusters, a label corresponding to a cluster number is assigned to each data point.

K-means clustering separates data by Euclidean distance within the multivariate data space, so, within the context of this appendix, it assumes that observations with similar variable values across all parameters have similar drivers of rain rate bias. Despite possible drawbacks within these confines, K-means clustering provides a useful way to delineate possible causes of bias for a multivariate dataset where observation

errors can come from many sources.

9.3 Results

9.3.1 Dataset Observations

An exploratory analysis of the matched MRMS/DPR dataset was performed to gain insight into the primary sources of bias resulting from the DPR's use of the R-D_m relation. The analysis described in this section provides a highlight of DPR algorithm biases relative to the variables introduced in section 2a and motivation for a narrowed analysis focused on convective precipitation within the DPR dataset, which will be described in section 3b.

The full dataset is split between observations with high rain rate bias and low rain rate bias values. High bias is here defined to be either an overestimate or an underestimate R_{DPR} by 10 mm/hr or more. The bias is defined to be R_{MRMS} subtracted from R_{DPR} (Bias = $R_{DPR} - R_{MRMS}$). 7% of the dataset represents bias values greater than 10 mm/hr, with 4% of these observations overestimating the rain rate and 3% of these observations underestimating the rain rate.

To uncover impacting parameters on DPR high rain rate bias, the exploratory K-means cluster separation was performed on the full dataset considering the parameters stdpix, elt, lst, lza, hst, flh, bbh, bbw, fip, piams, sigms, and rain rate bias. Choosing two clusters according to the "elbow" method (Kumar et al. (2011)), the K-means separation resulted in a Cluster 0 associated with relatively lower bias values and a Cluster 1 associated with high bias outliers (i.e., bias > 10 mm/hr). As shown in Figure 9.2, a series of strip plots that depict a random subset of data from each cluster show how the clusters are separated in value for the considered MRMS and DPR variables. For

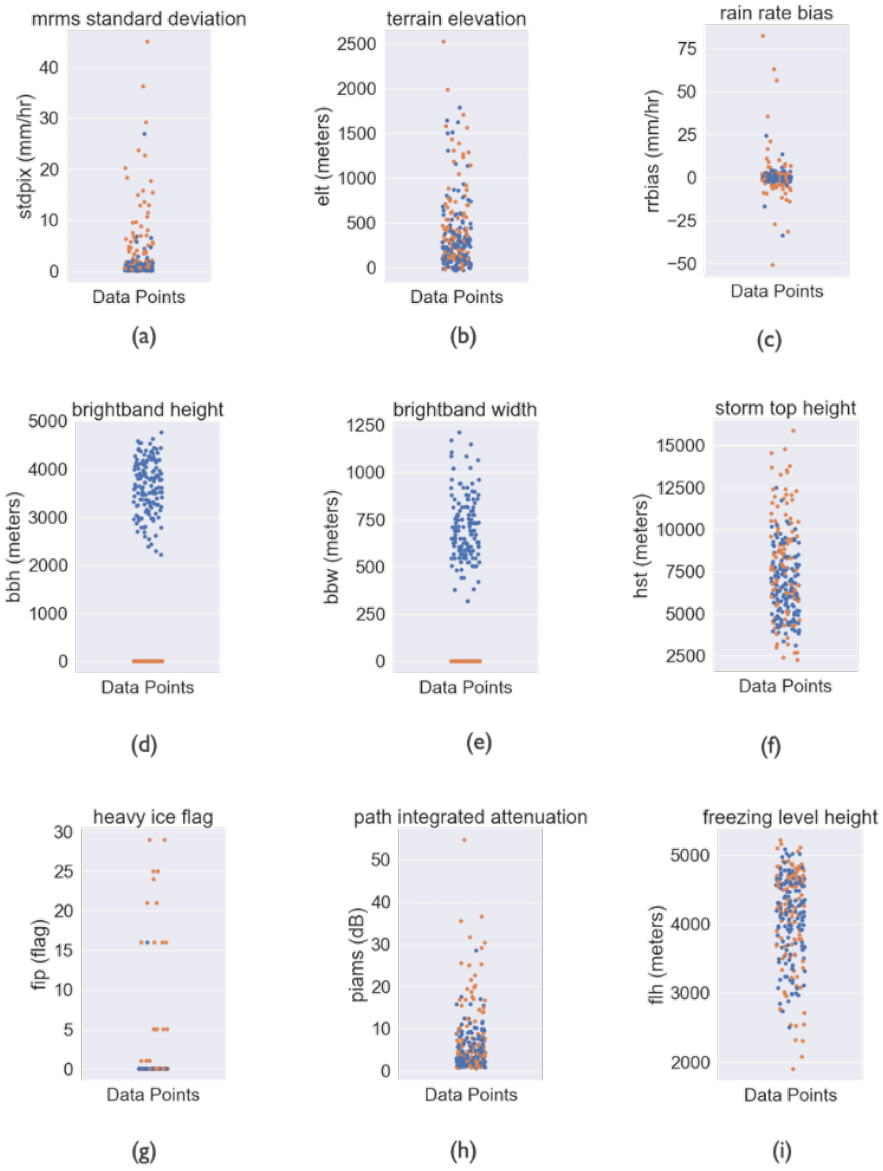


Figure 9.2: Strip-plot analysis illustrating the separation of variables between Cluster 0 (blue) and Cluster 1 (orange) through K-means clustering utilizing the full dataset, including precipitation classified as convective, stratiform with no bright band, and stratiform with a bright band. Each strip-plot depicts the distribution of a specific variable within each cluster, highlighting distinctive patterns and cluster separations, including (a) stdpix, (b) elt, (c) rain rate bias defined to be the DPR rain rate minus the MRMS rain rate at the surface, (d) bbh, (e) bbw, (f) hst, (g) fip, (h) piams, and (i) flh. For visualization purposes the plot contains a random subset of the full data set of 255,586 data points for visualization.

example, it is demonstrated in Figures 9.2(g) and 9.2(h) that Cluster 1 is associated with observations that have no detected brightband (no estimated brightband height and brightband width). Of the considered variables, stdpix, piams, fip, and elt show visible separation between Cluster 0 (also associated with low bias values) and Cluster 1 (associated with containing high bias values). The separability of these parameters between Cluster 0 and Cluster 1 is shown in Figures 9.2(a), 9.2(b), 9.2(i), and 9.2(j) and is summarized in Figure 9.3. Figure 9.3 shows the percentage of Cluster 1 that is associated with high or low values of these parameters, with a yellow shading corresponding to those observations that are predominantly classified by the DPR to be convective.

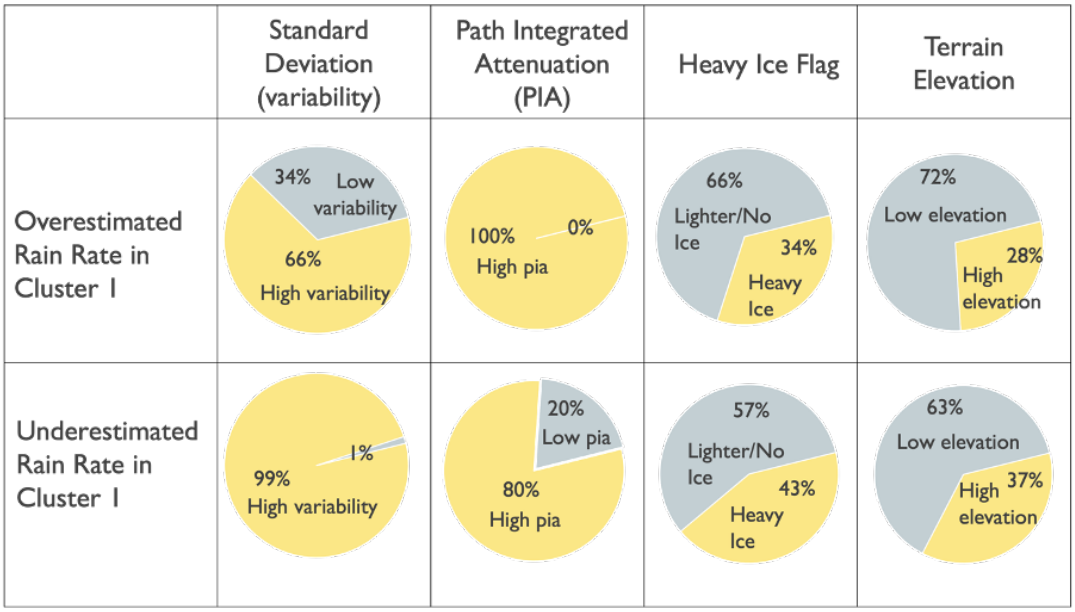


Figure 9.3: Percentage of outlier DPR observations (with a rain rate bias > 10 mm/hr) in Cluster 1 from the DPR two-year dataset associated with stdpix > 2.2 dB, indicating high R_{MRMS} variability within the DPR footprint; piams > 6.06 dB, indicating high matched scan path integrated attenuation; fip > 4 indicating heavy ice; and elt > 368 meters, indicating high elevation. Importantly, the portion of the data that is classified to be convective is shaded in yellow, motivating a further focus on convective-type precipitation in Section 3b.

Cluster 1 is marked by high rain rate bias. In the group of rain rate outliers

in Cluster 1, 66% of overestimates and 99% of underestimates have high rain rate variability (stdpix > 2.2) as measured by the MRMS grid within the footprint. 98.8% of the overestimates and 94.6% of the underestimates associated with high variability are also classified by the DPR algorithm to be convective-type precipitation. 100% of the overestimates and 80% of the underestimates in Cluster 1 are associated with high DPR-matched scan PIA. Of these, 95.7% of overestimates and 80% of underestimates associated with high PIA are classified as convective. All classified as convective, 34% of overestimates and 43% of underestimates in Cluster 1 are associated with heavy ice (Fig. > 4). Only 28% of overestimates and 37% of underestimates in Cluster 1 are associated with high elevation (elt > 368 meters), but of these outliers associated with high elevation, 98% of the overestimates and 100% of the underestimates are classified to be convective.

The exploratory K-means clustering analysis on the two-year dataset considered highlights several variables potentially influencing R_{DPR} bias through membership in Cluster 1 and motivates the in-depth analysis of convective-type precipitation in the following section. Some observations for this dataset are that R_{DPR} underestimates are likely linked to unaccounted variability within the DPR footprint for convective precipitation, even though overestimates may also be associated with high DPR footprint variability. Additionally, overestimates R_{DPR} often coincide with highly attenuated DPR return signals during convective events. Factors such as heavy ice and high terrain elevation further complicate rain rate accuracy, contributing to both underestimates and overestimates in DPR measurements.

9.3.2 Convective K-means Clustering Results

Following the analysis of rain rate bias outliers from the whole matched MRMS/DPR dataset, which showed high bias outlier correlation with the convective precipitation

type in Cluster 1, a refined K-means clustering analysis is performed in this section specific to those DPR observations classified as convective. The clustering is performed on the subset of MRMS and DPR variables exhibiting high cluster separation between the low-bias Cluster 0 and Cluster 1 containing high R_{DPR} bias values: stdpix, elt, hst, piams, rain rate bias, and fip.

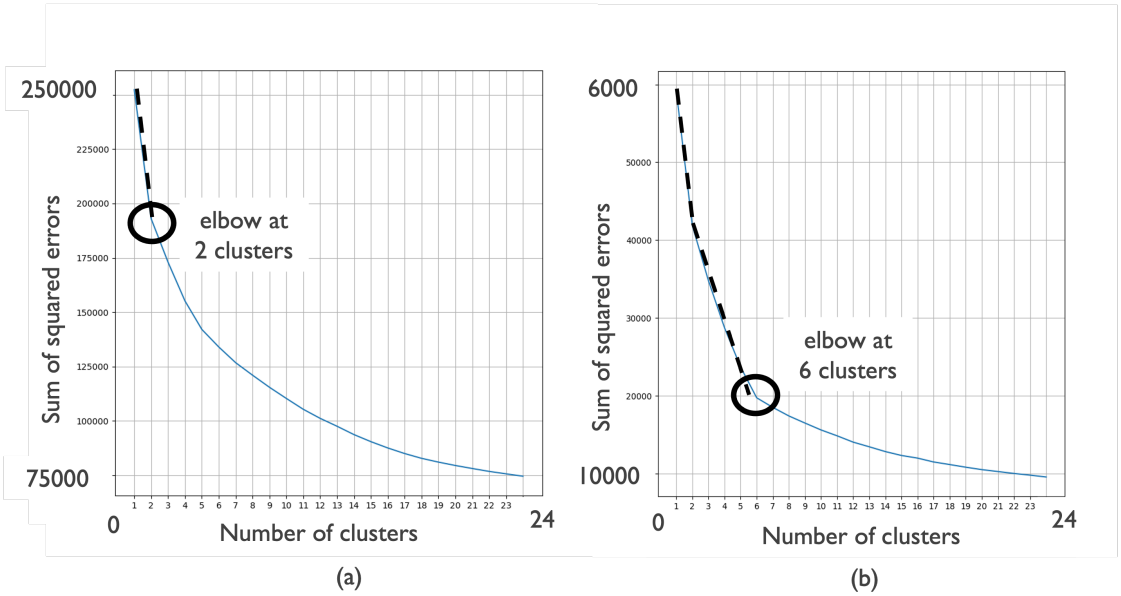


Figure 9.4: The elbow method (Kumar et al. (2011)) was used to choose the number of clusters for the K-means clustering analysis in (a) section 3a utilizing the complete dataset and (b) section 3b, a subset of the full dataset classified as convective precipitation

An elbow method was used for selecting the number of clusters to use for both the analysis in section 3a covering the full dataset and the analysis in this section focused on convection. The elbow method is performed by running k-means clustering on an increasing number of clusters, in this case 1-24 clusters and observing the convergence behavior of the sum of squared errors once the cluster centroids have converged for each application of k-means clustering. Sum of squared error quantifies the total squared distance of each data point to its nearest centroid in Euclidean space, and the K-means optimization aims to minimize the sum of squared errors to achieve optimal clustering

(Kumar et al. (2011)). As shown in Figure 9.4, a cluster is chosen when the slope of the number of clusters versus the sum of squared error slows its reduction as more clusters are added, indicating a reduction in the benefit of adding more clusters.

A summary series of strip plots showing the value-separation of the considered variables for the 6 different convective clusters is shown in Figure 9.5. Figure 9.5(e) shows a clear separation in rain rate bias values between the data clusters. Clusters 0 (red), 4 (orange), and 5 (yellow) exhibit primarily lower bias values of < 10 mm/hr. Cluster 0 is associated with low variability, storm top heights of < 8 km, low terrain elevations (< 500 m asl), low PIA, and a heavy ice flag of 0 (indicating no detected ice aloft). Cluster 1 is associated with low variability, high storm top heights, low terrain elevations, low PIA, and a heavy ice flag between 0 and 5 which may indicate some ice aloft. Cluster 5 is associated with low variability, high storm top heights, high terrain elevations, low PIA, and a heavy ice flag between 0 and 5. The primary focus in this section will be on the clusters showing higher rain rate bias values: Cluster 2 (green), Cluster 3 (purple), and Cluster 1 (blue). These clusters also show higher relative R_{MRMS} values relative to clusters 0, 4, and 5, as can be seen in the violin plot of Figure 9.6. Cluster 2 exhibits positive rain rate bias (R_{DPR} overestimations) and is associated with a wide range of stdpix values, high storm top heights, high PIA, and a heavy ice flag between 0 and 5. Cluster 3 exhibits negative rain rate bias (R_{DPR} underestimations) and is associated with high standard deviations, high storm top heights, moderately low PIA, and a heavy ice flag between 0 and 5. Cluster 1 exhibits both positive and negative rain rate bias values. Cluster 1 is associated with a wide range of standard deviations, high storm top heights, a wide range of terrain elevations, moderate to high PIA, and a heavy ice flag greater than 15, indicating the most ice aloft of any cluster. Thus, cluster 1 can be associated with the presence of heavy ice.

Figure 9.7 shows the spatial distribution of each cluster over CONUS. The rain rate bias points, in general, tend to fall on the eastern and southeasternmost half of CONUS, which follows the spatial distribution of the average annual precipitation trends over CONUS (Prat and Nelson (2015)). Cluster 2 and Cluster 3 likely represent strong convective events and share a similar spatial distribution and represent positive and negative rain rate bias samples, respectively. Cluster 1, marked by the presence of heavy ice aloft, appears to have a high occurrence concentration in the Great Plains and a density of observations focused on the easternmost half of CONUS.

9.3.3 Factors Contributing to Bias

It has been found that high rain rates in mesoscale convective systems are often caused by ice melting, large concentrations of small drops, or rain containing large drops (Rowe et al. (2011), Rowe et al. (2012)). Figure 9.6 shows that clusters 1, 2, and 3 have the highest rain rate values within the convective matched data subset, and Figure 9.5 shows that these clusters tend to have the highest rain rate bias outliers out of the six data clusters. Cluster 1 is characterized by a large population of observations with heavy ice aloft likely caused by ice melting, and it may be hypothesized that heavy ice drives the observed positive and negative biases for R_{DPR} in this cluster because the DPR algorithm depends in part on Ka-band observations, which are at risk of being impacted by multiple scattering in heavy convection with ice aloft (Battaglia et al. (2006)). Figure 9.8 shows how cluster 2 is characterized by a large concentration of small drops and cluster 3 contains large drops via histograms showing each cluster D_m and N_w distributions. Cluster 2 tends to have smaller DPR-algorithm-derived Dm than cluster 3 and a higher Nw than cluster 3. R_{DPR} associated with the high concentration of small drops in cluster 2 tends to be overestimated, and the population of larger drops in cluster 3 tends to be underestimated by the DPR.

An expected driver of bias in the convective dataset, and especially in Cluster 2 and Cluster 3, is nonuniform beamfilling (NUBF). NUBF is a term that can describe a beam only partially filled with precipitation or containing precipitation that is highly variable within the observation footprint. The matched MRMS dataset gives insight into this variability because of its higher resolution near the surface relative to the DPR footprint.

Figure 9.9 shows a violin plot depicting the spread of MRMS rain rate standard deviation for each cluster. Clusters 1, 2, and 3 show the highest standard deviations, which is expected for strong convection. Cluster 3, containing the highest rain rate values, also contains the highest amount of inter-footprint rain rate variability, which may be due to localized convective cells. Further evidence that the biases in Clusters 2 and 3 are driven by NUBF is given by Figure 1, 9.10 wherein a NUBF correction is applied to to Cluster 2 and Cluster 3 according to Seto et al. (2015) and Seto et al. (2021). The matched DPR/MRMS dataset used for this study contains only footprints that are completely filled with rainfall, though they may have large variability in rainfall rate within the footprints. The spatial variability within a sub-grid, according to Seto et al. (2015), is assumed follow be a gamma distribution

$$f(x) = \frac{q^q}{\Gamma(q)} x^{q-1} e^{-qx} \tag{9.6}$$

where, for the purposes of this study, x is a MRMS sub-grid location within the DPR footprint and q is the inverse of the normalized footprint variance:

$$q = \frac{ref}{stdpix}^{2}. \tag{9.7}$$

The DPR rain rate is a dependent on the matched-scan estimated D_m and N_w where in the non-uniform case D_m is assumed to remain constant and N_w is assumed

to vary according to the gamma distribution in Equation (9.6). Figure 9.10(b) corrects Figure 9.10(a) by allowing the overestimated cluster 2 rain rates (green) to take on the lower bound of the 75th confidence interval of the rain rate variation expected in the case of NUBF and allowing the underestimated cluster 3 rain rates (purple) to take on the upper bound of the 75th confidence interval. It is clear that both cluster 2 and especially cluster 3 have reduced bias with applied NUBF correction for most observations, with some exceptions. The attribution of NUBF as a leading cause of rain rate bias in Cluster 2 and Cluster 3 is motivated by the application of NUBF depicted in Figure 9.10.

Further evidence that indicates that Cluster 1 may be impacted by multiple scattering is shown in Figure 9.11 where red points indicate a subset of Cluster 1 from the convective dataset with a heavy ice flag greater than 20 and a difference between the DPR normal-scan reflectivity and the DPR matched-scan reflectivity, $R_{diff} = R_{Ku} - R_{DPR}$, greater than 6 dB. The blue points in Figure 9.11 indicate the same subset of points transformed using the Ku-band Tropical Rainfall Measurement Mission (TRMM) Rain Relationship from Iguchi et al. (2000):

$$R_{TRMM} = 0.04024 Z_{Ku}^{0.6434}. \tag{9.8}$$

A high Z_{diff} in addition to very heavy ice flag increases the likelihood of the presence of multiple scattering for the correction exercise in Figure 9.11 as the DPR dual-frequency algorithm depends on Ka- band which is more impacted by multiple scattering [36].

The adjustment shown in Figure 9.11 estimates rain rate with only Z_{Ku} using the TRMM algorithm because it doesn't use Ka-band measurements. It is concluded from Figure 9.11 that R_{DPR} underestimates have reduced bias under the application of the

Ku-only rain estimator. Overestimates cannot be claimed to be significantly improved using the TRMM rain relationship based on the results of the applied correction in Figure 9.11, indicating that biases in Cluster 1 have more than one overarching cause, one of which may very likely be NUBF due to the often localized nature of convection. It has been suggested by Battaglia et al. (2015) that multiple scattering must be addressed in the DPR algorithm because it impacts measurements of strong convective events. While reverting to the Ku-only TRMM algorithm is a simple solution, Battaglia et al. (2015) suggests that currently available fast-forward codes for multiple scattering correction be implemented in the algorithm. This would allow a correction to the estimated D_m to be performed in the case of multiple scattering so that the existing dual-frequency algorithm R-D_m relationship could still be employed. Battaglia et al. (2015) shows that the dual frequency ratio (difference between Ku- and Ka- band reflectivity values) may be reduced near the surface when multiple scattering occurs due to the increased attenuation at Ka-band. Since the DPR-algorithm estimates Z_{DPR} with the aid of Ka-band measurements it is expected that the difference between the matched scan and Ku-only normal scan measurements show a notable magnitude difference for the case of multiple scattering, making it a useful indicator of possible multiple scattering in the dataset. Under this assumption, it is clear from Figure 9.12 that multiple scattering is not unique to the large heavy ice detected in Cluster 1, but also exists for the strong convective Clusters 2 and 3 which have a large population of heavy ice flags below 6, further motivating the need for multiple scattering correction across all cases of strong convection to prevent biases in estimated surface rain rates.

This section has analyzed CONUS-wide observations of convection to conclude that NUBF and multiple scattering contribute to RR bias in the R_{DPR} biases observed for convective precipitation events where ice melting, large concentrations of small drops, or rain containing large drops are found. Towards this end, some approaches in

literature were tested for improving the bias such as NUBF correction and the use of Ku-only products for the case of multiple scattering. Informed by this, the next section will give an example of an alternative supervised learning strategy to further improve the RR bias in each observed cluster by developing new R-D_m relations and an R-Z_{ku} relation for the case of multiple scattering dependent on the variability within the DPR footprint as observed by MRMS.

9.3.4 Supervised Learning R-D_m Algorithm Improvements

To develop an enhanced rain rate estimator that considers surface variability, a regression model named GAMLSS in R is employed. GAMLSS, or Generalized Additive Models for Location, Scale, and Shape, offers a robust framework for fitting nonlinear probabilistic models linking predictors to a predictand. Specifically, penalized splines are utilized to model DPR variables (such as D_m, N_w, and stdpix for most clusters, and Z_{Ku} and stdpix for Cluster 1) as predictors to estimate the predictand, R_{MRMS}. These predictors are weighted appropriately to estimate both the mean and standard deviation curves (Rigby and Stasinopoulos (2005)). While other variables from Figure 9.5 could potentially serve as predictors due to their variability within the dataset, the chosen predictors are selected to demonstrate the impact of integrating NUBF and multiple-scattering relevant information into the R- D_m relationship.

The default DPR R-D_m relationship is derived so that it is independent of N_w assuming an R-Z relationship so that rain rate's dependency on N_w is cancelled out Seto et al. (2021). While eliminating N_w helps to simplify the relation, Seto et al. (2015) claimed that N_w is spatially variable within the footprint under the condition of NUBF motivating the use a rain relationship dependent on D_m, N_w, and stdpix. For the case of multiple scattering which may also be impacted by NUBF, the relationship is assumed to be dependent on stdpix but not on the dual-frequency derived D_m and

N_w but rather Ku-only products such as Z_{Ku}.

The rain rate estimates derived from these GAMLSS models are illustrated in Figure 9.13. For clusters 0, 2, 3, 4, and 5, the rain rate relationship $R(D_m, N_w, stdpix)$ is applied, whereas for cluster 1, a relationship $R(Z_{Ku}, stdpix)$ is used, ensuring independence from Ka-band observations to mitigate biases from multiple scattering effects. The $R(D_m, N_w, stdpix)$ relation addresses biases associated with NUBF, while $R(Z_{Ku}, stdpix)$ handles effects from multiple scattering and NUBF, albeit with potential accuracy trade-offs due to the absence of Ka-band information. To compare the rain rate estimates, two metrics are used: bias percentage (different from the R bias discussed in previous sections), which is the difference between the expected value of the estimator and R_{MRMS} normalized by R_{MRMS} and the correlation which is taken between the new estimated R_{DPR} and reference R_{MRMS}. The convective portion of the matched MRMS/DPR dataset is split into two random subsets: a training subset composed of 70% of the data and an independent test subset composed of 30% of the data. GAMLSS-derived R-D_m relationships are trained using the training set and the result metrics of correlation and bias percentage are computed using the test set. Figure 9.13 also shows scatter plots comparing the original R_{DPR} to R_{MRMS} for each cluster in the first row and an improved R_{DPR} compared to R_{MRMS} in the second row. It is clear from figure 9.13 that the rain relations are transformed by GAMLSS to more closely follow the 1-1 line. The 0.45 correlation and -25.71% bias percentage for the Cluster 1 test set is transformed by GAMLSS under the additive penalized spline (pb) relationship $R(Z_{Ku}, stdpix) = pb(Z_{Ku}) + pb(stdpix)$ to be a correlation of 0.65 and a bias percentage of 2.62%. Unique GAMLSS estimators are generated for cluster 2, cluster 3, and the group of cluster 0, 4, and 5. These all take the form of $R(D_m, N_w, stdpix) = pb(D_m) + pb(10log_{10}(N_w)) + pb(stdpix)$. Cluster 2 shows improvement from a R_{DPR} correlation of 0.39 and a bias percentage of 192.51% to a correlation

of 0.73 with R_{MRMS} and a bias percentage of -1.33%. Cluster 3 shows a n improvement from a correlation of 0.35 and a bias percentage of -2.55% to a correlation of 0.63 and a bias percentage of 1.18%. The combined group of cluster 0, 4, and 5 shows an improvement from a correlation of 0.34 and a bias percentage of 1.48% to a correlation of 0.66 and a bias percentage of 1.35%. Cluster 2 associated with a large concentration of small drops, shows the largest improvement with the use of the supervised learning estimator though all groups undergo notable metric improvements.

An unresolved factor in these estimators that was shown in Section 3c is that both NUBF and multiple scattering are likely to occur for most all heavy convective events (i.e. the observations in cluster 1, 2, and 3). In the future, rather than excluding Ka-band observations for dealing with multiple scattering as was done in this section it is suggested that multiple scattering be corrected for before the application of any R-D_m relationship such as was suggested by Battaglia et al. (2015). Next, footprint variability should be taken into account, so that both multiple scattering and NUBF can be corrected without degrading the accuracy of precipitation gained by the use of Ku- and Ka-band frequencies in the DPR dual frequency algorithm.

The supervised-learning estimators demonstrated in this section exemplify the capability of machine learning to improve bias handling when predictors are carefully chosen. This approach showcases how GAMLSS regression, coupled with insightful predictor selection, enhances rain rate estimation by accounting for various sources of variability and bias in precipitation data modeling.

9.4 Summary and Considerations for Future Work

The work in this appendix introduced a methodology to examine the DPR R-D_m relation performance for various rain regimes using a matched MRMS/DPR dataset con-

taining observations taken over CONUS from June 2014 to October 2016. The k-means clustering technique applied leans on input from both the DPR satellite measurements and variability information from MRMS gauge corrected ground-radar rainfall products. The k-means clustering technique revealed heavy rain regimes of high rainfall bias ($>$ 10 mm/hr) occurring most frequently on the easternmost half of CONUS: heavy ice, large concentration of small drops associated with R_{DPR} overestimations, and the presence of large drops associated with R_{DPR} underestimations. Existing NUBF and multiple scattering corrections were analyzed for their ability to correct the high rain rate biases in these regimes which helped to motivate the conclusion that both NUBF and multiple scattering drive biases in heavy convection. Recommendations towards developing new R-D_m relationships which consider NUBF and the presence of multiple scattering with supervised learning techniques such as GAMLSS were made, and some new relations were demonstrated. In terms of regional specificity, the default R-D_m relationship used in version 5 of the DPR dual-frequency algorithm relies on measurements taken in the tropics (Iguchi et al. (2010)) so the analysis and improvements in this work are more regionally significant to CONUS.

In concluding this work, numerous future studies suggested to the scientific community are listed including improvements to NUBF correction methods, expansion to areas of low radar-coverage, the use of longer-term datasets, studies considering both vertical and horizontal variability within the DPR ray, and improved technologies capable of observing km-scale precipitation variability:

- There is a need for the application of multiple scattering corrections at Ka-band prior to the application of NUBF correction so that the full benefits of the DPR dual-frequency algorithm are not lost by ignoring Ka-band observations.

- The supervised learning rain algorithms presented Section 3d are dependent on the

input of MRMS reference variability at the surface. It is relevant for observations over CONUS where a reliable ground-reference is available. Future work will involve improving the capture of inter-footprint variability over the ocean in orographic regions where a surface reference network of radar precipitation is absent. This may involve improving the currently developed fractal approach in Seto et al. (2015) or the utilization of other existing satellite or ground datasets.

- An extension to this work could utilize larger datasets extracted from the GPM ground validation network (Petersen et al. (2020a)).

- The role of vertical and horizontal variability may be studied for a more holistic view of variation within the DPR footprint.

- Looking further to the future, MRMS was introduced as a system capable spatially resolving mesoscale systems. Further accuracy can be achieved by satellite-systems capable of measuring below 1 km horizontal resolution to accurately resolve microscale convective effects.

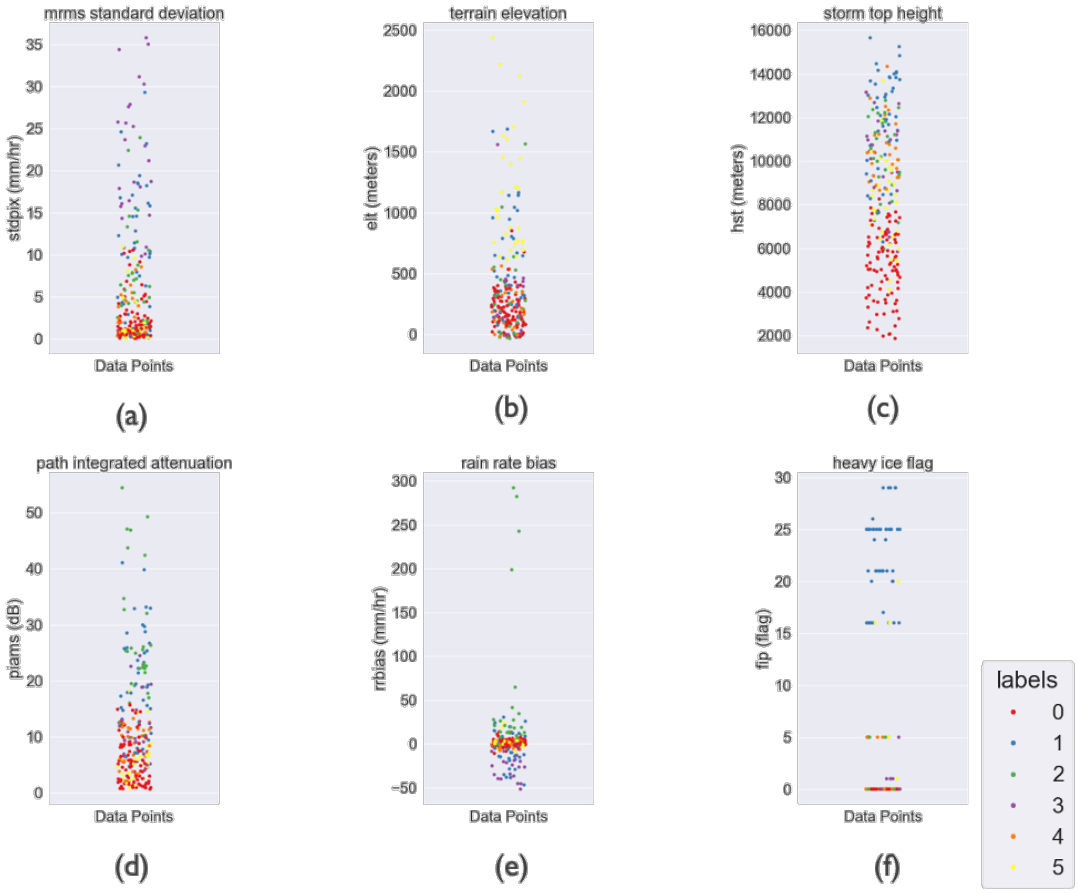


Figure 9.5: Strip-plot analysis illustrating the separation of variables between Cluster 0 (red), 1 (blue), 2 (green), 3 (purple), 4 (orange), and 5 (yellow) through K-means clustering utilizing only datapoints from the full dataset classified as convective. Each strip-plot depicts the distribution of a specific variable within each cluster, highlighting distinctive patterns and cluster separations, including (a) stdpix, (b) elt, (c) hst, (d) piams, (e) rain rate bias defined to be the DPR rain rate minus the MRMS rain rate at the surface, and (f) fip. For visualization purposes the plot contains a random subset of the full data set of 61,302 convective data points for visualization. This visual analysis provides insights into the role of individual variables in defining cluster boundaries and identifying key features that distinguish clusters within the dataset.

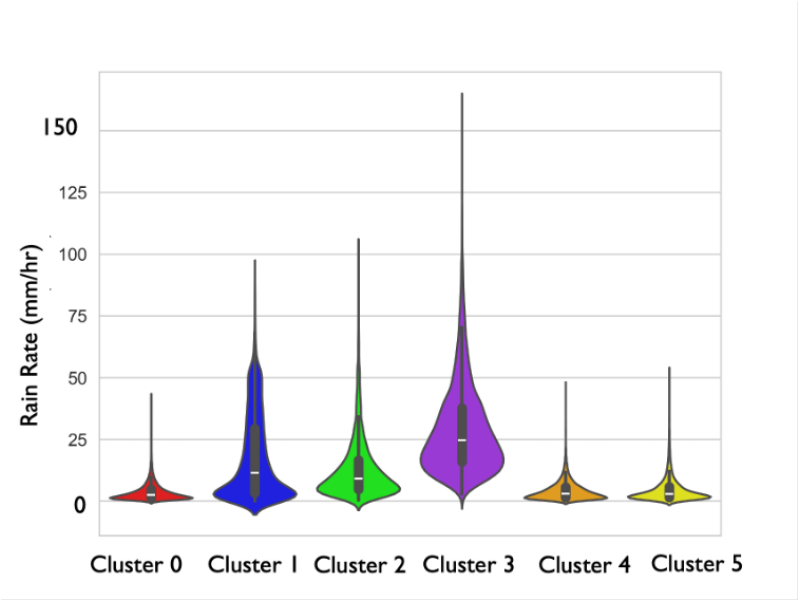


Figure 9.6: Violin plots showing MRMS rain rate (mm/hr) associated with each convective cluster.

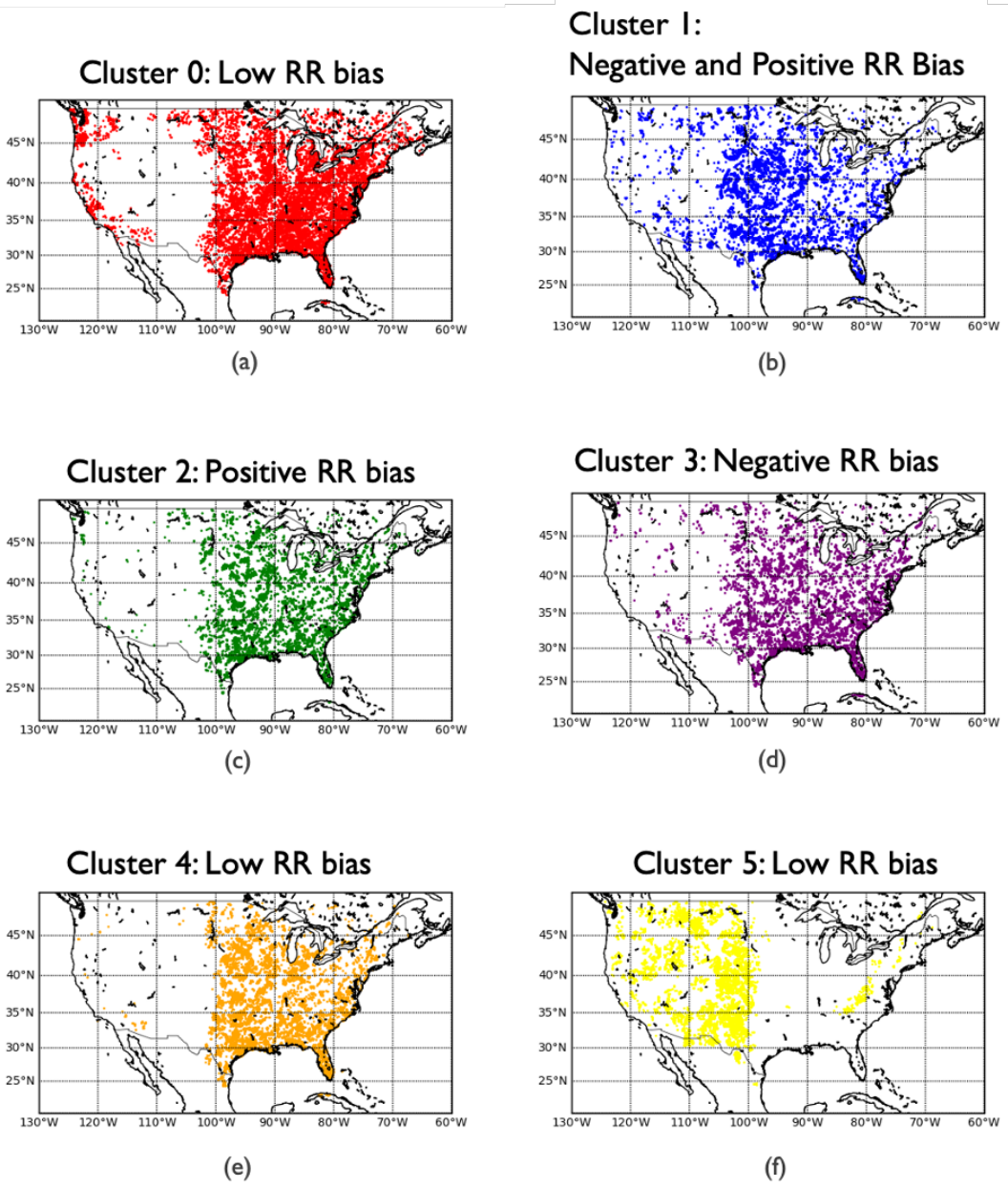


Figure 9.7: Spatial distribution of convective k-means clusters over CONUS.

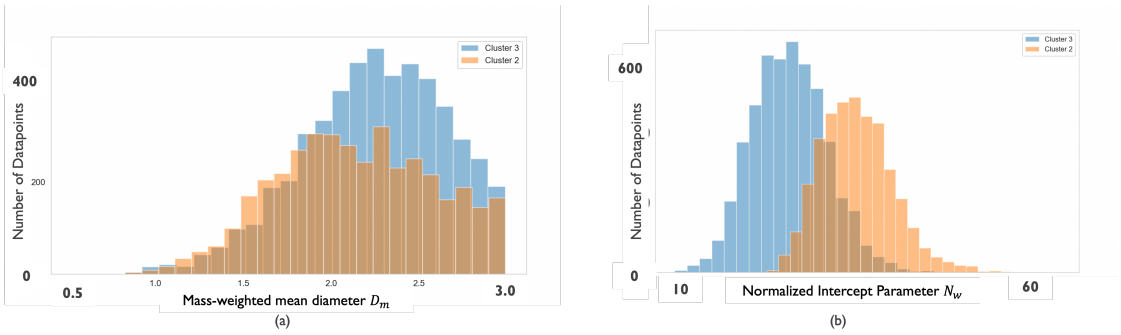


Figure 9.8: Separation between Cluster 2 and Cluster 3 in (a) D_m and (b) N_w

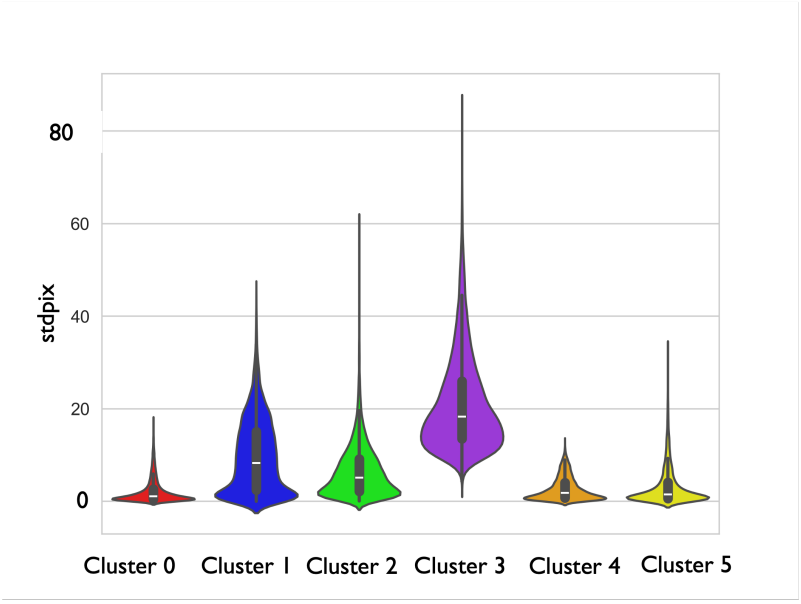


Figure 9.9: Violin plots showing MRMS standard deviation (mm/hr) associated with each convective cluster from Section 3b.

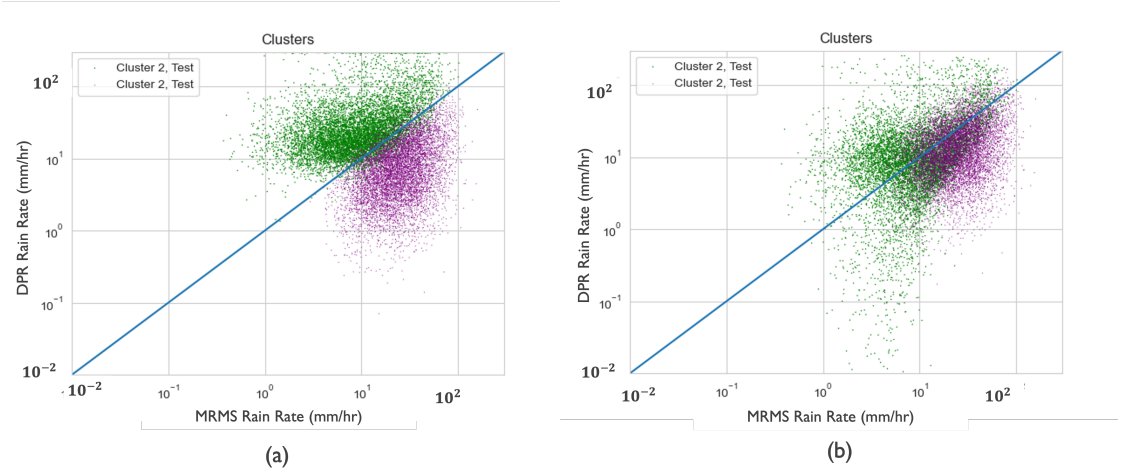


Figure 9.10: (a) Rain rate bias plots of Cluster 2 (green) and Cluster 3 (purple) and (b) after NUBF correction was applied allowing Cluster 2 to take the value of each individial data points lower 75th confidence bound for rain rate and allowing Cluster 2 to take the upper bound of each points confidence interval. A reduced RR bias due to NUBF correction motivates the conclusion that these clusters have biases driven by NUBF.

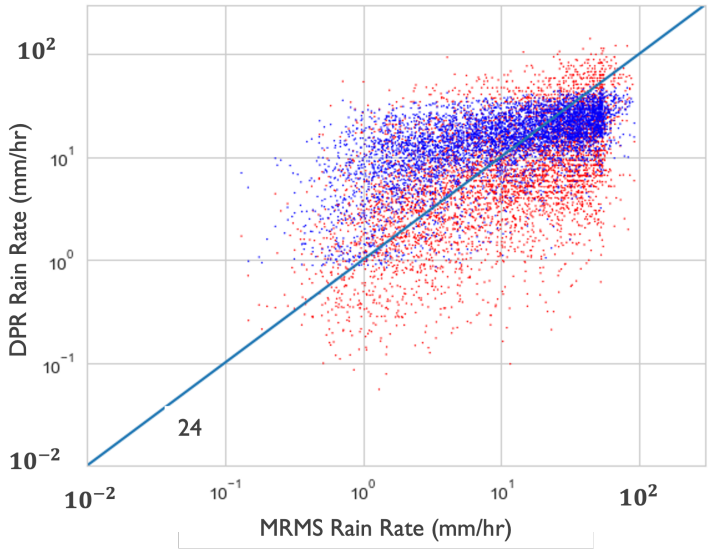


Figure 9.11: Depiction of multiple-scattering correction: red points indicate a subset of Cluster 1 from the convective dataset with a heavy ice flag greater than 20 and a difference between the DPR normal-scan reflectivity and the DPR matched-scan reflectivity greater than 6 dB. The blue points in indicate the same subset of points transformed using the Ku-band TRMM Rain Relationship as in Iguchi et al. (2000). A reduced RR bias due to multiple scattering correction motivates the conclusion that these clusters have a population of datapoints with biases driven by multiple scattering.

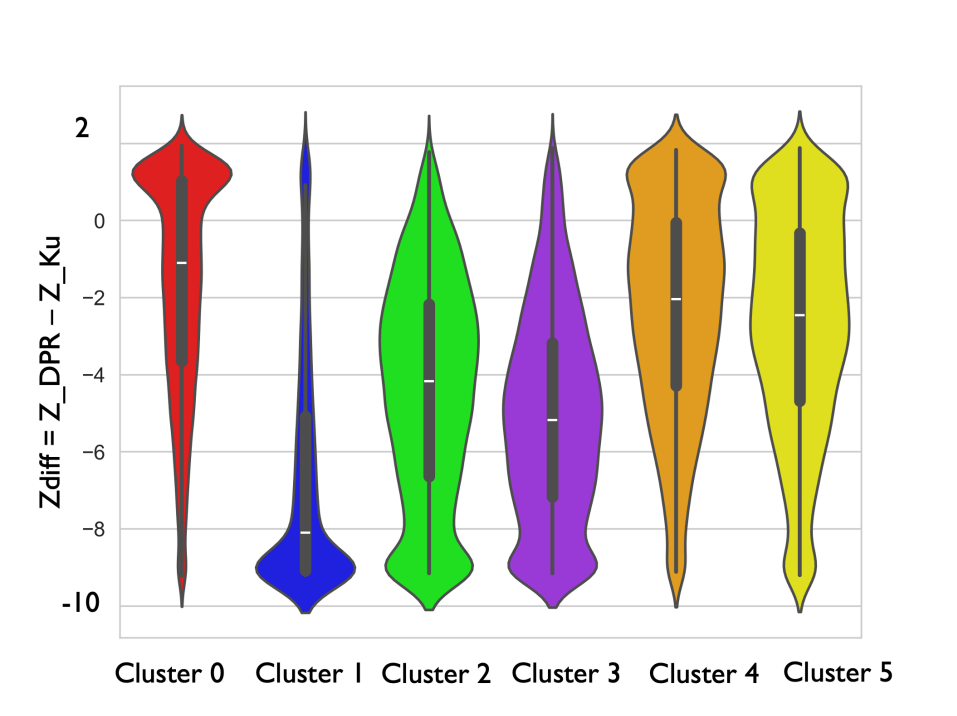


Figure 9.12: Violin plot of the difference in reflectivity between the matched scan (dependent on the dual-frequency algorithm) and the normal scan (Ku-only) reflectivities for each convective cluster.

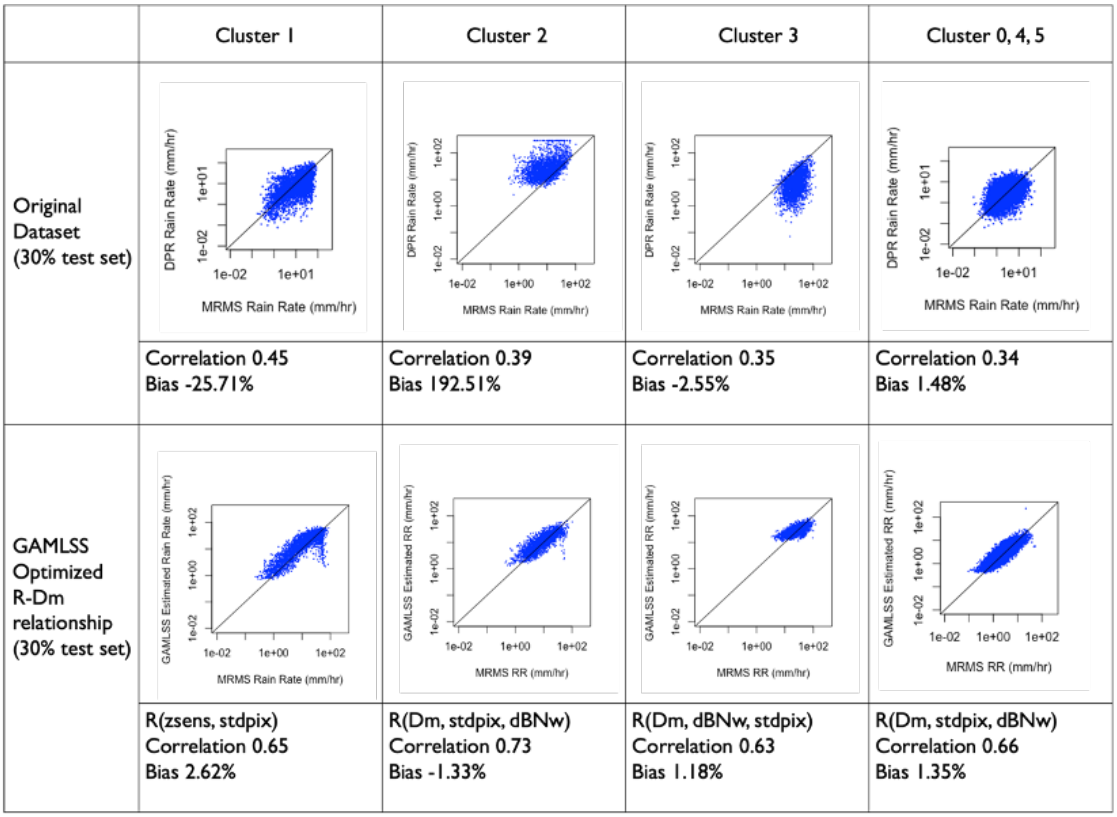


Figure 9.13: Convective cluster rain rate correlation and bias for a random test set containing 30% of the convective observations in the matched MRMS/DPR dataset (top row) and rain rate correlation and bias for the same 30% test set of data points passed through GAMLSS optimized R-D_m relationships trained on 70% of the dataset for each cluster

Chapter 10

Appendix D: Blueprint for Future Field Campaigns: Shared Leadership and Inclusive Decision-Making

This section outlines a proposed blueprint for future field campaigns that hinges on shared leadership and inclusive decision-making as well as equitable leadership credit.

To start, it is important to address the concept of resource ownership of instruments developed with federal funding. Who owns Horus?

As a public investment, PARs developed by NOAA are operated by but not owned by governmental agency sub-groups that acquire or develop them. NOAA promotes the sharing of PAR data among federal agencies and the public in its NOAA Public Access to Research Results (PARR) Plan (De La Beaujardière and Kaske (2015)). Beyond this, a White House memorandum on Ensuring Free, Immediate, and Equitable Access to Federally Funded Research discusses how the "free flow of information between the Government and the public is essential to a democratic society," indicating that the purpose of technology development is for the public benefit. It further advises that "Agencies should also provide for coordinated decision making... to bring together the perspectives from across an agency, and outside if appropriate... Interested groups

typically include functional users, managers of financial and human resources, information resources management specialists, and, as appropriate, the affected public" (White House Office of Science and Technology Policy (OSTP) (2022)).

Publicly funded research, weather radar development, and operation then have much to benefit from a broader use of distributed leadership models within agencies. These models help to ensure that strategic and operational decisions are made collaboratively and that perspectives from many stakeholders are appropriately accounted for. "Stakeholders" in this context refers to the people engaged in developing scientific advancements: students, research scientists, postdocs, and faculty. Rather than being isolated agency tools subject to the management of a few, this model puts developed technologies like weather radar prototypes under a broader agency scientist commons purview, which is more in line with the democratic intent of their development. Through shared oversight, this model is naturally transparent and has a built-in accountability mechanism to ensure that data access and science priorities accurately reflect the public's needs.

The purpose of field campaigns is to advance science through real-world observation of phenomena that may require coordinated measurements to achieve. Scientists must collaborate to achieve and interpret the science goals and set a direction for the campaign that maximizes the synergy of the campaign's science stakeholders. The structure of many field campaigns in academia tends to mirror the structural norms of academia itself in its hierarchical decision-making schemes.

Designating leaders of field campaigns with sole discretion to outline all science needs and to direct the execution of them can help to improve equity, assuming that all the science needs of the stakeholders have been comprehensively communicated to the leaders and that the leader in question remains unbiased in the collection of individual stakeholder needs. A leader in this context should be chosen for their ability to foster

a collaborative team environment by leading with both empathy (e.g., who embodies emotional intelligence (EQ)) and respect. Cultivating such a culture requires genuine kindness and a spirit of partnership, eschewing an air of authority over others in favor of working alongside them to achieve shared goals. An issue with this operating model in academia is related to credit and identity. This section draws from my own experience in campaign planning and relevant academic literature to help propose a blueprint for future field campaigns built on three categories: shared leadership, transparent credit, and participatory education. Together, these elements help to form the foundation of an evolved collaborative scientific research culture with built-in rotational facilitation safeguards to guard against centralized leadership.

In academia, graduate students and early-career scientists are often relegated to the margins of decision-making within research campaigns, despite their core role in the generation of the scientific questions and theories often being targeted by these campaigns. Faculty and senior scientists can consider themselves to be the heart of the university, dedicated to helping to shape and mentor students and early career scientists. This self-identity of function, while altruistic in its conception, is a dominant self-perception that can lead to exclusion and reinforcement of cultural and hierarchical norms. Advisors are varied in approach, however, with some seeing advisership as a way to help others practice their dialogue, engagement, and independent scientific formalization and decision-making skills so that students are empowered to become engaged democratic actors in their work-life. In other words, some advisors choose andragogy over pedagogy. A perception of the role of students as relatively passive, and sometimes child-like, rather than autonomous stakeholders engaged in the act of scientific creation is a pernicious problem because it reinforces this passive self-perception in the minds of students, many of whom already hold a child-like self-identity established and perpetuated through their undergraduate education by institutional and faculty

infantilization of students (Babich (2023)). Dominant and subordinate roles such as these in sociocultural contexts are described in literature with the terms "appropriated dominance" and "appropriated oppression" since they are self-identities adopted from existing social and structural stratifications (Tappan (2006)). It is important to note that when adults who recognize their own competence are infantilized, the resulting loss of autonomy and dignity can lead to heightened psychological distress; this dynamic undermines their sense of agency and self-worth (Epstein et al. (2023)). Now, no matter their personal identity, students have high potential for acting as directive guides in science, as one case example from this work that describes students' and early-career scientists' full capability to act as informed priority setters is the Student and Early-Career Workshop that was held as a part of the IPC-14 hosted in June of 2023, introduced in 1.2.1, wherein student and early-career researcher surveys on priority focus area needs in precipitation science were nearly identical to those priorities set by full-conference attendees, which included senior scientists.

Now, there is an argument to be made for the benefits of hierarchy, as it can help to provide clear organization to working groups and efficient decision-making, which can be laborious to realize if, on the other extreme, consensus is sought for all decisions. Leadership styles within hierarchical systems are on a spectrum of bias from one extreme embodiment, being extremely inclusive of stakeholder perspectives, to the other extreme, which is complete disconnection from the perspectives of the group. To reduce the risks associated with bias in organizational function, a distributed leadership model can be implemented. Field campaign organizations are modest in organizational size, typically involving less than fifty people and operating over limited timeframes, and are an excellent testbed for the exercise of distributed leadership approaches, similar to those demonstrated for health quality improvement collaboratives by Carstensen et al. (2024).

Before outlining a blueprint for the distributed operation and leadership of a field campaign, it is important, especially within academic settings, to consider the role of credit. Credit is the mechanism through which the community recognizes individual contributions, and it directly affects a researcher's ability to secure future funding. This recognition can emerge informally through peer perception or take formal shape as awards and honors from established organizations. Individuals who are seen as leaders in academic circles often receive such credit regardless of the precise extent of their tangible contributions. These individuals may include those who lead proposals, senior scholars, heads of research groups or laboratories, and those affiliated with prestigious institutions (Merton (1968)). Although various metrics and approaches have been proposed to address these patterns (Sauermann and Haeussler (2017)), this work advocates a different structural strategy. Distributed leadership, combined with student empowerment through active participation, can foster a more equitable distribution of credit among scientific contributors and counteract the formation of subordinate identities that tend to reinforce existing hierarchies.

A collaborative effort like a field campaign is ripe for piloting distributed leadership wherein interested stakeholders are enabled to take visible ownership of leadership roles because of the often limited number of participants and limited project time span. Stakeholders or stakeholder groups with specific project roles will be called agents herein. While agent domain ownership is important during the function of the campaign, transparent reporting and sharing of approaches is important for the holistic systems education of all interested group members. The educational opportunity built into project tasks is important to highlight here because academic research stakeholders tend to be lifelong learners who continually seek professional growth. Facilitators and rapporteurs are necessary to maintain cohesion between agents and ensure accountability. While facilitators have an important role in helping to guide the success of the

group, they should not be given dominant titles, e.g., program lead, which may tend to allocate an inequitable amount of credit and importance to their role over the roles of the agents. Below is an actionable breakdown of how a distributed leadership model might be facilitated, allowing for project agility and stakeholder input. Rotating roles are alluded to, and it should be noted the roles of facilitator and rapporteur, while under the purview of one or more persons for a single field campaign, can be considered rotating roles in future field campaigns or for efforts that do not have short-lived lifetimes. The plan below requires stakeholder buy-in and commitment to enhancing the education and leadership skills of the whole group.

Step 1: Facilitator and rapporteur selection should be performed via a transparent call for nominations or self-nominations. This allows interested stakeholders an opportunity for consideration. The facilitator should be evaluated for their experience in collaborative work environments and with conflict resolution, while a rapporteur may be a stakeholder with a desire to learn these skills and potential for growth.

Step 2: Planning meeting: Meet with all stakeholders to define required campaign tasks/outcomes (e.g., instrument operation, data processing, science analysis) while collaboratively assessing the level of effort of each task, required skill sets, tasks where responsibility rotation is possible, and metrics of success for each task. This planning meeting may also be used to define the frequency/timing of accountability meetings to ensure mission success. A rapporteur can operate to capture group resolutions.

Step 3: Query stakeholders in an open sign-up format for their interest in being assigned responsibility as agents for each task, the skillsets they can apply to the task, and the learning/development opportunities they are seeking.

Step 4: A facilitator can then assign agent roles, defining periodic rotation in those roles determined to be rotatable by the agreement of the stakeholders in step 1 to interested parties identified in step 2. Ensuring that role skillset coverage is

maintained at all times while also promoting stakeholder education may mean that the role should be assigned to more than one involved stakeholder. Assigned roles and rotation schedules should be posted and transparently accessible to all stakeholders by the facilitator or the rapporteur.

Step 5: Accountability meetings: Domain ownership and agency over assigned roles should be upheld within the role rotation, and accountability ensured through stakeholder round-table meetings where predefined task metrics from step 1 are updated and reassessments of campaign tasks by all stakeholders are considered. By these means, the rapporteur should be responsible for tracking metric progress, and the facilitator should help to influence solution dialogues between agents where needed.

Step 6: Project wrap-up: Outcomes should be collected from stakeholders and other deliverables closed (e.g., final project report and data filing). Post-project reflections and learnings should be discussed with the stakeholders.

The steps above are a collaborative alternative to traditional project management that maintains elements of scope definition, feasibility assessment, objective setting, scheduling, progress monitoring, and risk management. They also expand on traditional top-down leadership to empower task ownership, leading to more equitable credit distribution; encourage system learning and equitable access to operations for interested stakeholders; combat dominant and subordinate identity through roles as responsible agents or agent groups; and allow for opportunity equity through interest forms and task rotation. Distributed leadership workflows cannot be executed, however, without administrative support, as has also been mentioned by Carstensen et al. (2024), so administrator collaboration and open/transparent communication are critical.

Taking a step beyond field campaigns to close this section on high-level philosophy for the weather-research enterprise in the United States, an increase in democratic and

participatory management approaches at scale in academic leadership and government agency funding may hold promise for helping to democratize innovation, promote a culture of academic plurality, and encourage more realized embodiments of academic freedom. This promotes, through freedom of expression, the development of unconventional scientific and technological advancements that benefit society and reduces potential bias of knowledge and advancements by heavy influence from profit-seeking entities disinterested in the common good (Martin (1998)).

Reference List

Adamiec-Wójcik, I., L. Brzozowska, L. Drąg, and S. Wojciech, 2022: An iterative method for calculation of wind profiles at the mesoscale and microscale. *Boundary-Layer Meteorology*, **183 (3)**, 423–445, https://doi.org/10.1007/s10546-022-00690-0.

Aldana, M., S. Pulkkinen, A. von Lerber, M. R. Kumjian, and D. Moisseev, 2025: Benchmarking k dp in rainfall: a quantitative assessment of estimation algorithms using c-band weather radar observations. *Atmospheric Measurement Techniques*, **18 (3)**, 793–816.

Anagnostou, E. N., C. A. Morales, and T. Dinku, 2001: The use of trmm precipitation radar observations in determining ground radar calibration biases. *Journal of Atmospheric and Oceanic Technology*, **18 (4)**, 616–628.

Anthony, J., S. M. Martinaitis, Z. Barney, S. M. Waugh, D. Meyer, S. B. Cocks, and K. Howard, 2025: Telemetry of observed total accumulated liquid (total) precipitation trailer introduction and preliminary results. *105th Annual AMS Meeting 2025*, Vol. 105, 452143.

Aquino, C. M. S., B. Cheong, and R. D. Palmer, 2021a: Progressive pulse compression: A novel technique for blind range recovery for solid-state radars. *Journal of Atmospheric and Oceanic Technology*, **38 (9)**, 1599–1611, https://doi.org/10.1175/JTECH-D-20-0176.1.

Aquino, C. M. S., B. Cheong, and R. D. Palmer, 2021b: Progressive pulse compression: A novel technique for blind range recovery for solid-state radars. *Journal of Atmospheric and Oceanic Technology*, **38 (9)**, 1599 – 1611, https://doi.org/ https://doi.org/10.1175/JTECH-D-20-0164.1, URL https://journals.ametsoc.org/view/journals/atot/38/9/JTECH-D-20-0164.1.xml.

ARRC, 2020: Raxpol – rapid x-band polarimetric radar. University of Oklahoma, accessed: 2025-10-26, https://arrc.ou.edu/radar_raxpol.html.

ARRC, 2023: Horus — all-digital polarimetric phased array radar. University of Oklahoma, accessed: 2025-10-26, https://arrc.ou.edu/radar_horus.html.

ARRC, 2025: Polarimetric x-band 1000 (px-1000). Advanced Radar Research Center, University of Oklahoma, [Accessed: 2025-11-08], https://arrc.ou.edu/radar_px1000.html.

Austin, P. M., 1987: Relation between measured radar reflectivity and surface rainfall. *Monthly weather review*, **115 (5)**, 1053–1070.

Azevedo, K., and Coauthors, 2023: Weathering the hunt: The role of barometric pressure in predator insects' foraging behaviour. *Ecology and Evolution*, **13**, e10 416, https://doi.org/10.1002/ece3.10416.

Babich, C., 2023: Arrested educational development: Universities and the infantilization of students instead of andragogical competency - a systematic review. *Journal of Psychological and Educational Research*, **31 (2)**, 7–23, https://doi.org/10.31287/jper.31.2.2023.7-23.

Baldini, L., V. Chandrasekar, and D. Moisseev, 2012: Microwave radar signatures of precipitation from s band to ka band: Application to gpm mission. *European Journal of Remote Sensing*, **45 (1)**, 75–88.

Basara, J., 2022: Hydroclimatology course material. *Hydroclimatology Course Material Fall 2021*, Norman, OK, The University of Oklahoma.

Basics, P., 2009: Mrr_physical_basics. METEK, URL https://www.inscc.utah.edu/~u0546592/CFOG/ED/MRR/mrr-physicalbasics.pdf.

Battaglia, A., M. Ajewole, and C. Simmer, 2006: Evaluation of radar multiple-scattering effects from a gpm perspective. part i: Model description and validation. *Journal of applied meteorology and climatology*, **45 (12)**, 1634–1647, https://doi.org/https://doi.org/10.1175/JAM2424.1.

Battaglia, A., S. Tanelli, K. Mroz, and F. Tridon, 2015: Multiple scattering in observations of the gpm dual-frequency precipitation radar: Evidence and impact on retrievals. *Journal of Geophysical Research: Atmospheres*, **120 (9)**, 4090–4101, https://doi.org/https://doi.org/10.1002/2014JD022866.

Battaglia, A., and Coauthors, 2020: Spaceborne cloud and precipitation radars: Status, challenges, and ways forward. *Reviews of Geophysics*, **58 (3)**, e2019RG000 686.

Battan, L. J., 1973: *Radar Observation of the Atmosphere*. University of Chicago Press, Chicago, IL.

Biswas, S. K., and V. Chandrasekar, 2018: Cross-validation of observations between the gpm dual-frequency precipitation radar and ground based dual-polarization radars. *Remote Sensing*, **10 (11)**, 1773.

Bohren, C. F., and D. R. Huffman, 1983: *Absorption and Scattering of Light by Small*

Particles. Wiley, New York, NY.

Brandes, E. A., G. Zhang, and J. Vivekanandan, 2002: Experiments in rainfall estimation with a polarimetric radar in a subtropical environment. *Journal of Applied Meteorology*, **41 (6)**, 674–685.

Brauer, N., 2022: Satellite and radar remote sensing of tropical cyclones to quantify microphysical and precipitation processes. *Unknown*.

Brauer, N. S., P. E. Kirstetter, J. B. Basara, S. Hristova-Veleva, S. Tanelli, and F. Joseph Turk, 2024: Precipitation microphysics in tropical cyclones: A global perspective using the nasa global precipitation measurement mission dual-frequency precipitation radar. *Journal of Geophysical Research: Atmospheres*, **129 (1)**, e2023JD038 709.

Brauer, N. S., and Coauthors, 2022: Hurricane laura (2020): A comparison of drop size distribution moments using ground and radar remote sensing retrieval methods. *Journal of Geophysical Research: Atmospheres*, **127 (16)**, e2021JD035 845.

Bringi, V., V. Chandrasekar, J. Hubbert, E. Gorgucci, W. Randeu, and M. Schoenhuber, 2003: Raindrop size distribution in different climatic regimes from disdrometer and dual-polarized radar analysis. *Journal of the atmospheric sciences*, **60 (2)**, 354–365.

Bringi, V., V.Chandrasekar, E. Gorgucci, and G. Scarchilli, 2002: Estimation of raindrop size distribution parameters from polarimetric radar measurements. *Journal of the Atmospheric Sciences*, **59 (13)**, 2373–2384, https://doi.org/10.1175/1520-0469(2002)059<2373:EORSDP>2.0.CO;2.

Bringi, V. N., and V. Chandrasekar, 2001: *Polarimetric Doppler Weather Radar: Principles and Applications*. Cambridge University Press, Cambridge, UK.

Bringi, V. N., V. Chandrasekar, N. Balakrishnan, and D. S. Zrnić, 1990: An examination of propagation effects in rainfall on radar measurements at microwave frequencies. *Journal of Atmospheric and Oceanic Technology*, **7 (5)**, 829–840.

Cao, Q., G. Zhang, E. A. Brandes, and T. J. Schuur, 2010: Polarimetric radar rain estimation through retrieval of drop size distribution using a bayesian approach. *Journal of Applied Meteorology and Climatology*, **49 (5)**, 973–990.

Carr, N., P. Kirstetter, J. Gourley, and Y. Hong, 2017: Polarimetric signatures of midlatitude warm-rain precipitation events. *Journal of Applied Meteorology and Climatology*, **56 (3)**, 697–711.

Carstensen, K., A. M. Kjeldsen, and C. P. Nielsen, 2024: Distributed leadership in health quality improvement collaboratives. *Health Care Management Review*, **49 (1)**, 46–58, URL https://journals.lww.com/hcmrjournal/fulltext/2024/01000/distributed_leadership_in_health_quality.6.aspx.

Carvalho, M., P. Melo-Gonçalves, J. Teixeira, and A. Rocha, 2016: Regionalization of europe based on a k-means cluster analysis of the climate change of temperatures and precipitation. *Physics and Chemistry of the Earth, Parts A/B/C*, **94**, 22–28, https://doi.org/https://doi.org/10.1016/j.pce.2016.05.001.

Cavallo, S., 2021a: Dynamics. The University of Oklahoma, the University of Oklahoma, Oral Presentation, Fall 2021 METR5004.

Cavallo, S., 2021b: Fundamentals of atmospheric science course material fall 2021. *Fundamentals of Atmospheric Science Course Material*, Norman, OK, The University of Oklahoma.

Cecil, D. J., S. Braun, J. Yorks, T. Thorsen, and M. W. McLinden, 2023: Nasa's atmosphere observing system (aos), from a precipitation perspective. *14th International Precipitation Conference*.

Center, N. R. O., 2001: Wsr-88d system specification. Radar Operations Center, URL https://www.qsl.net/n9zia/2810000C.pdf, document Number 2810000C.

Center, S. P., 2015: Mesoscale analysis daily archive directory. Storm Prediction Center, URL https://www.spc.noaa.gov/exper/ma_archive/, accessed April 4, 2024.

Chandrakar, K. K., H. Morrison, W. W. Grabowski, and R. P. Lawson, 2024: Are turbulence effects on droplet collision–coalescence a key to understanding observed rain formation in clouds? *Proceedings of the National Academy of Sciences*, **121 (27)**, e2319664 121.

Chase, R. J., B. Dolan, K. L. Rasmussen, R. M. Schulte, G. Stephens, F. J. Turk, and S. C. Van den Heever, 2025: A multifrequency spaceborne radar perspective of deep convection. *Journal of Applied Meteorology and Climatology*, **64 (2)**, 133–145.

Chase, R. J., S. W. Nesbitt, and G. M. McFarquhar, 2020: Evaluation of the microphysical assumptions within gpm-dpr using ground-based observations of rain and snow. *Atmosphere*, **11 (6)**, 619.

Chen, Y., H. Liu, J. An, U. Görsdorf, and F. H. Berger, 2015: A field experiment on the small-scale variability of rainfall based on a network of micro rain radars and rain gauges. *Journal of Applied Meteorology and Climatology*, **54 (1)**, 243–255.

Cho, 2015: A historical review on the introduction of chugugi and the rainfall observation network during the joseon dynasty. *Atmosphere*, URL https://koreascience.kr/article/JAKO201504255079234.page, in the 23rd year of King Sejong (1441) the world's first rain gauge called Chugugi was invented; a nationwide rainfall observation network was established in 1442.

Cocks, S. B., and Coauthors, 2019: A prototype quantitative precipitation estimation algorithm for operational s-band polarimetric radar utilizing specific attenuation and specific differential phase. part ii: Performance verification and case study analysis. *Journal of Hydrometeorology*, **20 (5)**, 999–1014.

Compilations, T., 2025: Ef1 tornado near norman, oklahoma - june 3rd, 2025. YouTube, URL https://www.youtube.com/watch?v=uOqQrFlbaRQ, accessed: 2025-11-01, YouTube video.

Cooper, N. W., and Coauthors, 2023: Atmospheric pressure predicts probability of departure for migratory songbirds. *Movement Ecology*, **11 (1)**, 23, https://doi.org/10.1186/s40462-022-00356-z.

Crum, T. D., and R. L. Alberty, 1993: The wsr-88d and the wsr-88d operational support facility. *Bulletin of the American Meteorological Society*, **74 (9)**, 1669–1688.

Dai, A., 2011: Drought under global warming: a review. *Wiley Interdisciplinary Reviews: Climate Change*, **2 (1)**, 45–65, https://doi.org/https://doi.org/10.1002/wcc.81.

De Bruijn, R., and L. M. Romero, 2018: The role of glucocorticoids in the vertebrate response to weather-related stimuli. *General and Comparative Endocrinology*, **269**, 11–32, https://doi.org/10.1016/j.ygcen.2018.01.012.

De La Beaujardière, J., and N. K. Kaske, 2015: Noaa plan for increasing public access to research results. National Oceanic and Atmospheric Administration, URL https://repository.library.noaa.gov/view/noaa/10169, accessed: 2025-10-26.

Delrieu, G., B. Boudevillain, J. Nicol, B. Chapon, P.-E. Kirstetter, H. Andrieu, and D. Faure, 2009: Bollène-2002 experiment: Radar quantitative precipitation estimation in the cévennes–vivarais region, france. *Journal of Applied Meteorology and Climatology*, **48 (7)**, 1422–1447.

Derin, P., Y. Kirstetter, and D. Faure, 2023: Guiding the improvement of the global precipitation measurement (gpm) mission with radar networks over france and usa mountainous regions. *Session H32C: Space-Based Precipitation Observations: Innovations for Science and Applications*, San Francisco, CA, Amer. Geophys. Union.

Dixon, A., N. S. Brauer, and P. Kirstetter, 2024a: A multi-radar perspective on the stratiform precipitation region of landfalling hurricane ian (2022). *Proceedings of the 104th Annual Meeting of the American Meteorological Society*, Baltimore, MD, URL https://ams.confex.com/ams/104ANNUAL/meetingapp.cgi/Paper/436905, poster presentation.

Dixon, A., and coauthors, 2023: Precipitation quantification informed by polarimetric phased array radar process observations. *Proceedings of the American Geophysical Union Fall Meeting 2023*, San Francisco, CA, poster presentation.

Dixon, A., P. Kirstetter, R. D. Palmer, J. Carlin, and A. V. Ryzhkov, 2024b: Precipitation quantification informed by polarimetric phased array radar process observations. *Proceedings of the 104th Annual Meeting of the American Meteorological Society*, Baltimore, MD, URL https://ams.confex.com/ams/104ANNUAL/meetingapp.cgi/Paper/440069, oral presentation.

Dolan, B., B. Fuchs, S. Rutledge, E. Barnes, and E. Thompson, 2018: Primary modes of global drop size distributions. *Journal of the Atmospheric Sciences*, **75 (5)**, 1453–1476, https://doi.org/https://doi.org/10.1175/JAS-D-17-0242.1.

Dolan, B., and Coauthors, 2023: Time resolved reflectivity measurements of convective clouds. *Geophysical Research Letters*, **50 (22)**, e2023GL105 723.

Donovan, D. P., P. Kollias, A. Velázquez Blázquez, and G.-J. van Zadelhoff, 2023: The generation of earthcare l1 test data sets using atmospheric model data sets. *Atmospheric Measurement Techniques*, **16 (21)**, 5327–5356.

Doviak, R., V. Bringi, A. Ryzhkov, A. Zahrai, and D. Zrnić, 2000: Considerations for polarimetric upgrades to operational wsr-88d radars. *Journal of Atmospheric and Oceanic Technology*, **17 (3)**, 257–278.

Doviak, R. J., and D. S. Zrnić, 1993: *Doppler Radar and Weather Observations*. 2nd ed., Academic Press, San Diego, CA, see Section 2.2 for radar beam geometry; the beamwidth relation $D = 2r\tan(\theta/2)$ follows from basic trigonometry.

Emmerson, S., 2022: Observations and simulations of a multistatic weather radar network. M.S. thesis, Department of Meteorology, University of Oklahoma, master's thesis, full text available on ResearchGate.

Emmerson, S., R. Palmer, D. Bodine, D. Schvartzman, P. Kirstetter, P. Skinner, and C. Fulton, 2025: Retrieval and quantitative evaluation of three-dimensional winds in severe convection with multistatic radar. *Journal of Atmospheric and Oceanic Technology*, **42 (9)**, 1167–1183.

Epstein, R., S. D. Bock, M. J. Drew, and Z. Scandalis, 2023: Infantilization across the life span: A large-scale internet study suggests that emotional abuse is especially damaging. *Motivation and Emotion*, **47**, 137–163, https://doi.org/10.1007/s11031-022-09989-4, URL https://doi.org/10.1007/s11031-022-09989-4.

Eshel, A., H. Messer, H. Kunstmann, P. Alpert, and C. Chwala, 2021: Quantitative analysis of the performance of spatial interpolation methods for rainfall estimation using commercial microwave links. *Journal of Hydrometeorology*, **22 (4)**, 831–843.

Fabry, F., 1996: On the determination of scale ranges for precipitation fields. *Journal of Geophysical Research: Atmospheres*, **101 (D8)**, 12 819–12 826.

Fabry, F., and W. Szyrmer, 1999: Modeling of the melting layer. part ii: Electromagnetic. *Journal of the atmospheric sciences*, **56 (20)**, 3593–3600.

Franco, M., R. Sánchez-Diezma, D. Sempere-Torres, and I. Zawadzki, 2005: An improved methodology for classifying convective and stratiform rain. *Proceedings of the 32nd Conference on Radar Meteorology, Alvarado, Mexico*, 22–29.

Fulton, C. J., 2022: Digital array radar calibration and performance monitoring techniques. Ph.D. thesis, Purdue University, West Lafayette, IN, USA, ph.D. Dissertation.

Gao, J., M. Xue, A. Shapiro, and K. K. Droegemeier, 1999: A variational method for the analysis of three-dimensional wind fields from two doppler radars. *Monthly Weather Review*, **127 (9)**, 2128–2142, https://doi.org/10.1175/1520-0493(1999)127<2128:AVMFTA>2.0.CO;2, URL https://journals.ametsoc.org/view/journals/mwre/127/9/1520-0493_1999_127_2128_avmfta_2.0.co_2.xml.

Gatlin, P. N., W. A. Petersen, J. L. Pippitt, T. A. Berendes, D. B. Wolff, and A. Tokay, 2020: The gpm validation network and evaluation of satellite-based retrievals of the rain drop size distribution. *Atmosphere*, **11 (9)**, 1010.

Gourley, J. J., and Coauthors, 2017a: The flash project: Improving the tools for flash flood monitoring and prediction across the united states. *Bulletin of the American Meteorological Society*, **98 (2)**, 361–372.

Gourley, J. J., and Coauthors, 2017b: The flooded locations and simulated hydrographs (flash) project: improving the tools for flash flood monitoring and prediction across the united states. *Bulletin of the American Meteorological Society*.

Grabowski, W. W., and H. Morrison, 2017: Modeling condensation in deep convection. *Journal of the Atmospheric Sciences*, **74 (7)**, 2247–2267, https://doi.org/10.1175/

JAS-D-16-0255.1.

Guerra, J. E., P. S. Skinner, A. Clark, M. Flora, B. Matilla, K. Knopfmeier, and A. E. Reinhart, 2022: Quantification of nssl warn-on-forecast system accuracy by storm age using object-based verification. *Weather and Forecasting*, **37 (11)**, 1973–1983.

Gunn, R., and G. D. Kinzer, 1949: The terminal velocity of fall for water droplets in stagnant air. *Journal of Atmospheric Sciences*, **6 (4)**, 243–248.

Gupta, A. K., and Coauthors, 2023: The microphysics of the warm-rain and ice crystal processes of precipitation in simulated continental convective storms. *Communications Earth & Environment*, **4**, 226, https://doi.org/10.1038/s43247-023-00884-5, URL https://doi.org/10.1038/s43247-023-00884-5.

Habib, E., W. F. Krajewski, and A. Kruger, 2001: Sampling errors of tipping-bucket rain gauge measurements. *Journal of Hydrologic Engineering*, **6 (2)**, 159–166.

Habibi, H., R. Awal, A. Fares, and M. Temimi, 2021: Performance of multi-radar multi-sensor (mrms) product in monitoring precipitation under extreme events in harris county, texas. *Journal of Hydrology*, **598**, 126 385.

Haddad, Z. S., and O. O. Sy, 2024: From raincube to incus: Using miniaturized microwave instruments to analyze the dynamics of tropical convection. *IEEE Journal of Microwaves*.

Haddad, Z. S., and Coauthors, 2022: Observation strategy of the incus mission: Retrieving vertical mass flux in convective updrafts from low-earth-orbit convoys of miniaturized microwave instruments. *IGARSS 2022-2022 IEEE International Geoscience and Remote Sensing Symposium*, IEEE, 6448–6451.

Hagen, M., and S. E. Yuter, 2003: Relations between radar reflectivity, liquid-water content, and rainfall rate during the map sop. *Quarterly Journal of the Royal Meteorological Society: A journal of the atmospheric sciences, applied meteorology and physical oceanography*, **129 (588)**, 477–493.

Helmus, J. J., and S. M. Collis, 2016: The Python ARM Radar Toolkit (Py-ART), a Library for Working with Weather Radar Data in the Python Programming Language. *Journal of Open Research Software*, **4 (1)**, e25, https://doi.org/10.5334/jors.119.

Herndon, M., D. Schvartzman, C. Fulton, and M. B. Yeary, 2024: Self-calibration of the horus all-digital phased array using mutual coupling. *2024 IEEE Radar Conference (RadarConf24)*.

Heymsfield, A. J., M. A. Cecchini, A. Detwiler, R. Honeyager, and P. Field, 2023: Exploring the composited t-28 hailstorm penetration dataset to characterize hail properties within the updraft and downdraft regions. *Journal of Applied Meteorology and Climatology*, **62 (12)**, 1803–1826.

Hitschfeld, W., 1986: The invention of radar meteorology. *Bulletin of the American Meteorological Society*, **67 (1)**, 33–37.

Ho, J., Z. Li, and G. Zhang, 2024: Quantitative error analysis on polarimetric phased array radar weather measurements to reveal radar performance and configuration potential. *Atmospheric Measurement Techniques Discussions*, **2024**, 1–30.

Holton, J. R., and G. J. Hakim, 2013: *An Introduction to Dynamic Meteorology*. 5th ed., Academic Press, San Diego.

Hong, Y., and J. J. Gourley, 2017: *Radar Hydrology*. Taylor & Francis Limited Oxford, UK:.

Hou, A. Y., G. Skofronick-Jackson, C. D. Kummerow, and J. M. Shepherd, 2008: Global precipitation measurement. *Precipitation: Advances in measurement, estimation and prediction*, 131–169.

Hou, A. Y., and Coauthors, 2014: The global precipitation measurement mission. *Bulletin of the American meteorological Society*, **95 (5)**, 701–722.

Houssos, E., C. Lolis, and A. Bartzokas, 2008: Atmospheric circulation patterns associated with extreme precipitation amounts in greece. *Advances in Geosciences*, **17**, 5–11, https://doi.org/https://doi.org/10.5194/adgeo-17-5-2008.

Houze, R. A., 1993: *Cloud Dynamics*, International Geophysics Series, Vol. 53. Academic Press, San Diego, CA.

Houze Jr, R. A., 1997a: Stratiform precipitation in regions of convection: A meteorological paradox? *Bulletin of the American Meteorological Society*, **78 (10)**, 2179–2196.

Houze Jr, R. A., 1997b: Stratiform precipitation in regions of convection: A meteorological paradox? *Bulletin of the American Meteorological Society*, **78 (10)**, 2179–2196, https://doi.org/https://doi.org/10.1175/1520-0477(1997)078<2179:SPIROC>2.0.CO;2.

Howarth, R., 1979: Journel and (ch. j.) huijbregts. mining geostatistics. london & new york (academic press), 1978. x+ 600 pp., 267 figs. price£ 32· 00. *Mineralogical*

Magazine, **43 (328)**, 563–564.

Huang, Y., and X. Cui, 2015: Dominant cloud microphysical processes of a torrential rainfall event in sichuan, china. *Advances in Atmospheric Sciences*, **32 (3)**, 389–400, https://doi.org/10.1007/s00376-014-4066-7.

Huddleston, L. L., 2012: Dual-doppler feasibility study. Tech. rep., Your Institution Name.

Huuskonen, A., E. Saltikoff, and I. Holleman, 2014: The operational weather radar network in europe. *Bulletin of the American Meteorological Society*, **95 (6)**, 897–907.

Iguchi, T., T. Kozu, R. Meneghini, J. Awaka, and K. Okamoto, 2000: Rain-profiling algorithm for the trmm precipitation radar. *Journal of applied meteorology*, **39 (12)**, 2038–2052, https://doi.org/https://doi.org/10.1175/1520-0450(2001)040<2038:RPAFTT>2.0.CO;2.

Iguchi, T., S. Seto, R. Meneghini, N. Yoshida, J. Awaka, M. Le, V. Chandrasekar, and T. Kubota, 2010: Gpm/dpr level-2 algorithm theoretical basis document. *NASA Goddard Space Flight Center*.

Iguchi, T., and Coauthors, 2012: An overview of the precipitation retrieval algorithm for the dual-frequency precipitation radar (DPR) on the global precipitation measurement (GPM) mission's core satellite. *Earth Observing Missions and Sensors: Development, Implementation, and Characterization II*, H. Shimoda, X. Xiong, C. Cao, X. Gu, C. Kim, and A. S. K. Kumar, Eds., SPIE, International Society for Optics and Photonics, Vol. 8528, 85281C, https://doi.org/10.1117/12.977352, URL https://doi.org/10.1117/12.977352.

Illingworth, A. J., and Coauthors, 2015: The earthcare satellite: The next step forward in global measurements of clouds, aerosols, precipitation, and radiation. *Bulletin of the American Meteorological Society*, **96 (8)**, 1311–1332.

Kathiravelu, G., T. Lucke, and P. Nichols, 2016: Rain drop measurement techniques: A review. *Water*, **8 (1)**, 29.

Kidd, C., T. Matsui, W. Blackwell, S. Braun, R. Leslie, and Z. Griffith, 2022: Precipitation estimation from the nasa tropics mission: Initial retrievals and validation. *Remote Sensing*, **14 (13)**, 2992.

Kim, Y., Z. Haddad, S. Tanelli, J. Nastal, J. Gayle, A. Austin, B. Donitz, and S. Van den Heever, 2023: Implementation plan for the incus mission. *2023 IEEE*

Aerospace Conference, IEEE, 1–7.

Kirstetter, P., 2022: Metr 5643 – quantitative hydrometeorology. School of Meteorology, University of Oklahoma, graduate course (3 credit hours).

Kirstetter, P.-E., H. Andrieu, B. Boudevillain, and G. Delrieu, 2013: A physically based identification of vertical profiles of reflectivity from volume scan radar data. *Journal of applied meteorology and climatology*, **52 (7)**, 1645–1663.

Kirstetter, P.-E., G. Delrieu, B. Boudevillain, and C. Obled, 2010: Toward an error model for radar quantitative precipitation estimation in the cévennes–vivarais region, france. *Journal of Hydrology*, **394 (1-2)**, 28–41.

Kirstetter, P.-E., J. J. Gourley, Y. Hong, J. Zhang, and Z. L. Flamig, 2015a: Probabilistic precipitation rate estimates with ground-based radar networks. *Water Resources Research*, **51 (3)**, 1422–1442, https://doi.org/10.1002/2014WR016498.

Kirstetter, P.-E., J. J. Gourley, Y. Hong, J. Zhang, S. Moazamigoodarzi, C. Langston, and A. Arthur, 2015b: Probabilistic precipitation rate estimates with ground-based radar networks. *Water Resources Research*, **51 (3)**, 1422–1442, https://doi.org/https://doi.org/10.1002/2014WR015672, URL https://agupubs.onlinelibrary.wiley.com/doi/abs/10.1002/2014WR015672.

Kirstetter, P.-E., W. A. Petersen, C. D. Kummerow, and D. B. Wolff, 2020: Integrated multi-satellite evaluation for the global precipitation measurement: Impact of precipitation types on spaceborne precipitation estimation. *Satellite Precipitation Measurement: Volume 2*, 583–608.

Kirstetter, P.-E., and Coauthors, 2012: Toward a framework for systematic error modeling of spaceborne precipitation radar with noaa/nssl ground radar–based national mosaic qpe. *Journal of Hydrometeorology*, **13 (4)**, 1285–1300, https://doi.org/https://doi.org/10.1175/JHM-D-11-0139.1.

Kitchen, M., R. Brown, and A. G. Davies, 1994: Real-time correction of weather radar data for the effects of bright band, range and orographic growth in widespread precipitation. *Quarterly Journal of the Royal Meteorological Society*, **120 (518)**, 1231–1254.

Klugmann, D., K. Heinsohn, and H.-J. Kirtzel, 1996: A low cost 24 ghz fm-cw doppler radar rain profiler. *Contributions to Atmospheric Physics/Beitraege zur Physik der Atmosphaere*, **61 (9)**, 247–253.

Kollias, P., A. Battaglia, K. Lamer, B. P. Treserras, and S. A. Braun, 2022: Mind the

gap-part 3: Doppler velocity measurements from space. *Frontiers in Remote Sensing*, **3**, 860 284.

Kollias, P., S. Tanelli, A. Battaglia, and A. Tatarevic, 2014: Evaluation of earthcare cloud profiling radar doppler velocity measurements in particle sedimentation regimes. *Journal of Atmospheric and Oceanic Technology*, **31 (2)**, 366–386.

Kumar, L. S., Y. H. Lee, and J. T. Ong, 2011: Two-parameter gamma drop size distribution models for singapore. *IEEE Transactions on Geoscience and Remote Sensing*, **49 (9)**, 3371–3380, https://doi.org/10.1109/TGRS.2011.2124464.

Kumjian, M. R., 2012: Dual-polarization radar applications in meteorology. *Bulletin of the American Meteorological Society*, **93 (12)**, 1855–1870, https://doi.org/10.1175/BAMS-D-11-00255.1.

Kumjian, M. R., O. P. Prat, K. J. Reimel, M. van Lier-Walqui, and H. C. Morrison, 2022: Dual-polarization radar fingerprints of precipitation physics: A review. *Remote Sensing*, **14 (15)**, 3706, https://doi.org/10.3390/rs14153706.

Kumjian, M. R., A. V. Ryzhkov, S. Trömel, M. Diederich, K. Mühlbauer, and C. Simmer, 2012: Retrievals of warm-rain microphysics using x-band polarimetric radar data. *26th Conf. on Hydrology, New Orleans, LA, Amer. Meteor. Soc.*

Kummerow, C., and Coauthors, 2000: The status of the tropical rainfall measuring mission (trmm) after two years in orbit. *Journal of Applied Meteorology*, **39 (12)**, 1965 – 1982, https://doi.org/10.1175/1520-0450(2001)040<1965:TSOTTR>2.0.CO;2.

Kurdzo, J. M., M. F. Donovan, J. Y. Cho, and B. J. Bennett, 2024: Impact of wsr-88d meso-sails usage on mrms-based quantitative precipitation estimation. *2024 IEEE Radar Conference (RadarConf24)*, IEEE, 1–6.

Leinonen, J., 2014: High-level interface to t-matrix scattering calculations: architecture, capabilities and limitations. *Optics Express*, **22 (2)**, 1655–1660, https://doi.org/10.1364/OE.22.001655, the PyTMatrix software package is described in this article. It relies on the Fortran T-matrix code by M. I. Mishchenko and L. D. Travis.

Leinonen, J., D. Moisseev, V. Chandrasekar, and J. Koskinen, 2011: Mapping radar reflectivity values of snowfall between frequency bands. *IEEE transactions on geoscience and remote sensing*, **49 (8)**, 3047–3058.

Liao, L., and R. Meneghini, 2022: Gpm dpr retrievals: Algorithm, evaluation, and

validation. *Remote Sensing*, **14 (4)**, 843, https://doi.org/https://doi.org/10.3390/rs14040843.

Liao, L., R. Meneghini, and A. Tokay, 2014: Uncertainties of gpm dpr rain estimates caused by dsd parameterizations. *Journal of Applied Meteorology and Climatology*, **53 (11)**, 2524–2537, https://doi.org/https://doi.org/10.1175/JAMC-D-14-0003.1.

Llort, X., 2010: A study of the structure of radar rainfall and its errors. Ph.D. thesis, Tesis doctoral, Universidad Politécnica de Cataluña.

Maggioni, V., M. R. Sapiano, and R. F. Adler, 2016: Estimating uncertainties in high-resolution satellite precipitation products: Systematic or random error? *Journal of Hydrometeorology*, **17 (4)**, 1119–1129.

Mamalakis, A., and Coauthors, 2021: Zonally contrasting shifts of the tropical rainbelt in response to climate change. *Nature Climate Change*, **11 (2)**, 242–248, https://doi.org/10.1038/s41558-020-00959-8.

Mandapaka, P. V., and U. Germann, 2010: Radar-rainfall error models and ensemble generators. *Rainfall: state of the science*, **191**, 247–264.

Marshall, J., and W. M. Palmer, 1948: Shorter contributions. *J. Meteorol*, **5**, 166.

Martin, B., 1998: Tied knowledge: Power in higher education. University of Wollongong, URL https://documents.uow.edu.au/~bmartin/pubs/98tk/, accessed: 2025-10-25.

Masaki, T., T. Iguchi, K. Kanemaru, K. Furukawa, N. Yoshida, T. Kubota, and R. Oki, 2020: Calibration of the dual-frequency precipitation radar onboard the global precipitation measurement core observatory. *IEEE Transactions on Geoscience and Remote Sensing*, **60**, 1–16.

Matrosov, S. Y., 1992: Radar reflectivity in snowfall. *IEEE Transactions on Geoscience and Remote Sensing*, **30 (3)**, 454–461, https://doi.org/10.1109/36.134085.

Matrosov, S. Y., A. Korolev, M. Wolde, and C. Nguyen, 2022: Sizing ice hydrometeor populations using the dual-wavelength radar ratio. *Atmospheric Measurement Techniques*, **15 (21)**, 6373–6386, https://doi.org/10.5194/amt-15-6373-2022.

Matsuyama, T., 2006: Derivation of mie theory of light scattering. *Journal of the Society of Powder Technology, Japan*, **43 (2)**, 115–124, https://doi.org/10.4164/sptj.43.115.

Media, S., 2025: Norman, ok. tornado june 3 2025. YouTube, URL https://www.youtube.com/watch?v=tAgaegow_9I, accessed: 2025-11-01, YouTube video.

Merton, R. K., 1968: The matthew effect in science. *Science*, **159 (3810)**, 56–63, https://doi.org/10.1126/science.159.3810.56, URL https://doi.org/10.1126/science.159.3810.56.

Min, C., S. Chen, J. J. Gourley, H. Chen, A. Zhang, Y. Huang, and C. Huang, 2019: Coverage of china new generation weather radar network. *Advances in Meteorology*, **2019 (1)**, 5789358.

Moncrieff, M. W., 2010: The multiscale organization of moist convection and the intersection of weather and climate. *Climate dynamics: Why does climate vary*, **189**, 3–26.

Moroda, Y., K. Tsuboki, S. Satoh, K. Nakagawa, T. Ushio, and S. Shimizu, 2021: Structure and evolution of precipitation cores in an isolated convective storm observed by phased array weather radar. *Journal of the Meteorological Society of Japan. Ser. II*, **99 (3)**, 765–784.

Morrison, H., 2012: On the robustness of aerosol effects on an idealized supercell storm simulated with a cloud system-resolving model. *Atmospheric Chemistry and Physics*, **12**, 7689–7705, https://doi.org/10.5194/acp-12-7689-2012.

Mroz, K., A. Battaglia, and A. M. Fridlind, 2023: Enhancing consistency of microphysical properties of precipitation across the melting layer in the dual-frequency precipitation radar data. *EGUsphere*, **2023**, 1–31.

Munchak, S. J., C. D. Kummerow, and G. Elsaesser, 2012: Relationships between the raindrop size distribution and properties of the environment and clouds inferred from trmm. *Journal of climate*, **25 (8)**, 2963–2978, https://doi.org/https://doi.org/10.1175/JCLI-D-11-00274.1.

Murphy, A. M., A. Ryzhkov, and P. Zhang, 2020: Columnar vertical profile (cvp) methodology for validating polarimetric radar retrievals in ice using in situ aircraft measurements. *Journal of Atmospheric and Oceanic Technology*, **37 (9)**, 1623–1642.

Nakamura, K., 2021: Progress from trmm to gpm. *Journal of the Meteorological Society of Japan. Ser. II*, **99 (3)**, 697–729.

NASA, 2020: IMERG: Integrated Multi-satellitE Retrievals for GPM. NASA, accessed: 2025-11-17, https://gpm.nasa.gov/data/imerg.

NASA, 2023a: Gpm dual-frequency precipitation radar (dpr). NASA, URL https://gpm.nasa.gov/missions/GPM/DPR, accessed: 2024-09-29.

NASA, 2023b: Nasa atmosphere observing system: Spaceborne architecture. NASA, accessed 2023-02-01, https://aos.gsfc.nasa.gov/spaceborne.htm.

NASA Global Precipitation Measurement Mission, 2020: Dual-frequency precipitation radar (dpr). NASA, accessed: 2025-10-26, https://gpm.nasa.gov/missions/GPM/DPR.

National Academies of Sciences, Engineering, and Medicine, 2019: *Thriving on Our Changing Planet: A Decadal Strategy for Earth Observation from Space*. National Academies Press.

National Oceanic and Atmospheric Administration, 2000: Atmosphere–ocean: Radar scattering and hydrometeor-size regimes. Tech. rep., NOAA. URL https://repository.library.noaa.gov/view/noaa/59391/noaa_59391_DS1.pdf.

National Severe Storms Laboratory, 2025: Nssl publications: Par reports. National Severe Storms Laboratory, accessed: 2025-11-15, https://www.nssl.noaa.gov/publications/par_reports/.

National Severe Storms Laboratory, National Oceanic and Atmospheric Administration, 2023: Mrms qvs product viewer. National Oceanic and Atmospheric Administration, URL https://mrms.nssl.noaa.gov/qvs/product_viewer/, accessed on October 30, 2023.

National Severe Storms Laboratory, NOAA, 2024: Multi-radar/multi-sensor (mrms) operational product viewer. National Severe Storms Laboratory, NOAA, accessed: 2025-11-24, https://mrms.nssl.noaa.gov/qvs/product_viewer/.

National Weather Service, 2015: Wsr-88d volume coverage pattern (vcp) improvement initiatives. Technical Report New_VCP_Paradigm_Public_Oct_2015, Office of Radar Operations Center. URL https://www.weather.gov/media/roc/NewScience/New_VCP_Paradigm_Public_Oct_2015.pdf, accessed: 2025-11-15.

Neeman, H., Z. Gray, D. Brunson, E. Huebsch, D. Horton, J. Deaton, and D. Gentis, 2013: The oklahoma cyberinfrastructure initiative. *Proceedings of the Conference on Extreme Science and Engineering Discovery Environment: Gateway to Discovery*, 1–6.

Neuper, M., and U. Ehret, 2019: Quantitative precipitation estimation with weather radar using a data-and information-based approach. *Hydrology and Earth System*

Sciences, **23 (9)**, 3711–3733.

Niu, S., X. Jia, J. Sang, X. Liu, C. Lu, and Y. Liu, 2010: Distributions of raindrop sizes and fall velocities in a semiarid plateau climate: Convective versus stratiform rains. *Journal of Applied Meteorology and Climatology*, **49 (4)**, 632–645.

NOAA National Severe Storms Laboratory, 2025a: Mrms operational product viewer. URL https://mrms.nssl.noaa.gov/qvs/product_viewer/, accessed: 2025-11-16, Web application.

NOAA National Severe Storms Laboratory, 2025b: Noaa noxp mobile radar. NOAA, accessed: 2025-10-29, https://www.nssl.noaa.gov/projects/torus/noxp.php.

NOAA National Severe Storms Laboratory, 2025c: Total trailer. NOAA National Severe Storms Laboratory, URL https://inside.nssl.noaa.gov/total/trailer/, accessed: 2025-11-16, Web page.

NOAA Physical Sciences Laboratory, ????: *Operating Instructions for the Optical Disdrometer: Present Weather Sensor OTT Parsivel2*. National Oceanic and Atmospheric Administration, URL https://psl.noaa.gov/data/obs/instruments/OpticalDisdrometer.pdf, accessed: 2026-01-03.

NOAA Storm Prediction Center, 2025: Mesoscale analysis archive. URL https://www.spc.noaa.gov/exper/mesoanalysis/, accessed: 2025-11-16, Web page.

NWS, 2025: The nexrad network: Nationwide high-resolution doppler radar coverage for storm, tornado, and flood detection. National Weather Service/NOAA, accessed: 2025-11-15, https://www.weather.gov/roc/About.

Oklahoma Mesonet, Oklahoma Climatological Survey, 2025: Mesonet data files – past data. Oklahoma Mesonet, URL https://www.mesonet.org/past-data/mesonet-resources/mesonet-data-files, accessed: 2025-11-16, Web page.

Olea, R. A., 2000: Geostatistics for engineers and earth scientists. Taylor & Francis.

Oue, M., A. Tatarevic, P. Kollias, D. Wang, K. Yu, and A. M. Vogelmann, 2020: The cloud-resolving model radar simulator (cr-sim) version 3.3: description and applications of a virtual observatory. *Geoscientific Model Development*, **13 (4)**, 1975–1998.

Palmer, R. D., and Coauthors, 2023a: Horus – An All-Digital Phased Array Weather Radar Developed at the University of Oklahoma. *103rd AMS Annual Meeting*, AMS.

Palmer, R. D., and Coauthors, 2023b: Horus—A Fully Digital Polarimetric Phased Array Radar for Next-Generation Weather Observations. *IEEE Transactions on Radar Systems*, **1**, 96–117, https://doi.org/10.1109/TRS.2023.3280033.

Paulitsch, H., F. Teschl, and W. L. Randeu, 2009: Dual-polarization c-band weather radar algorithms for rain rate estimation and hydrometeor classification in an alpine region. *Advances in Geosciences*, **20**, 3–8, https://doi.org/10.5194/adgeo-20-3-2009.

Peleg, N., M. Ben-Asher, and E. Morin, 2013: Radar subpixel-scale rainfall variability and uncertainty: lessons learned from observations of a dense rain-gauge network. *Hydrology and Earth System Sciences*, **17 (6)**, 2195–2208.

Pendergrass, A. G., 2020: Changing degree of convective organization as a mechanism for dynamic changes in extreme precipitation. *Current Climate Change Reports*, **6 (2)**, 47–54, https://doi.org/10.1007/s40641-020-00157-9.

Pendergrass, A. G., K. A. Reed, and B. Medeiros, 2016: The link between extreme precipitation and convective organization in a warming climate: Global radiative-convective equilibrium simulations. *Geophysical Research Letters*, **43 (21)**, 11–445.

Petersen, W. A., P.-E. Kirstetter, J. Wang, D. B. Wolff, and A. Tokay, 2020a: The gpm ground validation program. *Satellite Precipitation Measurement: Volume 2*, 471–502.

Petersen, W. A., and Coauthors, 2020b: *The GPM Ground Validation Program*, 471–502. Springer International Publishing, Cham, https://doi.org/10.1007/978-3-030-35798-6_2, URL https://doi.org/10.1007/978-3-030-35798-6_2.

Pinsky, M., A. Khain, and H. Krugliak, 2008: Collisions of cloud droplets in a turbulent flow. part v: Application of detailed tables of turbulent collision rate enhancement to simulation of droplet spectra evolution. *Journal of the Atmospheric Sciences*, **65**, 357–374, https://doi.org/10.1175/2007JAS2358.1.

Porcacchia, L., P. Kirstetter, J. Gourley, V. Maggioni, B. Cheong, and M. Anagnostou, 2017: Toward a polarimetric radar classification scheme for coalescence-dominant precipitation: Application to complex terrain. *Journal of Hydrometeorology*, **18 (12)**, 3199–3215.

Porcacchia, L., P.-E. Kirstetter, V. Maggioni, and S. Tanelli, 2019: Investigating the gpm dual-frequency precipitation radar signatures of low-level precipitation enhancement. *Quarterly Journal of the Royal Meteorological Society*, **145 (724)**, 3161–3174.

Pöschmann, J. M., D. Kim, R. Kronenberg, and C. Bernhofer, 2020: An analysis on temporal scaling behavior of extreme rainfall of germany based on radar precipitation

qpe data. *Natural Hazards and Earth System Sciences Discussions*, **2020**, 1–21.

Potvin, C. K., A. Shapiro, and J. Gao, 2012: A comparison of horizontal wind retrievals from single- and dual-doppler radar observations of deep convection. *Journal of Atmospheric and Oceanic Technology*, **29 (7)**, 924–944, https://doi.org/10.1175/JTECH-D-11-00112.1, URL https://journals.ametsoc.org/view/journals/atot/29/7/jtech-d-11-00112_1.xml.

Pradhan, R. K., and Coauthors, 2022a: Review of gpm imerg performance: A global perspective. *Remote Sensing of Environment*, **268**, 112 754.

Pradhan, R. K., and Coauthors, 2022b: Review of gpm imerg performance: A global perspective. *Remote Sensing of Environment*, **268**, 112 754.

Prat, O., and B. Nelson, 2015: Evaluation of precipitation estimates over conus derived from satellite, radar, and rain gauge data sets at daily to annual scales (2002–2012). *Hydrology and Earth System Sciences*, **19 (4)**, 2037–2056, https://doi.org/https://doi.org/10.5194/hess-19-2037-2015.

Radar Operations Center, National Weather Service / NOAA, 2011: Automated volume scan evaluation and termination (avset) for wsr-88d. Technical report, https://www.roc.noaa.gov/radar-techniques/avset.php, National Weather Service, NOAA. URL https://www.roc.noaa.gov/radar-techniques/avset.php, describes the concept and implementation of AVSET to dynamically terminate VCPs early.

Radar Operations Center, National Weather Service / NOAA, 2016: Mid-volume rescan of low-level elevations (mrle) for wsr-88d. Technical report, https://www.roc.noaa.gov/radar-techniques/mrle.php, National Weather Service, NOAA. URL https://www.roc.noaa.gov/radar-techniques/mrle.php, describes MRLE rescan of up to the four lowest elevation angles.

Raghunathan, K. D., and S. P. Gowri, 2018: Reconstruction of reflector surface deformations using back-projection. *NAECON 2018-IEEE National Aerospace and Electronics Conference*, IEEE, 618–621.

Ray, P. S., C. L. Ziegler, E. N. Rasmussen, and R. J. Serafin, 1978: Dual-doppler observations of a tornadic thunderstorm: The evolution of precipitation loading and the tornado circulation. *Journal of Applied Meteorology*, **17 (5)**, 563–585, https://doi.org/10.1175/1520-0450(1978)017<0563:DDOOAT>2.0.CO;2, URL https://journals.ametsoc.org/view/journals/apme/17/5/1520-0450_1978_017_0563_ddooat_2_0_co_2.xml.

Rigby, R. A., and D. M. Stasinopoulos, 2005: Generalized additive models for location,

scale and shape. *Journal of the Royal Statistical Society Series C: Applied Statistics*, **54 (3)**, 507–554.

Rosenfeld, D., and C. W. Ulbrich, 2003: Cloud microphysical properties, processes, and rainfall estimation opportunities. *Meteorological Monographs*, **30 (52)**, 237–258.

Rosenfeld, D., D. B. Wolff, and D. Atlas, 1993: General probability-matched relations between radar reflectivity and rain rate. *Journal of Applied Meteorology and Climatology*, **32 (1)**, 50–72.

Rowe, A. K., S. A. Rutledge, and T. J. Lang, 2011: Investigation of microphysical processes occurring in isolated convection during name. *Monthly weather review*, **139 (2)**, 424–443, https://doi.org/https://doi.org/10.1175/2010MWR3494.1.

Rowe, A. K., S. A. Rutledge, and T. J. Lang, 2012: Investigation of microphysical processes occurring in organized convection during name. *Monthly Weather Review*, **140 (7)**, 2168–2187, https://doi.org/https://doi.org/10.1175/MWR-D-11-00124.1.

Ryzhkov, A., M. Diederich, P. Zhang, and C. Simmer, 2014: Potential utilization of specific attenuation for rainfall estimation, mitigation of partial beam blockage, and radar networking. *Journal of Atmospheric and Oceanic Technology*, **31 (3)**, 599–619.

Ryzhkov, A., S. Giangrande, A. Khain, M. Pinsky, and A. Pokrovsky, 2008: Exploring model-based polarimetric retrieval of vertical profiles of precipitation. *Extended Abstracts, Fifth European Conf. on Radar in Meteorology and Hydrology.*

Ryzhkov, A., S. Giangrande, and D. Zrnic, 2002: Using multiparameter data to calibrate polarimetric weather radars in the presence of a partial beam blockage. *IEEE International Geoscience and Remote Sensing Symposium*, IEEE, Vol. 5, 2832–2834.

Ryzhkov, A., M. Pinsky, A. Pokrovsky, and A. Khain, 2011: Polarimetric radar observation operator for a cloud model with spectral microphysics. *Journal of Applied Meteorology and Climatology*, **50 (4)**, 873–894.

Ryzhkov, A., T. J. Schuur, P. Zhang, M. R. Kumjian, and Y. Wang, 2022: Polarimetric radar quantitative precipitation estimation. *Remote Sensing*, **14 (7)**, 1695, https://doi.org/10.3390/rs14071695.

Ryzhkov, A., P. Zhang, H. Reeves, M. Kumjian, T. Tschallener, S. Trömel, and C. Simmer, 2016: Quasi-vertical profiles—a new way to look at polarimetric radar data. *Journal of Atmospheric and Oceanic Technology*, **33 (3)**, 551–562.

Ryzhkov, A., and Coauthors, 2007: Comparison of polarimetric algorithms for hydrom-

eteor classification at s and c bands. *Journal Name*.

Ryzhkov, A. V., 2001: Interpretation of polarimetric radar covariance matrix for meteorological scatterers: Theoretical analysis. *Journal of Atmospheric and Oceanic Technology*, **18 (3)**, 315–328.

Ryzhkov, A. V., M. R. Kumjian, S. M. Ganson, and A. P. Khain, 2013a: Polarimetric radar characteristics of melting hail. part i: Theoretical simulations using spectral microphysical modeling. *Journal of Applied Meteorology and Climatology*, **52 (12)**, 2849–2870, https://doi.org/10.1175/JAMC-D-13-073.1.

Ryzhkov, A. V., M. R. Kumjian, S. M. Ganson, and A. P. Khain, 2013b: Polarimetric radar characteristics of melting hail. Part I: Theoretical simulations using spectral microphysical modeling. *Journal of Applied Meteorology and Climatology*, **52 (12)**, 2849 – 2870, https://doi.org/10.1175/JAMC-D-13-073.1.

Ryzhkov, A. V., T. J. Schuur, D. W. Burgess, P. L. Heinselman, S. E. Giangrande, and D. S. Zrnic, 2005: The Joint Polarization Experiment: Polarimetric Rainfall Measurements and Hydrometeor Classification. *Bulletin of the American Meteorological Society*, **86 (6)**, 809–824, https://doi.org/10.1175/BAMS-86-6-809, URL https://doi.org/10.1175/BAMS-86-6-809, https://journals.ametsoc.org/bams/article-pdf/86/6/809/3735590/bams-86-6-809.pdf.

Salazar, C. M., B. Cheong, R. D. Palmer, D. Schvartzman, and A. Ryzhkov, 2024: Improvements in the compression filter and calibration factor of the progressive pulse compression technique. *IEEE Transactions on Geoscience and Remote Sensing*, **62**, 1–14, https://doi.org/10.1109/TGRS.2024.3401814.

Sauermann, H., and C. Haeussler, 2017: Authorship and contribution disclosures. *Science Advances*, **3 (11)**, e1700 404, https://doi.org/10.1126/sciadv.1700404, URL https://doi.org/10.1126/sciadv.1700404.

Schvartzman, D., S. M. Torres, and T.-Y. Yu, 2021: Distributed beams: Concept of operations for polarimetric rotating phased array radar. *IEEE Transactions on Geoscience and Remote Sensing*, **59 (11)**, 9173–9191.

scikit-learn contributors, 2024a: KMeans - scikit-learn 0.24.2 documentation. scikit-learn, accessed: 2024-06-20, https://scikit-learn.org/stable/modules/generated/sklearn.cluster.KMeans.html.

scikit-learn contributors, 2024b: Standardscaler - scikit-learn 0.24.2 documentation. scikit-learn, accessed: 2024-06-25, https://scikit-learn.org/stable/modules/generated/sklearn.preprocessing.StandardScaler.html.

Searls, M., 2022: Assessing precipitation delineation capabilities of spaceborne radars. *Journal Name*.

Seliga, T. A., V. Bringi, and H. Al-Khatib, 1981: A preliminary study of comparative measurements of rainfall rate using the differential reflectivity radar technique and a raingage network. *Journal of Applied Meteorology (1962-1982)*, 1362–1368.

Senesac, E., 2020: Key advances in weather history: Dual-pol radar. Accessed: 2025-12-07, https://vlab.noaa.gov/web/nws-heritage/-/key-advances-in-weather-history-dual-pol-radar.

Seo, D.-J., J. Breidenbach, R. Fulton, D. Miller, and T. O'Bannon, 2000: Real-time adjustment of range-dependent biases in wsr-88d rainfall estimates due to nonuniform vertical profile of reflectivity. *Journal of Hydrometeorology*, **1 (3)**, 222–240.

Seto, S., T. Iguchi, R. Meneghini, J. Awaka, T. Kubota, T. Masaki, and N. Takahashi, 2021: The precipitation rate retrieval algorithms for the gpm dual-frequency precipitation radar. *Journal of the Meteorological Society of Japan. Ser. II*, **99 (2)**, 205–237, https://doi.org/https://doi.org/10.2151/jmsj.2021-011.

Seto, S., T. Iguchi, T. Shimozuma, and S. Hayashi, 2015: Nubf correction methods for the gpm/dpr level-2 algorithms. *2015 IEEE International Geoscience and Remote Sensing Symposium (IGARSS)*, IEEE, 2612–2614, https://doi.org/10.1109/IGARSS.2015.7326347.

Shpund, J., and Coauthors, 2019: Simulating a mesoscale convective system using wrf with a new spectral bin microphysics: 1: Hail vs graupel. *Journal of Geophysical Research: Atmospheres*, **124 (24)**, 14 072–14 101.

Simpson, M. J., and N. I. Fox, 2018: Dual-polarized quantitative precipitation estimation as a function of range. *Hydrology and Earth System Sciences*, **22 (6)**, 3375–3396, https://doi.org/10.5194/hess-22-3375-2018, URL https://hess.copernicus.org/articles/22/3375/2018/.

Skofronick-Jackson, G., D. Kirschbaum, W. Petersen, G. Huffman, C. Kidd, E. Stocker, and R. Kakar, 2018: The global precipitation measurement (gpm) mission's scientific achievements and societal contributions: Reviewing four years of advanced rain and snow observations. *Quarterly Journal of the Royal Meteorological Society*, **144**, 27–48, https://doi.org/https://doi.org/10.1002/qj.3313.

Slater, D., 1994: An integrated near-field emc measurement system. *Proceedings of the IEEE EMC Conference*, 1330 E 223rd St #524, Carson, CA 90745, NSI-MI Technologies, URL https://www.nsi-mi.com/-/media/project/oneweb/oneweb/nsi/

files/technical-papers/1994/an-integrated-nf-emc-measurement-system.pdf, technical paper, Nearfield Systems Inc. / NSI-MI Technologies.

Spurr, R., J. Wang, J. Zeng, and M. I. Mishchenko, 2012: Linearized t-matrix and mie scattering computations. *Journal of Quantitative Spectroscopy & Radiative Transfer*, **113**, 425–439, https://doi.org/10.1016/j.jqsrt.2011.11.014.

Stasinopoulos, D. M., and R. A. Rigby, 2008: Generalized additive models for location scale and shape (gamlss) in r. *Journal of Statistical Software*, **23**, 1–46.

Steiner, M., R. A. Houze Jr, and S. E. Yuter, 1995: Climatological characterization of three-dimensional storm structure from operational radar and rain gauge data. *Journal of Applied Meteorology and Climatology*, **34 (9)**, 1978–2007.

Stephens, G. L., and Coauthors, 2019: A distributed small satellite approach for measuring convective transports in the earth's atmosphere. *IEEE Transactions on Geoscience and Remote Sensing*, **58 (1)**, 4–13.

Tao, W.-K., T. Iguchi, S. Lang, X. Li, K. Mohr, T. Matsui, S. Van den Heever, and S. Braun, 2022: Relating vertical velocity and cloud/precipitation properties: A numerical cloud ensemble modeling study of tropical convection. *Journal of Advances in Modeling Earth Systems*, **14 (9)**, e2021MS002 677, https://doi.org/10.1029/2021MS002677.

Tappan, M. B., 2006: Reframing internalized oppression and internalized domination: From the psychological to the sociocultural. *Teachers College Record*, **108 (10)**, 2115–2144, https://doi.org/10.1111/j.1467-9620.2006.00776.x, URL https://eric.ed.gov/?id=EJ743643, accessed: 2025-10-25.

Team, R. C., 2021: R: A language and environment for statistical computing.

Thomas, L., W. W. Grabowski, and B. Kumar, 2020: Diffusional growth of cloud droplets in homogeneous isotropic turbulence: Dns, scaled-up dns, and stochastic model. *Atmospheric Chemistry and Physics*, **20 (14)**, 9087–9100.

Thurai, M., V. Bringi, D. Wolff, D. Marks, and C. Pabla, 2021: Testing the drop-size distribution-based separation of stratiform and convective rain using radar and disdrometer data from a mid-latitude coastal region. *Atmosphere*, **12 (3)**, 392.

Tokay, A., L. P. D'Adderio, D. B. Wolff, and W. A. Petersen, 2020: Development and evaluation of the raindrop size distribution parameters for the nasa global precipitation measurement mission ground validation program. *Journal of Atmospheric and Oceanic Technology*, **37 (1)**, 115–128.

Torres, S., and D. Wasielewski, 2022: The advanced technology demonstrator at the national severe storms laboratory: Challenges and successes. *2022 IEEE Radar Conference (RadarConf22)*, IEEE, 1–6.

Torres, S. M., and Coauthors, 2016: Adaptive-weather-surveillance and multifunction capabilities of the national weather radar testbed phased array radar. *Proceedings of the IEEE*, **104 (3)**, 660–672.

Tremblay, A., 2005: The stratiform and convective components of surface precipitation. *Journal of the atmospheric sciences*, **62 (5)**, 1513–1528.

Ulbrich, C. W., and D. Atlas, 1978: The rain parameter diagram: Methods and applications. *Journal of Geophysical Research: Oceans*, **83 (C3)**, 1319–1325, https://doi.org/https://doi.org/10.1029/JC083iC03p01319.

University Corporation for Atmospheric Research (UCAR), 2012–2017: Weather radar fundamentals — reflectivity scales. https://research.atmos.ucla.edu/weather/C110/Documents/tmp/basic_wxradar/navmenu.php_tab_1_page_2_4_0_type_text.htm.

University of Wyoming Department of Atmospheric Science, 2023: University of wyoming upper-air data. University of Wyoming Department of Atmospheric Science, URL https://weather.uwyo.edu/upperair/sounding.html, accessed on October 30, 2023.

Upadhyaya, S. A., P.-E. Kirstetter, R. J. Kuligowski, J. J. Gourley, and H. M. Grams, 2021: Classifying precipitation from geo satellite observations: Prognostic model. *Quarterly Journal of the Royal Meteorological Society*, **147 (739)**, 3394–3409.

Valdivia, J. M., P. N. Gatlin, S. Kumar, D. Scipión, Y. Silva, and W. A. Petersen, 2022: The gpm-dpr blind zone effect on satellite-based radar estimation of precipitation over the andes from a ground-based ka-band profiler perspective. *Journal of Applied Meteorology and Climatology*, **61 (4)**, 441–456.

Van den Heever, S., and Coauthors, 2022: The incus mission. *Egu general assembly conference abstracts*, EGU22–9021.

Van den Heever, S. C., Z. S. Haddad, S. Tanelli, D. J. Posselt, O. Sy, L. D. Grant, S. Prasanth, and G. L. Stephens, 2024: The delta-t approach of the nasa incus mission. *AGU Fall Meeting Abstracts*, Vol. 2024, A31N–192.

Wang, J., and D. B. Wolff, 2010: Evaluation of trmm ground-validation radar-rain errors using rain gauge measurements. *Journal of Applied Meteorology and Clima-*

tology, **49 (2)**, 310–324.

Wang, Y., S. Cocks, L. Tang, A. Ryzhkov, P. Zhang, J. Zhang, and K. Howard, 2019: A prototype quantitative precipitation estimation algorithm for operational s-band polarimetric radar utilizing specific attenuation and specific differential phase. part i: Algorithm description. *Journal of Hydrometeorology*, **20 (5)**, 985–997.

White House Office of Science and Technology Policy (OSTP), 2022: Memorandum for the heads of executive departments and agencies: "ensuring free, immediate, and equitable access to federally funded research". White House Office of Science and Technology Policy, URL https://www.whitehouse.gov/wp-content/uploads/2022/08/08-2022-OSTP-Public-Access-Memo.pdf, issued August 25 2022, Policy memorandum.

Williams, C. R., 2016: Reflectivity and liquid water content vertical decomposition diagrams to diagnose vertical evolution of raindrop size distributions. *Journal of Atmospheric and Oceanic Technology*, **33 (3)**, 579–595.

Williams, C. R., and S. E. Giangrande, 2023: Vertical structure of raindrop size distributions below the radar brightband. *AGU Fall Meeting Abstracts*, A31B–2376, 2376.

World Meteorological Organization, 2024: Rainfall intensity classification guidelines. Commonly used intensity categories: light (<2.5 mm/hr), moderate (2.5–7.6 mm/hr), heavy (>7.6 mm/hr), violent/torrential (>50 mm/hr), Technical reference.

Young, A. T., 1982: Rayleigh scattering. *Phys. Today*, **35 (1)**, 42–48.

Zhang, G., and Coauthors, 2019: Current status and future challenges of weather radar polarimetry: Bridging the gap between radar meteorology/hydrology/engineering and numerical weather prediction. *Advances in Atmospheric Sciences*, **36 (6)**, 571–588, https://doi.org/10.1007/s00376-019-8172-4, URL https://doi.org/10.1007/s00376-019-8172-4.

Zhang, J., C. Langston, and K. Howard, 2008: Brightband identification based on vertical profiles of reflectivity from the wsr-88d. *Journal of Atmospheric and Oceanic Technology*, **25 (10)**, 1859–1872.

Zhang, J., and Coauthors, 2011: National mosaic and multi-sensor qpe (nmq) system: Description, results, and future plans. *Bulletin of the American Meteorological Society*, **92 (10)**, 1321–1338.

Zhang, J., and Coauthors, 2016a: Multi-radar multi-sensor (mrms) quantitative pre-

cipitation estimation: Initial operating capabilities. *Bulletin of the American Meteorological Society*, **97 (4)**, 621–638.

Zhang, J., and Coauthors, 2016b: Multi-radar multi-sensor (mrms) quantitative precipitation estimation: Initial operating capabilities. *Bulletin of the American Meteorological Society*, **97 (4)**, 621–638, https://doi.org/https://doi.org/10.1175/BAMS-D-14-00174.1.

Zhao, C., and Coauthors, 2025: An investigation into the dominant cloud microphysical processes in extreme-rain-producing storms occurred on 7 may 2017 over southern china. *Atmospheric Research*, **314**, 107 820, https://doi.org/10.1016/j.atmosres.2024.107820.

Zrnić, D. S., and A. V. Ryzhkov, 1996: Advantages of rain measurements using specific differential phase. *Journal of Atmospheric and Oceanic Technology*, **13 (2)**, 454–464, https://doi.org/10.1175/1520-0426(1996)013<0454:AORMUS>2.0.CO;2, demonstrated that K_{DP} is approximately proportional to liquid water content and is well suited for quantitative precipitation estimation (QPE) applications.